SLAC-R-923
May 2009

STUDY OF B-MESON DECAYS TO FINAL STATES WITH A SINGLE CHARM BARYON

A DISSERTATION
SUBMITTED TO THE DEPARTMENT OF APPLIED PHYSICS
AND THE COMMITTEE ON GRADUATE STUDIES
OF STANFORD UNIVERSITY
IN PARTIAL FULFILLMENT OF THE REQUIREMENTS
FOR THE DEGREE OF
DOCTOR OF PHILOSOPHY

Stephanie A. Majewski
August 2007

SLAC National Accelerator Laboratory, Menlo Park, Ca 94025

Work supported in part by US Department of Energy contract DE-AC02-76SF00515

I certify that I have read this dissertation and that, in my opinion, it is fully adequate in scope and quality as a dissertation for the degree of Doctor of Philosophy.

(Patricia Burchat) Principal Adviser

I certify that I have read this dissertation and that, in my opinion, it is fully adequate in scope and quality as a dissertation for the degree of Doctor of Philosophy.

(Ian Fisher)

I certify that I have read this dissertation and that, in my opinion, it is fully adequate in scope and quality as a dissertation for the degree of Doctor of Philosophy.

(Dong Su)

Approved for the University Committee on Graduate Studies.

Abstract

A study of B-meson decays to final states with a single charm baryon is presented based on data recorded by the *BABAR* detector at the Stanford Linear Accelerator Center. Although the B meson is the lightest bottom-flavored meson, it is heavy enough to decay to a baryon made of three quarks and an antibaryon made of three antiquarks. By studying the baryonic weak decays of the B meson, we can investigate baryon production mechanisms in heavy meson decays. In particular, we measure the rates of the decays $B^- \rightarrow \mathit{\Lambda}_c^+ \overline{p} \pi^-$ and $\overline{B}^0 \rightarrow \mathit{\Lambda}_c^+ \overline{p}$. Comparing these rates, we confirm an observed trend in baryonic B decays that the decay with the lower energy release, $B^- \rightarrow \mathit{\Lambda}_c^+ \overline{p} \pi^-$, is favored over $\overline{B}^0 \rightarrow \mathit{\Lambda}_c^+ \overline{p}$. The dynamics of the baryon-antibaryon ($\mathit{\Lambda}_c^+ \overline{p}$) system in the three-body decay also provide insight into baryon-antibaryon production mechanisms. The $B^- \rightarrow \mathit{\Lambda}_c^+ \overline{p} \pi^-$ system is a laboratory for searches for excited $\mathit{\Sigma}_c$ baryon states; we observe the resonant decays $B^- \rightarrow \mathit{\Sigma}_c(2455)^0 \overline{p}$ and $B^- \rightarrow \mathit{\Sigma}_c(2800)^0 \overline{p}$. This is the first observation of the decay $B^- \rightarrow \mathit{\Sigma}_c(2800)^0 \overline{p}$; however, the mass of the observed $\mathit{\Sigma}_c(2800)^0$ state is inconsistent with previous measurements. Finally, we examine the angular distribution of the $B^- \rightarrow \mathit{\Sigma}_c(2455)^0 \overline{p}$ decays and measure the spin of the $\mathit{\Sigma}_c(2455)^0$ baryon to be $J = 1/2$, as predicted by the quark model.

Acknowledgements

Thank you to my adviser, Pat, for being a true mentor throughout graduate school, for demonstrating that one can be successful and highly respected while exemplifying balance. Pat is the kind of physicist I strive to be, and I admire her immensely. Thanks to the Burchat group: Brian and Adam for being my officemates for the past five years, for our enjoyable physics and non-physics discussions. Thanks also to Ariel, Beth, Brendan, Chris, Leif, Michael, and Tomo; I look forward to hearing about your future accomplishments.

This dissertation would not have been possible without the support of over 500 *BABAR* colleagues. Thank you especially to Bill Dunwoodie for performing the angular analysis calculations and providing invaluable insight. Thank you also to my review committee, Denis Bernard, Giampiero Mancinelli, and Gabriele Simi.

Thank you to my parents, who have been there every step of the way, from moving to one coast through moving to the opposite one. I would also like to thank my brother Tim; I am very proud to be his big sister. Thank you also to my extended family: Anka, Aunt Helen, Bridget, Maria, Matt, Nona, Pete, Tom, and welcome baby Thomas.

It all started with late-night problem sets around a table in my living room. Thanks to Bill (the first one out!), Eric, Erica, Ginel, and Nick for sharing the pain. Between Nuthouse Thursdays and Physics beer, football and basketball season, thanks to the physicists who knew how to have fun and kept me sane... Brian, Chad, Eugene, Geert, Guillaume, Jason, Kaushik, Mark^2, Mike, Nick, Praj, Tommer, Wells. Keep those pitchers coming and don't forget the peanuts. Thank you to the women in Physics and Applied Physics for being brilliant and fun girls, especially Ann, Fen, Ginel, Ileana, Naoko, Sara, Susan, Yvonne. And also thanks to the non-physics girls: Becky, Emmalynne, Jamie, Jen, Madonna, Margie, Sarah, Wendy. You are all amazingly talented and successful, and I treasure our friendships.

I am grateful for the inspiring people I have met and the lifelong friends I have made at Stanford.

Contents

List of Tables

List of Figures

Chapter 1

Introduction

Particle physics is the study of the elementary constituents of matter: quarks and leptons. The field also comprises the study of the fundamental interactions, which bind the quarks and leptons into composite particles, allow new particles to be produced, and mediate the decay of unstable particles. The properties of composite particles and the interactions between their constituents can be investigated by studying their production rates, decay characteristics and spectroscopy. In this dissertation, we analyze the weak decay of a heavy quark in a bound state of a quark and antiquark (a *meson*), focusing on decays in which a bound state of three quarks (a *baryon*) is produced.

The weakly decaying meson that we study is called the B meson because it contains a bottom quark. An abundant sample of B mesons has been produced at the B Factory and recorded by the *BABAR* detector at the Stanford Linear Accelerator Center (SLAC) located in Menlo Park, CA. By studying the baryonic decays of B mesons, we can

- investigate baryon production in heavy meson decays, including trends in decay rates and baryon production mechanisms;
- search for exotic states such as pentaquarks and glueballs [1, 2];
- search for excited baryon resonances;
- examine the angular distributions of B meson decay products to determine baryon spins;
- measure radiative baryonic B decays that could be sensitive to new physics through flavor-changing neutral currents [3, 4]; this relies heavily on improving our theoretical

understanding of baryonic B decays in general [5,6].

In particular, we investigate the decays $\overline{B}^0 \to \Lambda_c^+ \overline{p}$ and $B^- \to \Lambda_c^+ \overline{p} \pi^-$ [7]. Each of these modes contains a single charm baryon (Λ_c^+) in the final state. We can investigate baryon production in B decays in this system by comparing the two-body ($\overline{B}^0 \to \Lambda_c^+ \overline{p}$) and three-body ($B^- \to \Lambda_c^+ \overline{p} \pi^-$) decay rates. Furthermore, the dynamics of the baryon-antibaryon ($\Lambda_c^+ \overline{p}$) system in the three-body decay provide insight into baryon production mechanisms. The $B^- \to \Lambda_c^+ \overline{p} \pi^-$ system is also a laboratory for searches for excited baryon states and charm baryon spin measurements.

1.1 Bound States of Quarks

Quarks are spin-1/2 fermions that come in six flavors: up (u), down (d), strange (s), charm (c), bottom (b), and top (t). The u, c, and t quarks have an electric charge of $+\frac{2}{3}$ and the d, s, and b quarks have an electric charge of $-\frac{1}{3}$ in units of the charge of the electron. The estimated masses of the quark are listed in Table 1.1. Quarks have a "color charge" that comes in three types: red, green, and blue (similarly, anti-quarks are anti-red, anti-green, or anti-blue). Free quarks do not exist; they are found only in colorless bound states, such as mesons and baryons (collectively we call these *hadrons*). Mesons are a bound state of a quark and an anti-quark that are in a superposition of red anti-red, blue anti-blue, and green anti-green states. Examples of mesons are the π, K, D, and B mesons, which are pseudoscalar (spin-0) mesons, and the $\Upsilon(4S)$, which is a vector (spin-1) meson. Baryons are bound states of three quarks (red + green + blue = colorless). Examples of spin-1/2 baryons are the nucleons (proton = uud and neutron = udd) and the less-familiar charm baryons, such as the Λ_c^+ and Σ_c baryons (both contain udc). These particular mesons and baryons are summarized in Table 1.2, along with other mesons and baryons that will play a role in this thesis.

1.2 Charm baryon spectroscopy

Spectroscopy in particle physics is the investigation of the arrangement of composite particles by mass. The available states can be predicted from their required symmetries. A familiar example is the hydrogen atom, which consists of two spin-1/2 particles: an electron and a proton.

If we combine two spin-1/2 particles such as the electron and proton in the ground state of the hydrogen atom, or the electron and positron in positronium, we get the following spin states:

$$\begin{array}{c}\uparrow\uparrow \\ \frac{1}{\sqrt{2}}(\uparrow\downarrow + \downarrow\uparrow) \quad \text{(triplet, spin 1)} \\ \downarrow\downarrow\end{array}$$

$$\frac{1}{\sqrt{2}}(\uparrow\downarrow - \downarrow\uparrow) \quad \text{(singlet, spin 0)}$$

The triplet states are symmetric under the interchange of the two particles, while the singlet state is antisymmetric. Spin-1/2 states can be represented as spinors, and transform under rotations according to the 2×2 Pauli matrices. These matrices are representations of the SU(2) group, where S stands for special (determinant = 1), U stands for unitary, and the number 2 describes the dimensionality (in this case, that there are 2 possible spin states: $\uparrow$ and $\downarrow$). We use group theory notation to succinctly represent the combination of two

Table 1.1: Estimated quark masses [8]. Note the five orders of magnitude between the mass of the u quark and the mass of the t quark.

Quark	Mass
u	$(1.5 - 3.0)$ MeV/c^2
d	$(3 - 7)$ MeV/c^2
s	(95 ± 25) MeV/c^2
c	(1.25 ± 0.09) GeV/c^2
b	(4.20 ± 0.07) GeV/c^2
t	(172.5 ± 2.7) GeV/c^2

Table 1.2: Quark content and masses of selected mesons and baryons [9].

Meson	Quark Content	Mass (MeV/c^2)
π^+	$u\bar{d}$	139.6
π^0	$(u\bar{u} - d\bar{d})/\sqrt{2}$	135.0
K^+	$u\bar{s}$	493.7
K^0	$d\bar{s}$	497.6
D^+	$\bar{d}c$	1869.3
D^0	$\bar{u}c$	1864.5
B^+	$u\bar{b}$	5279.0
B^0	$d\bar{b}$	5279.4
$\Upsilon(4S)$	$b\bar{b}$	10579

Baryon	Quark Content	Mass (MeV/c^2)
p	uud	938.3
n	udd	939.6
Λ	uds	1115.7
Ξ^0	uss	1314.8
Ξ^-	dss	1321.3
Λ_c^+	udc	2286.5
$\Sigma_c(2455)^{++}$	uuc	2454.0
$\Sigma_c(2455)^+$	udc	2452.9
$\Sigma_c(2455)^0$	ddc	2453.8
$\Sigma_c(2520)^{++}$	uuc	2518.4
$\Sigma_c(2520)^+$	udc	2517
$\Sigma_c(2520)^0$	ddc	2518.0
$\Sigma_c(2800)^{++}$	uuc	2801
$\Sigma_c(2800)^+$	udc	2792
$\Sigma_c(2800)^0$	ddc	2802

spin-1/2 states to form a triplet and a singlet:

$$2 \otimes 2 = 3 \oplus 1. \tag{1.1}$$

We can extend this analogy to spin-1/2 quarks, except that in baryon spectroscopy we must combine three spin-1/2 states:

$$2 \otimes 2 \otimes 2 = 4 \oplus 2 \oplus 2. \tag{1.2}$$

The spin-3/2 combination (four possible states) is completely symmetric under the interchange of two quarks. The spin-1/2 combinations (each with two possible states) are antisymmetric under the interchange of only two of the three constituent quarks (so we say that these states have “mixed” symmetry).

The mathematical language of group theory is not only applicable to spin, but also works for other symmetries of a multi-particle system. When combining three quarks to form a baryon, the relevant parts of the wave function are spin, orbital angular momentum (which determines the spatial part of the wave function), quark flavor, and color. Therefore, we can construct a wave function for the baryon with these four components. And we must not forget the Pauli exclusion principle: since each constituent quark is a fermion, the combined wave function must be antisymmetric under the interchange of any two quarks.

The exact form of the spatial part of the wave function is not known, but is analogous to the hydrogen atom in that it consists of a radial component times an orbital angular momentum component. There are actually two independent orbital angular momenta (ℓ and ℓ') in a system of three particles. One can imagine that the orbital angular momentum component is the product of spherical harmonics

$$Y_\ell^{m_\ell}(\theta, \phi) = \sqrt{\frac{(2\ell+1)}{4\pi}\frac{(\ell-m_\ell)}{(\ell+m_\ell)}}(-1)^{m_\ell} P_\ell^{m_\ell}(\cos\theta) e^{i m_\ell \phi}, \tag{1.3}$$

where m_ℓ is the z-component of the angular momentum in units of $\hbar$, θ is the polar angle and ϕ is the azimuthal angle. The quantum number m_ℓ can take on integer values in the range $[-\ell, \ell]$. For even ℓ, the function is symmetric and for odd ℓ it is antisymmetric under the interchange of the two particles. Thus the spatial part of the wave function is symmetric in the ground state ($\ell = \ell' = 0$).

The flavor component for charm baryons is represented by the SU(4) group (since we are considering states containing only u, d, s, and c). Flavor symmetry is only valid if we neglect the different masses of the different quark flavors[1]. Combining three quarks with four possible flavors for each quark, we obtain

$$4 \otimes 4 \otimes 4 = 20 \oplus 20'_1 \oplus 20'_2 \oplus \bar{4}. \tag{1.4}$$

The 20-plet is completely symmetric. Each of the $20'$-plets are antisymmetric under the interchange of two of the three constituents, and the $\bar{4}$-plet is completely antisymmetric.

The final component of the wave function is the color component[2]. There are three possible colors for each quark in a baryon, so it is represented by the SU(3) group. The colors combine as

$$3 \otimes 3 \otimes 3 = 10 \oplus 8_1 \oplus 8_2 \oplus 1. \tag{1.5}$$

The decuplet is completely symmetric, the singlet is completely antisymmetric, and the octets are each antisymmetric under the interchange of two of the three quarks. Since every baryon must be colorless, the corresponding representation is the completely antisymmetric singlet, which can be written

$$\left(rgb - rbg + gbr - grb + brg - bgr\right) / \sqrt{6}, \tag{1.6}$$

where r = red, g = green, and b = blue.

We can combine the different components of the baryon wave function, with the requirement that the entire wave function ($|qqq\rangle$) be antisymmetric:

$$|qqq\rangle_A = |\text{color}\rangle_A \times |\text{space}\rangle_S \times |\text{spin, flavor}\rangle_S, \tag{1.7}$$

where $|\text{color}\rangle_A$ is the asymmetric color part of the wave function and $|\text{space}\rangle$ is the spatial part of the wave function (and must be symmetric for ground states where $\ell = \ell' = 0$). Thus the product of the spin and flavor components $|\text{spin, flavor}\rangle$ must be symmetric.

The allowed ground states are illustrated in Figure 1.1. Combining the fully symmetric flavor states (20-plet) with the fully symmetric spin states, we obtain the spin-3/2 20-plet of charm baryon states shown in Figure 1.1(b). The combination of the mixed-symmetry

---

[1] This symmetry is the basis of the quark model, and was proposed by Murray Gell-Mann in 1961.

[2] Historically, the color charge was proposed by O.W. Greenberg in 1964 to explain the existence of the Δ^{++}. According to the quark model, this particle should contain uuu—three identical quarks that would violate the Pauli exclusion principle if there were not three colors.

20′-plet flavor states with the mixed-symmetry spin states is not trivial, but the resulting states have a completely symmetric product of the flavor and spin components of the wave function. This is illustrated by the states on the second level of the 20′-plet in Figure 1.1(a). The Λ_c^+ and Σ_c^+ have the same quark content (*udc*), but in the Λ_c^+ baryon, the *u* and *d* quarks are antisymmetric under interchange (the Λ_c^+ is a flavor singlet) and in the Σ_c^+ baryon, the *u* and *d* quarks are symmetric under interchange (there are three Σ_c states: Σ_c^0, Σ_c^+, and Σ_c^{++})[3].

The symmetries of these multiplets are somewhat broken because of the mass differences

---

[3] Similarly, note the two *dsc* states and two *usc* states on the second level of Figure 1.1(a). The *u* and *d* quarks are antisymmetric under interchange for the Ξ_c^0 and Ξ_c^+ states, but there are two more states that are not labeled on the figure. In these states, *u* and *d* are symmetric under interchange, and we call them the $\Xi_c^{\prime 0}$ and $\Xi_c^{\prime +}$.

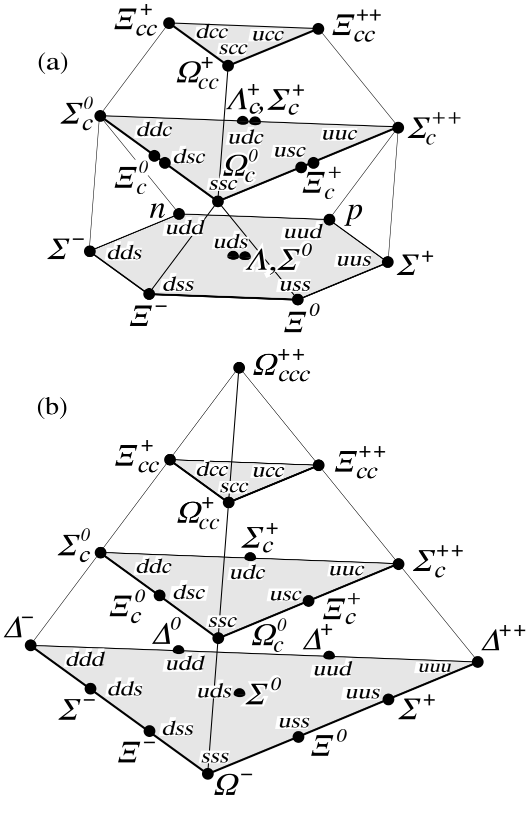

Figure 1.1: SU(4) multiplets representing the possible baryon states and their quark content [10]. The 20′-plet (a) represents the spin-1/2 states and the 20-plet (b) represents the spin-3/2 states.

of the quarks, but in general the baryon states get heavier as one moves up the levels of the multiplets in Figure 1.1. To set the scale, on the first level of the multiplet in Figure 1.1(a), the p and n masses are about $0.9\,\mathrm{GeV}/c^2$ and the Λ baryon has a mass of about $1.1\,\mathrm{GeV}/c^2$. On the second level, the Λ_c^+ has a mass of about $2.3\,\mathrm{GeV}/c^2$, the Σ_c^0, Σ_c^+, Σ_c^{++}, Ξ_c^0 and Ξ_c^+ all have masses of about $2.5\,\mathrm{GeV}/c^2$, and the Ω_c^0 has a mass of about $2.7\,\mathrm{GeV}/c^2$. Since the u and d quarks are much lighter than the c quark (see Table 1.1), the symmetry is especially good under the interchange of the two light quarks. Consequently, the mass differences between the Σ_c^0, Σ_c^+, and Σ_c^{++} states are very small ($< 1\,\mathrm{MeV}/c^2$) [9]. The top level of the $20'$-plet is reserved for baryons containing two c quarks; one might naively expect them to have masses between 3 and $5\,\mathrm{GeV}/c^2$, but they have not yet been definitively observed[4].

So far, we have discussed spin-1/2 and spin-3/2 charm baryon states. The stars of this dissertation are the Λ_c^+ baryon and three Σ_c baryons: the $\Sigma_c(2455)^0$, the $\Sigma_c(2520)^0$ and the $\Sigma_c(2800)^0$ (the masses of the states are in parentheses, in MeV/c^2). The $\Sigma_c(2455)$ and $\Sigma_c(2520)$ triplets are well-established states, and correspond to those seen in Figure 1.1(a) and (b), respectively. Evidence for a triplet of excited Σ_c states ($\Sigma_c(2800)^0$, $\Sigma_c(2800)^+$, and $\Sigma_c(2800)^{++}$) has been recently reported by the Belle Collaboration [14], with a tentative assignment of spin-3/2. However, we must make a caveat at this point. None of the spins of the charm baryons have been measured [15], although there is some evidence that the Λ_c^+ has spin-1/2. The broad success of the quark model casts little doubt on the spin-1/2 status of the Λ_c^+, or the spin-1/2 expectation of the ground state $\Sigma_c(2455)^0$. But since we have not even discovered all of the predicted states in the $20'$-plet and the 20-plet, it is not unfeasible that we have assigned observed particles to the wrong multiplets, or that perhaps some surprises exist in the charm baryon spectrum.

1.3 Measured Rates of B Meson Decays to Baryons

The B meson has a mass of $m_B = 5.279\,\mathrm{GeV}/c^2$—more than five times the mass of the proton. The weak interaction allows the b quark in the B meson to decay to a c quark or a u quark through the emission of the charged mediator of the weak interaction, the W boson. The mean lifetime of the B meson is measured to be $\sim 10^{-12}\,\mathrm{s}$. Weak decays of the B meson are illustrated by the Feynman diagrams shown in Figure 1.2. We define the

---

[4] Observation of these states has been claimed by the SELEX Collaboration [11], but has not been confirmed by other experiments [12, 13].

term “branching fraction” ($\mathcal{B}$) to indicate how often a particle decays to a particular final state. For example, about 1/3 of the time, the decay is *semileptonic*: the W boson becomes a lepton (e, μ, or τ) and a neutrino. The other 2/3 of the time, the final state is purely hadronic—it contains only mesons and/or baryons.

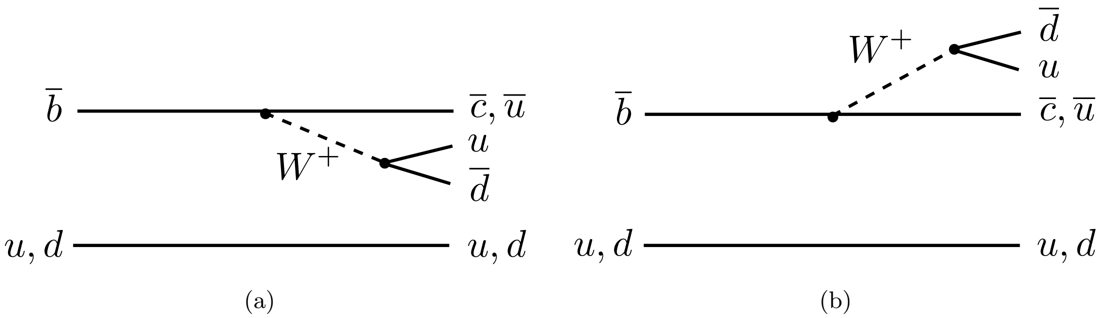

Figure 1.2: Feynman diagrams of a B meson decaying weakly through (a) internal and (b) external W emission at the quark level. The $\overline{b}$ quark changes flavor through this process to a $\overline{c}$ or $\overline{u}$ quark. The quark that does not change flavor (in this case the u or d quark) is called the *spectator quark*.

An interesting thing about the B meson (compared to lighter mesons discussed earlier, such as K and D mesons) is that the B is heavy enough to decay into a baryon-antibaryon pair. In fact, this happens $(6.8 \pm 0.6)\%$ of the time [17]. Many exclusive baryonic B decay modes have been observed, and the branching fractions for each of these modes are listed in Table 1.3. Note that the final states contain baryons that were introduced in the previous section. One might notice that the lowest measured branching fraction is of the order 10^{-6}; this is the current limit of our experimental sensitivity for measuring these branching fractions. Potentially interesting B decays such as $B \to p\overline{p}$, $B \to \Lambda\overline{\Lambda}$, and $B \to \Lambda_c^+\overline{\Lambda}_c^-$ have not yet been seen.

Most of the final states in Table 1.3 include a meson or baryon containing a charm quark. However, some decays do not have a charm quark in the final state (e.g., $B \to p\overline{p}X$, $B \to \Lambda\overline{p}X$ and $B \to \Lambda\overline{\Lambda}X$). These charmless decay rates are “Cabibbo-suppressed” by a factor of $\lambda^2 \sim 0.04$ compared to their charmed counterparts[5] and therefore one should not compare the charmless and charmed modes directly.

---

[5] The quantity λ is a (Wolfenstein) parameter of the Cabibbo-Kobayashi-Maskawa quark mixing matrix. This matrix describes how the W boson couples to different flavors of quarks.

Table 1.3: Observed B-meson decays to baryonic final states [9].

Decay Mode	Q-value (MeV/c^2)	Branching Fraction
$B^+ \to p\bar{p}\pi^+$	3263	$\left(3.1\ {}^{+\,0.8}_{-\,0.7}\right) \times 10^{-6}$
$B^+ \to p\bar{p}K^+$	2909	$(5.6 \pm 1.0) \times 10^{-6}$
$B^0 \to p\bar{p}K^0$	2905	$\left(2.1\ {}^{+\,0.6}_{-\,0.4}\right) \times 10^{-6}$
$B^+ \to p\bar{p}K^{*+}$	2511	$\left(1.0\ {}^{+\,0.4}_{-\,0.3}\right) \times 10^{-5}$
$B^+ \to p\bar{\Lambda}\gamma$	3225	$(2.2 \pm 0.6) \times 10^{-6}$
$B^0 \to p\bar{\Lambda}\pi^-$	3086	$(2.6 \pm 0.5) \times 10^{-6}$
$B^0 \to \bar{D}^0 p\bar{p}$	1538	$(1.1 \pm 0.1) \times 10^{-4}$
$B^0 \to \bar{D}^\star(2007)^0 p\bar{p}$	1396	$(1.0 \pm 0.1) \times 10^{-4}$
$B^0 \to D^- p\bar{p}\pi^+$	1367	$(3.4 \pm 0.3) \times 10^{-4}$
$B^0 \to D^{*-} p\bar{p}\pi^+$	1253	$(4.8 \pm 0.5) \times 10^{-4}$
$B^0 \to \bar{\Lambda}_c^- p$	2055	$(2.2 \pm 0.8) \times 10^{-5}$
$B^+ \to \bar{\Lambda}_c^- p\pi^+$	1915	$(2.1 \pm 0.6) \times 10^{-4}$
$B^+ \to \bar{\Lambda}_c^- p\pi^+\pi^0$	1780	$(1.8 \pm 0.6) \times 10^{-3}$
$B^0 \to \bar{\Lambda}_c^- p\pi^+\pi^-$	1775	$(1.1 \pm 0.3) \times 10^{-3}$
$B^+ \to \bar{\Lambda}_c^- p\pi^+\pi^+\pi^-$	1635	$(2.3 \pm 0.7) \times 10^{-3}$
$B^+ \to \bar{\Sigma}_c(2455)^0 p$	1887	$(3.7 \pm 1.3) \times 10^{-5}$
$B^+ \to \bar{\Sigma}_c(2455)^0 p\pi^0$	1752	$(4.4 \pm 1.8) \times 10^{-4}$
$B^0 \to \bar{\Sigma}_c(2455)^0 p\pi^-$	1748	$(1.5 \pm 0.5) \times 10^{-4}$
$B^0 \to \bar{\Sigma}_c(2455)^{--} p\pi^+$	1747	$(2.2 \pm 1.7) \times 10^{-4}$
$B^0 \to \bar{\Sigma}_c(2520)^{--} p\pi^+$	1683	$(1.2 \pm 0.4) \times 10^{-4}$
$B^+ \to \bar{\Sigma}_c(2455)^0 p\pi^-\pi^+$	1608	$(4.4 \pm 1.7) \times 10^{-4}$
$B^+ \to \bar{\Sigma}_c(2455)^{--} p\pi^+\pi^+$	1608	$(2.8 \pm 1.2) \times 10^{-4}$
$B^+ \to \Lambda\bar{\Lambda}K^+$	2554	$\left(2.9\ {}^{+\,1.0}_{-\,0.8}\right) \times 10^{-6}$
$B^+ \to \Lambda_c^+\bar{\Lambda}_c^- K^+$	2123	$(7 \pm 4) \times 10^{-4}$
$B^0 \to \Lambda_c^+\bar{\Lambda}_c^- K^0$	2088	$(8 \pm 5) \times 10^{-4}$
$B^0 \to \bar{\Xi}_c^- \Lambda_c^+ \times \mathcal{B}(\bar{\Xi}_c^- \to \bar{\Xi}^+\pi^-\pi^-)$	525	$\left(9\ {}^{+\,5}_{-\,4}\right) \times 10^{-5}$
$B^+ \to \bar{\Xi}_c^0 \Lambda_c^+ \times \mathcal{B}(\bar{\Xi}_c^0 \to \bar{\Xi}^+\pi^-)$	522	$\left(5.6\ {}^{+\,2.7}_{-\,2.4}\right) \times 10^{-5}$
$B^+ \to \bar{\Xi}_c^0 \Lambda_c^+ \times \mathcal{B}(\bar{\Xi}_c^0 \to \bar{\Lambda}K^+\pi^-)$	522	$(4.0 \pm 1.6) \times 10^{-5}$

To look for a pattern in these decay rates, we can define a quantity of particular relevance to baryonic B decays called the Q-value:

$$Q = m_B - \sum_i m_{d_i}, \tag{1.8}$$

where m_{d_i} is the mass of each daughter in the B decay. The Q-value therefore has units of mass, and is listed for each baryonic B-decay mode in Table 1.3. If we plot the branching fraction vs. the Q-value of the decay for baryons, we see a general trend (Figure 1.3): the branching fraction decreases as the sum of the daughter masses becomes smaller compared to the B mass. This is true even for *different types of baryons* in the final state.

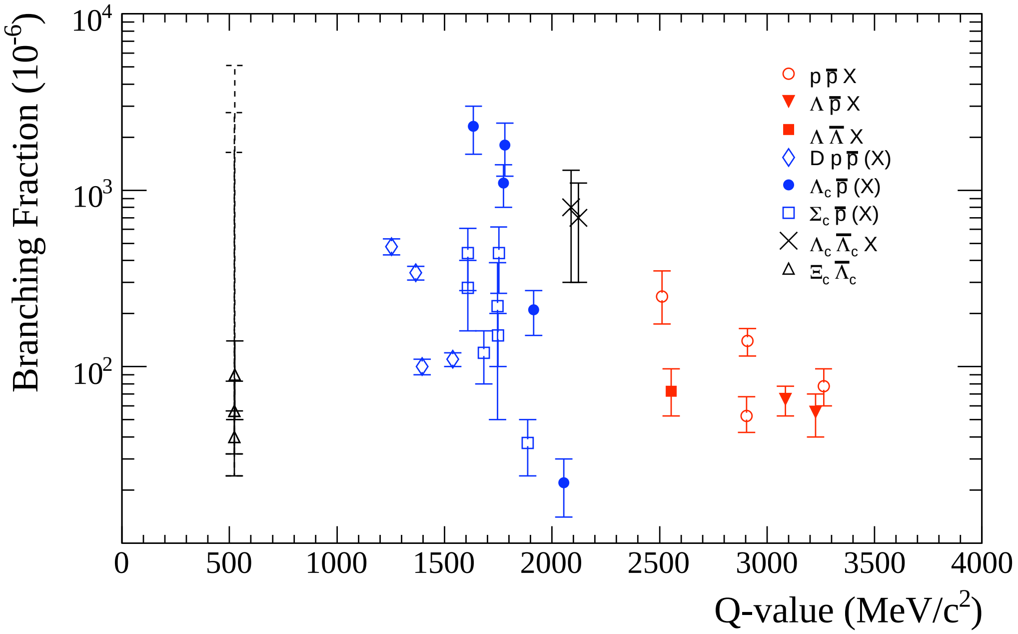

Figure 1.3: Branching fraction (in units of 10^{-6}) vs. Q-value for B decays with baryons in the final state (see Table 1.3). The general trend is that the baryonic B branching fractions decrease as the Q-value increases. The branching fractions for the first three (Cabibbo suppressed) modes in the legend are divided by $\lambda^2 = 0.04$. The central values for $\mathcal{B}(B \to \Xi_c \Lambda_c)$ should be divided by the (unknown) Ξ_c branching fractions; the dashed uncertainties conservatively assume a 1% sub-branching fraction for the Ξ_c decays.

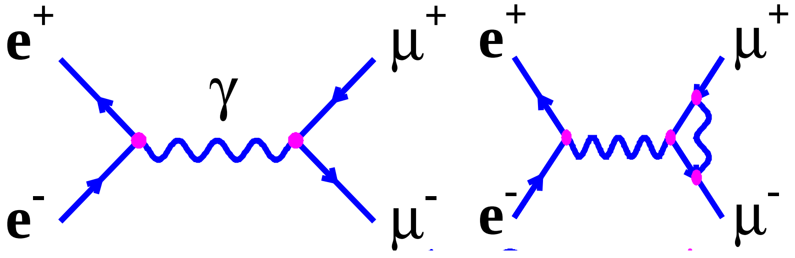

(a) (b)

Figure 1.4: (a) Tree and (b) one-loop Feynman diagrams for electron-positron annihilation into $\mu^+\mu^-$. In (a) the amplitude is proportional to α and the rate is proportional to α^2; in (b) the amplitude is proportional to α^2 and the rate is proportional to α^4 [16].

1.4 Theoretical Interpretation of Baryonic B Decays

Although the decay of the B meson to baryonic final states is through the weak interaction, the formation of the baryons occurs through gluon emission and *hadronization*, which are strong interactions described by quantum chromodynamics (QCD). QCD is extremely difficult to calculate at low energies because it is non-perturbative. To understand this further, we can contrast QCD with QED: quantum electrodynamics. QED processes can be calculated through the use of Feynman diagrams such as the diagrams in Figure 1.4. In Figure 1.4(a), an electron and positron annihilate, forming a virtual photon, which then becomes a $\mu^+\mu^-$ pair. The amplitude for this process is proportional to the strength of the interaction: $\alpha = 1/137$ (each vertex in the diagram contributes a factor proportional to $\sqrt{\alpha}$). If we add the loop in Figure 1.4(b), the amplitude for the electron and positron to annihilate into a $\mu^+\mu^-$ pair is proportional to α^2. And thus, as we add vertices, we add small corrections to the overall amplitude, which can be calculated using perturbation theory. However, at low energies the strength of the strong interaction in QCD is $\alpha_s \gtrsim 1$, making perturbation theory inapplicable except at very small distances or high energies. Therefore, as the diagrams become more complex, they contribute more to the overall amplitude, and calculations become very difficult or impossible at low energies.

In B decays to mesons (such as $B \to \pi\pi$), in the limit that the mass of the b quark is much greater than the scale of QCD interaction, some simplifications occur that ease the calculation of the amplitude of the decay (the amplitude becomes somewhat "factorizable"). However, especially for two-body baryonic final states, the amplitudes are not factorizable.

1.4.1 Theoretical Models of Baryonic B Decays

Since exact QCD calculations are so difficult, theorists have developed strategies to attempt calculations of baryonic B decay rates. Examples of these are models such as "pole" models and "diquark" models, and QCD sum rules. The history of the application of these models to baryonic B decays is that the techniques were developed in the early 1990s in response to a claimed observation of $B \to p\overline{p}\pi(\pi)$ by the ARGUS Collaboration in 1988 [18]. The rate claimed by the ARGUS collaboration was much higher than expected, which piqued theoretical interest. The claim was then refuted by the CLEO Collaboration [19], and after a few years the theoretical frenzy died down. Since the turn of the century, new measurements of baryonic B decays by the *BABAR*, Belle, and CLEO Collaborations has sparked a rebirth of theoretical activities that are largely based on the models developed in the early 1990s.

An example of a pole model, as applied to B decays to baryons, is illustrated in Figure 1.5(a) and was developed between 1988 and 1991 [20, 21]. The concept is that the decay proceeds through an intermediate b-flavored baryon state, which then decays weakly into one of the final state baryons. This model has been resurrected by Cheng and Yang [22, 23]. But it is not clear that the pole model is reliable for baryon poles, and the predictions/postdictions given in the literature vary significantly.

In the diquark model [24], illustrated in Figure 1.5(b), the heavy b quark emits a W boson that produces a quark and an antiquark. The quark from the W combines with the resulting heavy quark to form a diquark. The antiquark from the W combines with the spectator quark (the light quark originally in the B meson) to form an antidiquark. Gluon emission produces an extra quark-antiquark pair; the quark combines with the diquark to form the baryon and the antiquark combines with the antidiquark to form the antibaryon.

The technique of QCD sum rules [25–27] equates the constituent quark and gluon degrees of freedom in a bound state with the phenomenological hadronic degrees of freedom. The constituent quark and gluon degrees of freedom are described by a QCD momentum-space *correlation function* that is easiest to calculate when the energy scale is large. The phenomenological description of the correlation function is a spectral density (a sum over physical hadronic ground and excited states). The ground state(s) can be separated from the excited states in the spectral density when the energy scale is small. Thus, in order to match the constituent QCD correlation function with the phenomenological one, a compromise must be reached: the calculations of both quantities are performed in an intermediate energy regime. In this regime, corrections called *condensates* must be introduced in the

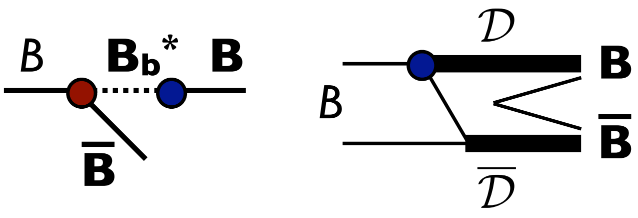

(a) (b)

Figure 1.5: Illustrations of (a) the pole model and (b) the diquark model. The red dot represents a strong interaction, and the blue dots represent weak interactions. The bold **B** represents a generic baryon, and the script $\mathcal{D}$ represents a diquark. In the pole model, a b-flavored baryon resonance is formed, which then weakly decays to one of the baryons in the final state. In the diquark model, the b quark decays weakly to a diquark and an additional antiquark. The antiquark from the b decay forms an antidiquark with the spectator antiquark.

constituent QCD correlation function calculation. These quantities include color singlet quark-antiquark pairs and configurations of gluons that can be extracted from other processes with limited accuracy. In the phenomenological spectral density calculation, in order to separate the ground from the excited states at an intermediate energy scale, one must choose a cutoff energy; this choice induces a systematic uncertainty that is difficult to quantify. Once the two descriptions are matched at a particular energy scale, the equation is called a "sum rule". One can then extract the relevant parameters (e.g., the mass of a hadron or the rate of $\overline{B}^0 \to \Lambda_c^+ \overline{p}$).

Unfortunately, the three theoretical methods presented are inherently unreliable, and the flurry of papers in the early 1990s made predictions that were orders of magnitude too large. The most recent work has been in predictions based on pole models, but in such a difficult regime to calculate QCD, experimental measurements must lead the way.

Perhaps the most satisfying theoretical interpretation of baryonic B decay rates is the qualitative one proposed by Hou and Soni in 2001 [28], who argue that B decays to a two-body baryon-antibaryon final state are suppressed compared to a three-body final state containing the same baryon-antibaryon system, but with an additional meson. The explanation for the suppression is the "large energy release" of the two-body final state compared to the three-body final state. This energy release is simply the Q-value that we calculated for each of the baryonic B decay modes in Section 1.3, and the body of measurements indeed supports Hou and Soni's prediction.

1.5 Three-body Decay Kinematics

When a parent particle with mass M decays to 3 daughters with masses m_1, m_2, m_3, there are kinematic restrictions on the momenta of the individual daughters so that the decay satisfies energy and momentum conservation. We can construct a combined mass for any two of the three daughters by combining their energies and momenta: $m_{12} = \sqrt{(E_1 + E_2)^2 - |\vec{p_1} + \vec{p_2}|^2}$. This quantity, m_{12}, must be in the range $m_1 + m_2$ through $M - m_3$ and its distribution has a kinematically defined shape ("phase space"). Deviations from phase space give information about the dynamics of the decay; e.g., if the decay occurred through an intermediate resonance A, where $M \to m_A m_3, m_A \to m_1 m_2$, then the distribution of m_{12} will peak near m_A.

1.6 Baryon-Antibaryon Threshold Enhancement

In multibody baryonic B decays, the distribution of the invariant mass of the baryon-antibaryon system ($m_{\mathbf{B}\overline{\mathbf{B}}}$) peaks at the lower kinematic limit (i.e., where $m_{\mathbf{B}\overline{\mathbf{B}}} \sim m_{\mathbf{B}} + m_{\overline{\mathbf{B}}}$). An example of this peaking is shown in Figure 1.6 for $B \to D p\overline{p}(\pi)$, $B \to p\overline{p}K$, and $e^+e^- \to p\overline{p}\gamma$ [2]. The $m_{p\overline{p}}$ distribution is corrected for phase space to allow a direct comparison of the three modes.

This feature was also discussed by Hou and Soni [28], and can be explained in conjunction with the preferred low energy release of the baryon-antibaryon system. In a two-body baryonic B decay, kinematically the invariant mass of the baryon-antibaryon system must be the mass of the B meson. However, if there are one or more additional particles in the final state, the baryon-antibaryon system can have a mass lower than m_B. This latter configuration minimizes the energy release of the baryon-antibaryon system, and so the production of the baryon-antibaryon system from the B meson is enhanced.

1.7 Outline of this Document

This dissertation describes the study of B-meson decays to final states with a single charm baryon, $\overline{B}^0 \to \Lambda_c^+ \overline{p}$ and $B^- \to \Lambda_c^+ \overline{p} \pi^-$. Chapter 2 gives an overview of the analysis of these

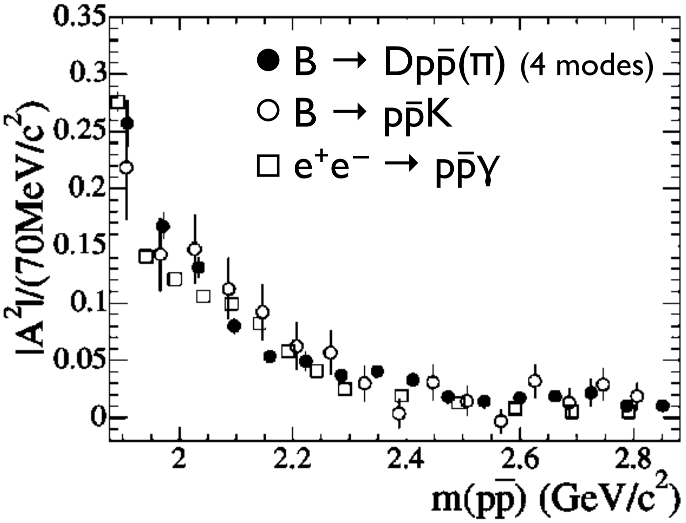

Figure 1.6: The phase-space-corrected distribution of $m_{p\overline{p}}$ for $B \rightarrow Dp\overline{p}(\pi)$, $B \rightarrow p\overline{p}K$, and $e^+e^- \rightarrow p\overline{p}\gamma$ [2]. An enhancement is clearly visible at low $p\overline{p}$ mass.

decays, including a brief description of relevant prior measurements. Chapter 3 describes the *BABAR* detector, the PEP-II e^+e^- storage ring, and the data samples used in this dissertation. Chapters 4, 5, and 6 describe the event selection procedures and determination of the detection reconstruction efficiencies. Chapter 7 discusses the background sources considered and Chapter 8 describes the validation of the maximum likelihood fits. The results of these fits and the event weighting and background subtraction method are described in Chapters 9 and 10. The measurements of the branching fractions $\mathcal{B}(\overline{B}^0 \rightarrow \Lambda_c^+\overline{p})$ and $\mathcal{B}(B^- \rightarrow \Lambda_c^+\overline{p}\pi^-)$, and the branching ratio $\mathcal{B}(B^- \rightarrow \Lambda_c^+\overline{p}\pi^-)/\mathcal{B}(\overline{B}^0 \rightarrow \Lambda_c^+\overline{p})$ are described in Chapter 11, followed by the evaluation of systematic uncertainties in Chapter 12. The study of the resonant substructure in the three-body final state can be found in Chapter 13 and the $\Sigma_c(2455)^0$ spin measurement is described in Chapter 14. Chapter 15 contains a summary of the measurements presented in this dissertation and a comparison to existing measurements.

Chapter 2

Analysis Overview

The $\overline{B}^0 \to \Lambda_c^+ \overline{p}$ and $B^- \to \Lambda_c^+ \overline{p}\pi^-$ decay modes are representative of baryonic B decays and are experimentally accessible, with branching fractions on the order of 10^{-5} and 10^{-4}, respectively. The Feynman diagrams for these decays are illustrated in Figure 2.1 in which the B meson decays weakly via W boson emission to $\Lambda_c \overline{p}$ and $\Lambda_c \overline{p}\pi$.

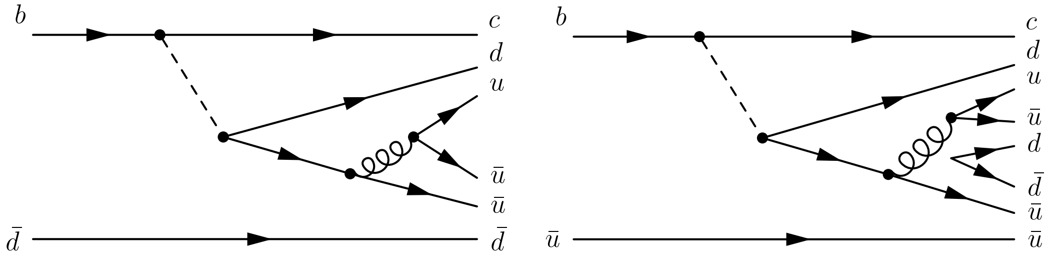

(a) (b)

Figure 2.1: Feynman diagrams for (a) $\overline{B}^0 \to \Lambda_c^+ \overline{p}$ and (b) $B^- \to \Lambda_c^+ \overline{p}\pi^-$, in which the B meson decays weakly via internal W boson emission.

2.1 Previous measurements

Charmed baryonic B decays in the modes $\overline{B}^0 \to \Lambda_c^+ \overline{p}\pi^+\pi^-$, $B^- \to \Lambda_c^+ \overline{p}\pi^-$, $B^- \to \Sigma_c(2455)^0 \overline{p}$, and $\overline{B}^0 \to \Lambda_c^+ \overline{p}$ have been previously measured by the CLEO [29] and Belle [30–32] collaborations with smaller data samples. These measurements are summarized in Table 2.1. We presented preliminary measurements of $\mathcal{B}(\overline{B}^0 \to \Lambda_c^+ \overline{p})$, $\mathcal{B}(B^- \to \Lambda_c^+ \overline{p}\pi^-)$, and

Table 2.1: Summary of previous branching fraction measurements for B decays to final states with a single charmed baryon. The errors on the branching fractions are statistical, systematic, and from the $\Lambda_c^+ \to pK^-\pi^+$ branching fraction measurement, respectively. All results use $\mathcal{B}(\Lambda_c^+ \to pK^-\pi^+) = (5.0 \pm 1.3)\%$ [9].

Decay Mode	Branching Fraction $(\mathbf{10^{-4}})$	Experiment	$N_{B\overline{B}}(10^6)$
$\overline{B}^0 \to \Lambda_c^+\overline{p}$	$0.22 \pm 0.04 \pm 0.01 \pm 0.06$	BABAR [33]	232
	$0.22\ ^{+\,0.06}_{-\,0.05} \pm 0.03 \pm 0.06$	Belle [31]	85
$B^- \to \Sigma_c(2455)^0\overline{p}$	$0.37 \pm 0.07 \pm 0.04 \pm 0.10$	Belle [30]	152
$B^- \to \Lambda_c^+\overline{p}\pi^-$	$2.0 \pm 0.2 \pm 0.2 \pm 0.5$	Belle [30]	152
	$1.9 \pm 0.4 \pm 0.3 \pm 0.5$	Belle [32]	32
	$2.4 \pm 0.6 \pm 0.2 \pm 0.6$	CLEO [29]	10
$\overline{B}^0 \to \Lambda_c^+\overline{p}\pi^+\pi^-$	$11.0 \pm 1.2 \pm 2.0 \pm 2.9$	Belle [32]	32
	$16.7 \pm 1.9\ ^{+\,1.9}_{-\,1.6} \pm 4.3$	CLEO [29]	10

$\mathcal{B}(B^- \to \Lambda_c^+\overline{p}\pi^-)/\mathcal{B}(\overline{B}^0 \to \Lambda_c^+\overline{p})$ at ICHEP 2006 using a portion of the BABAR dataset (232 million $B\overline{B}$ pairs) [33]. The measurements presented in this dissertation supersede those results.

The Belle collaboration previously observed the resonant decay mode $B^- \to \Sigma_c(2455)^0\overline{p}$ and the enhancement in rate at low $m_{\Lambda_c p}$. There have been no previous measurements of the spin of the $\Sigma_c(2455)^0$ baryon.

2.2 Branching Fraction Measurements

In this dissertation, we measure the branching fractions of the decays $\overline{B}^0 \to \Lambda_c^+\overline{p}$ and $B^- \to \Lambda_c^+\overline{p}\pi^-$. We also measure the branching ratio $\mathcal{B}(B^- \to \Lambda_c^+\overline{p}\pi^-)/\mathcal{B}(\overline{B}^0 \to \Lambda_c^+\overline{p})$. These measurements are based on 383 million $B\overline{B}$ pairs ($347.2\,\mathrm{fb}^{-1}$). The Λ_c^+ baryon is reconstructed in five decay modes[1]:

- $\Lambda_c^+ \to pK^-\pi^+$
- $\Lambda_c^+ \to pK_S^0$
- $\Lambda_c^+ \to pK_S^0\pi^+\pi^-$

---

[1] The $\Lambda_c^+ \to \Lambda\pi^+\pi^-\pi^+$ decay mode is not used to measure $\mathcal{B}(\overline{B}^0 \to \Lambda_c^+\overline{p})$.

- $\Lambda_c^+ \to \Lambda\pi^+$
- $\Lambda_c^+ \to \Lambda\pi^+\pi^-\pi^+$.

A blinded signal region is defined for each B decay mode, and studies of the optimal event selection criteria, background distributions, and signal extraction strategy are performed before unblinding so as not to bias the results. The detection efficiency is determined using samples of simulated events. For $B^- \to \Lambda_c^+\overline{p}\pi^-$, we take into account the efficiency variation due to the kinematics of the three-body decay. A 2-D maximum likelihood fit is performed on the selected B candidates in data, simultaneous across Λ_c^+ decay modes, to extract the signal yields. The branching fraction measurement uncertainties are dominated by the uncertainty on the intermediate branching fraction $\mathcal{B}(\Lambda_c^+ \to pK^-\pi^+)$. For $\mathcal{B}(\overline{B}^0 \to \Lambda_c^+\overline{p})$, statistical uncertainties dominate over systematic uncertainties. For $\mathcal{B}(B^- \to \Lambda_c^+\overline{p}\pi^-)$, statistical and systematic uncertainties are comparable, and the dominant systematic uncertainties are due to the Λ_c^+ branching ratios compared to $\Lambda_c^+ \to pK^-\pi^+$ and the detection efficiency.

The uncertainties on the Λ_c^+ branching fractions cancel in the measurement of the branching ratio $\mathcal{B}(B^- \to \Lambda_c^+\overline{p}\pi^-)/\mathcal{B}(\overline{B}^0 \to \Lambda_c^+\overline{p})$. This measurement is dominated by statistical uncertainties.

2.3 $B^- \to \Lambda_c^+\overline{p}\pi^-$ Resonant Substructure

The decay $B^- \to \Lambda_c^+\overline{p}\pi^-$ proceeds non-resonantly and through several intermediate Σ_c resonances. We examine the invariant mass distribution $m_{\Lambda_c\pi}$ for Σ_c resonances. The significant resonant decay modes are $B^- \to \Sigma_c(2455)^0\overline{p}$ and $B^- \to \Sigma_c(2800)^0\overline{p}$. The observation of $B^- \to \Sigma_c(2800)^0\overline{p}$ is the first observation of the $\Sigma_c(2800)^0$ baryon in B decays. We do not see a signal for $B^- \to \Sigma_c(2520)^0\overline{p}$.

We also observe an enhancement at threshold in the $m_{\Lambda_c p}$ invariant mass distribution, indicating that a low $m_{\Lambda_c p}$ invariant mass is favored in $B^- \to \Lambda_c^+\overline{p}\pi^-$ decays.

2.4 $\Sigma_c(2455)^0$ Spin Measurement

We determine the spin of the $\Sigma_c(2455)^0$ through an angular analysis of the decay $B^- \to \Sigma_c(2455)^0\overline{p}$, $\Sigma_c(2455)^0 \to \Lambda_c^+\pi^-$. If we assume $J(\Lambda_c^+) = 1/2$, the angular distributions for the spin-1/2, spin-3/2, and spin-5/2 hypotheses for the $\mathit{\Sigma}_c(2455)^0$ are

$$\begin{aligned}
J(\mathit{\Sigma}_c^0) = \frac{1}{2}: &\quad \frac{dN}{d\cos\theta_h} \propto 1 \\
J(\mathit{\Sigma}_c^0) = \frac{3}{2}: &\quad \frac{dN}{d\cos\theta_h} \propto 1 + 3\cos^2\theta_h \\
J(\mathit{\Sigma}_c^0) = \frac{5}{2}: &\quad \frac{dN}{d\cos\theta_h} \propto 1 - 2\cos^2\theta_h + 5\cos^4\theta_h,
\end{aligned} \tag{2.1}$$

where θ_h is the helicity angle between the $\mathit{\Lambda}_c^+$ and the recoiling $\overline{p}$ in the $\mathit{\Sigma}_c(2455)^0$ rest frame.

This type of analysis was first performed by the *BABAR* Collaboration to measure the spin of the $\mathit{\Omega}^-$ in $\mathit{\Xi}_c^0 \rightarrow \mathit{\Omega}^- K^+, \mathit{\Omega}^- \rightarrow \mathit{\Lambda} K^-$ [34]. The predicted angular distributions are nearly identical to those in the $\mathit{\Omega}^-$ analysis. The decay $\mathit{\Omega}^- \rightarrow \mathit{\Lambda} K^-$ is a weak decay, so additional terms could appear in the angular distributions in Eqn. 2.1 to account for a possible asymmetry due to parity violation. However, parity is conserved for the strong decay $\mathit{\Sigma}_c(2455)^0 \rightarrow \mathit{\Lambda}_c^+ \pi^-$, so the angular distributions are symmetric.

Although the true angular distributions are symmetric, the measured angular distributions will be somewhat degraded due to resolution effects, nonuniform detector efficiencies and background contamination.

Chapter 3

The *BABAR* Experiment and Data Set

The analysis described in this dissertation is based on data recorded with the *BABAR* detector at the PEP-II e^+e^- asymmetric-energy B Factory at SLAC. The *BABAR* Collaboration consists of over 500 members in ten countries. In the previous chapter, we discussed B meson decays to baryons. In this chapter on the *BABAR* experiment, we explain how B mesons are produced from electron-positron collisions, the design and components of the *BABAR* detector [35], and the data sample.

3.1 Electron-Positron Production of B Mesons with PEP-II

Electrons and positrons are accelerated along the 2-mile long Stanford linear accelerator (linac) and then are continuously injected into the 2200- m circumference PEP-II storage ring [36], as illustrated in Figure 3.1. The linac is capable of accelerating electrons and positrons to more than 45 GeV, but only a fraction of the linac is needed to operate the B Factory; the electrons are accelerated to 9 GeV and the positrons are accelerated to 3.1 GeV. PEP-II contains two storage rings: the high-energy ring (HER) stores the 9- GeV e^- beam and the low-energy ring (LER) stores the 3.1- GeV e^+ beam. We call PEP-II an "asymmetric" B Factory due to the unequal beam energies; the resulting Lorentz boost of the B mesons in the laboratory frame is $\beta\gamma = 0.56$. The typical operating current for the HER (LER) beam is about 1.8A (3.0A) distributed over 1700 bunches.

The PEP-II interaction region is shown in Figure 3.2. The e^- and e^+ beams are brought

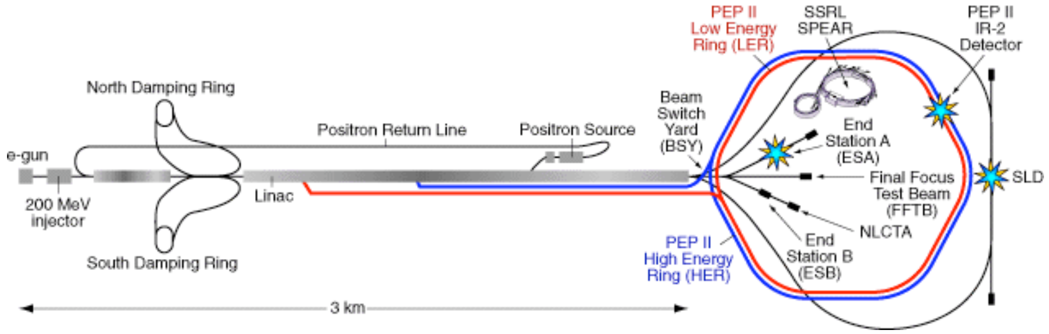

Figure 3.1: Illustration of the SLAC linear accelerator and the PEP-II storage rings. The *BABAR* detector is at the PEP-II interaction region labeled "IR-2" in the figure.

to collision in the approximate center of the *BABAR* detector. Quadrupole magnets focus the beams to about a $6\,\mu\text{m} \times 120\,\mu\text{m} \times 1\,\text{mm}$ $(x \times y \times z)$ spot at the interaction point. The design luminosity of the machine was $3 \times 10^{33}\,\text{cm}^{-2}\,\text{s}^{-1}$; currently PEP-II operates at up to 4 times the design luminosity: $1.2 \times 10^{34}\,\text{cm}^{-2}\,\text{s}^{-1}$.

The e^- and e^+ beam energies are tuned so that when an e^- and e^+ annihilate at the interaction point, the energy in the center-of-mass frame is 10.58 GeV, the mass of the $\Upsilon(4S)$. The $\Upsilon(4S)$ is the least massive $b\bar{b}$ resonance that can decay to $B\overline{B}$. At this energy, the $b\bar{b}$ cross-section is about 1 nb. The $\Upsilon(4S)$ decays almost exclusively to a pair of $B\overline{B}$ mesons: half of the time to B^+B^- and the other half to $B^0\overline{B}^0$. The *BABAR* detector surrounds the PEP-II interaction region and is designed to maximize the geometric acceptance for the boosted $\Upsilon(4S)$ decay products.

3.2 The *BABAR* Detector

The *BABAR* detector was designed to study the physics of neutral B-meson decays in order to measure CP-violating asymmetries in this system[1]. This is achieved by measurements of the lifetimes of neutral B mesons and complete reconstruction of their decay products. Therefore the design of the detector must include a large geometric acceptance, excellent reconstruction efficiency for charged particles and photons, very good vertex resolution, and

---

[1] C stands for charge conjugation, which is the operation of turning particles into antiparticles. P stands for parity, which is the operation of mirror reflection $(x \to -x, y \to -y, z \to -z)$.

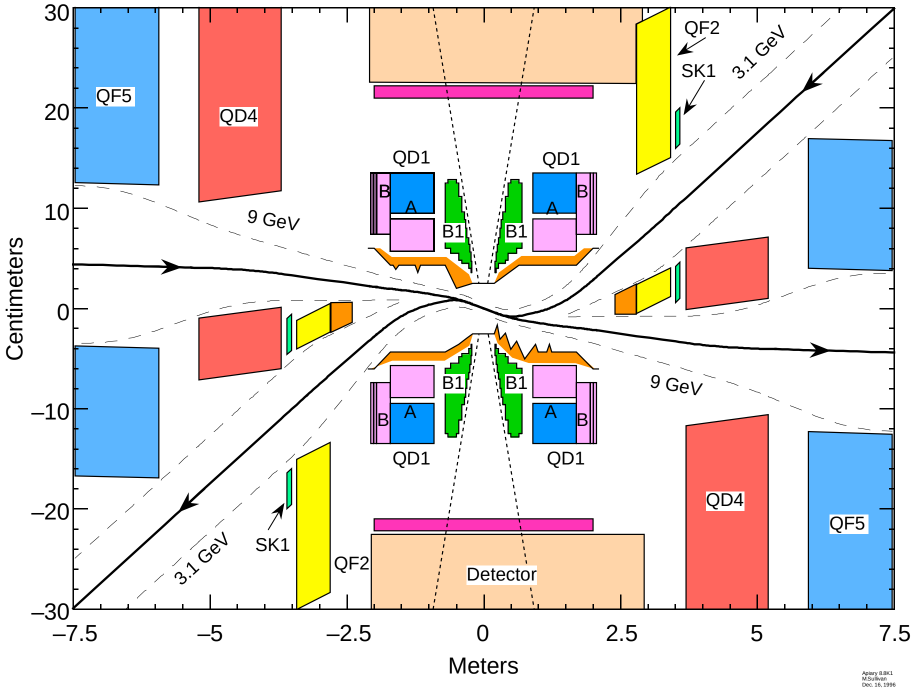

Figure 3.2: PEP-II Interaction Region. The trajectory of the 9 GeV e^- beam is from left to right, and the trajectory of the 3.1 GeV e^+ beam is from right to left. The beam collision point is at the center of the plot $(0, 0)$. The *BABAR* detector is labeled, as well as the permanent (B1, QD1) and iron (QF2, SK1, QD4, QF5) magnets used to bend and focus the beams. Note the very different scales on the horizontal and vertical axes.

efficient and accurate particle identification over a wide kinematic range. These design elements of the *BABAR* detector also make it very well-suited to reconstruct exclusive baryonic B decays.

The detector is composed of several different subdetectors that must work together to accomplish the physics goals of the *BABAR* Collaboration. Figures 3.3 and 3.4 show the side- and end-views, respectively, of the *BABAR* detector. The four innermost subdetectors are surrounded by a superconducting solenoid that provides a 1.5 T magnetic field (uniform to within 2% in the tracking chamber). We describe the six subdetectors from the innermost (closest to the interaction region) outward.

- **Silicon Vertex Tracker** (SVT): Five layers of double-sided silicon strip detectors are used to perform precise measurements of the positions and angles of charged particle trajectories, and the positions of vertices formed by these trajectories.

- **Drift Chamber** (DCH): Forty layers of hexagonal cells containing low-mass wires and helium-isobutane gas are used to provide measurements of the momentum and the energy loss ($\mathrm{d}E/\mathrm{d}x$) of charged particles.

- **Detector of Internally Reflected Cherenkov light** (DIRC): Cherenkov radiation is produced when charged particles pass through 144 bars of synthetic fused quartz. The light is transported by total internal reflection to an array of $11,000$ photomultiplier tubes (PMTs). The detected positions of the light are used to measure the opening angle of the Cherenkov radiation and thus discriminate between pions, kaons, and protons.

- **Electromagnetic Calorimeter** (EMC): A segmented array of 6580 thallium-doped cesium iodide (CsI(Tl)) crystals detects electromagnetic showers from photons, π^0 decay products, and electrons.

- **Instrumented Flux Return** (IFR): $18-19$ layers of segmented iron return the magnetic flux. The gaps between the layers of steel are instrumented with active detectors (originally resistive plate chambers, replaced by limited streamer tubes) to provide muon and neutral-hadron detection.

- **Trigger**: A hardware- (Level 1) and then software-based (Level 3) filter retains physics events with high efficiency.

In this section, we provide details about the design and performance of each subdetector. The SVT, DCH, DIRC, and Trigger systems are essential for the analysis described in this dissertation; brief descriptions of the EMC and IFR are included for completeness.

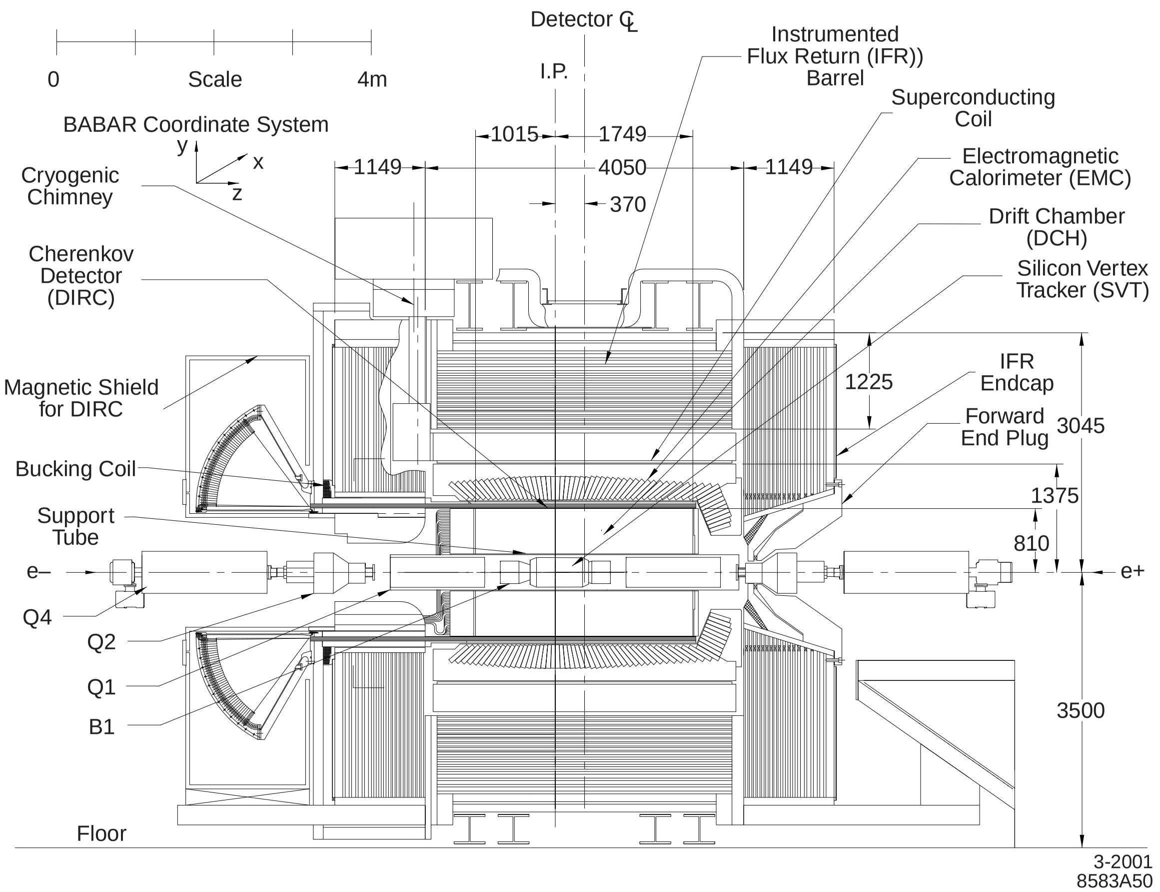

Figure 3.3: The side view of the *BABAR* detector. The e^- beam enters from the left and the e^+ beam enters from the right. The interaction point is at the center of the figure. B1 refers to the final bending magnet, and Q1, Q2, and Q4 are focusing magnets. Distances are given in cm.

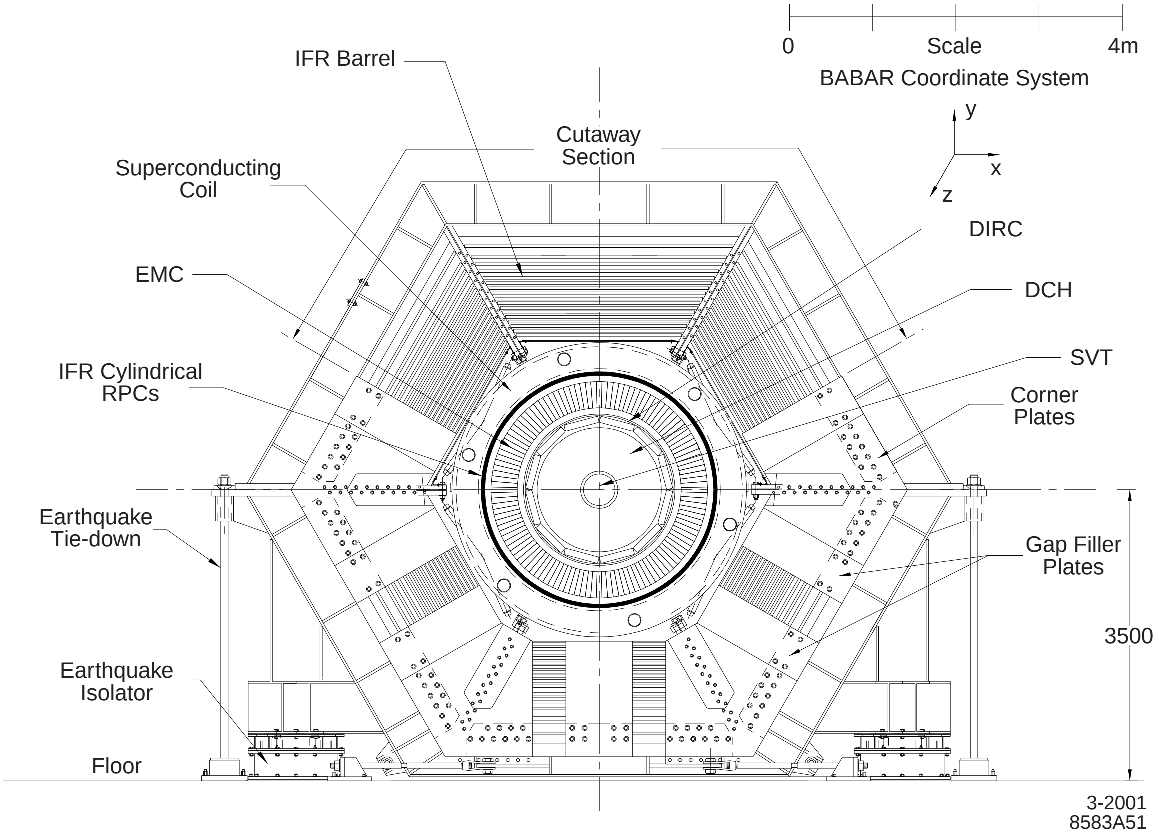

Figure 3.4: The end view of the *BABAR* detector. Distances are given in cm.

3.2.1 Silicon Vertex Tracker

The SVT is designed to precisely reconstruct charged particle trajectories and particle decay vertices near the interaction region. It is the closest subdetector to the beamline; the five concentric layers of double-sided silicon strip detectors are arranged around the beam pipe as shown in Figures 3.5 and 3.6. Layer 1 has a minimum radius of 32 mm and Layer 5 has a radius of $114 - 144$ mm. The three inner layers are mounted as close to the beam pipe (with a radius of 27.8 mm) as practical, minimizing the impact of multiple scattering. The water-cooled beam pipe is also designed to reduce multiple scattering; it is composed of two layers of beryllium that are 0.83 mm and 0.53 mm thick and 1.48 mm apart (the water channel runs between the two layers).

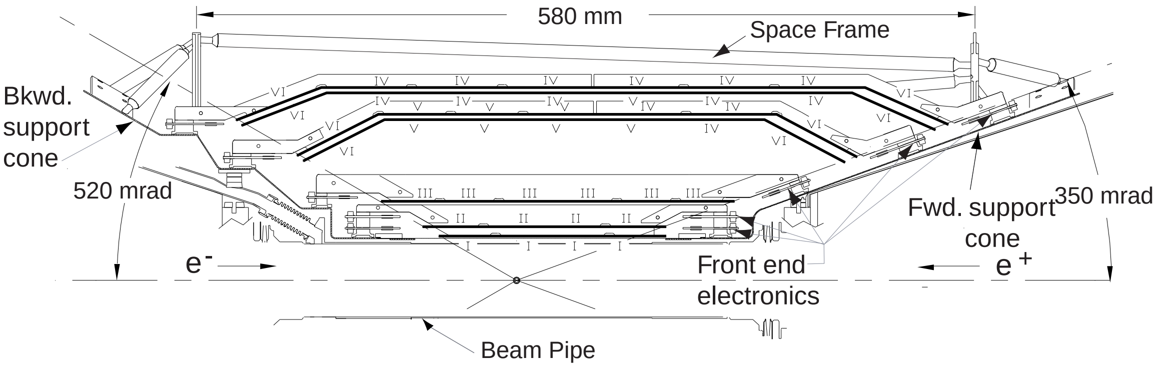

Figure 3.5: The side view of the SVT showing the five layers and the beampipe. The lower half of the detector is not shown.

The design of the SVT is asymmetric because the Lorentz boost propels the decay products forward into the detector. An *arch* shape is visible in Layers 4 and 5 in Figure 3.5; this design element increases the solid angle coverage while minimizing the amount of silicon traversed by the particles. The angular coverage is restricted by the PEP-II permanent dipole magnets (B1 in Figure 3.2) that bring the beams into collision.

The SVT is made up of 104 individual 300-μm-thick silicon wafer sensors ($0.96\,\mathrm{m}^2$ of silicon). Each wafer is a high-resistivity n-type silicon (intrinsic) substrate with p^+ and n^+ strips on opposite sides, forming a PIN junction. A voltage of ~ 40 V is applied across the sensor. When a minimum ionizing particle passes through the sensor, it typically creates $24,000$ electron-hole pairs (3.6 fC). The amount of charge is read out through AC-coupled electronics from approximately $150,000$ channels in total. If the amount of charge is above a given threshold (typically 0.4 fC), a *hit* is recorded.

The strips on opposite sides of the sensors run in perpendicular directions: strips parallel to the beam axis measure the azimuthal angle ϕ and strips perpendicular to the beam axis (along the circumference of the detector) measure the position z in the direction of the beam axis. The SVT can thus measure the trajectory of charged particles traversing the detector by recording a pattern of hits. The resolution of the SVT depends on the distance between readout strips (the *pitch*), which ranges from $50\,\mu$m in the inner layers to $210\,\mu$m in the outer layers. The measured hit resolution is $10 - 15\,\mu$m in the three inner layers and about $40\,\mu$m in the two outer layers for perpendicular trajectories. The B meson vertex resolution is $60 - 100\,\mu$m, depending on its decay mode.

The trajectories of charged particles with a transverse momentum $40\,\mathrm{MeV}/c < p_T < 100\,\mathrm{MeV}/c$ are measured by the SVT alone. For charged particles with $p_T > 100\,\mathrm{MeV}/c$, the SVT is used in conjunction with the DCH (see Section 3.2.2).

The amount of charge deposited in each silicon sensor is the energy loss ($\mathrm{d}E/\mathrm{d}x$) due to electron-hole pair production in the SVT. The $\mathrm{d}E/\mathrm{d}x$ information can be used to identify the type of charged particle detected (e.g., p, K, or π). Although particle identification is primarily performed with the DCH and DIRC, the $\mathrm{d}E/\mathrm{d}x$ information from the SVT is used as well.

SVT Radiation Protection and Monitoring

The proximity of the SVT to the beamline makes it especially vulnerable to radiation damage. Therefore, a set of silicon PIN diode sensors was installed between the beam pipe and innermost SVT layer to both monitor the radiation dose and protect the SVT against high instantaneous radiation doses by aborting the beams. The diodes are reverse-biased,

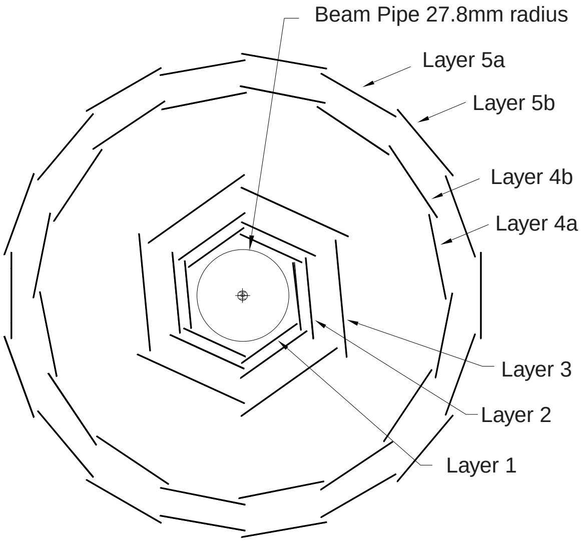

Figure 3.6: The end view of the SVT. The radius of the beam pipe is 27.8 mm. The minimum radius of the SVT is 32 mm for Layer 1 and $114 - 144$ mm for Layer 5.

and the leakage current is proportional to the dose rate (after correcting for temperature and radiation damage effects). However, the silicon diode sensors themselves are subject to radiation damage, and therefore additional radiation-hard polycrystalline Chemical Vapor Deposition (CVD) diamond sensors were installed in 2002 [37]. The combination of the silicon diodes and CVD diamond sensors form a radiation monitoring system that protects the SVT and monitors the radiation damage.

3.2.2 Drift Chamber

The DCH is a gas-filled volume containing nearly $29,000$ wires under tension. The primary purpose of the DCH is to detect the ionization created by charged particles and precisely measure the momenta and angles of the particles. Furthermore, for a particle that decays outside the SVT (e.g. a K_S^0 or Λ), the DCH is used to reconstruct the *displaced* decay vertex. The DCH also provides particle identification information through measurements of $\mathrm{d}E/\mathrm{d}x$.

The DCH is approximately 3 m long with an inner cylinder of 1 mm-thick beryllium and an outer cylinder of carbon fiber. Inside the chamber, there are 7104 hexagonal cells of wires arranged in 40 cylindrical layers. Sequential layers are staggered by a half cell (a schematic is shown in Figure 3.7). Each cell contains a gold-plated tungsten-rhenium "sense" wire surrounded by six gold-plated aluminum "field" wires. The field wires are held at ground potential, while a positive high voltage of 1930 V is applied to the sense wire[2]. The gas mixture is an 80:20 ratio of helium[3] to isobutane (C_4H_{10}). A helium-based gas mixture and low-mass aluminum field wires are chosen to minimize multiple scattering. Polyatomic isobutane is used as a "quenching" gas to absorb the broad energy range of the photons released from exited helium atoms[4].

When a charged particle passes through a DCH cell, it ionizes a gas molecule. The resulting electrons drift to the sense wire and the resulting ions drift to the field wires. The drift velocity is $22\,\mu\mathrm{m}/ns$ (without a magnetic field). The acceleration of the electrons toward the sense wire causes an *avalanche* of secondary ionizations that serves to amplify

---

[2] The DCH operating voltage originally was changed from 1900 V to 1960 V and finally to 1930 V within the first year of operation.

[3] A noble gas is generally chosen in DCH design in order to minimize energy loss due to molecular excitations. Also, noble gases do not interact with the DCH structure or wires.

[4] Energetic photons can interact with the field wires and liberate additional electrons due to the photoelectric effect. This process results in a positive feedback loop that can cause chamber breakdown, so a quenching gas is added to absorb the photons.

the ionization signal. Since the electric field strength is proportional to the inverse of the distance to the center of the wire, the diameter of the sense wire (20 μm in the BABAR DCH) should be as small as possible.

Position information in the z direction is obtained by placing the wires in 24 out of 40 layers at small angles with respect to the z-axis (these are labeled as the "stereo" layers in Figure 3.7). The drift time measurement is triggered by the leading edge of the ionization signal and has a precision of 1 ns. The precise relation between the measured drift time and drift distance is measured empirically from samples of e^+e^- and $\mu^+\mu^-$ events. The position resolution for the trajectories of charged particles ranges from $0.1 - 0.4$ mm as a function of the drift distance in a cell. The resolution in a typical cell is shown in Figure 3.8. The transverse momentum resolution (σ_{p_T}) is

$$\frac{\sigma_{p_T}}{p_T} = (0.13 \pm 0.01)\,\% \cdot p_T + (0.45 \pm 0.03)\,\%, \tag{3.1}$$

where p_T is measured in GeV/c.

The total ionization in each drift cell is proportional to the energy lost by the charged particle. The Bethe-Bloch relation describes the connection between dE/dx and velocity (β) for a given particle:

$$-\frac{dE}{dx} = 4\pi r_e^2 m_e c^2 N_A \frac{Z}{A}\frac{1}{\beta^2}\left[\frac{1}{2}\ln\left(\frac{2m_e c^2\beta^2\gamma^2 T_{\max}}{I^2} - \beta^2 - \frac{\delta(\beta\gamma)}{2}\right)\right], \tag{3.2}$$

where r_e and m_e are the classical radius and mass of the electron, N_A is Avogadro's number, Z and A are the atomic number and atomic mass of the absorbing medium, respectively, $T_{\max}$ is the maximum kinetic energy that can be imparted to a free electron in a single collision, I is the mean excitation energy, and $\delta(\beta\gamma)$ is a density-effect correction. Since the Bethe-Bloch equation depends on velocity (not momentum), dE/dx measurements can be combined with momentum measurements to discriminate between particles of different mass. Figure 3.9 shows dE/dx vs. momentum for charged particles passing through the DCH, with the Bethe-Bloch predictions overlaid. The typical RMS resolution for the dE/dx measurement is 7.5%.

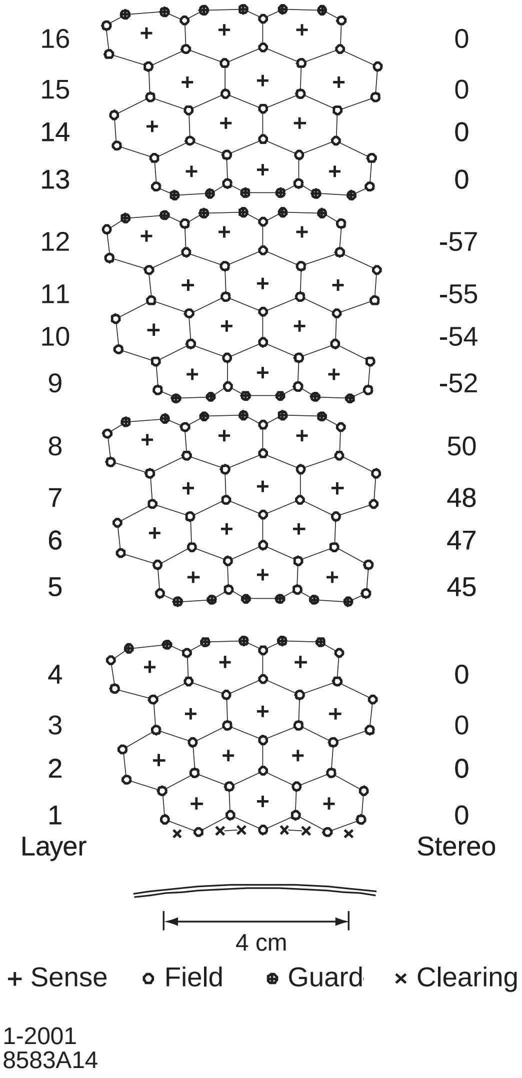

Figure 3.7: First 16 layers of hexagonal DCH cells. The potential of the sense wires (+) is 1930 V while the field wires (○) are grounded. The numbers on the right side give the stereo angles (mrad) of sense wires in each layer.

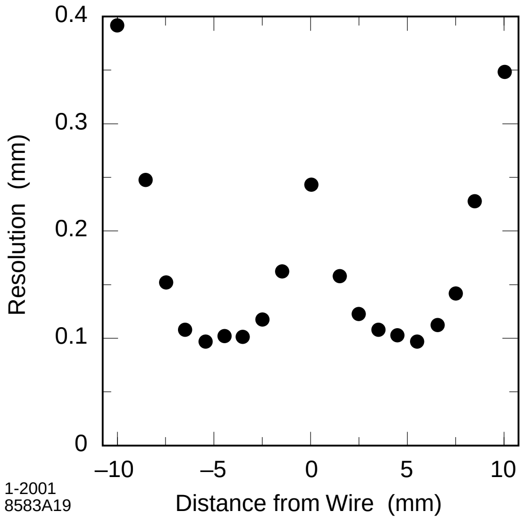

Figure 3.8: Position resolution vs. drift distance in layer 18 of the DCH, averaged over all of the cells in the layer. The sense wire is at 0 mm.

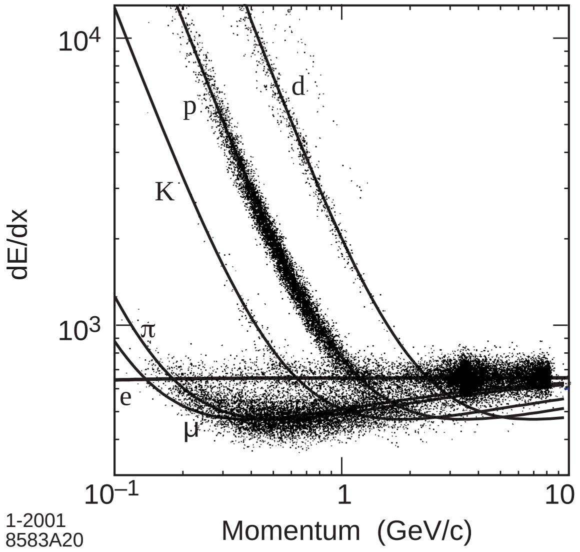

Figure 3.9: DCH dE/dx vs. momentum for particles of different momentum. The curves indicate the Bethe-Bloch predictions.

3.2.3 Detector of Internally Reflected Cherenkov light

The novel particle identification detector in *BABAR* is the DIRC. The goal of the DIRC design is to provide discrimination among protons, kaons, and pions with momenta in the range $0.7 - 4\,\mathrm{GeV}/c$.

Cherenkov radiation is produced when a charged particle travels faster through a medium than the speed of light in that medium. The photons are emitted at an angle (θ_c) with respect to the direction of the charged particle. This Cherenkov angle is related to the index of refraction of the medium (n) and the speed of the charged particle (β):

$$\cos\theta_c = \frac{1}{n}\frac{1}{\beta}. \tag{3.3}$$

Again, since θ_c depends on β and not momentum, we can discriminate between charged particles of different mass by measuring their momentum and θ_c. In the DIRC, the "radiator" medium is one of 144 polished synthetic fused silica (quartz) bars. The index of refraction n in quartz is 1.473. These bars, with rectangular cross-sections, serve as light guides for the resulting Cherenkov radiation. Some of the light is totally internally reflected and the angles of incidence and reflection are conserved when reflecting off a flat surface.

The layout of the DIRC is illustrated in Figure 3.10 (a). The light is guided down quartz bars to the backward end of the detector with $\sim 80\%$ efficiency until it is emitted in the *standoff box*. Typically $\sim 20 - 65$ photons reach the standoff box for a single charged track. The standoff box is made of stainless steel and contains about 6000 liters of purified de-ionized water ($n \sim 1.346$). The far end of the standoff box is instrumented with nearly $11,000$ closely packed photomultiplier tubes (PMTs), which are shielded from the magnetic field of the solenoid. Each PMT is mounted with a hexagonal "light-catcher" and typically operated at 1.14 kV. The distance from the end of the quartz bar to the PMTs is about 1.17 m, which together with the size of the PMTs and the quartz bars contributes ~ 7 mrad to the single photon θ_c resolution ($\sigma_{c,\gamma}$). The overall single photon resolution (including the RMS spread of the photon production and transmission dispersion) is $\sigma_{c,\gamma} \approx 10$ mrad. The arrival time of the photons is measured with a resolution of 1.7 ns.

A typical physics event is shown in Figure 3.10 (b) with a ring of photons imaged by the DIRC PMT array. An unbinned maximum likelihood fit is performed to incorporate the emission angle and the arrival time of the Cherenkov photons.

The θ_c resolution (σ_c) for a charged particle is

$$\sigma_c = \frac{\sigma_{c,\gamma}}{\sqrt{N_\gamma}}, \tag{3.4}$$

where N_γ is the number of photons detected. The overall $K - \pi$ separation is 4σ at a momentum of 3 GeV/c.

3.2.4 Electromagnetic Calorimeter

The EMC is designed to efficiently detect photons that are produced from electromagnetic and radiative processes as well as from π^0 and η decays. The EMC also must achieve excellent energy and angular resolution and contribute to electron identification.

The EMC is made of a hermetic finely segmented array of 6580 thallium-doped cesium iodide (CsI(Tl)) crystals, arranged in 56 azimuthal rings. The detector is symmetric around the beam axis, and the layout is shown in Figure 3.11.

A scintillator absorbs electromagnetic radiation and then fluoresces photons at (characteristic) longer wavelengths. Each CsI crystal is doped with 0.1% Tl, machined into tapered trapezoids, and polished. An incoming electron or photon deposits energy that is proportionally converted into scintillation light up to a maximum wavelength of 565 nm.

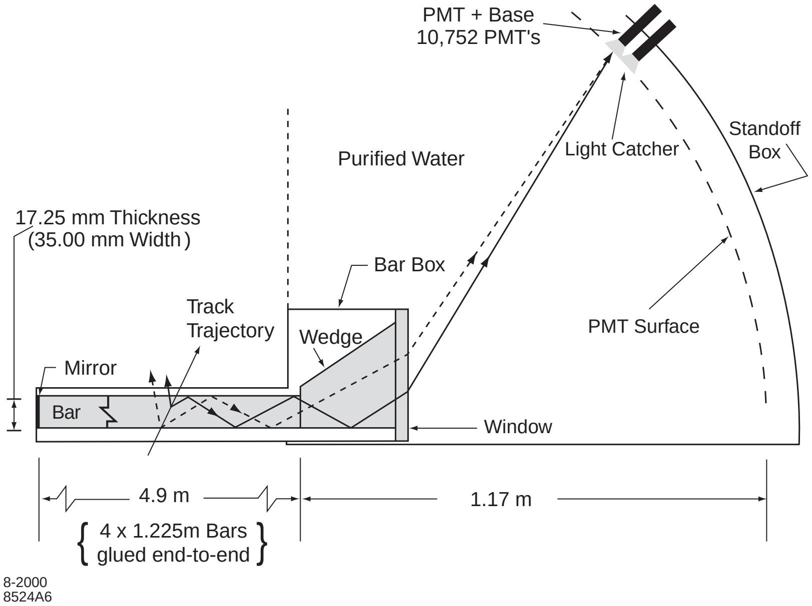

(a) Layout of the DIRC.

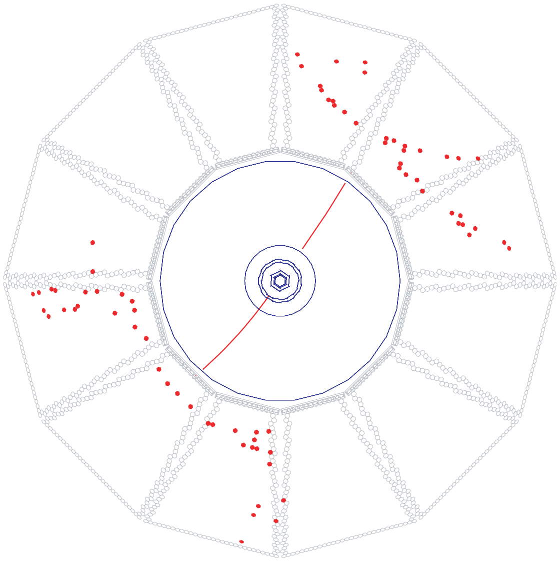

(b) A DIRC Cherenkov ring.

Figure 3.10: (a) The layout of the DIRC detector, showing a charged particle producing Cherenkov light that is guided down quartz bars to the standoff box, which is filled with water and instrumented with PMTs. (b) An $e^+e^- \rightarrow \mu^+\mu^-$ event illustrates a Cherenkov ring with a timing selection of $\pm 8\,\mathrm{ns}$ from the expected arrival time of the Cherenkov photons.

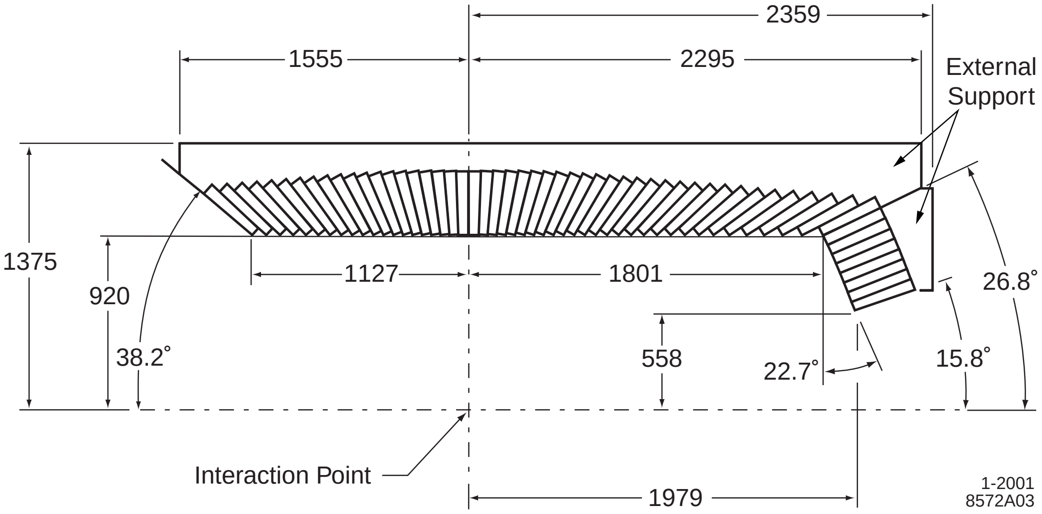

Figure 3.11: The side view of the EMC showing the arrangement of the 56 CsI(Tl) crystal rings. The lower half of the detector is not shown. All dimensions are in mm.

The crystal also acts as a light guide, and light is detected by two (redundant) silicon PIN diodes glued to the rear face of the crystal.

The EMC is over 96% efficient for detecting photons with an energy greater than 20 MeV. The energy resolution of the EMC is

$$\frac{\sigma_E}{E} = \frac{(2.3 \pm 0.3)\%}{\sqrt[4]{E}} \oplus (1.9 \pm 0.1)\,\%, \tag{3.5}$$

where E is the energy of a photon (in GeV) and σ_E is its RMS uncertainty. The first term comes from photon statistics (primarily) and electronics noise, and is dominant at low energies ($E < 1\,\text{GeV}$). The second (constant) term arises from non-uniformities in light collection and uncertainties in calibration, and is dominant at higher energies ($E > 1\,\text{GeV}$).

The angular resolution is determined by the transverse crystal size (the area of the front face of the crystals is typically $4.7 \times 4.7\,\text{cm}^2$, chosen to be comparable to the Molière radius[5]) and the distance from the interaction point:

$$\sigma_\theta = \sigma_\phi = \left(\frac{3.9 \pm 0.1}{\sqrt{E}} \oplus 0.00 \pm 0.04 \right) \text{mrad}, \tag{3.6}$$

---

[5] The Molière radius is a constant characteristic of a material that describes the transverse size of an electromagnetic shower.

where σ_θ (σ_ϕ) is the resolution on the polar (azimuthal) angle. E is again measured in GeV.

3.2.5 Instrumented Flux Return

The flux of the 1.5-T superconducting solenoid magnet is returned through the hexagonal IFR that surrounds the EMC. Sandwiched between sections of iron yoke are active detectors to identify long-lived, deeply penetrating muons and to detect neutral hadrons (such as the K^0_L and the neutron). The total area of the active detector is about $2000\,\mathrm{m}^2$.

The active detectors were originally resistive plate chambers (RPCs) consisting of two highly resistive Bakelite (phenolic polymer) cathodes coated with graphite on one side and linseed oil on the side facing a 2-mm gap (see Figure 3.12). The graphite surfaces are connected to high voltage ($\sim$ 8 kV across the gap) and ground. The gap is filled with a gas mixture of 57% Argon, 39% Freon 134a, and 4% isobutane.

The RPCs are operated in *streamer* mode. When a charged particle passes through an RPC, it ionizes the gas and produces an avalanche similar to the process that occurs in the DCH. Now the Bakelite plates are the cathode and anode analogous to the field and sense wires in the DCH. However, the voltage across an RPC is higher than the the voltage in the DCH, and so the avalanche becomes saturated. An electric field is produced between the front of the avalanche and the anode, and as a result excited atoms emit photons that ionize the gas ahead of the streamer. The electrons from the head of the avalanche recombine with the ionized gas atoms, and the streamer propagates in this way to the anode, producing a signal.

However, issues with the linseed oil coating and graphite electrodes caused the efficiency of the RPCs to drop dramatically, prompting a replacement of the IFR RPCs with a different technology. Limited streamer tubes (LSTs) were chosen to replace[6] the RPCs, and the upgrade proceeded in stages during $2002 - 2006$ [38–40].

The physics of charged particle detection is the same for both technologies. In an LST, the cathode is the graphite coating along the inside of polyvinyl chloride (PVC) walls, and the anode is a gold-plated wire at 5500 V and strung along the center of a cell. Each cell is 17 mm wide, 15 mm high, and 380 mm long. The gas mixture is 89% CO_2, 8% isobutane, and 3% Argon. A cross section of an LST is show in Figure 3.13. Each tube contains

---

[6] In the upgrade to LSTs, some of the RPCs were replaced by brass layers to increase the amount of absorber material. The RPCs in the forward region were replaced with improved RPCs.

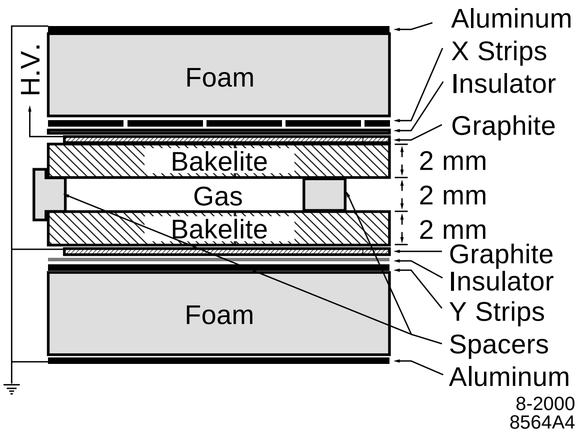

Figure 3.12: A cross section of a resistive plate chamber (RPC), the original IFR active detector technology. The high voltage is connected across the graphite coating on the top layer of Bakelite and the graphite coating on the bottom Bakelite layer.

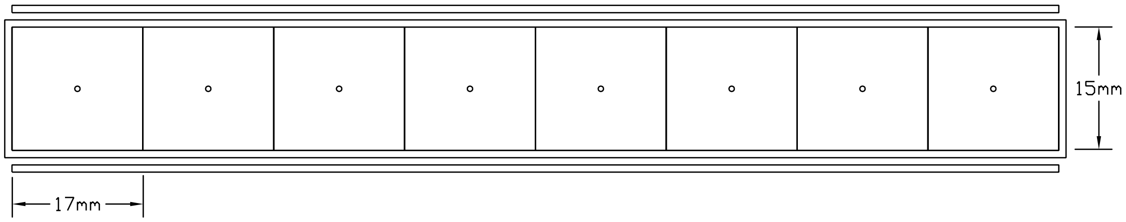

Figure 3.13: A cross section of a limited streamer tube with eight cells.

seven or eight cells. The muon identification efficiency after the upgrade is $> 90\%$ and the z-resolution is $\sim 2\,\text{cm}$.

3.2.6 Trigger

The trigger system must provide a fast, efficient filter to select events of interest (e.g., $B\overline{B}$, $c\overline{c}$, $\tau^+\tau^-$, ...). The BABAR trigger system was designed to select $B\overline{B}$ events with $> 99\%$ efficiency, and achieves $> 99.9\%$ efficiency. It also selects other interesting events with excellent efficiency (e.g., the $e^+e^- \to c\overline{c}$ efficiency is 99.9% and the $e^+e^- \to \tau^+\tau^-$ efficiency is 94.5%). Each BABAR subdetector stores the data from an event in a buffer; the trigger system has $12.9\,\mu\text{s}$ to make the decision whether or not to keep an event.

The trigger consists of two stages. The Level 1 (L1) filter occurs in hardware, and reduces the beam-induced background rates (> 20 kHz) to a typical rate of 2.5 kHz. High PEP-II luminosity means a high background rate, and the goal is to keep the L1 trigger rate less than 4 kHz at a luminosity of $\sim 2 \times 10^{34}$. The L1 trigger decision is primarily based on information from the DCH and EMC. Raw data is sent to the DCH and EMC trigger systems about $2\,\mu$s after an e^+e^- collision. Timing and position information from the DCH cells is used to find track segments, which are then linked together into complete tracks that must have a set p_T above a given threshold. Energy deposition information is collected from the EMC; the amount of energy deposited must be greater than a threshold. The processing times for the DCH and EMC trigger systems are $4-5\,\mu$s, and are followed by another $3\,\mu$s of processing in a global L1 trigger stage. If the event passes either the DCH or the EMC L1 requirements, a signal is sent to all the detector subsystems to initiate event readout. An additional IFR trigger is mainly used for $\mu^+\mu^-$ events and cosmic rays (for calibration). The entire L1 decision is made within the subsystems' electronics buffer capacity limit.

The Level 3 (L3) filter[7] receives the output from L1 and further reduces the event rate to about 300 Hz. The L3 processing is accomplished in software on an online computer farm. The L3 decision process has access to information from all detector subsystems and operates by refining and augmenting the selection methods used in L1, including track finding and EMC energy reconstruction. Most Bhabha ($e^+e^- \rightarrow e^+e^-$) events are vetoed, and special categories of events for luminosity determination and calibration purposes are flagged.

3.3 PEP-II / *BABAR* Performance and Data Samples

Since 1999, the integrated luminosity recorded by *BABAR* is about $440\,\mathrm{fb}^{-1}$ (see Figure 3.14 for the history of the integrated luminosity), which corresponds to about 440 million $B\overline{B}$ events. Included in the complete data sample are *continuum* $e^+e^- \rightarrow q\overline{q}$ events, where $q = c, s, u, d$. An additional $40\,\mathrm{fb}^{-1}$ of data is recorded when PEP-II operates at an energy approximately 40 MeV below the $\Upsilon(4S)$ resonance. The number of $B\overline{B}$ pairs ($N_{B\overline{B}}$) produced in the *BABAR* data sample [41] is determine from this "off-resonance" data. The number of $e^+e^- \rightarrow \mu^+\mu^-$ events in the on-resonance data sample is scaled by the ratio of off-resonance hadronic events to off-resonance $e^+e^- \rightarrow \mu^+\mu^-$ events. This quantity

---

[7] There is no Level 2 trigger for historical reasons.

is subtracted from the total number of hadronic events in the on-resonance data sample to determine $N_{B\overline{B}}$. The statistical uncertainty on the ratio of off-resonance hadronic to $e^+e^- \rightarrow \mu^+\mu^-$ events dominates the 1.1% systematic uncertainty on $N_{B\overline{B}}$.

This dissertation is based on a sample of nearly 383 million $B\overline{B}$ events. Table 3.1 summarizes the number of $B\overline{B}$ events in this sample by Run period.

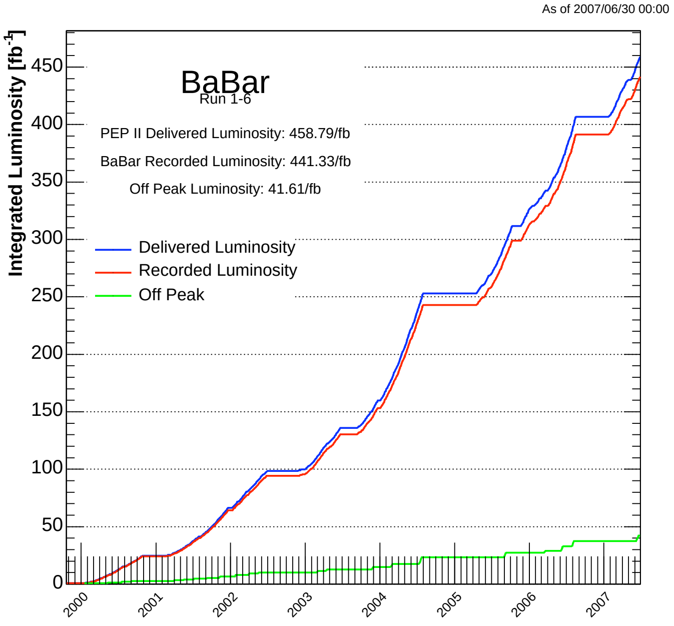

Figure 3.14: The integrated luminosity delivered by PEP-II (blue line) and recorded by *BABAR* (red line) since the beginning of the experiment in 1999.

3.3.1 Exclusive Signal Monte Carlo Samples

Exclusive B meson decays are simulated with the Monte Carlo (MC) event generator **EvtGen** [42]. **EvtGen** uses stochastic MC methods to generate complicated sequences of decays. The decay amplitudes (instead of probabilities) are calculated so that the correct kinematic distributions are generated. We generate large samples of simulated signal events and propagate the decay products through a detailed detector simulation (modeled using the **GEANT4** simulation package [44]). **GEANT4** simulates the decay products' interaction with

Table 3.1: Integrated luminosity and number of produced $B\overline{B}$ events, by Run. The errors on the number of $B\overline{B}$ pairs are statistical and systematic, respectively.

	Int. Luminosity (fb^{-1})	Number of $B\overline{B}$ pairs (10^6)
Run 1	20.4	$22.43 \pm 0.03 \pm 0.25$
Run 2	61.1	$67.47 \pm 0.04 \pm 0.74$
Run 3	32.3	$35.61 \pm 0.03 \pm 0.39$
Run 4	100.3	$110.48 \pm 0.06 \pm 1.22$
Run 5	133.0	$146.93 \pm 0.06 \pm 1.62$
Total	347.2	$382.9 \pm 0.1 \pm 4.2$

detector material and a detailed map of the magnetic field. It includes detector imperfections such as finite resolution, extra material needed for electronics and support structure, and any broken or damaged sections (although these are limited). The simulation is also overlaid with extraneous hits in the detector due to noise and PEP-II backgrounds based on the evolving integrated luminosity and background conditions since 1999. Once the simulated events are propagated through the full detector simulation, they are reconstructed in the same way as data events so that the detector efficiency can be accurately determined.

Table 3.2 summarizes the exclusive signal MC samples used to calculate the detection efficiency (see Chapter 6). We also use these samples in the selection criteria optimization and the fit validation studies.

The value of the MC samples is that we know exactly which decays were generated in each event. The original generated particle trajectories are turned into "hits" in the detector, which are then reconstructed. However, the process of matching the reconstructed charged particle trajectories with the original generated particle trajectories has some nuances. For example, there may not be a one-to-one correspondence between the generated hits and the reconstructed hits. Soft photons could be emitted at any stage in a decay process. Long-lived particles may have a non-zero probability of decaying within the detector volume. The process of matching the reconstructed decays with the generated (or "true") decays is called *truth-matching*.

For example, in order to truth-match the $\overline{B}^0 \to \mathit{\Lambda}_c^+ \overline{p}$, $\mathit{\Lambda}_c^+ \to pK^-\pi^+$ signal MC sample, we require that the four reconstructed charged tracks in each event are consistent with a generated p, K^-, π^+, and $\overline{p}$. The three $\mathit{\Lambda}_c^+$ daughter tracks must come from the same

Table 3.2: Exclusive signal MC samples used to calculate the selection efficiency for each mode.

Mode	# Events
$\overline{B}^0 \to \Lambda_c^+ \overline{p}$, $\Lambda_c^+ \to pK^-\pi^+$	350,000
$\overline{B}^0 \to \Lambda_c^+ \overline{p}$, $\Lambda_c^+ \to pK_S^0$	175,000
$\overline{B}^0 \to \Lambda_c^+ \overline{p}$, $\Lambda_c^+ \to pK_S^0\pi^+\pi^-$	350,000
$\overline{B}^0 \to \Lambda_c^+ \overline{p}$, $\Lambda_c^+ \to \Lambda\pi^+$	350,000
$\overline{B}^0 \to \Lambda_c^+ \overline{p}$, $\Lambda_c^+ \to \Lambda\pi^+\pi^-\pi^+$	350,000
$B^- \to \Lambda_c^+ \overline{p}\pi^-$, $\Lambda_c^+ \to pK^-\pi^+$	$1,612,000$
$B^- \to \Lambda_c^+ \overline{p}\pi^-$, $\Lambda_c^+ \to pK_S^0$	350,000
$B^- \to \Lambda_c^+ \overline{p}\pi^-$, $\Lambda_c^+ \to pK_S^0\pi^+\pi^-$	350,000
$B^- \to \Lambda_c^+ \overline{p}\pi^-$, $\Lambda_c^+ \to \Lambda\pi^+$	350,000
$B^- \to \Lambda_c^+ \overline{p}\pi^-$, $\Lambda_c^+ \to \Lambda\pi^+\pi^-\pi^+$	350,000
$B^- \to \Sigma_c(2455)^0\overline{p}$, $\Sigma_c(2455)^0 \to \Lambda_c^+\pi^-$, $\Lambda_c^+ \to pK^-\pi^+$	350,000

parent, which must be a Λ_c^+. Finally, the grandparent of the Λ_c^+ daughter tracks must be the same as the parent of the $\overline{p}$ and must be a $\overline{B}^0$. We also allow for events in which the π^+ decays into a μ^+ and a $\overline{\nu}_\mu$, although this is a small effect. Truth-matching is performed on all of the signal MC samples in an analogous fashion.

3.3.2 Background Monte Carlo Samples

Large MC samples are used to make quantitative comparisons with the data sample and to investigate sources of background. Samples of $e^+e^- \to \Upsilon(4S) \to B^+B^-$ and $e^+e^- \to \Upsilon(4S) \to B^0\overline{B}^0$ events are based on simulations of many exclusive B decays (using `EvtGen`). We use these samples to identify and reject B decays that closely resemble the modes of interest. Samples of $e^+e^- \to u\overline{u}, d\overline{d}, s\overline{s}$ and $e^+e^- \to c\overline{c}$ events are simulated using `Jetset7.4` [43] to model these generic hadronization processes. For example, Λ_c^+ baryons are copiously produced in $e^+e^- \to c\overline{c}$ events, but are not of interest since they do not originate from B meson decays. We use the generic $e^+e^- \to c\overline{c}$ sample to study how to best reject these background events. Again, the decays in each of these samples are propagated through the detailed detector simulation package `GEANT4`. Table 3.3 shows the number of events in the generic MC samples and the equivalent integrated luminosity of these samples.

Table 3.3: Equivalent integrated luminosity and number of events for the generic MC samples.

Mode	Int. Luminosity(fb^{-1})	# Events
$e^+e^- \to u\overline{u}, d\overline{d}, s\overline{s}$	286.7	599,254,000
$e^+e^- \to c\overline{c}$	413.4	537,402,000
$e^+e^- \to B^+B^-$	426.5	468,804,000
$e^+e^- \to B^0\overline{B}^0$	429.0	471,556,000

Table 3.4: Exclusive background MC samples used to investigate background sources from similar B decay modes.

Mode	# Events
$\overline{B}^0 \to \Sigma_c(2455)^+\overline{p}$, $\Sigma_c(2455)^+ \to \Lambda_c^+\pi^0$, $\Lambda_c^+ \to pK^-\pi^+$	175,000
$\overline{B}^0 \to \Lambda_c^+\overline{p}\pi^0$, $\Lambda_c^+ \to pK^-\pi^+$	350,000
$\overline{B}^0 \to \Lambda_c^+\overline{p}\pi^+\pi^-$, $\Lambda_c^+ \to pK^-\pi^+$	350,000
$B^- \to \Lambda_c^+\overline{p}\pi^-\pi^0$, $\Lambda_c^+ \to pK^-\pi^+$	350,000

Additional exclusive MC samples were generated to investigate particular types of background for the baryonic B decays studied in this analysis. In particular, these background decay modes are similar to the signal modes but have one more or one fewer (charged or neutral) daughter particle in the final state. These additional samples are listed in Table 3.4. Note that the "signal" samples listed in Table 3.2 are also used as background samples for the corresponding decay modes.

3.3.3 Toy Monte Carlo Samples

The final class of simulated data samples are used to study a particular probability density function or kinematic distribution. In these cases, it is not necessary or prudent to perform the time-consuming and computation-intensive simulation of entire events and the full detector simulation and reconstruction process. Therefore, we simulate MC samples to model a simplified aspect of the data analysis; these samples are called "toy" MC samples.

Chapter 4

Event Preselection

In this section we present the basic requirements used to efficiently select events that might contain the decays $\overline{B}^0 \to \Lambda_c^+ \overline{p}$ and $B^- \to \Lambda_c^+ \overline{p} \pi^-$. We describe charged particle tracking and identification as well as the decay chain reconstruction used in this analysis. Finally, we present kinematic variables that are used to discriminate signal candidates from background candidates.

4.1 Charged Particle Tracking

The reconstruction of charged particle trajectories, or "tracks", uses information from both the SVT and the DCH [35]. Five parameters describe the helix of a charged track:

$$\begin{pmatrix} d_0 & \phi_0 & \omega & z_0 & \tan\lambda \end{pmatrix}, \tag{4.1}$$

where d_0 is the distance between the point of closest approach to the z-axis and the origin in the $x - y$ plane, ϕ_0 is the azimuthal angle at the point of closest approach, ω is the curvature (which is equal to the inverse of the transverse momentum of the particle, p_T), and z_0 is the perpendicular distance between the point of closest approach to the z-axis and the $x - y$ plane. The track finding and fitting algorithm is based on a Kalman filter [45], and includes a model of the detector material and a full map of the magnetic field.

Tracks that have at least four points in space and are consistent with being a true charged particle trajectory are called *ChargedTracks*. Additional quality requirements can be placed on these tracks; we define two sets of these requirements as *GoodTracksVeryLoose* and *GoodTracksLoose*. For *GoodTracksVeryLoose*, we require that

- the momentum p of the particle must be less than 10 GeV/c;
- the distance of closest approach to the e^+e^- interaction point (IP) in the $x-y$ plane must be less than 1.5 cm;
- the track must be within ±10 cm of the IP in the z-direction;

For the more rigorous *GoodTracksLoose* requirement, the track must pass all of the *GoodTracksVeryLoose* requirements along with the following additional criteria:

- the transverse momentum p_T must be greater than 100 MeV/c;
- there must be at least 12 interactions in the DCH associated with the track.

The tighter quality requirements are appropriate for charged particles that originate from close to the IP. Daughters of long-lived particles are required to satisfy only *ChargedTracks*.

4.2 Charged Particle Identification

All *ChargedTracks* are assigned a pion mass hypothesis by default. Additional information such as dE/dx measurements from the SVT and DCH and the opening angle of the cone of Cherenkov radiation from the DIRC are considered in determining the correct mass hypothesis. We calculate a likelihood that a given particle is a pion, kaon, or proton:

$$\mathcal{L}_i = \mathcal{L}_i^{\mathrm{SVT}} \times \mathcal{L}_i^{\mathrm{DCH}} \times \mathcal{L}_i^{\mathrm{DIRC}}, \tag{4.2}$$

where $i = \pi, K, p$.

For the SVT and DCH, the measured energy loss ($\mathrm{d}E/\mathrm{d}x_{\mathrm{meas}}$) is compared to the expected energy loss ($\mathrm{d}E/\mathrm{d}x_{\text{B-B}}$) based on the Bethe-Bloch relation (see Eqn. 3.2):

$$\frac{\mathrm{d}E/\mathrm{d}x_{\mathrm{meas}} - \mathrm{d}E/\mathrm{d}x_{\text{B-B}}}{\sigma_{\mathrm{meas}}}, \tag{4.3}$$

where σ_{meas} is the uncertainty on the measured energy loss. The dE/dx uncertainty for the DCH is a function of the polar angle of the track and the number of interactions in the

DCH, and $\mathcal{L}_i^{\mathrm{DCH}}$ is calculated based on a Gaussian Probability Density Function (PDF). The dE/dx uncertainty for the SVT is a function of the number of silicon wafers traversed in the SVT, and is asymmetric—the uncertainty takes on different values depending on whether the measured dE/dx is above or below the predicted value. Therefore $\mathcal{L}_i^{\mathrm{SVT}}$ is calculated based on a bifurcated[1] Gaussian PDF.

The $\mathcal{L}_i^{\mathrm{DIRC}}$ is divided into two momentum regions: $\mathcal{L}_i^{\mathrm{DIRC}} = \mathcal{L}_i^{\mathrm{DIRC}}(\text{binned}) \times \mathcal{L}_i^{\mathrm{DIRC}}(p > 1.5\,\mathrm{GeV}/c)$. A binned likelihood ($\mathcal{L}_i^{\mathrm{DIRC}}(\text{binned})$) is constructed from a lookup table in bins of lab momentum, Cherenkov angle, the number of detected photons, and the track quality. For $p > 1.5\,\mathrm{GeV}/c$, the binned likelihood is multiplied by a Gaussian PDF based on the measured Cherenkov angle.

Particle identification (PID) is performed using likelihood ratios. These likelihood ratios are defined as $\mathcal{L}(i/j) = \mathcal{L}_i/(\mathcal{L}_i + \mathcal{L}_j)$, where i and j can each be π, K, or p. We define a set of requirements for protons, kaons, and pions as *pLHVeryLoose*, *KLHVeryLoose*, and *piLHVeryLoose*[2]:

- *pLHVeryLoose* requires $\mathcal{L}(K/p) < 0.75$ and $\mathcal{L}(p/\pi) > 0.5$;
- *KLHVeryLoose* requires $\mathcal{L}(K/\pi) > 0.5$ and $\mathcal{L}(K/p) > 0.018$;
- *piLHVeryLoose* requires $\mathcal{L}(K/\pi) < 0.98$ and $\mathcal{L}(p/\pi) < 0.98$.

We also define a set of more restrictive requirements *pLHLoose*, *KLHLoose*, and *piLHLoose*:

- *pLHLoose* requires $\mathcal{L}(K/p) < 0.3$, $\mathcal{L}(p/\pi) > 0.5$, and $p < 0.75\,\mathrm{GeV}/c$ or $\mathcal{L}(e) < 0.98$;
- *KLHLoose* requires $\mathcal{L}(K/\pi) > 0.8176$, $\mathcal{L}(K/p) > 0.018$, and $p < 0.4\,\mathrm{GeV}/c$ or $\mathcal{L}(e) < 0.98$;
- *piLHLoose* requires $\mathcal{L}(K/\pi) < 0.82$, $\mathcal{L}(p/\pi) < 0.98$, and $\mathcal{L}(e) < 0.98$.

Note that we indirectly use a similar likelihood fraction $\mathcal{L}(e)$ to reject electrons. This likelihood is based on information from the DCH (dE/dx), DIRC (Cherenkov angle, number

---

[1] A bifurcated Gaussian is asymmetric; it has one σ parameter to describe the width of the Gaussian above the mean, and a second σ parameter to describe the width of the Gaussian below the mean.

[2] Note that *LH* stands for likelihood.

of photons), and EMC (energy deposited, number of crystals hit, lateral energy distribution, longitudinal energy distribution):

$$\mathcal{L}(e) = \frac{\mathcal{L}_e}{\mathcal{L}_e + 5\mathcal{L}_\pi + \mathcal{L}_K + 0.1\mathcal{L}_p}. \tag{4.4}$$

In summary, a *ChargedTrack* that passes, for example, the *pLHVeryLoose* requirements is assigned a proton mass and is called a “proton candidate”. Since we then have the mass and measured momentum of all the pion, kaon, and proton candidates in an event, we have a complete description of each candidate in terms of its energy-momentum four-vector

$$p^\mu = (E, p_x, p_y, p_z)\,, \tag{4.5}$$

since $E^2 - |\vec{p}|^2 = m^2$.

4.3 Reconstruction of Decay Vertices

Once tracks are identified and mass hypotheses are assigned, we can combine the four-vectors of tracks in an event to determine 1) if the particles originated from the same parent and 2) the invariant mass of the parent particle.

We can use as a simple example the decay $\mathit{\Lambda}_c^+ \to pK^-\pi^+$. In each event, *ChargedTracks* are identified by the tracking algorithm. Then PID is applied to each track to determine if it passes *pLHVeryLooose*, *KLHVeryLoose*, and/or *piLHVeryLoose*. We can determine if the three tracks are consistent with coming from the same point and assign coordinates to the best estimate of that point, called the *vertex* (x, y, z). Combining the four-vectors of the three $\mathit{\Lambda}_c^+$ daughters, we construct the *invariant mass* of the combination:

$$m_{pK^-\pi^+} = \sqrt{(E_p + E_{K^-} + E_{\pi^+})^2 - |\vec{p}_p + \vec{p}_{K^-} + \vec{p}_{\pi^+}|^2}. \tag{4.6}$$

We can then select candidates whose $m_{pK^-\pi^+}$ is within a certain range of the $\mathit{\Lambda}_c^+$ mass.

We use a fitting algorithm called `TreeFitter` [46] (again, based on a Kalman filter) to form parent candidates based on each combination of daughter tracks in the event. The algorithm takes the measured track parameters and related uncertainties and performs a least-squares (χ^2) fit, returning a fit probability $P(\chi^2)$. This sophisticated algorithm can also impose *constraints*. For example, a geometric constraint forces the tracks to come from the same location in space and a mass constraint forces the invariant mass of the parent to take a certain value. When constraints are imposed, the momenta of the daughter particles are each adjusted within their uncertainties to achieve the best fit.

The novel feature of `TreeFitter` is that it can extract all the parameters in a complicated decay chain simultaneously, enforcing energy and momentum conservation and constraints at each vertex.

4.4 Candidate Preselection

We build on the framework described in this chapter to describe the specific candidate selection related to this analysis. The requirements described here are imposed to select a manageable sample of candidates that have the same general properties as candidates from true $\overline{B}^0 \rightarrow \mathit{\Lambda}_c^+ \overline{p}$ and $B^- \rightarrow \mathit{\Lambda}_c^+ \overline{p} \pi^-$ decays. The same selection criteria are applied to data and MC samples, except where indicated.

Building from the bottom up, we select $\mathit{\Lambda}_c^+$ candidates in the following decay modes:

1. $\mathit{\Lambda}_c^+ \rightarrow p K^- \pi^+$
2. $\mathit{\Lambda}_c^+ \rightarrow p K_S^0$
3. $\mathit{\Lambda}_c^+ \rightarrow p K_S^0 \pi^+ \pi^-$
4. $\mathit{\Lambda}_c^+ \rightarrow \mathit{\Lambda} \pi^+$
5. $\mathit{\Lambda}_c^+ \rightarrow \mathit{\Lambda} \pi^+ \pi^- \pi^+$.

Modes $2-5$ contain metastable particles: K_S^0 mesons and $\mathit{\Lambda}$ baryons. The average decay length of a K_S^0 meson is characterized by $c\tau = 2.7\,\mathrm{cm}$ and it decays predominantly to two pions. We select $K_S^0 \rightarrow \pi^+ \pi^-$ decays; the branching fraction for the decay of the K_S^0 to charged pions is $\mathcal{B}(K_S^0 \rightarrow \pi^+ \pi^-) = (69.20 \pm 0.05)\%$. The average decay length of a $\mathit{\Lambda}$ baryon is characterized by $c\tau = 7.9\,\mathrm{cm}$. A $\mathit{\Lambda}$ decays predominantly to a nucleon and a pion. We select $\mathit{\Lambda} \rightarrow p \pi^-$ decays; the branching fraction for this process is $\mathcal{B}(\mathit{\Lambda} \rightarrow p \pi^-) = (63.9 \pm 0.5)\%$. In contrast, the $\mathit{\Lambda}_c^+$ decay length is characterized by $c\tau = 59.9\,\mu\mathrm{m}$, and the branching fractions of the $\mathit{\Lambda}_c^+$ decay modes listed above range from $1-5\%$ [9].

The next few subsections describe the selection of candidates. All of the intermediate vertex fits are performed twice: once with a geometric constraint only, and again with a geometric plus a mass constraint on the intermediate particles in the decay chain.

4.4.1 K_S^0 candidate selection

K_S^0 candidates are reconstructed from two *ChargedTracks* that must come from a common vertex. The unconstrained invariant mass of the two pion candidates must be between 486 and 510 MeV/c^2, the vertex $P(\chi^2) > 0.1\%$, and the flight significance (ℓ/σ_ℓ, where ℓ is the flight distance from the Λ_c^+ vertex in the $x - y$ plane) must be greater than 0. The mass of each pair of pion candidates is constrained to the world average K_S^0 mass of 497.7 MeV/c^2 [9].

4.4.2 Λ candidate selection

Each proton candidate that satisfies *pLHVeryLoose* is combined with an oppositely charged *ChargedTrack* to form a Λ candidate. The fitted $p\pi^-$ unconstrained mass is required to be in the range $1.106 - 1.125$ GeV/c^2. The mass of each pair of proton and pion candidates is constrained to the world average Λ mass of 1.1156 GeV/c^2 [9].

4.4.3 Λ_c^+ candidate selection

The Λ_c^+ candidates are reconstructed in each of the five decay modes, with the masses of the composite daughters (e.g. K_S^0 and Λ) constrained to the world average values. All p candidates must satisfy the requirements of *pLHVeryLoose*, K candidates must satisfy *KLHVeryLoose*, and π candidates must be *ChargedTracks*. The Λ_c^+ candidates are selected if the unconstrained invariant mass is in the range $2.235 - 2.335$ GeV/c^2.

A mass constraint is applied to the Λ_c^+ candidates. For the data samples, we use a value of 2.2865 GeV/c^2, in accordance with the most recent world average value [9]. In the MC samples, Λ_c^+ baryons were generated with a (obsolete) mass of 2.2849 GeV/c^2, and therefore we mass-constrain the Λ_c^+ candidates in those samples to their generated mass.

4.4.4 B candidate selection

Each mass-constrained Λ_c^+ candidate is combined with an antiproton (*pLHVeryLoose*) to form a $\overline{B}^0 \to \Lambda_c^+ \overline{p}$ candidate. Each mass-constrained Λ_c^+ candidate is also combined with an antiproton (*pLHVeryLoose*) and a pion (*ChargedTracks*) to form a $B^- \to \Lambda_c^+ \overline{p} \pi^-$ candidate. A vertex fit is performed using `TreeFitter` (note that this fits the entire decay chain of each candidate). Each B candidate must have a mass in the range $5.0 - 6.0$ GeV/c^2 and the χ^2 probability for the fit must be greater than 1×10^{-6}.

The entire decay chain of each candidate is fit again, this time constraining the mass of the B candidate to the world average value ($5279.0\,\mathrm{GeV}/c^2$ for charged B candidates and $5279.4\,\mathrm{GeV}/c^2$ for neutral B candidates) [9]. The results of this fit are used to calculate certain kinematic variables (e.g., the invariant mass $m_{\Lambda_c\pi}$ in the $B^- \to \Lambda_c^+\overline{p}\pi^-$ decay mode) that will be discussed later in this dissertation.

4.5 Kinematic Variables

In *BABAR* we define certain kinematic quantities to distinguish between signal and background in B meson decays. The standard choice of kinematic variables for B decays is the difference (ΔE) between the measured energy of the B candidate and the expected energy, and the energy-substituted mass (m_{ES}). The expected energy is half the total energy ($\sqrt{s}$) in the e^+e^- center of mass (CM) frame, since the energy of the $\Upsilon(4S)$ is about twice the nominal CM beam energy and the $\Upsilon(4S)$ decays to a $B\overline{B}$ pair. The quantities ΔE and m_{ES} are defined

$$\begin{aligned} \Delta E &= E_B^* - \sqrt{s}/2 \quad \text{and} \\ m_{\mathrm{ES}} &= \sqrt{((s/2 + \mathbf{p}_i \cdot \mathbf{p}_B)^2/E_i^2 - \mathbf{p}_B^2)}, \end{aligned} \tag{4.7}$$

where E_B^* is the B candidate energy in the e^+e^- CM frame, $(E_i, \mathbf{p}_i)$ is the four-momentum of the initial e^+e^- system in the laboratory frame, and $\mathbf{p}_B$ is the momentum of the B candidate in the laboratory frame. For signal candidates, ΔE peaks at zero and m_{ES} peaks at the B mass of $5.279\,\mathrm{GeV}/c^2$.

However, we find these variables to be quite correlated in the modes of interest, which presents minor technical difficulties and a bias in extracting the number of signal candidates. The bias appears to be due to different signal components having different correlations (the majority of the signal has a significant ΔE, m_{ES} correlation, but a smaller component has little to no correlation). This can be seen in the scatter plots of ΔE vs. m_{ES} in signal MC samples in Figure 4.1(a) and (c). A study of various kinematics variables [47] suggests a different set of observables based on the unconstrained $\Lambda_c^+\overline{p}(\pi^-)$ invariant mass, m_{rec}, and the *missing* mass $m_{\mathrm{miss}} = |q_{e^+e^-} - \hat{q}_{\Lambda_c^+\overline{p}(\pi^-)}|$, where $q_{e^+e^-}$ is the four-momentum of the e^+e^- system and $\hat{q}_{\Lambda_c^+\overline{p}(\pi^-)}$ is the four-momentum of the B candidate after applying a constraint to m_B. The variables m_{rec} and m_{miss} are rescaled to provide comparable distributions to

ΔE and m_{ES}, respectively (which are more familiar within *BABAR*). The observables are then:

$$\begin{aligned} &(m_{\mathrm{rec}} - m_B) \quad \text{and} \\ &(m_{\mathrm{miss}} + m_B)/2. \end{aligned} \tag{4.8}$$

Figure 4.1 illustrates the distributions of the two sets of kinematic variables in signal MC samples for $\overline{B}^0 \to \Lambda_c^+ \overline{p}$ and $B^- \to \Lambda_c^+ \overline{p} \pi^-$, with $\Lambda_c^+ \to pK^-\pi^+$.

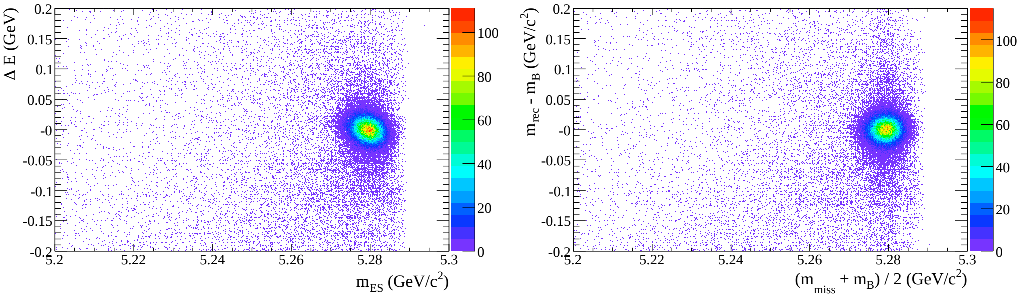

(a) ΔE vs. m_{ES}, B^0 candidates

(b) $(m_{\mathrm{rec}} - m_B)$ vs. $(m_{\mathrm{miss}} + m_B)/2$, B^0 candidates

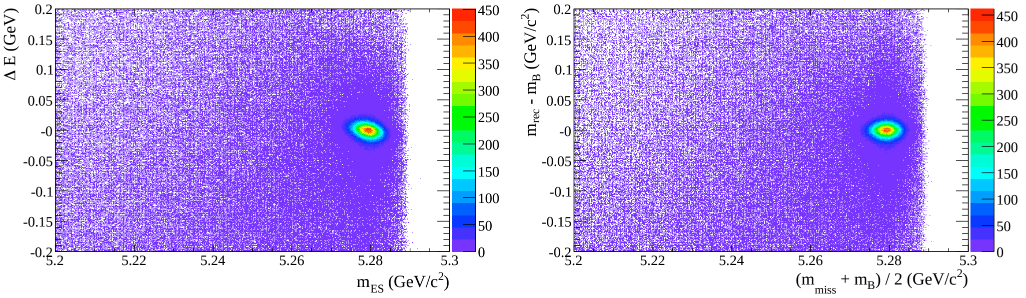

(c) ΔE vs. m_{ES}, B^- candidates

(d) $(m_{\mathrm{rec}} - m_B)$ vs. $(m_{\mathrm{miss}} + m_B)/2$, B^- candidates

Figure 4.1: Distributions of (a,c) ΔE vs. m_{ES} and (b,d) $(m_{\mathrm{rec}} - m_B)$ vs. $(m_{\mathrm{miss}} + m_B)/2$ for B signal MC candidates that pass the preselection criteria. Only candidates from the $\Lambda_c^+ \to pK^-\pi^+$ modes are shown. There are $145,357$ $\overline{B}^0 \to \Lambda_c^+ \overline{p}$ candidates in (a,b) and $708,278$ $B^- \to \Lambda_c^+ \overline{p} \pi^-$ candidates in (b,c). The correlation between ΔE and m_{ES} is more pronounced in the three-body mode, and no correlation between $(m_{\mathrm{rec}} - m_B)$ and $(m_{\mathrm{miss}} + m_B)/2$ is evident.

Chapter 5

Selection criteria optimization

In Chapter 4, we described efficient preselection criteria that select the B decays of interest. However, the resulting data sample has a large number of background events in addition to signal events. In this Chapter, we describe how we optimize the selection criteria to reject background events and maximize the expected significance of any possible signal. We choose a method that minimizes potential experimenters' bias.

5.1 Optimization strategy

We choose further selection criteria to optimize the quantity $S/\sqrt{S+B}$, where S is the expected number of signal events and B is the expected number of background events in the signal region. We define the signal region for the optimization as $|(m_{\text{rec}} - m_B)| < 0.020\,\text{GeV}/c^2$ and $5.274 < (m_{\text{miss}} + m_B)/2 < 5.284\,\text{GeV}/c^2$, which is roughly $\pm 2\sigma$ wide in $(m_{\text{rec}} - m_B)$ and $(m_{\text{miss}} + m_B)/2$. We also define a sideband region in data to estimate the background in the signal region: $0.100\,\text{GeV}/c^2 < (m_{\text{rec}} - m_B) < 0.200\,\text{GeV}/c^2$ and $5.274 < (m_{\text{miss}} + m_B)/2 < 5.284\,\text{GeV}/c^2$. This sideband is purposefully larger than the signal region to maximize the number of background events (particularly in the $\overline{B}^0 \to \Lambda_c^+ \overline{p}$ decay mode) in the optimization.

In the optimization, we use the signal MC samples in each Λ_c^+ decay mode to represent signal events. We truth-match these events to perform the optimization, removing combinatoric background. (This is especially important for the $\Lambda_c^+ \to p K_S^0 \pi^+ \pi^-$ and $\Lambda_c^+ \to \Lambda \pi^+ \pi^- \pi^+$ signal MC samples.) Figure 5.1 (5.2) shows the $(m_{\text{rec}} - m_B)$ vs. $(m_{\text{miss}} + m_B)/2$ distributions for the truth-matched B^0 (B^-) signal MC candidates in each

Table 5.1: Preselection efficiency for each truth-matched signal MC sample in the signal region ($|(m_{\text{rec}} - m_B)| < 20\,\text{MeV}/c^2$ and $5.274 < (m_{\text{miss}} + m_B)/2 < 5.284\,\text{GeV}/c^2$).

Mode	$\overline{B}^0$ Efficiency	B^- Efficiency
$\Lambda_c^+ \to pK^-\pi^+$	27.0%	21.0%
$\Lambda_c^+ \to pK_S^0$	22.4%	18.9%
$\Lambda_c^+ \to pK_S^0\pi^+\pi^-$	11.9%	8.6%
$\Lambda_c^+ \to \Lambda\pi^+$	18.9%	15.8%
$\Lambda_c^+ \to \Lambda\pi^+\pi^-\pi^+$	10.6%	7.2%

of the Λ_c^+ decay modes. Note that there is no correlation between the chosen kinematic variables, $(m_{\text{rec}} - m_B)$ and $(m_{\text{miss}} + m_B)/2$.

We determine S as follows for $\overline{B}^0 \to \Lambda_c^+\overline{p}$, $\Lambda_c^+ \to pK^-\pi^+$:

$$\begin{aligned} S_{\Lambda_c^+\overline{p}} &= \varepsilon \times N_{B\overline{B}} \times \mathcal{B}(\overline{B}^0 \to \Lambda_c^+\overline{p}) \times \mathcal{B}(\Lambda_c^+ \to pK^-\pi^+) \\ &= \varepsilon \times 383.64 \times 10^6 \times 2.15 \times 10^{-5} \times 0.05, \end{aligned} \tag{5.1}$$

and for $B^- \to \Lambda_c^+\overline{p}\pi^-$, $\Lambda_c^+ \to pK^-\pi^+$:

$$\begin{aligned} S_{\Lambda_c^+\overline{p}\pi^-} &= \varepsilon \times N_{B\overline{B}} \times \mathcal{B}(B^- \to \Lambda_c^+\overline{p}\pi^-) \times \mathcal{B}(\Lambda_c^+ \to pK^-\pi^+) \\ &= \varepsilon \times 383.64 \times 10^6 \times 3.53 \times 10^{-4} \times 0.05. \end{aligned} \tag{5.2}$$

The efficiency ε is calculated by dividing the number of signal MC events that pass a given set of selection criteria by the number of generated signal MC events (see Table 3.2), and $N_{B\overline{B}}$ is the number of $B\overline{B}$ pairs[1] produced in Runs 1 − 5. The values of $\mathcal{B}(\overline{B}^0 \to \Lambda_c^+\overline{p})$ and $\mathcal{B}(B^- \to \Lambda_c^+\overline{p}\pi^-)$ are from previous measurements [33], and the value of $\mathcal{B}(\Lambda_c^+ \to pK^-\pi^+) = (5.0 \pm 1.3)\%$ is the world average [9]. Each of the other Λ_c^+ decay modes is scaled by their relative branching fractions (compared to $\Lambda_c^+ \to pK^-\pi^+$), summarized in Table 5.2.

Table 5.1 shows the preselection efficiency for each Λ_c^+ decay mode with the additional requirement that the vertex status for each fit is successful.

The background in the signal region is determined from a $(m_{\text{rec}} - m_B)$ sideband that is

---

[1] Note that the $N_{B\overline{B}}$ used in the selection criteria optimization is slightly outdated compared to the number quoted in Chapter 3. The number in Chapter 3, Table 3.1 is correct and is used in the branching fraction measurements.

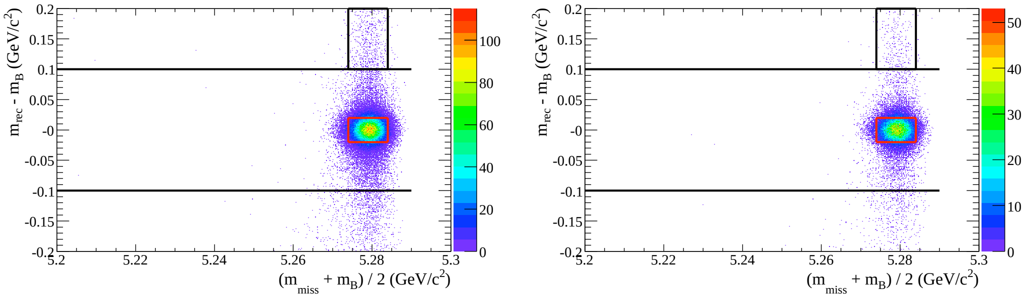

(a) 123, 864 $\Lambda_c^+ \to pK^-\pi^+$ candidates (b) 50, 581 $\Lambda_c^+ \to pK_S^0$ candidates

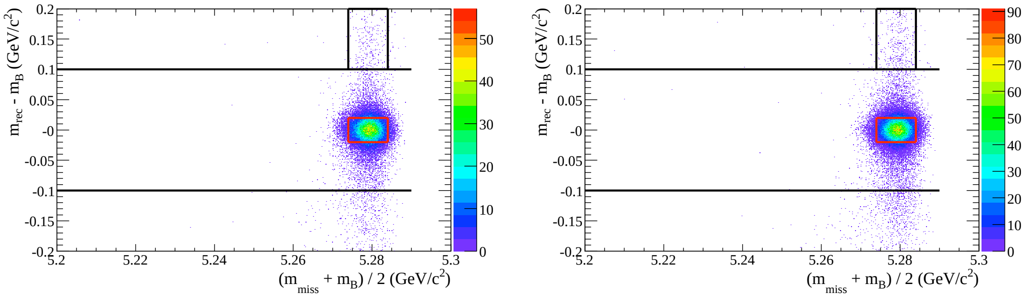

(c) 55, 626 $\Lambda_c^+ \to pK_S^0\pi^+\pi^-$ candidates (d) 85, 523 $\Lambda_c^+ \to \Lambda\pi^+$ candidates

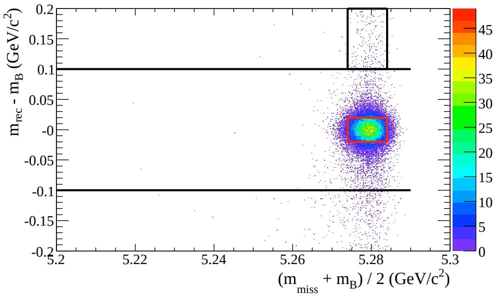

(e) 49, 213 $\Lambda_c^+ \to \Lambda\pi^+\pi^-\pi^+$ candidates

Figure 5.1: Distribution of $(m_{\text{rec}} - m_B)$ versus $(m_{\text{miss}} + m_B)/2$ for $\overline{B}^0 \to \Lambda_c^+\overline{p}$ truth-matched signal MC candidates that pass the preselection criteria, separated by Λ_c^+ decay mode. The red box indicates the signal region used in the optimization. The sideband and fit regions are also indicated.

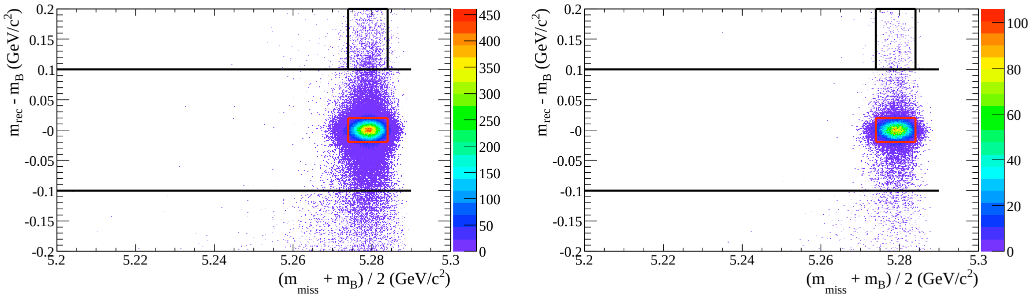

(a) 412, 849 $\Lambda_c^+ \to pK^-\pi^+$ candidates (b) 79, 106 $\Lambda_c^+ \to pK_S^0$ candidates

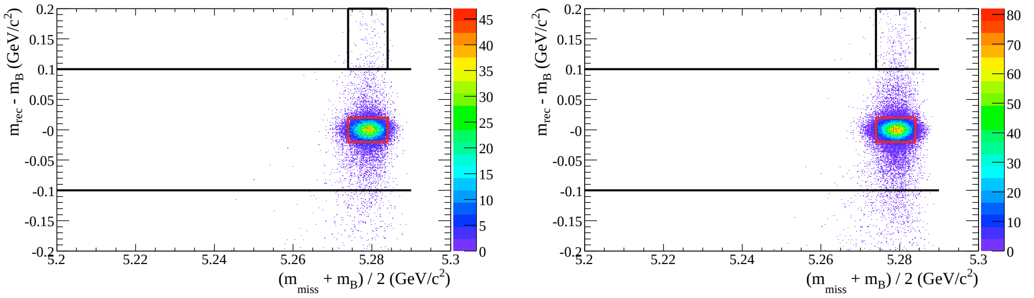

(c) 36, 865 $\Lambda_c^+ \to pK_S^0\pi^+\pi^-$ candidates (d) 66, 718 $\Lambda_c^+ \to \Lambda\pi^+$ candidates

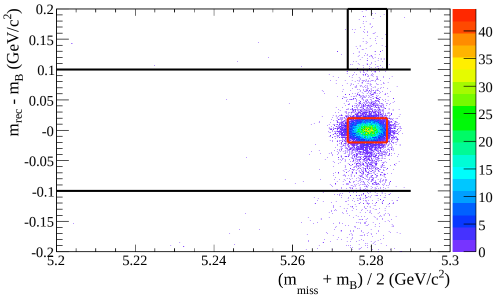

(e) 30, 722 $\Lambda_c^+ \to \Lambda\pi^+\pi^-\pi^+$ candidates

Figure 5.2: Distribution of $(m_{\rm rec} - m_B)$ versus $(m_{\rm miss} + m_B)/2$ for $B^- \to \Lambda_c^+\overline{p}\pi^-$ truth-matched signal MC candidates that pass the preselection criteria, separated by Λ_c^+ decay mode. The red box indicates the signal region used in the optimization. The sideband and fit regions are also indicated.

Table 5.2: Branching fractions with respect to $\Lambda_c^+ \to pK^-\pi^+$ [9] used in the selection criteria optimization. The relative branching fractions for the modes $\Lambda_c^+ \to pK_S^0$ and $\Lambda_c^+ \to pK_S^0\pi^+\pi^-$ are multiplied by $\mathcal{B}(K_S^0 \to \pi^+\pi^-)$ and those for the modes $\Lambda_c^+ \to \Lambda\pi^+$ and $\Lambda_c^+ \to \Lambda\pi^+\pi^-\pi^+$ are multiplied by $\mathcal{B}(\Lambda \to p\pi^-)$.

Mode	$\mathcal{B}/\mathcal{B}(\Lambda_c^+ \to pK^-\pi^+)$	
$\Lambda_c^+ \to pK^-\pi^+$	1	
$\Lambda_c^+ \to pK_S^0$	$(0.47 \pm 0.04)/2$	$\times 0.69$
$\Lambda_c^+ \to pK_S^0\pi^+\pi^-$	$(0.51 \pm 0.06)/2$	$\times 0.69$
$\Lambda_c^+ \to \Lambda\pi^+$	0.202 ± 0.018	$\times 0.64$
$\Lambda_c^+ \to \Lambda\pi^+\pi^-\pi^+$	0.525 ± 0.032	$\times 0.64$

outside the fit region. The region below $-0.100\,\mathrm{GeV}/c^2$ in $(m_{\mathrm{rec}} - m_B)$ contains feed-down from charmed baryonic modes containing more than one pion, so we are restricted to using the region above $+0.100\,\mathrm{GeV}/c^2$ (see Figures 5.1 and 5.2). In the three-body mode, feed-up from the two-body $\overline{B}^0 \to \Lambda_c^+\overline{p}$ mode is negligible (see Section 7.2).

To determine the expected number of background events B, we must scale the number of events in the sideband region to compensate for the different sizes of the signal and sideband regions and the negative slope in $(m_{\mathrm{rec}} - m_B)$ (shown in Figures 5.3 and 5.4 for each Λ_c^+ decay mode). In order to estimate this scale factor, we use events that fall between 5.200 and $5.265\,\mathrm{GeV}/c^2$ in $(m_{\mathrm{miss}} + m_B)/2$ (below the signal region).

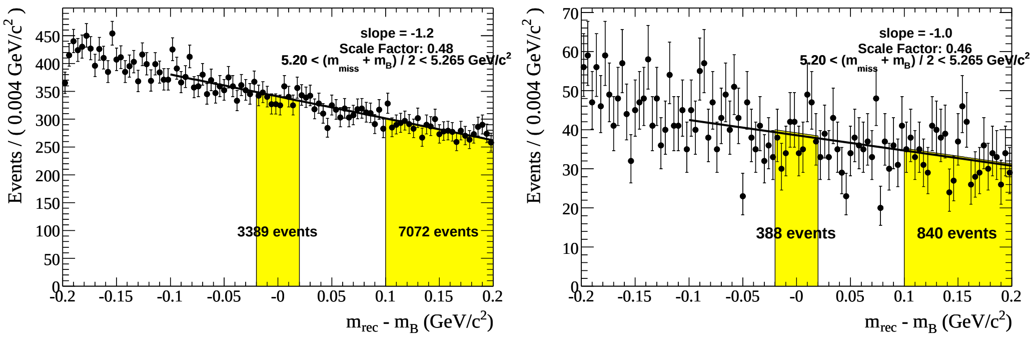

(a) $\Lambda_c^+ \to pK^-\pi^+$

(b) $\Lambda_c^+ \to pK_S^0$

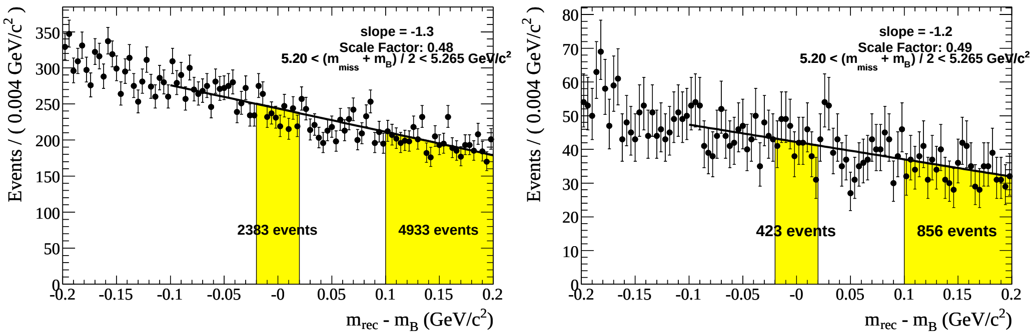

(c) $\Lambda_c^+ \to pK_S^0\pi^+\pi^-$

(d) $\Lambda_c^+ \to \Lambda\pi^+$

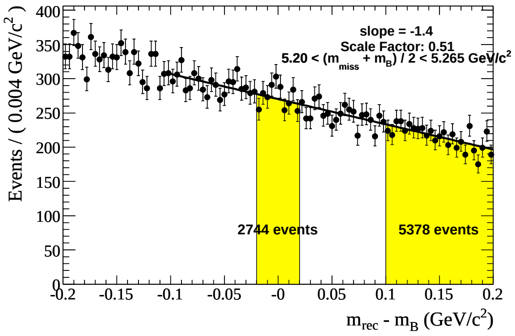

(e) $\Lambda_c^+ \to \Lambda\pi^+\pi^-\pi^+$

Figure 5.3: Distributions of $(m_{\text{rec}} - m_B)$ for B^0 candidates in data in the region $5.200\,\text{GeV}/c^2 < (m_{\text{miss}} + m_B)/2 < 5.265\,\text{GeV}/c^2$ (below the signal region). A negative slope in $(m_{\text{rec}} - m_B)$ is clearly visible, and we derive a scale factor to correct for this slope from the ratio of the numbers of events in the highlighted regions.

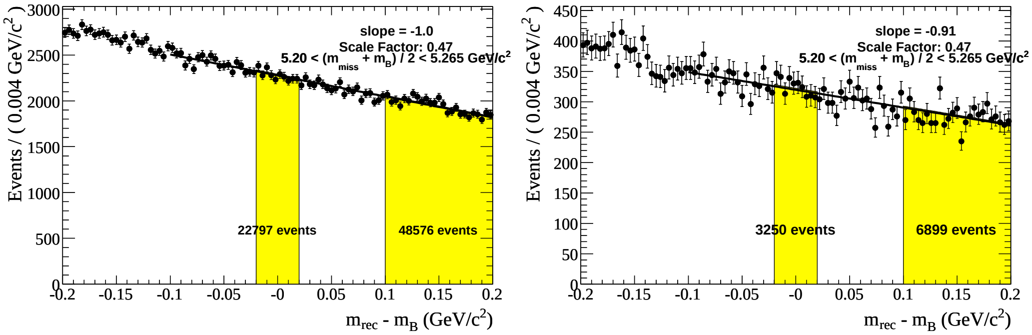

(a) $\Lambda_c^+ \rightarrow pK^-\pi^+$ (b) $\Lambda_c^+ \rightarrow pK_S^0$

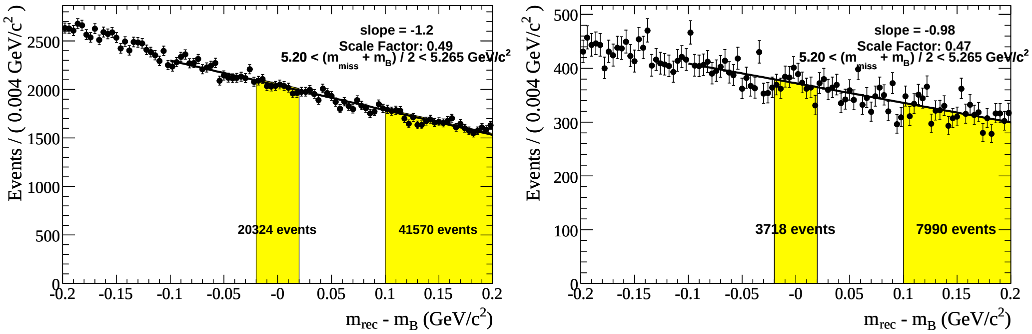

(c) $\Lambda_c^+ \rightarrow pK_S^0\pi^+\pi^-$ (d) $\Lambda_c^+ \rightarrow \Lambda\pi^+$

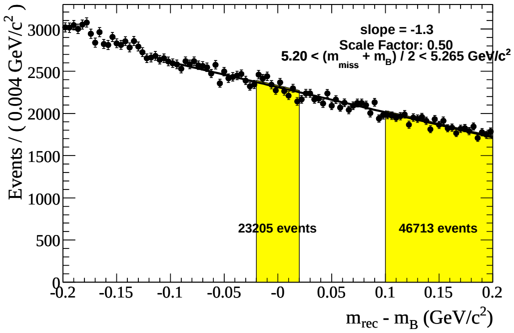

(e) $\Lambda_c^+ \rightarrow \Lambda\pi^+\pi^-\pi^+$

Figure 5.4: Distributions of $(m_{\rm rec} - m_B)$ for B^- candidates in data in the region $5.200\,{\rm GeV}/c^2 < (m_{\rm miss} + m_B)/2 < 5.265\,{\rm GeV}/c^2$ (below the signal region). A negative slope in $(m_{\rm rec} - m_B)$ is clearly visible, and we derive a scale factor to correct for this slope from the ratio of the numbers of events in the highlighted regions.

5.2 Optimization procedure and results

The variables that are considered in the optimization of the selection criteria are:

- PID of the K_S^0 daughter πs, the Λ daughter p, π, the Λ_c^+ daughter p, K, π, and the B daughter p, π
- track quality of the Λ_c^+ daughter p, K and the B daughter p (e.g., *GoodTracksVeryLoose* or *GoodTracksLoose*)
- unconstrained K_S^0, Λ, and Λ_c^+ candidate masses ($m_{K_S^0}, m_\Lambda, m_{\Lambda_c^+}$)
- K_S^0 and Λ flight significances $\ell_{K_S^0}/\sigma_{\ell_{K_S^0}}, \ell_\Lambda/\sigma_{\ell_\Lambda}$ in the $x-y$ plane with respect to the Λ_c^+ vertex
- χ^2 probability of the geometrically-constrained K_S^0, Λ, Λ_c^+, and B candidate vertex fit ($P_{K_S^0}(\chi^2), P_\Lambda(\chi^2), P_{\Lambda_c^+}(\chi^2), P_B(\chi^2)$)
- cosine of the angle of the B candidate momentum vector with respect to the beam axis in the e^+e^- center-of-mass frame ($\cos\theta^*$)
- ratio of the 2nd to the 0th Fox-Wolfram moment (R_2) of the entire event (including charged track and neutral candidate information)
- absolute value of the cosine of the angle between the B candidate thrust axis and the thrust axis of the rest of the event (ROE) in the e^+e^- center-of-mass frame ($|\cos\theta_{thr}^{ROE}|$)
- Fisher discriminant based on several event-shape variables, including CLEO energy cones:
  - $|\cos\theta^*|$, described above
  - Absolute value of the cosine of the angle of the B candidate thrust axis with respect to the beam axis in the e^+e^- center-of-mass frame, $|\cos\theta_{thr}|$
  - CLEO energy flow: Summed momentum of the ROE in nine cones centered around the thrust axis of the B candidate
- Fisher discriminant based on several event-shape variables, including Legendre momentum flow:

- $|\cos\theta^*|$, described above
- $|\cos\theta_{thr}|$, described above
- Legendre momentum flow: 0th and 2nd angular moments (L_0 and L_2, respectively) from the integration of Legendre expansions of the angles between the tracks in the ROE and the B thrust axis. The Legendre moments are defined as $L_j = \sum_i p_i |\cos\theta_i|^j$, where θ_i is the angle with respect to the B thrust axis of the ith track or neutral cluster in the ROE and p_i is its momentum.

Even though the CLEO energy flow and Legendre momentum flow event-shape variables were developed for charmless two-body decays, they provide signal-to-background discrimination power in $\overline{B}^0 \to \Lambda_c^+ \overline{p}$ and $B^- \to \Lambda_c^+ \overline{p} \pi^-$.

It is noted that the optimization procedure may not yield the overall maximally optimal set of selection criteria. However, we took care not to tune on statistical fluctuations in the background samples and made allowances to determine reasonable common values for the various B and Λ_c^+ decay modes studied. The variations in significance are reasonably small, and a non-optimal set of selection criteria does not bias the final result.

The results of the optimization are summarized in Tables 5.3 and 5.4. The significance $S/\sqrt{S+B}$ is optimized for each Λ_c^+ decay mode, and the optimal criteria and highest values are shown. Then, common selection criteria are chosen for all Λ_c^+ decay modes and the significances are computed for each mode. Individual values of the $L_{0,2}$ Fisher discriminant are chosen for each mode, since there is significant variation in the optimal values. The Λ_c^+ mass requirement is tighter for the two-body mode than for the three-body mode (the Λ_c^+ resolution in each signal MC sample is documented in Appendix A). The values of $S/\sqrt{S+B}$ are also shown for the common selection criteria (bottom row). There is little loss in sensitivity due to the choice of common selection criteria.

The track quality of the Λ_c^+ daughter p and K and the B daughter p (not shown in Tables 5.3, 5.4) is chosen to be *GoodTracksLoose*. All other tracks must only satisfy *ChargedTracks*, since the distance of closest approach requirement is unacceptable for tracks originating from a displaced vertex and the efficiency across the $B^- \to \Lambda_c^+ \overline{p} \pi^-$ Dalitz plane (see Chapter 6) is more uniform with a looser tracking requirement for pions.

Distributions of the continuous variables used in the selection criteria are shown in Figures 5.5 and 5.6. The samples in each subfigure have all other selection criteria applied. The signal MC samples are scaled to the expected branching fractions and the different

Λ_c^+ decay modes are weighted by their respective branching ratios and combined. The data sideband samples are scaled to compensate for the negative slope in $(m_{\mathrm{rec}} - m_B)$ and the different region sizes. Generic MC samples are shown for illustration; these samples were not used in the selection criteria optimization. Discrepancies between the generic MC samples and the data sideband samples illustrate the benefit of using the data sideband samples in the optimization; these discrepancies are particularly pronounced in the Fisher discriminant distributions.

Table 5.3: Results of the selection criteria optimization for $\overline{B}^0 \rightarrow \mathit{\Lambda}_c^+ \overline{p}$ signal in each $\mathit{\Lambda}_c^+$ decay mode, along with the chosen selection criteria. We report the best significance for the optimal criteria in each mode and the significance in each mode with the chosen overall selection criteria.

Selection Criteria	Optimal selection in each $\mathit{\Lambda}_c^+$ decay mode					
	$pK^-\pi^+$	pK_S^0	$pK_S^0\pi^+\pi^-$	$\mathit{\Lambda}\pi^+$	$\mathit{\Lambda}\pi^+\pi^-\pi^+$	All
$\lvert m_{K_S^0} - m_{K_S^0}^{\mathrm{PDG}} \rvert$	–	$< 10\,\mathrm{MeV}/c^2$	$< 10\,\mathrm{MeV}/c^2$	–	–	$< 10\,\mathrm{MeV}/c^2$
$\ell_{K_S^0}/\sigma_{\ell_{K_S^0}}$	–	> 2	> 3	–	–	> 2
K_S^0 daughter π PID	–	*LHVeryLoose*	*LHVeryLoose*	–	–	*LHVeryLoose*
$\lvert m_{\mathit{\Lambda}} - m_{\mathit{\Lambda}}^{\mathrm{PDG}} \rvert$	–	–	–	$< 10\,\mathrm{MeV}/c^2$	$< 10\,\mathrm{MeV}/c^2$	$< 10\,\mathrm{MeV}/c^2$
$\ell_{\mathit{\Lambda}}/\sigma_{\ell_{\mathit{\Lambda}}}$	–	–	–	> 2	> 2	> 2
$\mathit{\Lambda}$ daughter p PID	–	–	–	*LHVeryLoose*	*LHVeryLoose*	*LHVeryLoose*
$\mathit{\Lambda}$ daughter π PID	–	–	–	*LHLoose*	*LHLoose*	*LHLoose*
$P_{\mathit{\Lambda}_c^+}(\chi^2)$	$> 1 \times 10^{-6}$	$> 1 \times 10^{-3}$	$> 1 \times 10^{-6}$	$> 1 \times 10^{-6}$	$> 1 \times 10^{-6}$	$> 1 \times 10^{-6}$
$\lvert m_{\mathit{\Lambda}_c^+} - m_{\mathit{\Lambda}_c^+}^{\mathrm{PDG}} \rvert$	$< 10\,\mathrm{MeV}/c^2$	$< 10\,\mathrm{MeV}/c^2$	$< 12\,\mathrm{MeV}/c^2$	$< 10\,\mathrm{MeV}/c^2$	$< 10\,\mathrm{MeV}/c^2$	$< 10\,\mathrm{MeV}/c^2$
$\mathit{\Lambda}_c^+$ daughter p PID	*LHVeryLoose*	*LHVeryLoose*	*LHVeryLoose*	–	–	*LHVeryLoose*
$\mathit{\Lambda}_c^+$ daughter K PID	*LHVeryLoose*	–	–	–	–	*LHVeryLoose*
$\mathit{\Lambda}_c^+$ daughter π PID	*LHVeryLoose*	–	*LHVeryLoose*	*LHVeryLoose*	*LHVeryLoose*	*LHVeryLoose*
$P_B(\chi^2)$	$> 1 \times 10^{-3}$	$> 1 \times 10^{-3}$	$> 1 \times 10^{-5}$	$> 1 \times 10^{-6}$	$> 1 \times 10^{-6}$	$> 1 \times 10^{-5}$
B daughter p PID	*LHVeryLoose*	*LHVeryLoose*	*LHVeryLoose*	*LHLoose*	*LHVeryLoose*	*LHVeryLoose*
$L_{0,2}$ Fisher discriminant	< 0.4	< 2.0	< 0.4	< 1.2	< -0.2	varies by mode
Best $S/\sqrt{S+B}$	7.85	4.56	3.13	2.38	2.56	
Used $S/\sqrt{S+B}$	7.82	4.49	3.06	2.38	2.56	

Table 5.4: Results of the selection criteria optimization for $B^- \to \Lambda_c^+ \overline{p} \pi^-$ signal in each Λ_c^+ decay mode, along with the chosen selection criteria. We report the best significance for the optimal criteria in each mode and the significance in each mode with the chosen overall selection criteria.

Selection Criteria	Optimal selection in each Λ_c^+ decay mode					
	$pK^-\pi^+$	pK_S^0	$pK_S^0\pi^+\pi^-$	$\Lambda\pi^+$	$\Lambda\pi^+\pi^-\pi^+$	All
$\lvert m_{K_S^0} - m_{K_S^0}^{\mathrm{PDG}} \rvert$	–	$< 10\,\mathrm{MeV}/c^2$	$< 10\,\mathrm{MeV}/c^2$	–	–	$< 10\,\mathrm{MeV}/c^2$
$\ell_{K_S^0}/\sigma_{\ell_{K_S^0}}$	–	> 2	> 2	–	–	> 2
K_S^0 daughter π PID	–	*LHVeryLoose*	*LHVeryLoose*	–	–	*LHVeryLoose*
$\lvert m_\Lambda - m_\Lambda^{\mathrm{PDG}} \rvert$	–	–	–	$< 10\,\mathrm{MeV}/c^2$	$< 10\,\mathrm{MeV}/c^2$	$< 10\,\mathrm{MeV}/c^2$
$\ell_\Lambda/\sigma_{\ell_\Lambda}$	–	–	–	> 2	> 3	> 2
Λ daughter p PID	–	–	–	*LHVeryLoose*	*LHVeryLoose*	*LHVeryLoose*
Λ daughter π PID	–	–	–	*LHLoose*	*LHLoose*	*LHLoose*
$P_{\Lambda_c^+}(\chi^2)$	$> 1 \times 10^{-6}$	$> 1 \times 10^{-6}$	$> 1 \times 10^{-6}$	$> 1 \times 10^{-6}$	$> 1 \times 10^{-3}$	$> 1 \times 10^{-6}$
$\lvert m_{\Lambda_c^+} - m_{\Lambda_c^+}^{\mathrm{PDG}} \rvert$	$< 12\,\mathrm{MeV}/c^2$	$< 12\,\mathrm{MeV}/c^2$	$< 10\,\mathrm{MeV}/c^2$	$< 12\,\mathrm{MeV}/c^2$	$< 10\,\mathrm{MeV}/c^2$	$< 12\,\mathrm{MeV}/c^2$
Λ_c^+ daughter p PID	*LHVeryLoose*	*LHVeryLoose*	*LHVeryLoose*	–	–	*LHVeryLoose*
Λ_c^+ daughter K PID	*LHVeryLoose*	–	–	–	–	*LHVeryLoose*
Λ_c^+ daughter π PID	*LHVeryLoose*	–	*LHVeryLoose*	*LHVeryLoose*	*LHVeryLoose*	*LHVeryLoose*
$P_B(\chi^2)$	$> 1 \times 10^{-5}$	$> 1 \times 10^{-6}$	$> 1 \times 10^{-3}$	$> 1 \times 10^{-5}$	$> 1 \times 10^{-4}$	$> 1 \times 10^{-5}$
B daughter p PID	*LHVeryLoose*	*LHVeryLoose*	*LHVeryLoose*	*LHVeryLoose*	*LHVeryLoose*	*LHVeryLoose*
B daughter π PID	*LHVeryLoose*	*LHVeryLoose*	*LHVeryLoose*	*LHVeryLoose*	*LHVeryLoose*	*LHVeryLoose*
$L_{0,2}$ Fisher discriminant	< 1.0	< 1.4	< 0.6	< 1.0	< 0.0	varies by mode
Best $S/\sqrt{S+B}$	29.13	17.72	9.71	9.25	7.64	
Used $S/\sqrt{S+B}$	29.13	17.72	9.54	9.25	7.46	

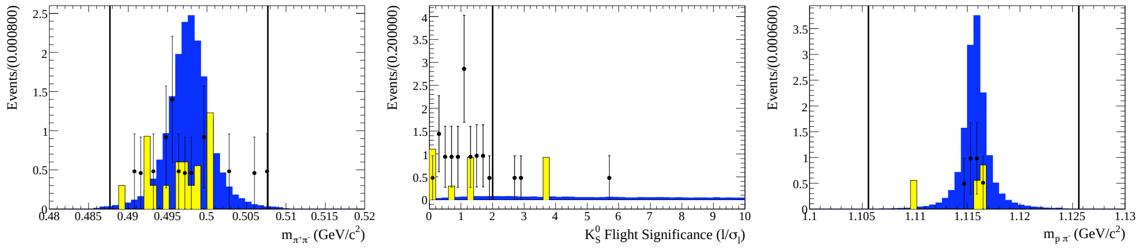

(a) K_S^0 candidate mass (b) K_S^0 candidate $\ell_{K_S^0}/\sigma_{\ell_{K_S^0}}$ (c) Λ candidate mass

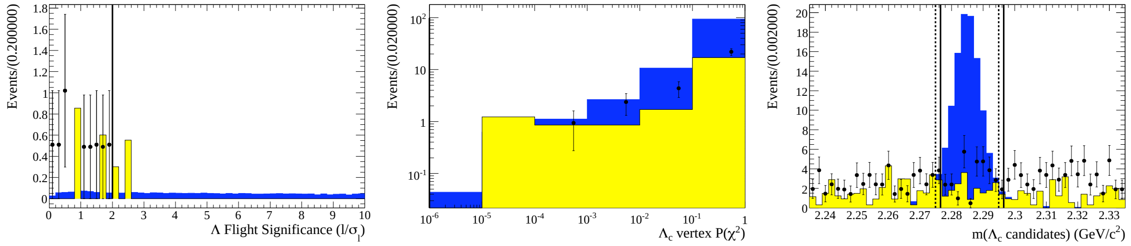

(d) Λ candidate $\ell_\Lambda/\sigma_{\ell_\Lambda}$ (e) $P_{\Lambda_c^+}(\chi^2)$ (f) Λ_c^+ candidate mass

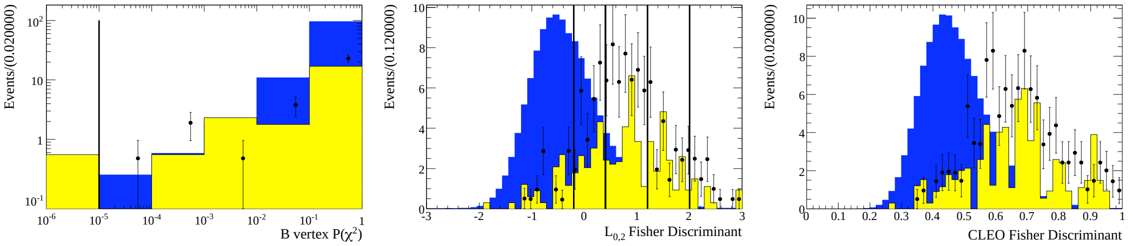

(g) $P_B(\chi^2)$ (h) $L_{0,2}$ Fisher discriminant (i) CLEO Fisher discriminant

Figure 5.5: Distributions of continuous variables for $\overline{B}^0 \to \Lambda_c^+ \overline{p}$ candidates in signal MC (blue), generic MC (yellow), and data (black points) samples in the signal (sideband) region for MC (data). Each component is scaled appropriately, and all of the Λ_c^+ decay modes are combined. Each subfigure illustrates a selection variable with all other criteria applied. The vertical lines indicate the final value chosen. In (f), the dashed vertical line indicates the selection in MC. In (h), the vertical lines indicate the selections for the various Λ_c^+ decay modes: $\Lambda\pi^+\pi^-\pi^+$, $pK^-\pi^+$ and $pK_S^0\pi^+\pi^-$, $\Lambda\pi^+$, and pK_S^0, from left to right. The CLEO Fisher discriminant is included for reference, but is not used in the final selection (the $L_{0,2}$ Fisher discriminant requirement is not applied in (i)).

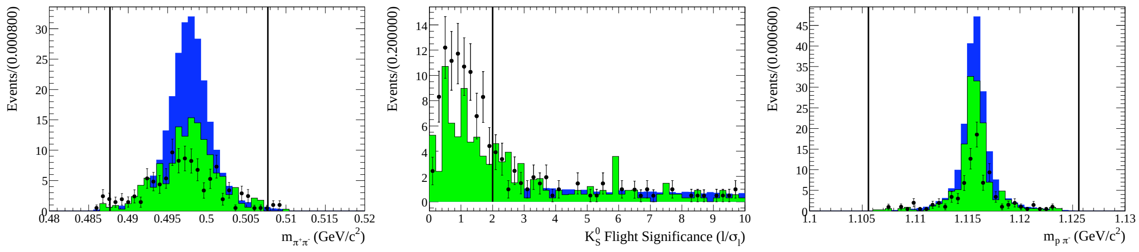

(a) K_S^0 candidate mass

(b) K_S^0 candidate $\ell_{K_S^0}/\sigma_{\ell_{K_S^0}}$

(c) Λ candidate mass

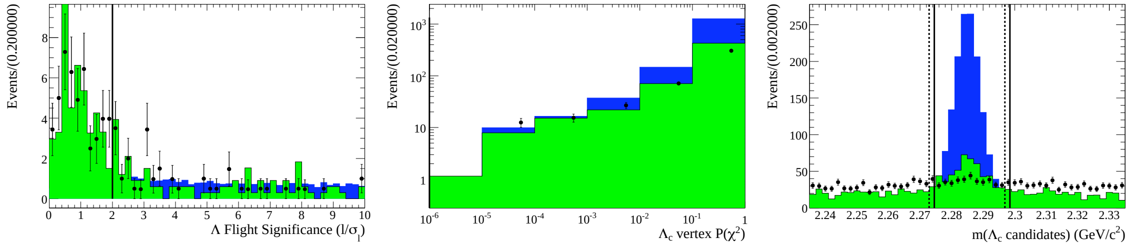

(d) Λ candidate $\ell_{\Lambda}/\sigma_{\ell_{\Lambda}}$

(e) $P_{\Lambda_c^+}(\chi^2)$

(f) Λ_c^+ candidate mass

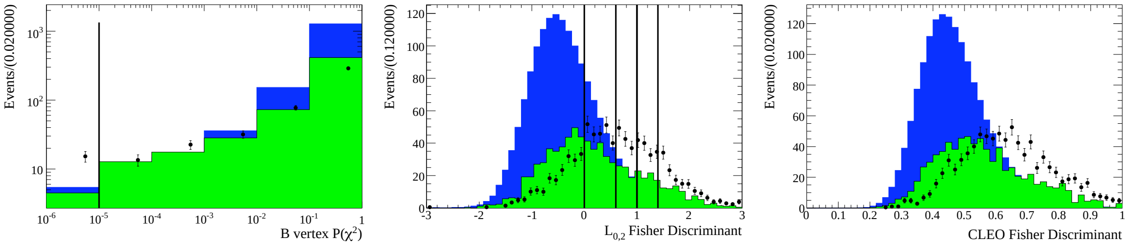

(g) $P_B(\chi^2)$

(h) $L_{0,2}$ Fisher discriminant

(i) CLEO Fisher discriminant

Figure 5.6: Distributions of continuous variables for $B^- \to \Lambda_c^+ \overline{p} \pi^-$ candidates in signal MC (blue), generic MC (green), and data (black points) samples in the signal (sideband) region for MC (data). Each component is scaled appropriately, and all of the Λ_c^+ decay modes are combined. Each subfigure illustrates a selection variable with all other criteria applied. The vertical lines indicate the final value chosen. In (f), the dashed vertical line indicates the selection in MC. In (h), the vertical lines indicate the selections for the various Λ_c^+ decay modes: $\Lambda\pi^+\pi^-\pi^+$, $pK_S^0\pi^+\pi^-$, $pK^-\pi^+$ and $\Lambda\pi^+$, and pK_S^0, from left to right. The CLEO Fisher discriminant is included for reference, but is not used in the final selection (the $L_{0,2}$ Fisher discriminant requirement is not applied in (i)).

Chapter 6

Efficiency

Inefficiencies in event reconstruction arise in the pattern recognition for identifying tracks, requirements on track quality, and requirements on particle identification. In Chapter 5, we described the selection criteria used to reject background, but some signal is lost as a result of those additional requirements. We use the signal MC samples to determine the reconstruction and selection efficiency for signal events in data. Some discrepancies between the simulated MC samples and data samples are known to exist; we apply additional corrections to compensate for these discrepancies.

A preliminary evaluation of the selection efficiency (counting truth-matched signal MC candidates) is summarized in Table 6.1. In this Chapter, we describe the determination of the selection efficiency for the $\overline{B}^0 \to \Lambda_c^+ \overline{p}$ mode from fits to the signal MC samples in each Λ_c^+ decay mode. We also describe the evaluation of binned efficiencies for $B^- \to \Lambda_c^+ \overline{p} \pi^-$ candidates. These binned efficiencies compensate for variations in detector efficiency due to the kinematics of the three-body decay (e.g., candidates with low-momentum pions in the final state).

6.1 Multiple Candidates

In some events, more than one combination of tracks satisfy the final selection criteria for a $\overline{B}^0 \to \Lambda_c^+ \overline{p}$ or $B^- \to \Lambda_c^+ \overline{p} \pi^-$ candidate. With the final selection criteria applied, the number of events that have multiple candidates in the signal region ranges from $0.1\% - 3.1\%$ in the signal MC samples, depending on the B and Λ_c^+ decay mode. The fraction of multiple candidates in each mode is calculated as the number of events with more than one candidate

Table 6.1: Selection efficiency for each signal MC sample (with the optimized selection criteria applied) in the fit region: ($|(m_{\rm rec} - m_B)| < 100\,{\rm MeV}/c^2$ and $5.200 < (m_{\rm miss} + m_B)/2 < 5.289\,{\rm GeV}/c^2$). These preliminary selection efficiencies are derived from counting truth-matched signal MC candidates.

Mode	$\overline{B}^0$ Efficiency	B^- Efficiency
$\Lambda_c^+ \to pK^-\pi^+$	22.9%	17.3%
$\Lambda_c^+ \to pK_S^0$	22.1%	17.4%
$\Lambda_c^+ \to pK_S^0\pi^+\pi^-$	9.9%	6.3%
$\Lambda_c^+ \to \Lambda\pi^+$	17.4%	13.6%
$\Lambda_c^+ \to \Lambda\pi^+\pi^-\pi^+$	6.1%	4.2%

Table 6.2: Summary of the fraction of multiple candidates in the signal region, in each signal MC sample. Each entry is the number of events with more than one candidate divided by the total number of events.

Mode	$\overline{B}^0$	B^-
$\Lambda_c^+ \to pK^-\pi^+$	0.2%	0.7%
$\Lambda_c^+ \to pK_S^0$	0.4%	0.4%
$\Lambda_c^+ \to pK_S^0\pi^+\pi^-$	1.0%	2.6%
$\Lambda_c^+ \to \Lambda\pi^+$	0.1%	0.5%
$\Lambda_c^+ \to \Lambda\pi^+\pi^-\pi^+$	1.2%	3.1%

divided by the total number of events. These fractions are summarized in Table 6.2. In order to select a single candidate per event, we select the candidate with the largest $P(\chi^2)$ from the vertex fit to the entire decay chain. The χ^2 probability of the $\Lambda_c^+\overline{p}\pi^-$ vertex is uncorrelated with $(m_{\rm rec} - m_B)$ and $(m_{\rm miss} + m_B)/2$, and so does not bias the selection.

6.2 Correction to Particle Identification Efficiencies

Corrections to the particle identification efficiencies are applied to the MC efficiencies so that they more accurately simulate data. Each MC event is assigned a weight based on each track's momentum and angle in the detector for each PID selector. We require the weight status to be "ok" or have a symmetrized error (if the original error is asymmetric). Distributions of the combined PID selector event weights for each Λ_c^+ decay mode are shown on a logarithmic scale in Figure 6.1. They are narrowly distributed around 1 and there are few outliers.

6.3 $\overline{B}^0 \rightarrow \Lambda_c^+ \overline{p}$ Efficiency

We determine the efficiency of the $\overline{B}^0 \rightarrow \Lambda_c^+ \overline{p}$ mode by performing a 2-D fit to the signal MC sample for each Λ_c^+ decay mode. The background probability density function (PDF) consists of a first-order polynomial in $(m_{\mathrm{rec}} - m_B)$ times an ARGUS function [48] in $(m_{\mathrm{miss}} + m_B)/2$:

$$\begin{aligned}
&\mathcal{P}_{bkg}((m_{\mathrm{rec}} - m_B), (m_{\mathrm{miss}} + m_B)/2; a, c_{ARG}) \propto \\
&\qquad (1 + a(m_{\mathrm{rec}} - m_B))(m_{\mathrm{miss}} + m_B)/2 \sqrt{1 - \left(\frac{(m_{\mathrm{miss}} + m_B)/2}{m_0}\right)^2} \\
&\qquad \times exp\left(-c_{ARG}\left(1 - \left(\frac{(m_{\mathrm{miss}} + m_B)/2}{m_0}\right)^2\right)\right),
\end{aligned} \tag{6.1}$$

where a is the slope in $(m_{\mathrm{rec}} - m_B)$, c_{ARG} is the ARGUS function slope parameter, and m_0 defines the endpoint of the ARGUS function (which is fixed to the CM beam energy, $5.290\,\mathrm{GeV}/c^2$). The signal PDF in $(m_{\mathrm{rec}} - m_B)$ is a modified asymmetric Gaussian ("Cruijff") function:

$$\begin{aligned}
&\mathcal{P}_{sig}^{m_{\mathrm{rec}}}((m_{\mathrm{rec}} - m_B); \mu, \sigma_L, \sigma_R, \alpha_L, \alpha_R) \propto \\
&\qquad exp\left(\frac{-((m_{\mathrm{rec}} - m_B) - \mu)^2}{2\sigma_{L/R}^2 + \alpha_{L/R}((m_{\mathrm{rec}} - m_B) - \mu)^2}\right),
\end{aligned} \tag{6.2}$$

where μ is the mean, $\sigma_{L(R)}$ is the left (right) standard deviation, and $\alpha_{L(R)}$ is the left (right) tail parameter. The signal PDF in $(m_{\mathrm{rec}} - m_B)$ is multiplied by a Gaussian in $(m_{\mathrm{miss}} + m_B)/2$:

$$\mathcal{P}_{sig}^{m_{\mathrm{miss}}}((m_{\mathrm{miss}} + m_B)/2; \mu, \sigma) \propto \frac{1}{\sigma\sqrt{2\pi}}\, e^{((m_{\mathrm{miss}} + m_B)/2 - \mu)^2/2\sigma^2}, \tag{6.3}$$

where μ is the mean and σ is the standard deviation.

An extended unbinned maximum likelihood fit is performed on each signal MC sample with the PID selector weights applied. The final efficiencies are summarized in Table 6.3. The fit results are summarized in Table 6.4 and projections of $(m_{\mathrm{rec}} - m_B)$ and $(m_{\mathrm{miss}} +$

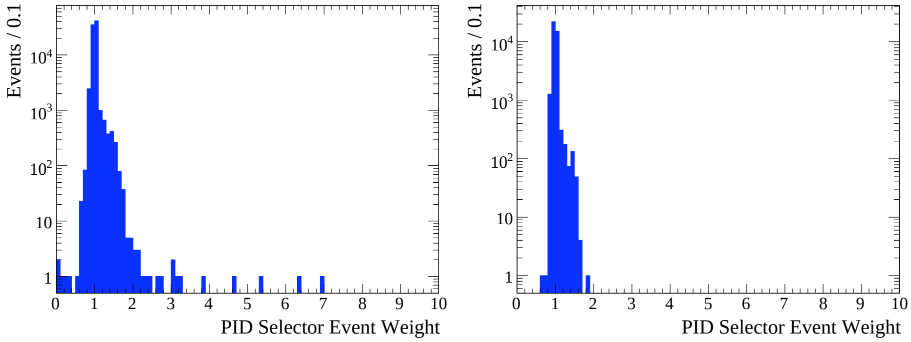

(a) $\Lambda_c^+ \to pK^-\pi^+$ (b) $\Lambda_c^+ \to pK_S^0$

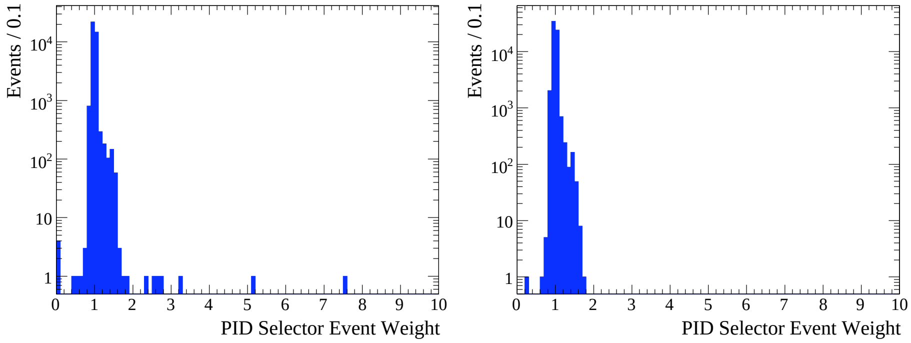

(c) $\Lambda_c^+ \to pK_S^0\pi^+\pi^-$ (d) $\Lambda_c^+ \to \Lambda\pi^+$

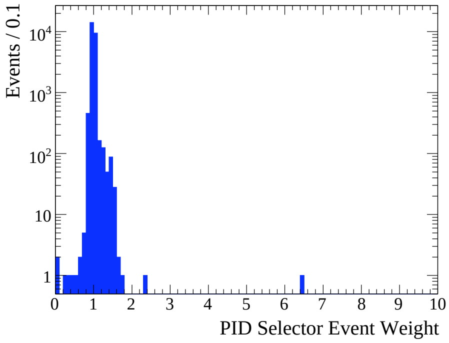

(e) $\Lambda_c^+ \to \Lambda\pi^+\pi^-\pi^+$

Figure 6.1: Combined PID selector weights for $\overline{B}^0 \to \Lambda_c^+\overline{p}$ events in each Λ_c^+ decay mode. The distributions are shown on a logarithmic scale.

$m_B)/2$ are shown on logarithmic scales in Figure 6.2.

Table 6.3: Selection efficiency for each signal MC sample (with the optimized selection criteria, single candidate selection, and PID selector corrections applied). Efficiencies are derived from unbinned maximum likelihood fits to signal MC samples.

Mode	$\overline{B}^0 \to \Lambda_c^+ \overline{p}$ Efficiency
$\Lambda_c^+ \to pK^-\pi^+$	22.9%
$\Lambda_c^+ \to pK_S^0$	22.0%
$\Lambda_c^+ \to pK_S^0\pi^+\pi^-$	9.7%
$\Lambda_c^+ \to \Lambda\pi^+$	17.3%
$\Lambda_c^+ \to \Lambda\pi^+\pi^-\pi^+$	6.0%

Table 6.4: Results of fits to official signal MC samples in order to determine the $\overline{B}^0 \to \Lambda_c^+ \overline{p}$ efficiency in each Λ_c^+ decay mode.

Variable	Fit Param.	$pK^-\pi^+$	pK^0_S	$pK^0_S\pi^+\pi^-$	$\Lambda\pi^+$	$\Lambda\pi^+\pi^-\pi^+$
$(m_{\text{miss}}+m_B)/2$	$\mu\,(\text{MeV}/c^2)$	$5,279.22 \pm 0.01$	$5,279.19 \pm 0.01$	$5,279.23 \pm 0.01$	$5,279.24 \pm 0.01$	$5,279.22 \pm 0.02$
	$\sigma\,(\text{MeV}/c^2)$	2.477 ± 0.006	2.493 ± 0.009	2.496 ± 0.010	2.473 ± 0.007	2.486 ± 0.013
	c_{ARG}	-152 ± 6	-197 ± 22	-159 ± 4	-249 ± 11	-144 ± 4
$(m_{\text{rec}}-m_B)$	$\mu\,(\text{MeV}/c^2)$	-0.3 ± 0.1	-0.2 ± 0.2	-0.3 ± 0.1	-0.1 ± 0.1	-0.2 ± 0.3
	$\sigma_L\,(\text{MeV}/c^2)$	10.9 ± 0.1	10.9 ± 0.1	11.4 ± 0.1	11.0 ± 0.1	11.2 ± 0.2
	$\sigma_R\,(\text{MeV}/c^2)$	12.0 ± 0.1	11.5 ± 0.2	12.4 ± 0.1	11.8 ± 0.1	12.2 ± 0.2
	α_L	0.140 ± 0.002	0.139 ± 0.003	0.132 ± 0.003	0.134 ± 0.002	0.128 ± 0.005
	α_R	0.093 ± 0.003	0.108 ± 0.003	0.089 ± 0.004	0.097 ± 0.002	0.099 ± 0.006
	$a\,(1/\,\text{GeV}/c^2)$	-3.4 ± 0.7	-5.3 ± 2.3	-2.8 ± 0.4	-4.6 ± 1.0	-3.9 ± 0.5
	N_{bkg}	997 ± 49	104 ± 20	1840 ± 58	330 ± 29	1498 ± 51
	N_{sig}	80112 ± 286	38543 ± 197	33866 ± 190	60549 ± 240	21127 ± 149

6.3.1 Efficiency Correction for K_S^0 Reconstruction

Tracking effects for `ChargedTracks` that originate within 15 mm of the beam spot (in the XY-plane) are well understood, so no correction is necessary. However, a correction is needed to compensate for discrepancies between data and MC samples where `ChargedTracks` originate outside the 15 mm radius. This correction is relevant for $\Lambda_c^+ \to pK_S^0$ and $\Lambda_c^+ \to pK_S^0\pi^+\pi^-$ decays. The signal MC samples are divided into Runs, and tables are provided in bins of p_T (transverse momentum), θ_{LAB} (the polar angle of the K_S^0 w.r.t. the z-axis), and d_{xy} (the transverse distance between the primary vertex and the K_S^0 vertex). A correction is also computed to account for the K_S^0 lineshape, given the $\pm 10\,\mathrm{MeV}/c^2$ K_S^0 mass window required in this analysis. Table 6.5 summarizes the corrections as well as the number of signal MC events in each category. The uncertainties on these corrections will be treated as a systematic uncertainty.

6.3.2 Efficiency Correction for Λ Reconstruction

Since the K_S^0 efficiency correction is valid for displaced vertices, we apply the same recipe to correct for the displaced Λ decay vertex in $\overline{B}^0 \to \Lambda_c^+\overline{p}$, $\Lambda_c^+ \to \Lambda\pi^+$ decays. No Λ mass window correction is necessary.

The procedure is the same as for the K_S^0 correction. Table 6.6 summarizes the corrections as well as the number of signal MC events in each category. The uncertainties on these corrections will be treated as a systematic uncertainty.

6.3.3 Final efficiencies for $\overline{B}^0 \to \Lambda_c^+\overline{p}$

We apply the weighted average of the K_S^0 and Λ tracking corrections to the efficiencies determined from the fitted signal MC sample yields. The final efficiency numbers can be found in Table 6.7.

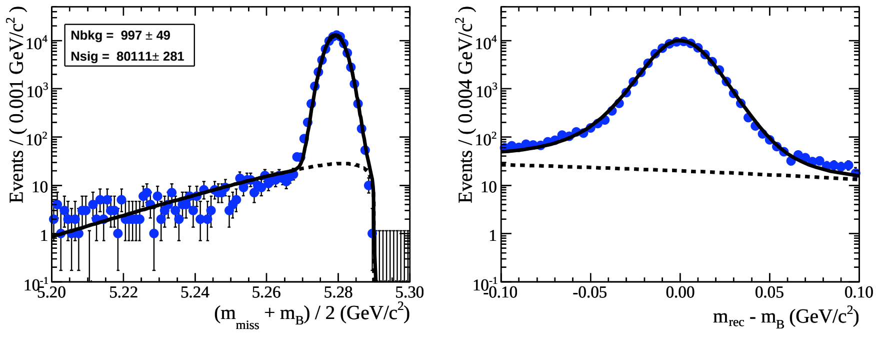

(a) $\Lambda_c^+ \to pK^-\pi^+$

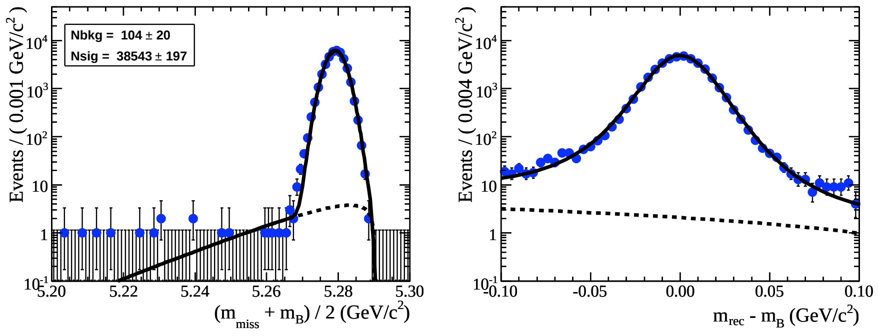

(b) $\Lambda_c^+ \to pK_S^0$

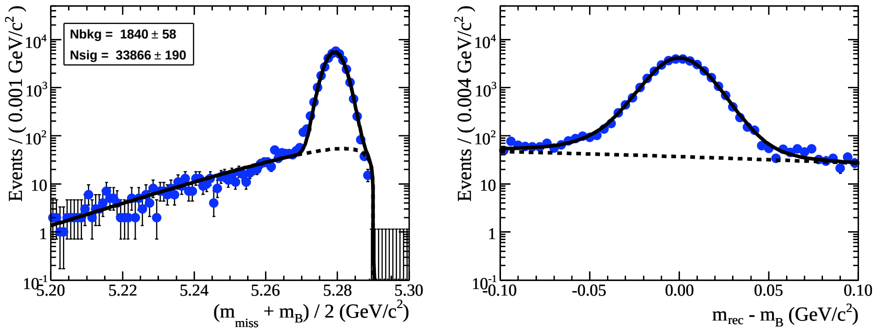

(c) $\Lambda_c^+ \to pK_S^0\pi^+\pi^-$

Figure 6.2: Each subfigure shows $(m_{\text{miss}} + m_B)/2$ (left) and $(m_{\text{rec}} - m_B)$ (right) projections of the 2-D fit to the $\overline{B}^0 \to \Lambda_c^+\overline{p}$ signal MC sample for each Λ_c^+ decay mode. The vertical axes are on a logarithmic scale to illustrate the fit quality in the tails of the $(m_{\text{miss}} + m_B)/2$ and $(m_{\text{rec}} - m_B)$ distributions. We allow for background due to misreconstructed events. Table 6.4 summarizes the results for each fit.

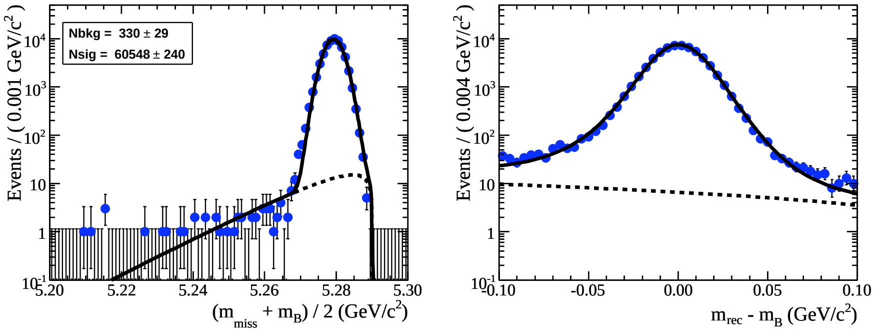

(d) $\Lambda_c^+ \to \Lambda\pi^+$

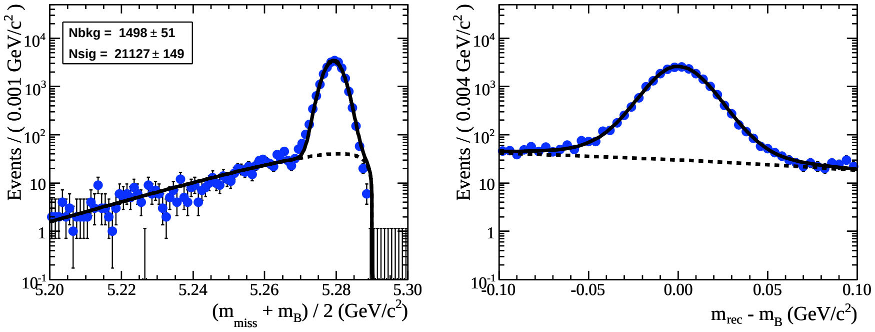

(e) $\Lambda_c^+ \to \Lambda\pi^+\pi^-\pi^+$

Figure 6.2: (cont.)

Table 6.5: Tracking efficiency corrections for $\overline{B}^0$ events with a K^0_S candidate. The overall correction is the product of the K^0_S mass window correction (derived from the ±10 MeV/c^2 mass window for K^0_S candidates) and the $p_T, \theta_{\text{LAB}}, d_{xy}$ correction factor.

$\overline{B}^0 \to \Lambda_c^+ \overline{p}$, $\Lambda_c^+ \to p K^0_S$

Run	# Events	DCH Voltage	Mass Window Correction	$p_T, \theta_{\text{LAB}}, d_{xy}$ Correction Factor	Overall Correction
1a	1049	1900	0.992	0.990	0.983
1b	1248	1960	0.993	1.013	1.007
2	7193	1930	0.993	1.004	0.997
3	3959	1930	0.993	1.009	1.002
4	11002	1930	0.992	0.984	0.977
5 (FEX bug)	2814	1930	0.992	0.977	0.968
5 (post-FEX)	9197	1930	0.992	0.984	0.976
				Weighted Average Correction	0.984

$\overline{B}^0 \to \Lambda_c^+ \overline{p}$, $\Lambda_c^+ \to p K^0_S \pi^+ \pi^-$

Run	# Events	DCH Voltage	Mass Window Correction	$p_T, \theta_{\text{LAB}}, d_{xy}$ Correction Factor	Overall Correction
1a	1309	1900	0.992	1.027	1.018
1b	1162	1960	0.995	1.009	1.004
2	7214	1930	0.993	1.005	0.997
3	3723	1930	0.991	1.004	0.996
4	10577	1930	0.991	0.983	0.974
5 (FEX bug)	2533	1930	0.992	1.000	0.991
5 (post-FEX)	7957	1930	0.993	0.991	0.984
				Weighted Average Correction	0.987

Table 6.6: Tracking efficiency corrections for $\overline{B}^0$ events with a $\mathit{\Lambda}$ candidate. The overall correction is the $p_T, \theta_{\mathrm{LAB}}, d_{xy}$ correction factor.

$\overline{B}^0 \to \mathit{\Lambda}_c^+ \overline{p}$, $\mathit{\Lambda}_c^+ \to \mathit{\Lambda}\pi^+$			
Run	# Events	DCH Voltage	$p_T, \theta_{\mathrm{LAB}}, d_{xy}$ Correction Factor
1a	2006	1900	0.985
1b	1978	1960	1.017
2	11751	1930	1.004
3	6083	1930	1.011
4	17541	1930	0.990
5 (FEX bug)	3998	1930	0.967
5 (post-FEX)	14190	1930	0.987
Weighted Average Correction			0.993

Table 6.7: Selection efficiency for each signal MC sample (with the optimized selection criteria, single candidate selection, and PID selector corrections applied). Efficiencies are derived from unbinned maximum likelihood (ML) fits to signal MC samples and then corrected according to the previously described K_S^0 or $\mathit{\Lambda}$ tracking correction method.

Mode	Efficiency (ML fit)	$K_S^0/\mathit{\Lambda}$ Corr	$\overline{B}^0 \to \mathit{\Lambda}_c^+ \overline{p}$ Efficiency
$\mathit{\Lambda}_c^+ \to pK^-\pi^+$	22.9%	–	22.9%
$\mathit{\Lambda}_c^+ \to pK_S^0$	22.0%	0.984	21.6%
$\mathit{\Lambda}_c^+ \to pK_S^0\pi^+\pi^-$	9.7%	0.987	9.6%
$\mathit{\Lambda}_c^+ \to \mathit{\Lambda}\pi^+$	17.3%	0.993	17.2%

6.4 $B^- \to \Lambda_c^+ \overline{p} \pi^-$ Binned Efficiency Correction

The kinematic information in a three-body decay can be represented by two variables. In 1953, R. H. Dalitz parameterized a three-body decay by m_{12}^2 vs. m_{23}^2, where m_{ij} is the invariant mass of daughters i and j [49]. This 2-D distribution became known as a "Dalitz plot". The distribution of events in a non-resonant three-body decay is uniform across this region, which makes it extremely useful for identifying variations in this distribution due to inefficiencies.

The efficiency of the three-body $B^- \to \Lambda_c^+ \overline{p} \pi^-$ decay mode varies considerably across the Dalitz plane. There are noticeable deficiencies in the corners of the $m_{p\pi}^2$ vs. $m_{\Lambda_c \pi}^2$ Dalitz plot where the π or Λ_c^+ candidates have low momentum in the B rest frame, even though the loose tracking requirement on the daughter pions somewhat compensates for this effect. Figure 6.3 shows the efficiency distribution across the Dalitz plane for $B^- \to \Lambda_c^+ \overline{p} \pi^-$ signal MC events for the various Λ_c^+ decay modes.

Aside: In order to calculate all momenta, invariant masses, and other quantities in this section, we refit the full $B^- \to \Lambda_c^+ \overline{p} \pi^-$ decay chain using `TreeFitter` for candidates that pass all selection criteria, imposing a mass constraint on the B^-. This ensures that all signal and background candidates fall in the physical Dalitz regions discussed.

We note that the Dalitz plot should have smooth borders that indicate the allowed physical region, and thus rectangular bins are somewhat incompatible with the traditional Dalitz plot. Therefore, in the binned efficiency correction of $B^- \to \Lambda_c^+ \overline{p} \pi^-$, we choose a rectangular set of variables, $\cos\theta_h(\Lambda_c \pi)$ vs. $m_{\Lambda_c \pi}$. The helicity angle, $\cos\theta_h(\Lambda_c \pi)$, is defined as the angle between the π^- and recoiling $\overline{p}$ in the B^- rest frame. This quantity is invariant under Lorentz transformations, and can be calculated in the following manner:

$$\cos\theta_h(\Lambda_c \pi) = \frac{\left(q_{B^-} \cdot q_{\pi^-}\right) m_{\Lambda_c^+}^2 - \left(q_{B^-} \cdot q_{\Lambda_c^+ \pi^-}\right)\left(q_{\Lambda_c^+ \pi^-} \cdot q_{\pi^-}\right)}{\sqrt{\left[\left(q_{B^-} \cdot q_{\Lambda_c^+ \pi^-}\right) - m_{\Lambda_c^+}^2 m_{B^-}^2\right]\left[\left(q_{\Lambda_c^+ \pi^-} \cdot q_{\pi^-}\right)^2 - m_{\Lambda_c^+}^2 m_{\Lambda_c^+ \pi^-}^2\right]}}, \tag{6.4}$$

where q_α represents the four-vector of particle α. A detailed discussion of this choice of coordinates can be found in Ref. [50]. The main drawback to using the variables $\cos\theta_h(\Lambda_c \pi)$ vs. $m_{\Lambda_c \pi}$ is that the plots are less intuitive: the distribution of events in a non-resonant three-body decay is *not* uniform across this 2-D space.

The binned efficiency correction is calculated as follows. We divide the rectangular

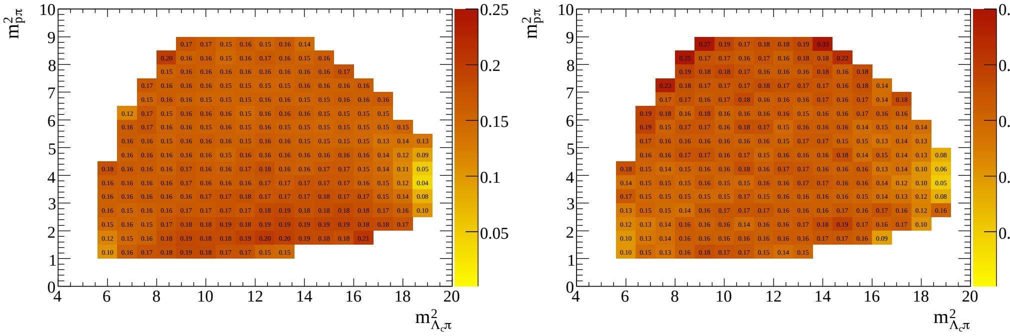

(a) $\Lambda_c^+ \to pK^-\pi^+$ (b) $\Lambda_c^+ \to pK_S^0$

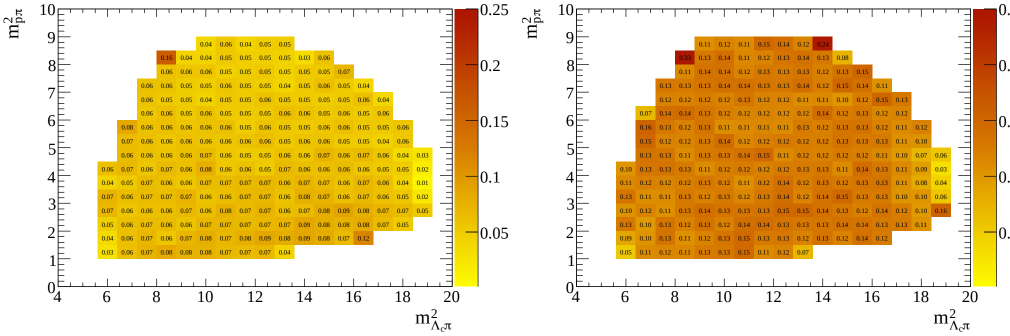

(c) $\Lambda_c^+ \to pK_S^0\pi^+\pi^-$ (d) $\Lambda_c^+ \to \Lambda\pi^+$

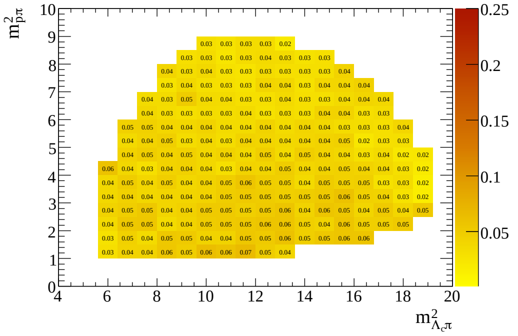

(e) $\Lambda_c^+ \to \Lambda\pi^+\pi^-\pi^+$

Figure 6.3: Efficiency distribution of $B^- \to \Lambda_c^+\overline{p}\pi^-$ signal MC candidates across the Dalitz plane. Subfigures $(a) - (e)$ indicate the B candidate efficiency distribution for each Λ_c^+ decay mode.

plane into reasonably sized bins that are uniform in $\cos\theta_h(\Lambda_c\pi)$ and nonuniform in $m_{\Lambda_c\pi}$. We calculate the efficiency for each bin individually, using N_{prod} reconstructed signal MC events (that are in the signal region and pass all selection criteria) and a ten-million event sample of $B^- \to \Lambda_c^+\overline{p}\pi^-$ toy MC events generated with the `ROOT` class `TGenPhaseSpace`. The toy MC events are weighted according to phase space (i.e. uniform in the $m^2_{p\pi}$ vs. $m^2_{\Lambda_c\pi}$ Dalitz plane, but distributed according to $|\vec{q}_{\pi^-}||\vec{q}_{\overline{p}}|/m^2_{B^-}$ in $m_{\Lambda_c\pi}$); the sum of the weights is 2.9×10^6. The efficiency for bin (i,j) is calculated:

$$\varepsilon_{ij} = \frac{N_{ij}^{\text{MC}}/N_{\text{prod}}}{N_{ij}^{\text{toy MC}}/2.9\times10^6}, \tag{6.5}$$

where N_{ij}^{MC} is the number of official signal MC events and $N_{ij}^{\text{toy MC}}$ is the number of (weighted) toy MC events in bin (i,j).

The binned efficiency correction procedure is carried out separately for each Λ_c^+ decay mode. We choose reasonable bin sizes based on the uncertainty in each bin and the structure of efficiency variation across the rectangular $\cos\theta_h(\Lambda_c\pi)$ vs. $m_{\Lambda_c\pi}$ plane. The nonuniform $m_{\Lambda_c\pi}$ bins are ideally chosen to be symmetric around the Σ_c^0 resonances. However, the $\Lambda_c^+ \to pK_S^0\pi^+\pi^-$ and $\Lambda_c^+ \to \Lambda\pi^+\pi^-\pi^+$ decay modes suffer from low statistics in the low $m_{\Lambda_c\pi}$ region, so coarser binning is required in those cases. We list the bin boundaries for reference in Table 6.8. The resulting rectangular distributions are shown in Figure 6.4.

The uncertainties on each Dalitz bin are calculated from the number of signal MC events in each bin. The fractional uncertainty on each bin $(\frac{\delta_{\varepsilon_{ij}}}{\varepsilon_{ij}})$ is thus:

$$\left(\frac{\delta_{\varepsilon_{ij}}}{\varepsilon_{ij}}\right)^2 = \left(\frac{\sqrt{N_{ij}^{\text{MC}}}}{N_{ij}^{\text{MC}}}\right)^2 + \left(\frac{\sqrt{N_{ij}^{\text{toy MC}}}}{N_{ij}^{\text{toy MC}}}\right)^2. \tag{6.6}$$

The central region (bins $4-10$ in Table 6.8) of each plot in Figure 6.4 has approximately the same uncertainty in each bin. However, in the low $m_{\Lambda_c\pi}$ region there are fewer reconstructed signal MC events, so the uncertainty is larger. The region with the least number of events is the low $m_{\Lambda_c\pi}$ region where $\cos\theta_h(\Lambda_c\pi)\approx 1$. We quantify these fractional uncertainties in Table 6.9. A systematic uncertainty is calculated due to the limited MC statistics in each bin; a description of this calculation can be found in Chapter 12.

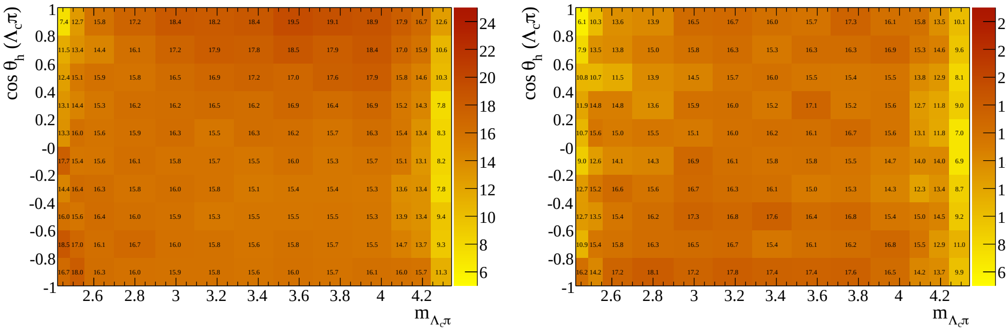

(a) $\Lambda_c^+ \to pK^-\pi^+$ (b) $\Lambda_c^+ \to pK_S^0$

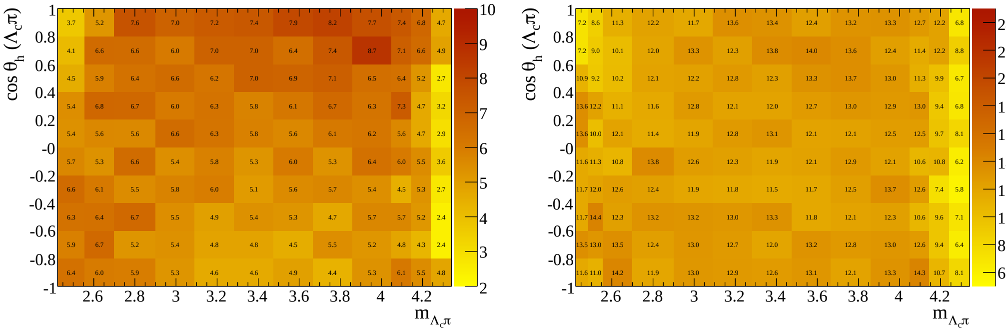

(c) $\Lambda_c^+ \to pK_S^0\pi^+\pi^-$ (d) $\Lambda_c^+ \to \Lambda\pi^+$

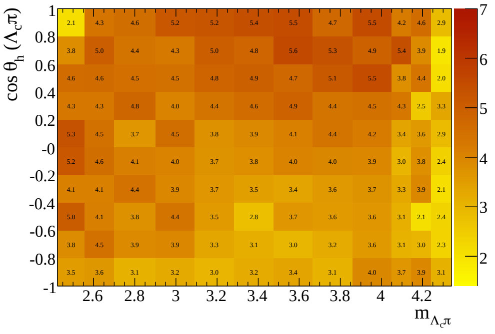

(e) $\Lambda_c^+ \to \Lambda\pi^+\pi^-\pi^+$

Figure 6.4: Efficiency distribution of $B^- \to \Lambda_c^+\overline{p}\pi^-$ signal MC candidates across the rectangular plane, $\cos\theta_h(\Lambda_c\pi)$ vs. $m_{\Lambda_c\pi}$. The values shown in each bin are efficiencies (in %). Note the suppressed zeros on the z-axes. Subfigures $(a) - (e)$ indicate the B candidate efficiency distribution for each Λ_c^+ decay mode. Subfigures (c) and (e) have coarser binning due to low statistics near the low $m_{\Lambda_c\pi}$ boundary.

Table 6.8: Bin boundaries in $m_{\Lambda_c\pi}$ for the rectangular distributions $\cos\theta_h(\Lambda_c\pi)$ vs. $m_{\Lambda_c\pi}$ shown in Figure 6.4. The lower $m_{\Lambda_c\pi}$ boundary is set to $m_{\Lambda_c^+}+m_{\pi^-}$ and the upper boundary is set to $m_{B^-}-m_{\overline{p}}$. Bin 1 is centered around $m_{\Sigma_c(2455)^0}$, bin 2 is centered around $m_{\Sigma_c(2520)^0}$, and bin 4 is centered around $m_{\Sigma_c(2800)^0}$. Bins 1 and 2 are merged for the $\Lambda_c^+ \rightarrow pK_S^0\pi^+\pi^-$ and $\Lambda_c^+ \rightarrow \Lambda\pi^+\pi^-\pi^+$ decay modes. Values are rounded to the nearest MeV/c^2.

Bin Number	Lower Boundary (GeV/c^2)
1	2.425
2	2.485
3	2.555
4	2.700
5	2.900
6	3.092
7	3.283
8	3.475
9	3.666
10	3.858
11	4.050
12	4.146
13	4.241

6.4.1 Efficiency Correction for K_S^0 Reconstruction

Table 6.10 summarizes the number of signal MC events in each Run category, the corrections due to the K_S^0 lineshape (given the required $\pm 10\,\text{MeV}/c^2$ K_S^0 mass window), and the $p_T, \theta_{\text{LAB}}, d_{xy}$ correction factors. These corrections are relevant for $B^- \rightarrow \Lambda_c^+\overline{p}\pi^-$, $\Lambda_c^+ \rightarrow pK_S^0$ and $\Lambda_c^+ \rightarrow pK_S^0\pi^+\pi^-$ decays. The uncertainties on these corrections will be treated as a systematic uncertainty.

6.4.2 Efficiency Correction for Λ Reconstruction

Since the K_S^0 efficiency correction is valid for displaced vertices, we apply the same recipe to correct for the displaced Λ decay vertex in $B^- \rightarrow \Lambda_c^+\overline{p}\pi^-$, $\Lambda_c^+ \rightarrow \Lambda\pi^+$ and $\Lambda_c^+ \rightarrow \Lambda\pi^+\pi^-\pi^+$ decays. No Λ mass window correction is necessary.

The procedure is the same as for the K_S^0 correction. Table 6.11 summarizes the corrections as well as the number of signal MC events in each category. The uncertainties on these corrections will be treated as a systematic uncertainty.

Table 6.9: Fractional uncertainty on the binned efficiencies for $B^- \to \Lambda_c^+ \overline{p} \pi^-$ for each Λ_c^+ decay mode. The second column shows $\frac{\delta_\varepsilon}{\varepsilon}$(avg), the average uncertainty in the central $m_{\Lambda_c \pi}$ region (bins $4 - 10$ in Table 6.8). The third column shows the maximum uncertainty $\frac{\delta_\varepsilon}{\varepsilon}$(max); this uncertainty is from the upper left bin in Figure 6.4.

Mode	$\frac{\delta_\varepsilon}{\varepsilon}$(avg)	$\frac{\delta_\varepsilon}{\varepsilon}$(max)
$\Lambda_c^+ \to pK^-\pi^+$	1.9%	12.3%
$\Lambda_c^+ \to pK_S^0$	4.2%	28.9%
$\Lambda_c^+ \to pK_S^0\pi^+\pi^-$	6.6%	23.3%
$\Lambda_c^+ \to \Lambda\pi^+$	4.7%	26.9%
$\Lambda_c^+ \to \Lambda\pi^+\pi^-\pi^+$	7.9%	27.0%

Table 6.10: Tracking efficiency corrections for B^- events with a K^0_S candidate. The overall correction is the product of the K^0_S mass window correction (derived from the $\pm 10\,\mathrm{MeV}/c^2$ mass window for K^0_S candidates) and the $p_T, \theta_{\mathrm{LAB}}, d_{xy}$ correction factor.

$B^- \to \Lambda_c^+ \overline{p} \pi^-$, $\Lambda_c^+ \to p K^0_S$

Run	# Events	DCH Voltage	Mass Window Correction	$p_T, \theta_{\mathrm{LAB}}, d_{xy}$ Correction Factor	Overall Correction
1a	1750	1900	0.992	1.005	0.997
1b	1719	1960	0.994	1.024	1.018
2	10159	1930	0.993	1.007	0.999
3	5356	1930	0.993	1.015	1.008
4	15598	1930	0.992	0.986	0.979
5 (FEX bug)	3838	1930	0.991	0.984	0.975
5 (post-FEX)	12598	1930	0.992	0.984	0.977
				Weighted Average Correction	0.987

$B^- \to \Lambda_c^+ \overline{p} \pi^-$, $\Lambda_c^+ \to p K^0_S \pi^+ \pi^-$

Run	# Events	DCH Voltage	Mass Window Correction	$p_T, \theta_{\mathrm{LAB}}, d_{xy}$ Correction Factor	Overall Correction
1a	714	1900	0.991	1.024	1.014
1b	695	1960	0.994	0.990	0.985
2	4125	1930	0.992	1.003	0.995
3	2153	1930	0.990	1.004	0.994
4	5948	1930	0.990	0.983	0.974
5 (FEX bug)	1444	1930	0.992	0.995	0.987
5 (post-FEX)	4446	1930	0.994	0.986	0.980
				Weighted Average Correction	0.985

Table 6.11: Tracking efficiency corrections for B^- events with a Λ candidate. The overall correction is the $p_T, \theta_{\mathrm{LAB}}, d_{xy}$ correction factor.

$B^- \to \Lambda_c^+ \overline{p} \pi^-$, $\Lambda_c^+ \to \Lambda \pi^+$			
Run	# Events	DCH Voltage	$p_T, \theta_{\mathrm{LAB}}, d_{xy}$ Correction Factor
1a	1403	1900	0.997
1b	1339	1960	1.029
2	7896	1930	1.007
3	4274	1930	1.016
4	12339	1930	0.991
5 (FEX bug)	3012	1930	0.978
5 (post-FEX)	9695	1930	0.987
Weighted Average Correction			0.996
$B^- \to \Lambda_c^+ \overline{p} \pi^-$, $\Lambda_c^+ \to \Lambda \pi^+ \pi^- \pi^+$			
Run	# Events	DCH Voltage	$p_T, \theta_{\mathrm{LAB}}, d_{xy}$ Correction Factor
1a	478	1900	1.018
1b	478	1960	1.025
2	2718	1930	1.008
3	1503	1930	1.022
4	3946	1930	0.994
5 (FEX bug)	1001	1930	0.987
5 (post-FEX)	3090	1930	0.989
Weighted Average Correction			1.000

Chapter 7

Backgrounds

In this Chapter, we describe the studies of generic MC background sources to provide a qualitative verification of the background levels and fit shapes. We also examine exclusive baryonic B decay modes that are not present in the generic MC samples. One of these modes, $\overline{B}^0 \to \Sigma_c(2455)^+\overline{p}$, $\Sigma_c(2455)^+ \to \Lambda_c^+\pi^0$, $\Lambda_c^+ \to pK^-\pi^+$, is misreconstructed often enough to accumulate with a signal-like shape in the signal region; we call this "peaking background". We perform a detailed study to quantify the contamination due to this background source.

7.1 Generic MC background

Four generic MC samples, uds, $c\overline{c}$, $B^0\overline{B}^0$, and B^+B^-, are used to compare simulated background levels to data. The uds and $c\overline{c}$ generic MC samples are each scaled to an equivalent luminosity of $349.0\,\text{fb}^{-1}$, and the $B^0\overline{B}^0$ and B^+B^- samples are each scaled to be equivalent to $\frac{1}{2} \times 383.6$ million $B\overline{B}$ pairs.

The $(m_{\text{rec}} - m_B)$ and $(m_{\text{miss}} + m_B)/2$ distributions for the generic MC samples are shown in Figure 7.1 (the colored histograms) . $\overline{B}^0 \to \Lambda_c^+\overline{p}$ and $B^- \to \Lambda_c^+\overline{p}\pi^-$ candidates in data are overlaid (black points) with events in the signal region removed from these distributions, or "blinded". The B^+B^- generic MC sample is generated with the $B^- \to \Lambda_c^+\overline{p}\pi^-$ mode included, but this mode is removed from the sample using truth-matching.

There are broad peaks in the region $(m_{\text{rec}} - m_B) < -0.1$ in Figure 7.1(a) and (b). These broad structures are due to the same effect in both plots, an effect that we call "feed-down". A higher-multiplicity B decay mode contains $\Lambda_c^+\overline{p}(\pi^-)$ in the final state, *plus an additional* *pion*. The additional pion is not reconstructed, and so an accumulation is observed. This peak is not in the signal region, but is instead shifted by $\sim -m_\pi$ in $(m_{\rm rec} - m_B)$.

In Figure 7.1(a), the structure is seen in data but not in the generic MC sample. This is due to the fact that the generic $B\overline{B}$ MC samples do not contain two-body B decays in which a Λ_c^+ is present in the final state, e.g., the decay modes $\overline{B}^0 \to \Sigma_c(2455)^+\overline{p}$ and $B^- \to \Sigma_c(2455)^0\overline{p}$. In Figure 7.1(b), the broad peak is seen in both the data and generic MC samples, but there is a slight discrepancy in the shape and yield of this peak in the two samples. This discrepancy is due to the somewhat inaccurate simulated branching fractions for the four-body feed-down modes (such as $\overline{B}^0 \to \Lambda_c^+\overline{p}\pi^+\pi^-$). In the generic MC sample, $\mathcal{B}(\overline{B}^0 \to \Lambda_c^+\overline{p}\pi^+\pi^-) = 1.7 \times 10^{-3}$, while the most recent measurement is $\mathcal{B}(\overline{B}^0 \to \Lambda_c^+\overline{p}\pi^+\pi^-) = 1.1 \pm 0.1 \pm 0.2 \pm 0.3 \times 10^{-3}$ [32]. A detailed investigation of these feed-down candidates can be found in Section 7.2.

As can be seen in Figure 7.1, no peaking background is evident in the generic MC sample. To further illustrate this point, the $\overline{B}^0 \to \Lambda_c^+\overline{p}$ and $B^- \to \Lambda_c^+\overline{p}\pi^-$ generic MC samples are fit using a two-dimensional background PDF and a signal PDF made up of Gaussian distributions for $(m_{\rm miss} + m_B)/2$ and $(m_{\rm rec} - m_B)$. The means and widths of the signal Gaussians are fixed to ensure that the fit converges, and the number of signal events is allowed to be positive or negative. The generic MC components are scaled to have equivalent luminosities to the data sample. The results of these fits are shown in Figures 7.2 and 7.3; they are broken down by Λ_c^+ decay mode and the combined result is shown. We find no significant signal in any of the fits.

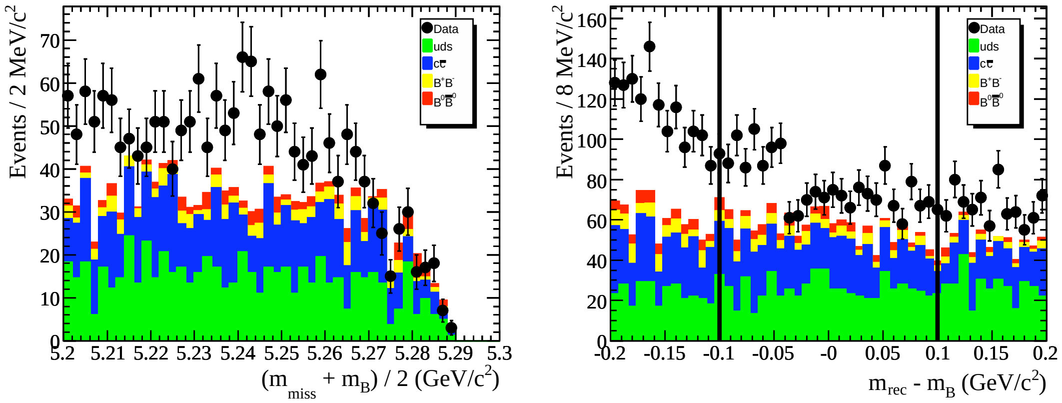

(a) $\overline{B}^0 \to \Lambda_c^+ \overline{p}$

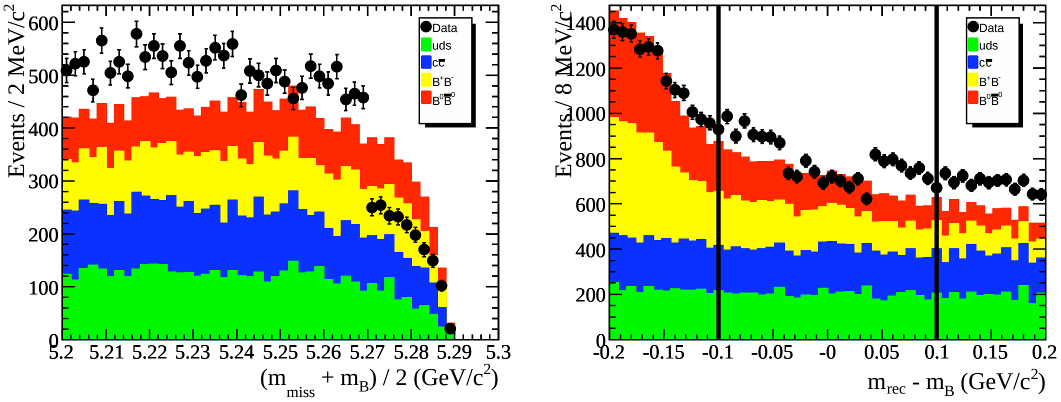

(b) $B^- \to \Lambda_c^+ \overline{p} \pi^-$

Figure 7.1: Distributions of $(m_{\text{miss}} + m_B)/2$ (left) for $|(m_{\text{rec}} - m_B)| < 0.1\,\text{GeV}/c^2$ and $(m_{\text{rec}} - m_B)$ (right) for $(m_{\text{miss}} + m_B)/2 > 5.2\,\text{GeV}/c^2$ with (a) $\overline{B}^0 \to \Lambda_c^+ \overline{p}$ and (b) $B^- \to \Lambda_c^+ \overline{p} \pi^-$ generic MC samples. The generic uds (red), $c\bar{c}$ (green), $B^0\overline{B}^0$ (blue), and B^+B^- (yellow) MC samples are individually scaled to have luminosities equal to the data sample (black points). The data sample is blinded. In the $(m_{\text{rec}} - m_B)$ distributions, the fit region is indicated.

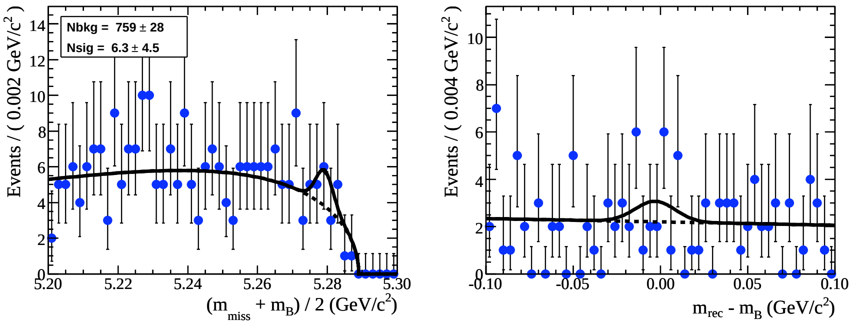

(a) $\Lambda_c^+ \to pK^-\pi^+$

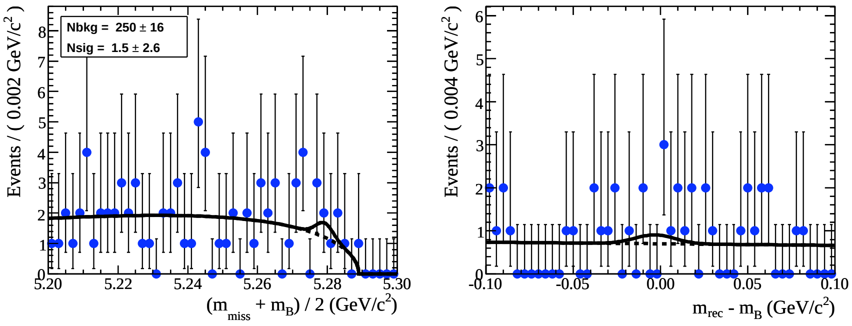

(b) $\Lambda_c^+ \to pK_S^0$

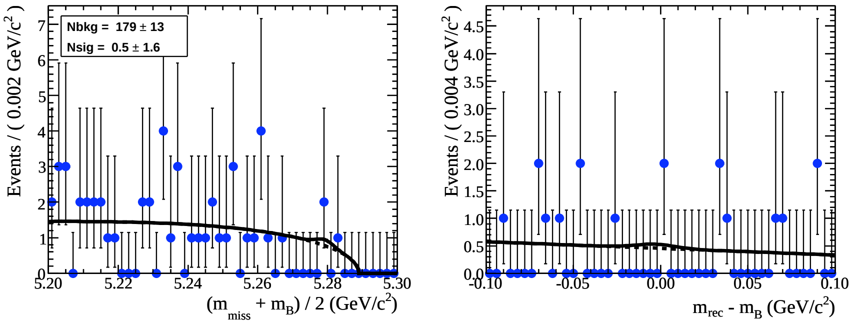

(c) $\Lambda_c^+ \to pK_S^0\pi^+\pi^-$

Figure 7.2: $(m_{\text{miss}} + m_B)/2$ (left) and $(m_{\text{rec}} - m_B)$ (right) projections of 2-D fits to scaled $\overline{B}^0 \to \Lambda_c^+\overline{p}$ generic MC candidates in the fit region. $(m_{\text{miss}} + m_B)/2$ is shown in the region $|(m_{\text{rec}} - m_B)| < 0.30\,\text{GeV}/c^2$ and $(m_{\text{rec}} - m_B)$ is shown in the region $(m_{\text{miss}} + m_B)/2 > 5.270\,\text{GeV}/c^2$. Each subfigure shows an individual Λ_c^+ decay mode $(a) - (e)$ or the combined Λ_c^+ decay modes (f). The means and widths of the signal Gaussians are fixed, and the number of signal events is allowed to vary between -50 and 50 events. The full PDF with uncorrelated signal Gaussians (solid line) and background PDF (dashed line) in each projection are shown. No peaking background is evident.

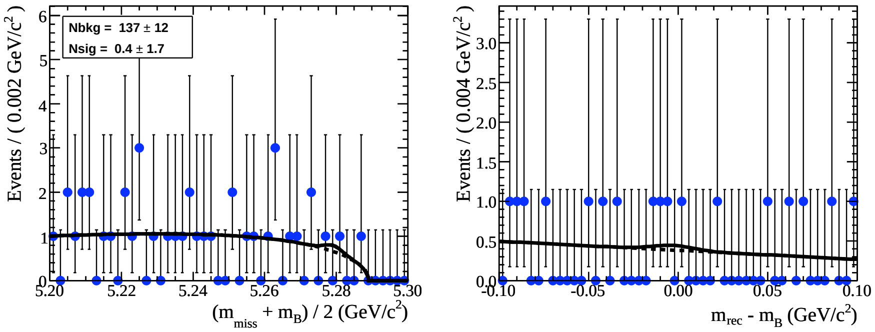

(d) $\Lambda_c^+ \to \Lambda\pi^+$

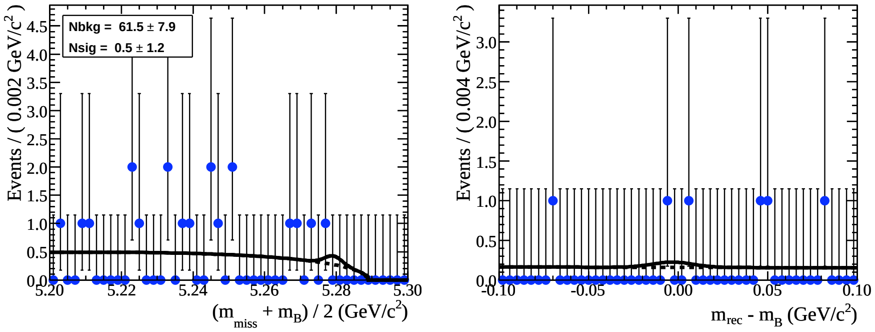

(e) $\Lambda_c^+ \to \Lambda\pi^+\pi^-\pi^+$

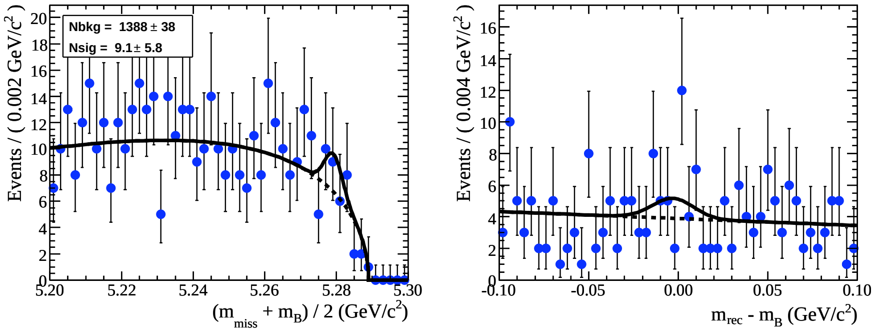

(f) all

Figure 7.2: (cont.)

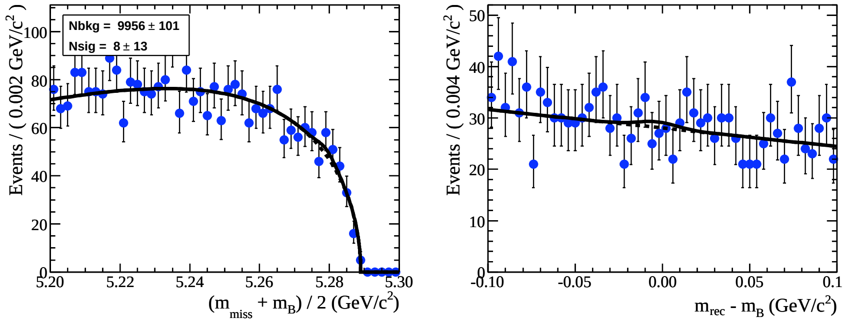

(a) $\Lambda_c^+ \to pK^-\pi^+$

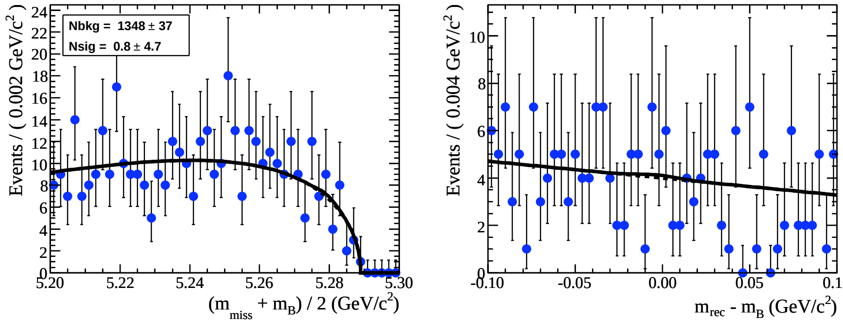

(b) $\Lambda_c^+ \to pK_S^0$

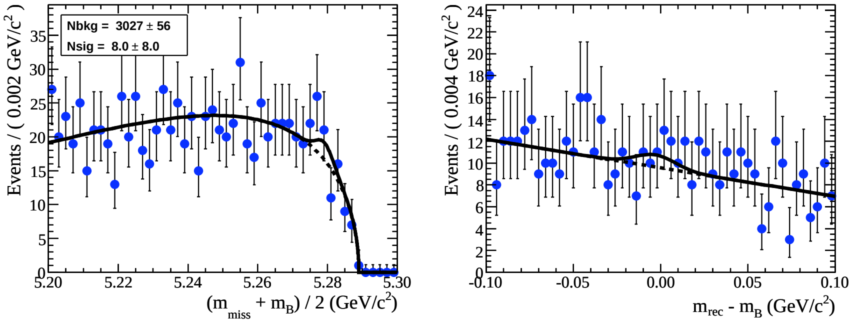

(c) $\Lambda_c^+ \to pK_S^0\pi^+\pi^-$

Figure 7.3: $(m_{\rm miss} + m_B)/2$ (left) and $(m_{\rm rec} - m_B)$ (right) projections of 2-D fits to scaled $B^- \to \Lambda_c^+\overline{p}\pi^-$ generic MC candidates in the fit region. $(m_{\rm miss} + m_B)/2$ is shown in the region $|(m_{\rm rec} - m_B)| < 0.30\,{\rm GeV}/c^2$ and $(m_{\rm rec} - m_B)$ is shown in the region $(m_{\rm miss} + m_B)/2 > 5.270\,{\rm GeV}/c^2$. Each subfigure shows an individual Λ_c^+ decay mode $(a) - (e)$ or the combined Λ_c^+ decay modes (f). The means and widths of the signal Gaussians are fixed, and the number of signal events is allowed to vary between -50 and 50 events. The full PDF with uncorrelated signal Gaussians (solid line) and background PDF (dashed line) in each projection are shown. No peaking background is evident.

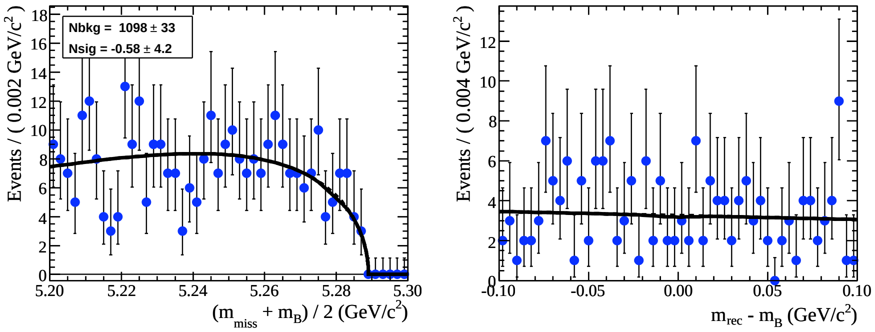

(d) $\Lambda_c^+ \to \Lambda\pi^+$

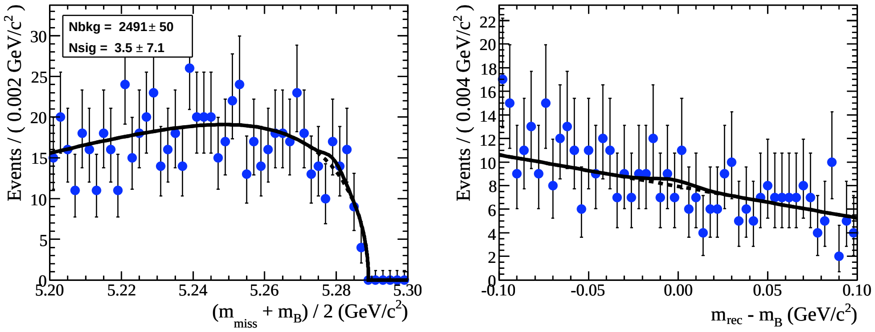

(e) $\Lambda_c^+ \to \Lambda\pi^+\pi^-\pi^+$

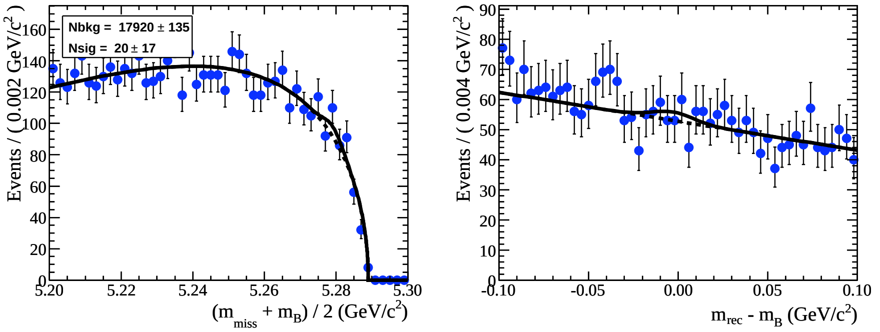

(f) all

Figure 7.3: (cont.)

Table 7.1: Results of fits to $\overline{B}^0 \rightarrow \Lambda_c^+ \overline{p}$ generic MC samples. No peaking background is present in any Λ_c^+ decay mode. Parameters without uncertainties were fixed in the fit.

Variable	Fit Parameter	$pK^-\pi^+$	pK_S^0	$pK_S^0\pi^+\pi^-$	$\Lambda\pi^+$	$\Lambda\pi^+\pi^-\pi^+$
$(m_{\text{miss}} + m_B)/2$	$\mu\,(\text{MeV}/c^2)$	$5,279.2$	$5,279.2$	$5,279.2$	$5,279.2$	$5,279.2$
	$\sigma\,(\text{MeV}/c^2)$	2.48	2.48	2.48	2.48	2.48
	c_{ARG}	-25 ± 4	-23 ± 7	-15 ± 8	-22 ± 10	-17 ± 14
	m^0_{ARG}	5.289	5.289	5.289	5.289	5.289
$(m_{\text{rec}} - m_B)$	$\mu\,(\text{MeV}/c^2)$	-3	-3	-3	-3	-3
	$\sigma\,(\text{MeV}/c^2)$	11.5	11.5	11.5	11.5	11.5
	$a\,(\text{GeV}^{-1})$	-0.6 ± 0.6	-0.5 ± 1.1	-2.7 ± 1.2	-3.0 ± 1.4	-0.3 ± 2.2
	N_{sig}	6.3 ± 4.5	1.5 ± 2.6	0.5 ± 1.6	0.4 ± 1.7	0.48 ± 1.2
	N_{bkg}	759 ± 28	250 ± 16	179 ± 13	137 ± 12	62 ± 8

Table 7.2: Results of fits to $B^- \to \mathit{\Lambda}_c^+ \overline{p} \pi^-$ generic MC samples. No peaking background is present in any $\mathit{\Lambda}_c^+$ decay mode. Parameters without uncertainties were fixed in the fit.

Variable	Fit Parameter	$pK^-\pi^+$	pK_S^0	$pK_S^0\pi^+\pi^-$	$\mathit{\Lambda}\pi^+$	$\mathit{\Lambda}\pi^+\pi^-\pi^+$
$(m_{\mathrm{miss}} + m_B)/2$	$\mu\,(\mathrm{MeV}/c^2)$	$5,279.2$	$5,279.2$	$5,279.2$	$5,279.2$	$5,279.2$
	$\sigma\,(\mathrm{MeV}/c^2)$	2.48	2.48	2.48	2.48	2.48
	c_{ARG}	-23 ± 1	-27 ± 3	-31 ± 2	-27 ± 3	-32 ± 2
	m^0_{ARG}	5.289	5.289	5.289	5.289	5.289
$(m_{\mathrm{rec}} - m_B)$	$\mu\,(\mathrm{MeV}/c^2)$	-3	-3	-3	-3	-3
	$\sigma\,(\mathrm{MeV}/c^2)$	11.5	11.5	11.5	11.5	11.5
	$a\,(\mathrm{GeV}^{-1})$	-1.3 ± 0.2	-1.8 ± 0.5	-2.7 ± 0.3	-0.6 ± 0.5	-3.4 ± 0.3
	N_{sig}	7.9 ± 12.6	0.8 ± 4.7	8.0 ± 8.0	-0.6 ± 4.2	3.5 ± 7.0
	N_{bkg}	9956 ± 101	1348 ± 37	3027 ± 56	1098 ± 33	2491 ± 50

7.2 Feed-through background contributions

Exclusive MC samples are investigated to determine the extent of background contributions from modes that may not be present in the generic MC samples. In both $\overline{B}^0 \to \Lambda_c^+ \overline{p}$ and $B^- \to \Lambda_c^+ \overline{p} \pi^-$, "feed-down" candidates arise from B decays with an additional pion that is misreconstructed; these candidates are shifted by $\sim -m_\pi$. In $B^- \to \Lambda_c^+ \overline{p} \pi^-$, "feed-up" candidates arise from $\overline{B}^0 \to \Lambda_c^+ \overline{p}$ candidates that are combined with a random additional pion; these candidates are located in the region $(m_{\text{rec}} - m_B) > 0.1\,\text{GeV}/c^2$. The efficiencies for selecting feed-through candidates in various modes in the fit region are summarized in Table 7.3. The distributions of $(m_{\text{rec}} - m_B)$ vs. $(m_{\text{miss}} + m_B)/2$ for both the feed-down and feed-up contributions are shown in Figure 7.4.

Table 7.3: Exclusive signal MC modes that contribute to feed-down and feed-up background. Summarized is the efficiency for selecting each mode in the **fit** region with the optimal selection criteria and the expected number of events in the **fit** region.

Category	Mode	BF	Efficiency	Exp. # Events
$\overline{B}^0 \to \Lambda_c^+ \overline{p}$ Feed-Down	$B^- \to \Lambda_c^+ \overline{p} \pi^-$	20.1×10^{-5}	0.01%	< 1
	$\overline{B}^0 \to \Lambda_c^+ \overline{p} \pi^0$	20.1×10^{-5}	0.00%	< 1
	$B^- \to \Sigma_c(2455)^0 \overline{p}$	3.7×10^{-5}	0.01%	1
$B^- \to \Lambda_c^+ \overline{p} \pi^-$ Feed-Down	$\overline{B}^0 \to \Lambda_c^+ \overline{p} \pi^+ \pi^-$	$110. \times 10^{-5}$	0.40%	84
	$B^- \to \Lambda_c^+ \overline{p} \pi^- \pi^0$	$110. \times 10^{-5}$	0.22%	45
$B^- \to \Lambda_c^+ \overline{p} \pi^-$ Feed-Up	$\overline{B}^0 \to \Lambda_c^+ \overline{p}$	2.2×10^{-5}	0.32%	1

7.3 Peaking background

Two-body charmed baryonic B decay modes are not present in the generic MC samples. Candidates from one such mode, $\overline{B}^0 \to \Sigma_c(2455)^+ \overline{p}$, $\Sigma_c(2455)^+ \to \Lambda_c^+ \pi^0$, peak in the $(m_{\text{rec}} - m_B)$ vs. $(m_{\text{miss}} + m_B)/2$ signal region when reconstructed as $B^- \to \Lambda_c^+ \overline{p} \pi^-$. The $\Sigma_c(2455)^+$ slow daughter π^0 is missed, and a random π^- from elsewhere in the event is picked up. The exclusive MC sample used to study this peaking background is a sample of $175,000$ $\overline{B}^0 \to \Sigma_c(2455)^+ \overline{p}$, $\Sigma_c(2455)^+ \to \Lambda_c^+ \pi^0$, $\Lambda_c^+ \to p K^- \pi^+$ events.

The efficiency for selecting the $\overline{B}^0 \to \Sigma_c(2455)^+ \overline{p}$ candidates is 11.5% in the entire fit

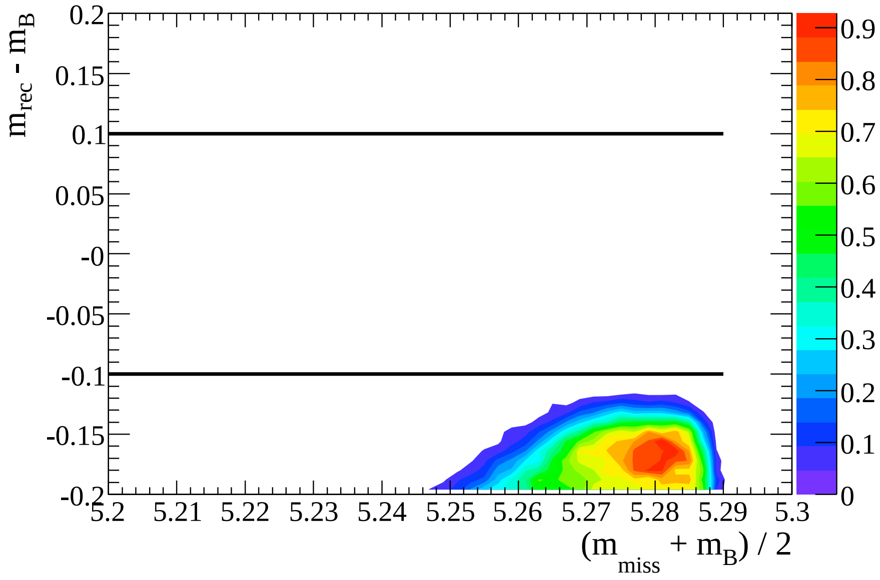

(a) $\overline{B}^0 \to \Lambda_c^+ \overline{p}$

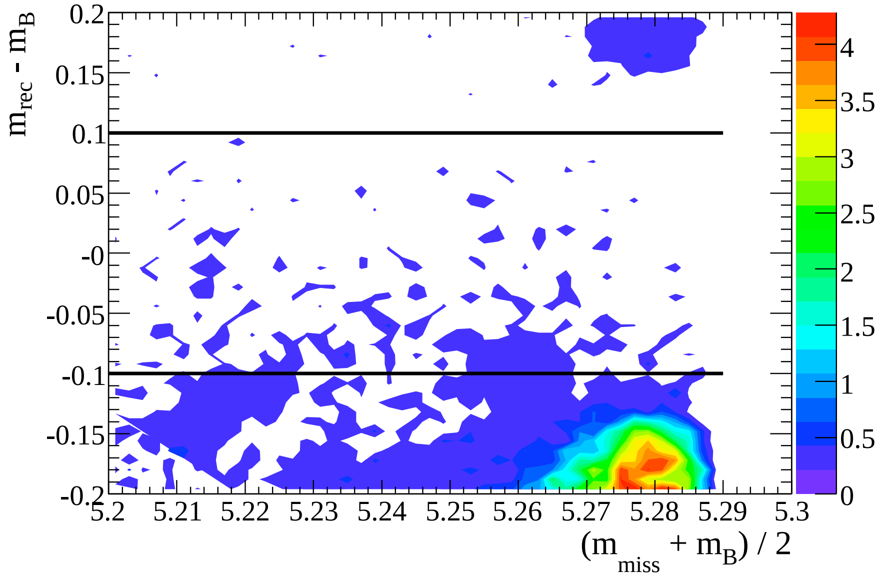

(b) $B^- \to \Lambda_c^+ \overline{p} \pi^-$

Figure 7.4: $(m_{\text{rec}} - m_B)$ vs. $(m_{\text{miss}} + m_B)/2$ for exclusive MC events reconstructed as $\overline{B}^0 \to \Lambda_c^+ \overline{p}$ (a) and $B^- \to \Lambda_c^+ \overline{p} \pi^-$ (b), $\Lambda_c^+ \to pK^-\pi^+$. The modes listed in Table 7.3 are combined and scaled to the expected number of events. The majority of events are located outside of the indicated fit region.

region, and 1.7% in the signal region. The branching fraction for this mode has not been measured, but it is expected to be of the order 10^{-5} (similar to other two-body charmed baryonic B decay modes such as $\overline{B}^0 \rightarrow \mathit{\Lambda}_c^+\overline{p}$). Belle has measured the branching fraction of the isospin partner decay $\mathcal{B}(B^- \rightarrow \mathit{\Sigma}_c(2455)^0\overline{p}) = (3.7 \pm 0.7 \pm 0.4 \pm 1.0) \times 10^{-5}$ [30], where the uncertainties are statistical, systematic, and the uncertainty due to $\mathcal{B}(\mathit{\Lambda}_c^+ \rightarrow pK^-\pi^+)$, respectively. Therefore we assume $\mathcal{B}(\overline{B}^0 \rightarrow \mathit{\Sigma}_c(2455)^+\overline{p}) \approx 2.9 - 4.5 \times 10^{-5}$. Using this estimate, we scale the number of expected events by $N_{B\overline{B}} \times \mathcal{B}(\overline{B}^0 \rightarrow \mathit{\Sigma}_c(2455)^+\overline{p}) \times \mathcal{B}(\mathit{\Lambda}_c^+ \rightarrow pK^-\pi^+)/175000$. Thus we expect between 64 and 99 events in the fit region, including between 9 and 14 events in the signal region (see Table 7.4). If we take the conservative estimate of the expected number of peaking background events and divide by the expected number of signal events, we obtain 1.4%, so an upper limit on the systematic uncertainty due to peaking background is 1.4%.

Table 7.4: Summary of the expected number of candidates in the **signal** region due to peaking background (given a range of $\overline{B}^0 \rightarrow \mathit{\Sigma}_c(2455)^+\overline{p}$ branching fractions), using the efficiency for selecting $\overline{B}^0 \rightarrow \mathit{\Sigma}_c(2455)^+\overline{p}$ in the **signal** region with the optimal selection criteria. These numbers can be compared to 1053 expected signal events in $\overline{B}^0 \rightarrow \mathit{\Lambda}_c^+\overline{p}$, $\mathit{\Lambda}_c^+ \rightarrow pK^-\pi^+$.

	Mode	BF	Efficiency	Expected # Events
low	$\overline{B}^0 \rightarrow \mathit{\Sigma}_c(2455)^+\overline{p}$	$\sim 2.9 \times 10^{-5}$	1.7%	9
mid	$\overline{B}^0 \rightarrow \mathit{\Sigma}_c(2455)^+\overline{p}$	$\sim 3.7 \times 10^{-5}$		12
high	$\overline{B}^0 \rightarrow \mathit{\Sigma}_c(2455)^+\overline{p}$	$\sim 4.5 \times 10^{-5}$		14

To understand this peaking background further, we perform a 2-D fit to the 20158 exclusive MC candidates in the fit region (scaled to the expected 82 events). Upon examining the 2-D distribution in $(m_{\text{miss}} + m_B)/2$ and $(m_{\text{rec}} - m_B)$, it is apparent that most of the candidates in the fit region will be absorbed into the background PDFs in the 2-D fit. However, a wide peak is evident in the $(m_{\text{rec}} - m_B)$ signal region. We perform a 2-D fit to quantify the peaking portion of this background. The peaking candidates are described by a Gaussian distribution in $(m_{\text{miss}} + m_B)/2$ times a Gaussian in $(m_{\text{rec}} - m_B)$. The mean of the $(m_{\text{miss}} + m_B)/2$ Gaussian is fixed, and the widths of both distributions are free parameters in the fit. The non-peaking candidates are described by an ARGUS function in $(m_{\text{miss}} + m_B)/2$ and a line in $(m_{\text{rec}} - m_B)$. Both the ARGUS parameter and slope are free parameters. Although the non-peaking shape is different from nominal $B\overline{B}$ backgrounds, it

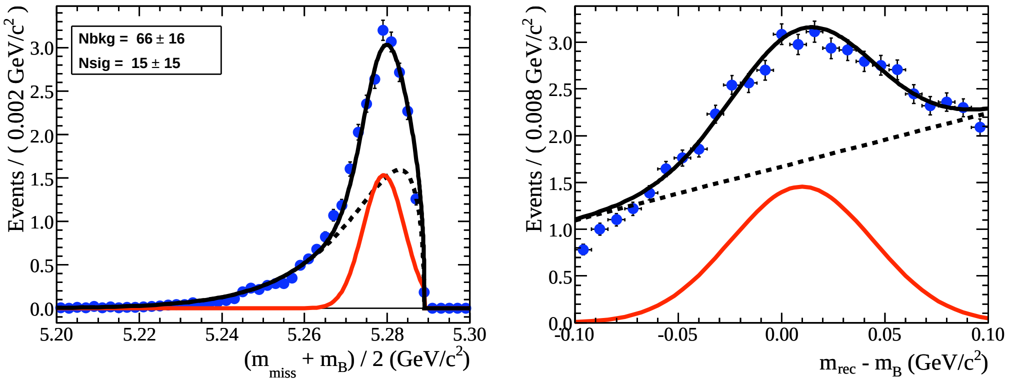

Figure 7.5: Projections of a 2-D fit (black line) to $(m_{\text{miss}} + m_B)/2$ (left) and $(m_{\text{rec}} - m_B)$ (right) for exclusive $\overline{B}^0 \to \Sigma_c(2455)^+\overline{p}$, $\Sigma_c(2455)^+ \to \Lambda_c^+\pi^0$, $\Lambda_c^+ \to pK^-\pi^+$ MC events (points) reconstructed as $B^- \to \Lambda_c^+\overline{p}\pi^-$, $\Lambda_c^+ \to pK^-\pi^+$ in the fit region. Candidates in the $(m_{\text{miss}} + m_B)/2$ distribution satisfy $|(m_{\text{rec}} - m_B)| < 0.30\,\text{GeV}/c^2$, and candidates in the $(m_{\text{rec}} - m_B)$ distribution satisfy $(m_{\text{miss}} + m_B)/2 > 5.270\,\text{GeV}/c^2$. Peaking candidates are described by a Gaussian PDF in $(m_{\text{miss}} + m_B)/2$ times a Gaussian PDF in $(m_{\text{rec}} - m_B)$ (red line). Non-peaking candidates are described by an ARGUS PDF in $(m_{\text{miss}} + m_B)/2$ times a linear PDF in $(m_{\text{rec}} - m_B)$ (dashed line). The MC candidates are scaled to the expected number of events given $\mathcal{B}(\overline{B}^0 \to \Sigma_c(2455)^+\overline{p}) \approx 3.7 \times 10^{-5}$.

is adequately described and will presumably be absorbed into the background PDF in the fit to data. The projections of the 2-D fit are shown in Figure 7.5 and the fit results are summarized in Table 7.5. These fit results indicate 15 ± 15 peaking events.

However, examination of Table 7.5 indicates that the $(m_{\text{miss}} + m_B)/2$ resolution of the peaking events is wider than the nominal signal width ($5\,\text{MeV}/c^2$ compared to $2.5\,\text{MeV}/c^2$) and the resolution of $(m_{\text{rec}} - m_B)$ is also wider than the nominal signal width ($30\,\text{MeV}/c^2$ compared to $12\,\text{MeV}/c^2$). Therefore, some of the "peaking" events may be absorbed into the statistical fluctuations of the background and not counted as signal. Figure 7.6 shows the scaled $\overline{B}^0 \to \Sigma_c(2455)^+\overline{p}$, $\Sigma_c(2455)^+ \to \Lambda_c^+\pi^0$, $\Lambda_c^+ \to pK^-\pi^+$ MC events (reconstructed as $B^- \to \Lambda_c^+\overline{p}\pi^-$, $\Lambda_c^+ \to pK^-\pi^+$) superimposed on the luminosity-weighted generic MC background samples. A fit to the combined MC sample is performed (with all means and widths fixed) resulting in a yield of 13 ± 13 peaking events. The fit results are summarized in Table 7.6.

The final measure of the effect of the peaking background on the signal yield is obtained through fits of toy MC background samples (based on generic MC PDFs), signal

Table 7.5: Results of the fit to exclusive $\overline{B}^0 \to \Sigma_c(2455)^+\overline{p}$, $\Sigma_c(2455)^+ \to \Lambda_c^+\pi^0$, $\Lambda_c^+ \to pK^-\pi^+$ MC events reconstructed as $B^- \to \Lambda_c^+\overline{p}\pi^-$, $\Lambda_c^+ \to pK^-\pi^+$. The parameters σ_L and σ_R refer to the lower and upper standard deviations, respectively, of the bifurcated Gaussian. Parameters without uncertainties were fixed in the fit.

Variable	Fit Parameter	$pK^-\pi^+$
$(m_{\text{miss}} + m_B)/2$	$\mu\,(\text{MeV}/c^2)$	$5,279.2$
	$\sigma\,(\text{MeV}/c^2)$	5 ± 3
	c_{ARG}	-220 ± 30
	m^0_{ARG}	5.289
$(m_{\text{rec}} - m_B)$	$\mu\,(\text{MeV}/c^2)$	10 ± 30
	$\sigma\,(\text{MeV}/c^2)$	30 ± 20
	$a\,(\text{GeV}^{-1})$	$+3 \pm 2$
	N_{sig}	15 ± 15
	N_{bkg}	66 ± 16

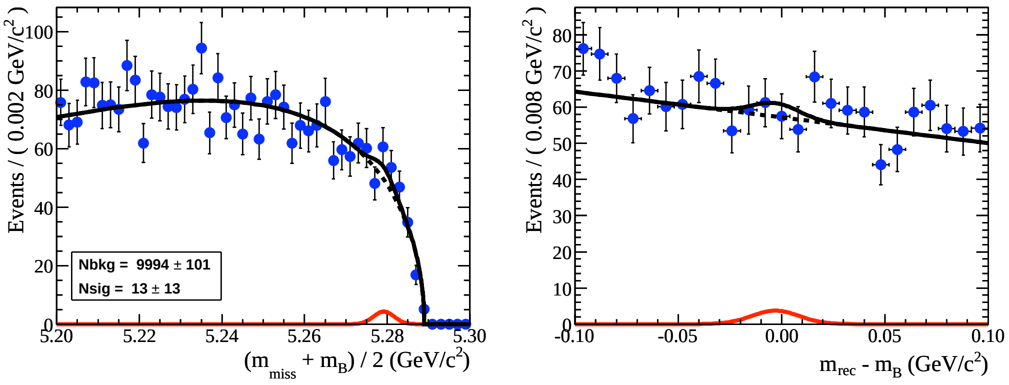

Figure 7.6: Slices of a 2-D fit to $(m_{\text{miss}} + m_B)/2$ (left) and $(m_{\text{rec}} - m_B)$ (right) for exclusive $\overline{B}^0 \to \Sigma_c(2455)^+\overline{p}$, $\Sigma_c(2455)^+ \to \Lambda_c^+\pi^0$, $\Lambda_c^+ \to pK^-\pi^+$ MC events reconstructed as $B^- \to \Lambda_c^+\overline{p}\pi^-$, $\Lambda_c^+ \to pK^-\pi^+$ and generic MC events in the fit region. The combined sample (points) is fit with a 2-D PDF (black line). Peaking candidates are described by Gaussian PDFs (red line) in $(m_{\text{miss}} + m_B)/2$ and $(m_{\text{rec}} - m_B)$. Non-peaking candidates are described by an Argus PDF in $(m_{\text{miss}} + m_B)/2$ times a linear PDF in $(m_{\text{rec}} - m_B)$ (dashed line). The $\overline{B}^0 \to \Sigma_c(2455)^+\overline{p}$, $\Sigma_c(2455)^+ \to \Lambda_c^+\pi^0$, $\Lambda_c^+ \to pK^-\pi^+$ MC candidates are scaled to the expected number of events given $\mathcal{B}(\overline{B}^0 \to \Sigma_c(2455)^+\overline{p}) \approx 3.7 \times 10^{-5}$ and the generic MC candidates are scaled according to their luminosity.

Table 7.6: Results of the fit to exclusive $\overline{B}^0 \rightarrow \Sigma_c(2455)^+\overline{p}$, $\Sigma_c(2455)^+ \rightarrow \Lambda_c^+\pi^0$, $\Lambda_c^+ \rightarrow pK^-\pi^+$ plus generic MC candidates reconstructed as $B^- \rightarrow \Lambda_c^+\overline{p}\pi^-$, $\Lambda_c^+ \rightarrow pK^-\pi^+$. Parameters without uncertainties were fixed in the fit.

Variable	Fit Parameter	$pK^-\pi^+$
$(m_{\rm miss} + m_B)/2$	$\mu\,(\,{\rm MeV}/c^2)$	$5,279.2$
	$\sigma\,(\,{\rm MeV}/c^2)$	2.48
	c_{ARG}	-24 ± 1
	m^0_{ARG}	5.289
$(m_{\rm rec} - m_B)$	$\mu\,(\,{\rm MeV}/c^2)$	-3
	$\sigma\,(\,{\rm MeV}/c^2)$	11.5
	$a\,(\,{\rm GeV}^{-1})$	-1.2 ± 0.2
	N_{sig}	13 ± 13
	N_{bkg}	$10,002 \pm 101$

MC samples, and exclusive MC peaking background events from the $\overline{B}^0 \rightarrow \Sigma_c(2455)^+\overline{p}$, $\Sigma_c(2455)^+ \rightarrow \Lambda_c^+\pi^0$, $\Lambda_c^+ \rightarrow pK^-\pi^+$ sample. The full procedure for evaluating these toy studies is discussed in detail in Chapter 8. In this study, 2-D fits in $(m_{\rm rec} - m_B)$ and $(m_{\rm miss} + m_B)/2$ are performed to 1053 signal MC $B^- \rightarrow \Lambda_c^+\overline{p}\pi^-$, $\Lambda_c^+ \rightarrow pK^-\pi^+$ events and toy MC background events based on generic MC PDFs, but we include 82 MC events from the $\overline{B}^0 \rightarrow \Sigma_c(2455)^+\overline{p}$, $\Sigma_c(2455)^+ \rightarrow \Lambda_c^+\pi^0$, $\Lambda_c^+ \rightarrow pK^-\pi^+$ sample in the fit region. (Note that all numbers are allowed to fluctuate according to Poisson statistics.) The results of this study are shown in Figure 7.7. The signal yields from 100 fits are plotted minus the true number of signal events injected in each sample in the distribution of $S - S_{True}$. A Gaussian fit to this distribution demonstrates an offset of 11 ± 2 events. The yields derived from the final fit to data will be corrected by $11/1053 = 1.0\%$ to compensate for the peaking background events.

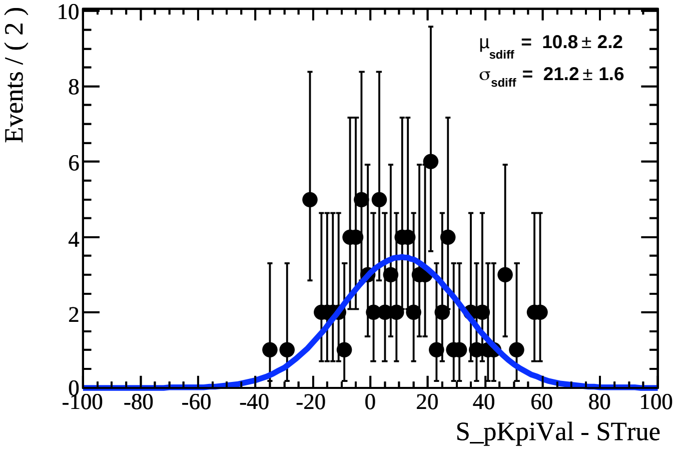

Figure 7.7: Distribution of fitted $B^- \to \Lambda_c^+ \overline{p} \pi^-$, $\Lambda_c^+ \to pK^- \pi^+$ signal events minus the true number of signal events for 100 fits to toy MC background (based on generic MC PDFs), signal MC, and exclusive MC peaking background samples. The Gaussian fit of this distribution illustrates an offset of 11 ± 2 events. This offset is used to correct the signal yields in the final simultaneous fit.

Chapter 8

Fit Parameterization and Validation Studies

Validation of the combined signal and background probability density function is necessary to ensure that the fit to the unblinded data sample is robust and unbiased. All studies are performed with the final selection criteria presented in Section 5.

8.1 Description of the 2-D PDF in $(m_{\mathbf{miss}} + m_B)/2$ and $(m_{\mathbf{rec}} - m_B)$

The background PDF is the same as for the efficiency determination described in Chapter 6, a first-order polynomial in $(m_{\rm rec} - m_B)$ times an ARGUS function in $(m_{\rm miss} + m_B)/2$:

$$\begin{aligned} \mathcal{P}_{bkg}((m_{\rm rec} - m_B), (m_{\rm miss} + m_B)/2; a, c_{ARG}) \propto\ & (1 + a(m_{\rm rec} - m_B)) \\ & \times (m_{\rm miss} + m_B)/2 \sqrt{1 - \left(\frac{(m_{\rm miss} + m_B)/2}{m_0}\right)^2} \\ & \times exp\left(-c_{ARG}\left(1 - \left(\frac{(m_{\rm miss} + m_B)/2}{m_0}\right)^2\right)\right), \end{aligned} \tag{8.1}$$

where a is the slope in $(m_{\rm rec} - m_B)$, c_{ARG} is the ARGUS function slope parameter, and m_0 defines the endpoint of the ARGUS function (which is fixed to the CM beam energy, $5.289\,{\rm GeV}/c^2$).

The signal PDF for $\overline{B}^0 \to \Lambda_c^+ \overline{p}$ is a Gaussian in $(m_{\rm rec} - m_B)$ times a Gaussian in

$(m_{\mathrm{miss}} + m_B)/2$:

$$\mathcal{P}_{sig}^{m_{\mathrm{rec}}}((m_{\mathrm{rec}} - m_B); \mu, \sigma) \propto \frac{1}{\sigma\sqrt{2\pi}}\ e^{((m_{\mathrm{rec}}-m_B)-\mu)^2/2\sigma^2}, \tag{8.2}$$

where μ is the mean and σ is the standard deviation. The signal PDF in $(m_{\mathrm{rec}} - m_B)$ is multiplied by a Gaussian in $(m_{\mathrm{miss}} + m_B)/2$:

$$\mathcal{P}_{sig}^{m_{\mathrm{miss}}}((m_{\mathrm{miss}} + m_B)/2; \mu, \sigma) \propto \frac{1}{\sigma\sqrt{2\pi}}\ e^{((m_{\mathrm{miss}}+m_B)/2-\mu)^2/2\sigma^2}, \tag{8.3}$$

where μ is the mean and σ is the standard deviation.

The signal PDF for $B^- \to \Lambda_c^+ \overline{p}\pi^-$ is a double Gaussian in $(m_{\mathrm{rec}} - m_B)$:

$$\begin{aligned}&\mathcal{P}_{sig}^{m_{\mathrm{rec}}}((m_{\mathrm{rec}} - m_B); \mu, \sigma_1, \sigma_2) \propto \\ &\qquad\left(\frac{f}{\sigma_1\sqrt{2\pi}}\ e^{((m_{\mathrm{rec}}-m_B)-\mu)^2/2\sigma_1^2} + \frac{1-f}{\sigma_2\sqrt{2\pi}}\ e^{((m_{\mathrm{rec}}-m_B)-\mu)^2/2\sigma_2^2}\right),\end{aligned} \tag{8.4}$$

where μ is the mean and σ_1 and σ_2 are the standard deviations. This PDF is multiplied by the single Gaussian PDF in Eqn. 8.3.

The unbinned 2-D fit is performed by minimizing the negative logarithm of the extended likelihood $\mathcal{L}$ of a particular Λ_c^+ decay mode:

$$\begin{aligned}\mathcal{L} = e^{-(N_{sig}+N_{bkg})}\,&\frac{(N_{sig} + N_{bkg})^N}{N!}\times \\ &\prod_{i=1}^{N}\left(\frac{N_{sig}}{N_{sig} + N_{bkg}}\mathcal{P}_{sig,i}\left((m_{\mathrm{rec}} - m_B), (m_{\mathrm{miss}} + m_B)/2; \vec{s}_{sig}\right)\right. \\ &\qquad \left. + \frac{N_{bkg}}{N_{sig} + N_{bkg}}\mathcal{P}_{bkg,i}\left((m_{\mathrm{rec}} - m_B), (m_{\mathrm{miss}} + m_B)/2; \vec{s}_{bkg}, a\right)\right),\end{aligned} \tag{8.5}$$

where N_{sig} and N_{bkg} are the numbers of signal and background events, respectively, N is the total number of events, and the index i runs over each event. The variable $\vec{s}_{sig}$ ($\vec{s}_{bkg}$) represents the set of signal (background) parameters. Note that the background slope a in $(m_{\mathrm{miss}} + m_B)/2$ is treated separately.

The likelihood in Eqn. 8.5 is used in the $\overline{B}^0 \to \Lambda_c^+ \overline{p}$, $\Lambda_c^+ \to pK^-\pi^+$ and $B^- \to \Lambda_c^+ \overline{p}\pi^-$, $\Lambda_c^+ \to pK^-\pi^+$ fit validations described in the next section. However, a simultaneous fit to all the Λ_c^+ decay modes is performed for the extraction of the five signal yields in each B decay mode. We construct the total likelihood ($\mathcal{L}_{tot}$) from the products of the individual likelihoods (Eqn. 8.5) for each Λ_c^+ decay mode m:

$$\mathcal{L}_{tot} = \prod_m \mathcal{L}_m \left(\vec{x}_m; N_{sig,m}, N_{bkg,m}, \vec{s}_{sig}, \vec{s}_{bkg}, a_m\right). \tag{8.6}$$

The variable $\vec{x}$ represents the variables used in the 2-D fit $\{(m_{\rm rec} - m_B), (m_{\rm miss} + m_B)/2\}$. Separate signal and background yields are extracted for each Λ_c^+ decay mode, and the background slope in $(m_{\rm rec} - m_B)$ is also allowed to vary. The rest of the signal (background) parameters $\vec{s}_{sig}(\vec{s}_{bkg})$ are shared.

8.2 Monte Carlo Sample Fit Validation

The MC fit validation is performed using independent samples of signal MC events to simulate signal events and toy MC samples to represent the background events in the entire fitted region.

We generate 100 samples each of signal MC events and toy MC events. The signal MC events are selected from (unweighted) truth-matched official signal MC B candidates that pass all selection criteria and are in a $\pm 3\sigma$ signal region ($5.27 < (m_{\rm miss} + m_B)/2 < 5.29\,{\rm GeV}/c^2$ and $|(m_{\rm rec} - m_B)| < 0.030\,{\rm GeV}/c^2$). Toy MC samples are generated according to the $(m_{\rm rec} - m_B)$ and $(m_{\rm miss} + m_B)/2$ shape ($\mathcal{P}_{bkg}$) of the generic MC sample in the fit region. The resulting PDF is used to generate toy MC events in the fit region in each of the 100 samples. The number of events in each sample is allowed to vary according to Poisson statistics.

Each combined signal MC and toy MC sample is fit using the likelihood described in Eqn. 8.5. For each of the 100 fits, the values of and errors on each of the fit parameters, including N_{sig} and N_{bkg}, are tabulated along with the minimum negative log likelihood values. The pulls, defined as the parameter values from each fit result minus the original nominal value, divided by the error, are also tabulated.

8.2.1 $\Lambda_c^+ \to pK^-\pi^+$ Fit Validation Results

As a preliminary check, we perform a fit validation study using the dominant $\Lambda_c^+ \to pK^-\pi^+$ mode only in each B decay mode. Note that m_0 is fixed to $5.290\,{\rm GeV}/c^2$ for only this study.

The fit validation for $\overline{B}^0 \to \Lambda_c^+\overline{p}$, $\Lambda_c^+ \to pK^-\pi^+$ ($B^- \to \Lambda_c^+\overline{p}\pi^-$, $\Lambda_c^+ \to pK^-\pi^+$) contains 90 (1000) expected signal events. For each study, all 100 fits converge and in

$\overline{B}^0 \to \Lambda_c^+\overline{p}$ ($B^- \to \Lambda_c^+\overline{p}\pi^-$) 100 (96) fits have a full, accurate covariance matrix. (The four remaining fits in the $B^- \to \Lambda_c^+\overline{p}\pi^-$, $\Lambda_c^+ \to pK^-\pi^+$ study have an error matrix that is not positive definite). Plots of the distributions of the N_{sig} and N_{bkg} pulls are shown in Figure 8.1. The mean (width) of each signal pull distribution is consistent with 0 (1) within uncertainties, demonstrating that the single-mode fit PDF is robust and unbiased. We conclude that the fit to the new kinematic variables $(m_{\rm miss} + m_B)/2$ and $(m_{\rm rec} - m_B)$ in data will yield an unbiased result.

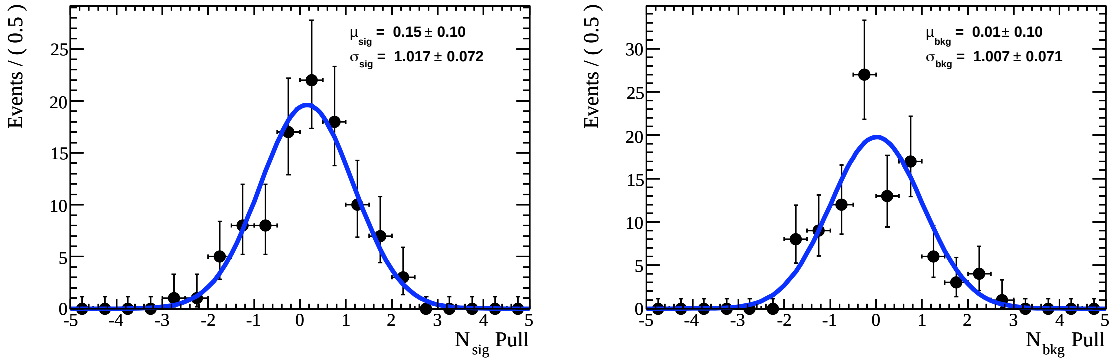

(a) $\overline{B}^0 \to \Lambda_c^+\overline{p}$, $\Lambda_c^+ \to pK^-\pi^+$

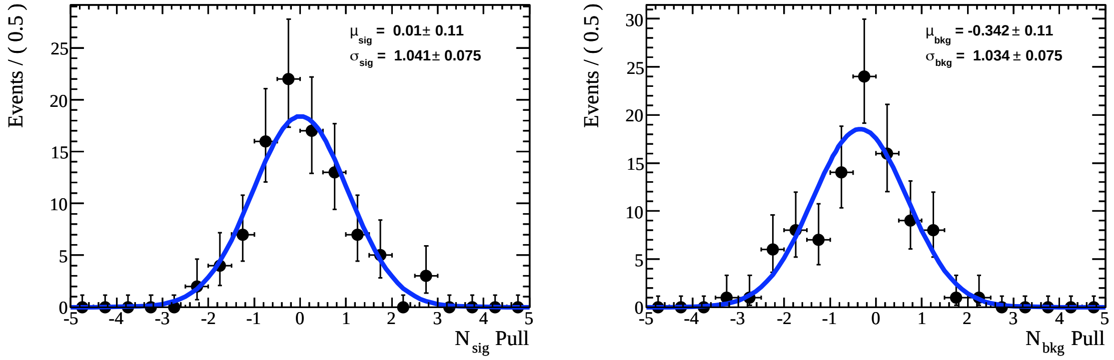

(b) $B^- \to \Lambda_c^+\overline{p}\pi^-$, $\Lambda_c^+ \to pK^-\pi^+$

Figure 8.1: Pull distributions for N_{sig} (left plots) and N_{bkg} (right plots) from 100 fits to signal MC + toy MC samples for (a) $\overline{B}^0 \to \Lambda_c^+\overline{p}$, $\Lambda_c^+ \to pK^-\pi^+$ and (b) $B^- \to \Lambda_c^+\overline{p}\pi^-$, $\Lambda_c^+ \to pK^-\pi^+$, with an average of 1000 and 90 signal events, respectively. Only fit results with good error matrices are included. The standard deviations of the distributions are consistent with 1 and the means of the distributions are consistent with 0, indicating no bias.

8.2.2 Simultaneous Fit Validation Results

The full check must be performed on a simultaneous fit to all of the Λ_c^+ decay modes in each B decay mode. Because there is only 1 expected signal event for $\overline{B}^0 \to \Lambda_c^+\overline{p}$, $\Lambda_c^+ \to \Lambda\pi^+\pi^-\pi^+$, we do not include this mode in the measurement of $\mathcal{B}(\overline{B}^0 \to \Lambda_c^+\overline{p})$.

Table 8.1 summarizes the number of expected signal events for each decay mode[1], along with the number of fits in each category that converge, the number of fits that have a full, accurate covariance matrix, and the signal pull results for each mode. The results of the fit validation indicate that the PDF model is robust and yields unbiased results. Fits that do not have a full, accurate covariance matrix have converged but the error matrix is not positive definite.

The pull distributions for the signal and background yields in each Λ_c^+ decay mode are plotted in Figures 8.2 and 8.3.

Table 8.1: Results from fits to 100 combined toy MC background and fully-simulated signal MC samples. For each decay mode, we present the number of signal events, the number of fits (out of 100) with a successful fit status from `Minuit` and, in the same column in parentheses, the number of fits with a full, accurate covariance matrix from `Hesse`. Also listed is the mean uncertainty on each yield ($\sigma_{N_{sig}}$). The pull distributions for the number of signal events (see Figures 8.2, 8.3) only include the fits that have a full, accurate covariance matrix.

Mode	Mean N_{sig}	# Good Status	Mean $\sigma_{N_{sig}}$	Signal Pull Mean	Signal Pull Width
$\overline{B}^0 \to \Lambda_c^+\overline{p}$, $\Lambda_c^+ \to pK^-\pi^+$	94	100 (98)	11	0.16 ± 0.11	1.09 ± 0.08
$\overline{B}^0 \to \Lambda_c^+\overline{p}$, $\Lambda_c^+ \to pK_S^0$	29$*$		6.0	0.01 ± 0.10	1.00 ± 0.07
$\overline{B}^0 \to \Lambda_c^+\overline{p}$, $\Lambda_c^+ \to pK_S^0\pi^+\pi^-$	14$*$		4.4	0.01 ± 0.11	1.15 ± 0.08
$\overline{B}^0 \to \Lambda_c^+\overline{p}$, $\Lambda_c^+ \to \Lambda\pi^+$	9		3.4	-0.30 ± 0.14	1.37 ± 0.10
$B^- \to \Lambda_c^+\overline{p}\pi^-$, $\Lambda_c^+ \to pK^-\pi^+$	1053	100 (94)	38	0.07 ± 0.09	0.91 ± 0.07
$B^- \to \Lambda_c^+\overline{p}\pi^-$, $\Lambda_c^+ \to pK_S^0$	339$*$		20	-0.07 ± 0.12	1.17 ± 0.09
$B^- \to \Lambda_c^+\overline{p}\pi^-$, $\Lambda_c^+ \to pK_S^0\pi^+\pi^-$	139$*$		14	-0.25 ± 0.09	0.86 ± 0.06
$B^- \to \Lambda_c^+\overline{p}\pi^-$, $\Lambda_c^+ \to \Lambda\pi^+$	106		12	0.01 ± 0.10	1.01 ± 0.07
$B^- \to \Lambda_c^+\overline{p}\pi^-$, $\Lambda_c^+ \to \Lambda\pi^+\pi^-\pi^+$	89		12	-0.21 ± 0.10	1.02 ± 0.07

---

[1] Note that the actual expected number of signal events for modes including a K_S^0 is 1/2 of the values listed in Table 8.1 (affected values are indicated by a $*$). The difference should have no impact on the conclusions of the fit validation study.

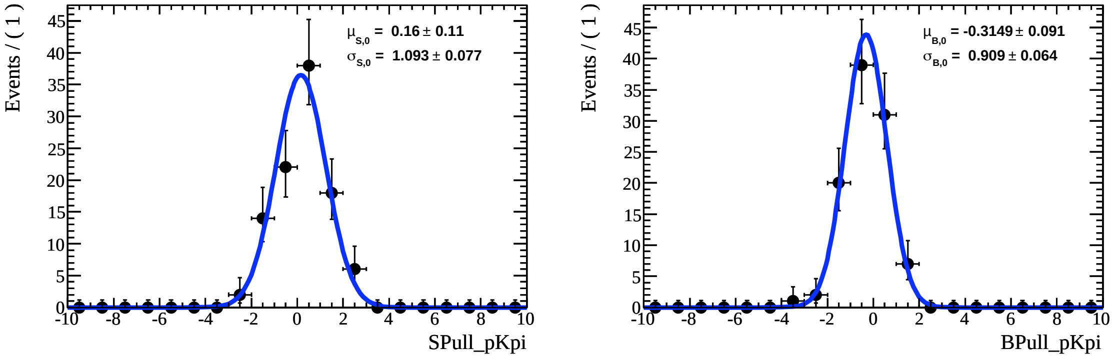

(a) $\Lambda_c^+ \to pK^-\pi^+$

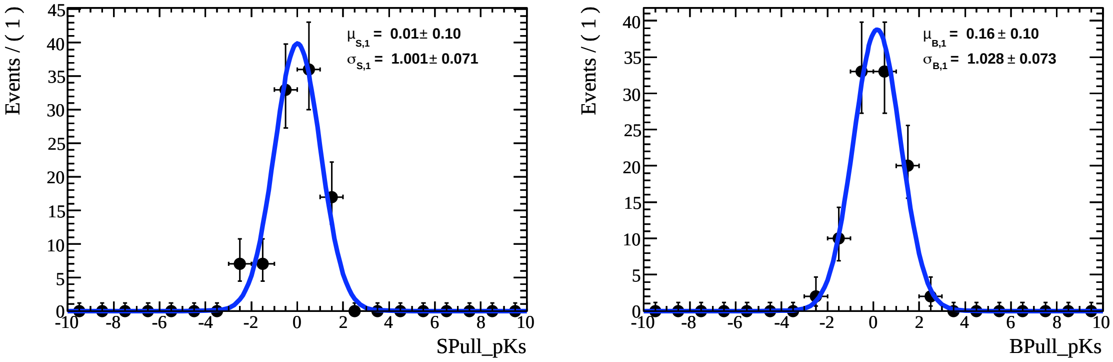

(b) $\Lambda_c^+ \to pK_S^0$

Figure 8.2: Pull distributions for N_{sig} and N_{bkg} from 100 simultaneous fits to signal MC + toy MC samples for $\overline{B}^0 \to \Lambda_c^+\overline{p}$. The number of signal events injected in each mode is summarized in Table 8.1. Only fit results with good error matrices are included. The standard deviations of the distributions are consistent with 1 and the means of the distributions are consistent with 0, indicating no bias.

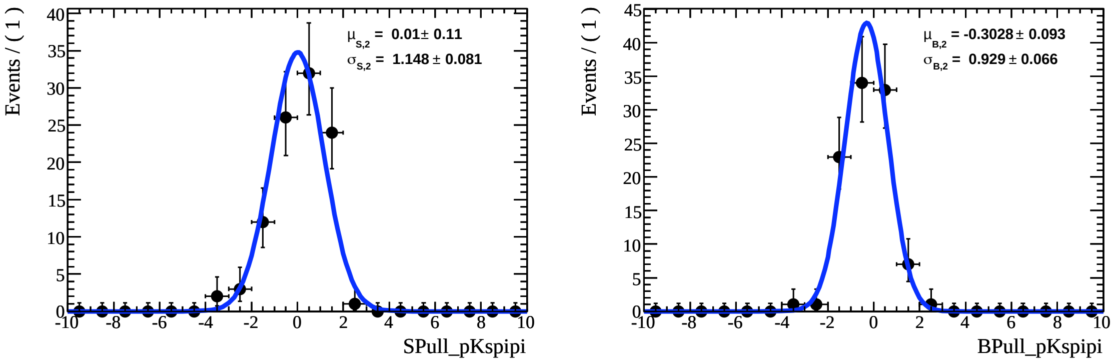

(c) $\Lambda_c^+ \to pK_S^0\pi^+\pi^-$

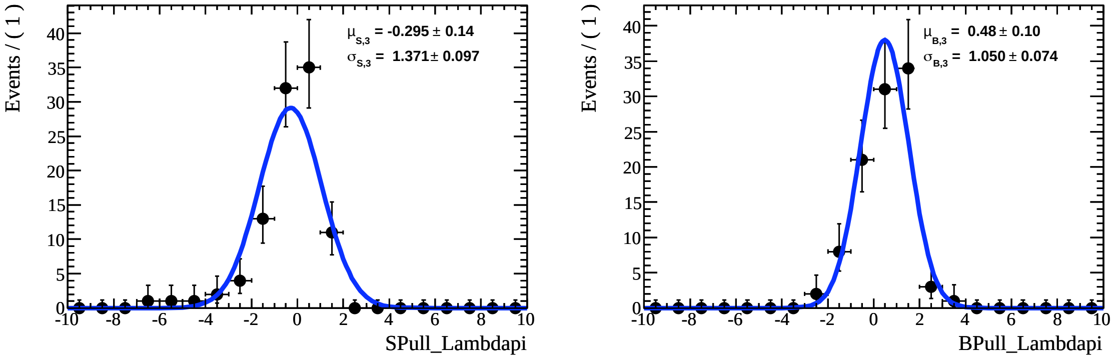

(d) $\Lambda_c^+ \to \Lambda\pi^+$

Figure 8.2: (cont.)

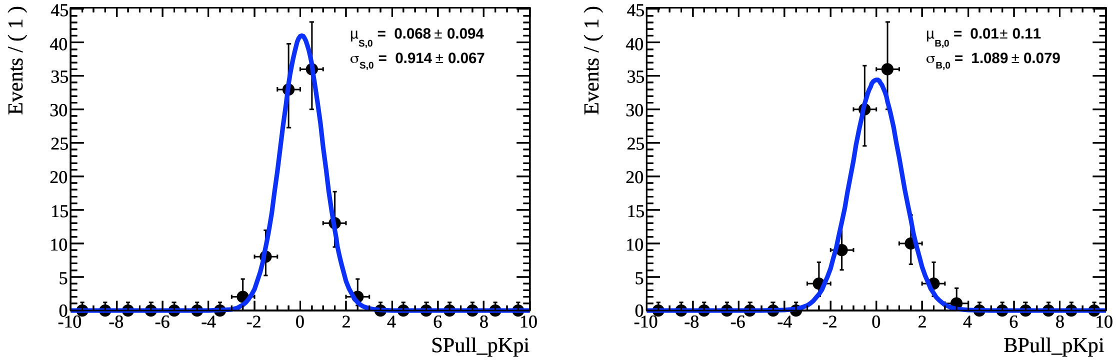

(a) $\Lambda_c^+ \to pK^-\pi^+$

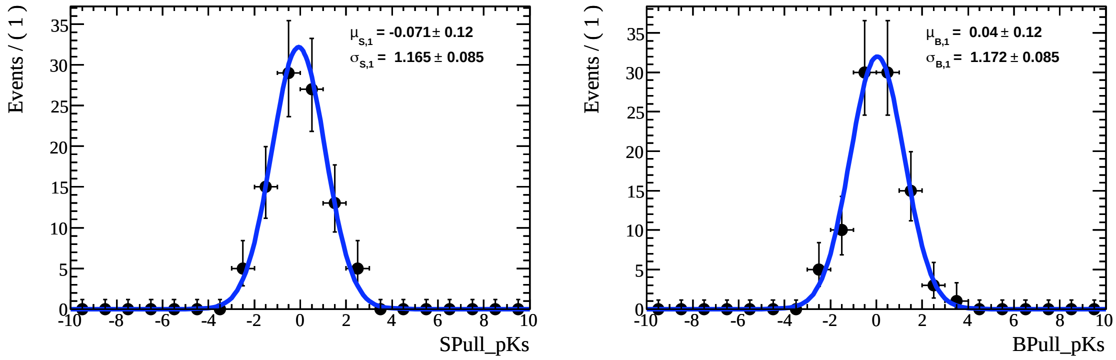

(b) $\Lambda_c^+ \to pK_S^0$

Figure 8.3: Pull distributions for N_{sig} and N_{bkg} from 100 simultaneous fits to signal MC + toy MC samples for $B^- \to \Lambda_c^+\overline{p}\pi^-$. The number of signal events injected in each mode is summarized in Table 8.1. Only fit results with good error matrices are included. The standard deviations of the distributions are consistent with 1 and the means of the distributions are consistent with 0, indicating no bias.

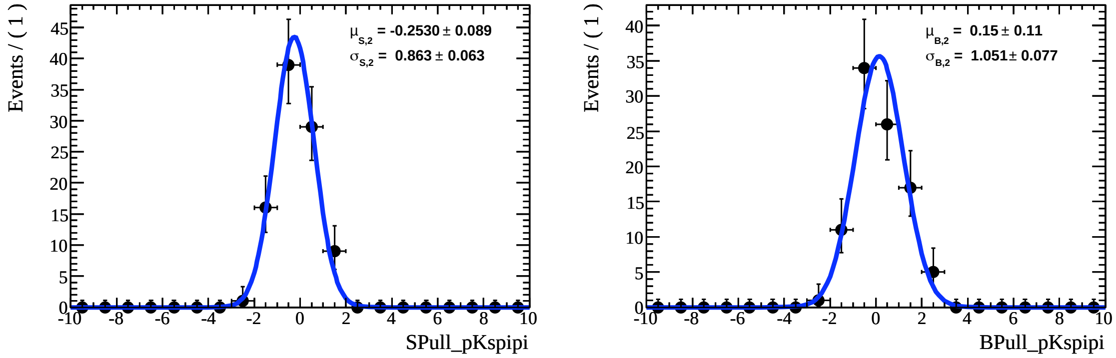

(c) $\Lambda_c^+ \to p K_S^0 \pi^+ \pi^-$

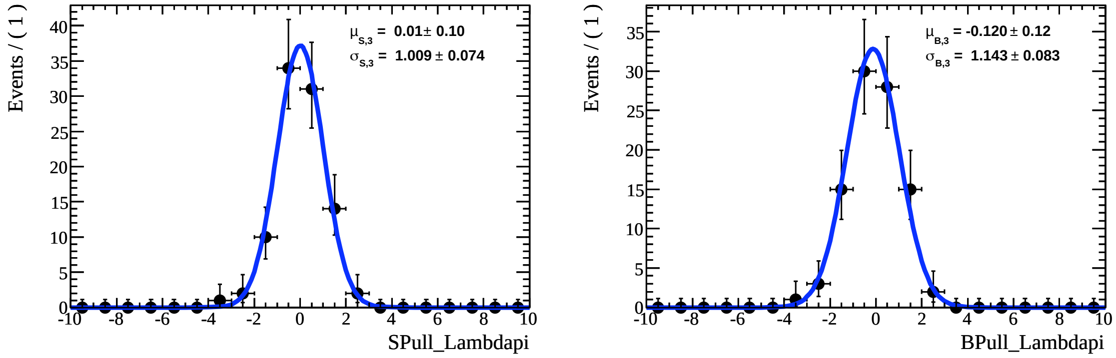

(d) $\Lambda_c^+ \to \Lambda \pi^+$

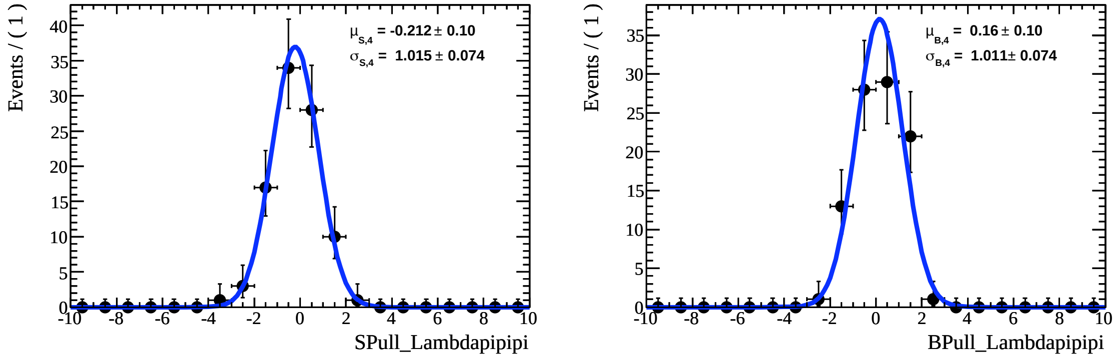

(e) $\Lambda_c^+ \to \Lambda \pi^+ \pi^- \pi^+$

Figure 8.3: (cont.)

Table 8.2: We summarize the expected (calculated) mean (μ_{exp}) and ideal uncertainty ($\sigma_{ideal} = \sqrt{\mu_{exp}}$, for reference) and the mean (μ) and RMS of the fit validation distributions for $N_{tot}^{prod} \times \mathcal{B}(\Lambda_c^+ \to pK^-\pi^+)$. The plots of these distributions are shown in Figure 8.4.

Mode	$N_{tot}^{prod} \times \mathcal{B}(\Lambda_c^+ \to pK^-\pi^+)$			
	μ_{exp}	σ_{ideal}	μ	RMS
$\overline{B}^0 \to \Lambda_c^+\overline{p}$	412	20	410 ± 5	46 ± 3
$B^- \to \Lambda_c^+\overline{p}\pi^-$	6771	82	6766 ± 19	181 ± 13

8.2.3 Total Yield Validation Results

The resulting yields are combined according to a weighted average[2]:

$$N_{tot}^{prod} \times \mathcal{B}(\Lambda_c^+ \to pK^-\pi^+) = \frac{\sum_i \frac{1}{\sigma_i^2} \frac{N_i}{\varepsilon_i \mathcal{R}_i}}{\sum_i \frac{1}{\sigma_i^2}}, \tag{8.7}$$

where N_{tot}^{prod} is the total number of $\overline{B}^0 \to \Lambda_c^+\overline{p}$ ($B^- \to \Lambda_c^+\overline{p}\pi^-$) events produced at BABAR, N_i is the number of fitted signal events in Λ_c^+ decay mode i, ε_i is the detection efficiency for mode i, $\mathcal{R}_i$ is the branching ratio of Λ_c^+ decay mode i compared to $\mathcal{B}(\Lambda_c^+ \to pK^-\pi^+)$ (see Table 5.2), and $\sigma_i = \sigma(N_i)/(\varepsilon_i \mathcal{R}_i)$ (statistical uncertainty only). We can use the simultaneous fit validation results to plot distributions for $N_{tot}^{prod} \times \mathcal{B}(\Lambda_c^+ \to pK^-\pi^+)$ for $\overline{B}^0 \to \Lambda_c^+\overline{p}$ and $B^- \to \Lambda_c^+\overline{p}\pi^-$, which are shown in Figure 8.4. Using the efficiencies calculated previously and the expected N_{sig} values summarized in Table 8.1, we can calculate the expected mean $N_{tot}^{prod} \times \mathcal{B}(\Lambda_c^+ \to pK^-\pi^+)$ for $\overline{B}^0 \to \Lambda_c^+\overline{p}$ and $B^- \to \Lambda_c^+\overline{p}\pi^-$ using $\mathcal{B}(\overline{B}^0 \to \Lambda_c^+\overline{p}) = 2.1 \times 10^{-5}$ and $\mathcal{B}(B^- \to \Lambda_c^+\overline{p}\pi^-) = 3.54 \times 10^{-4}$. For the purposes of this study we assume that the efficiencies and relative branching fractions are perfectly well-known. Table 8.2 summarizes the expected mean, actual mean, and actual RMS of $N_{tot}^{prod} \times \mathcal{B}(\Lambda_c^+ \to pK^-\pi^+)$ for each B decay mode.

---

[2] Of the various ways to combine separate yields, this method resulted in the lowest RMS of the $N_{tot}^{prod} \times \mathcal{B}(\Lambda_c^+ \to pK^-\pi^+)$ distribution. We use the BLUE method to compute the combined branching fractions (see Chapter 11).

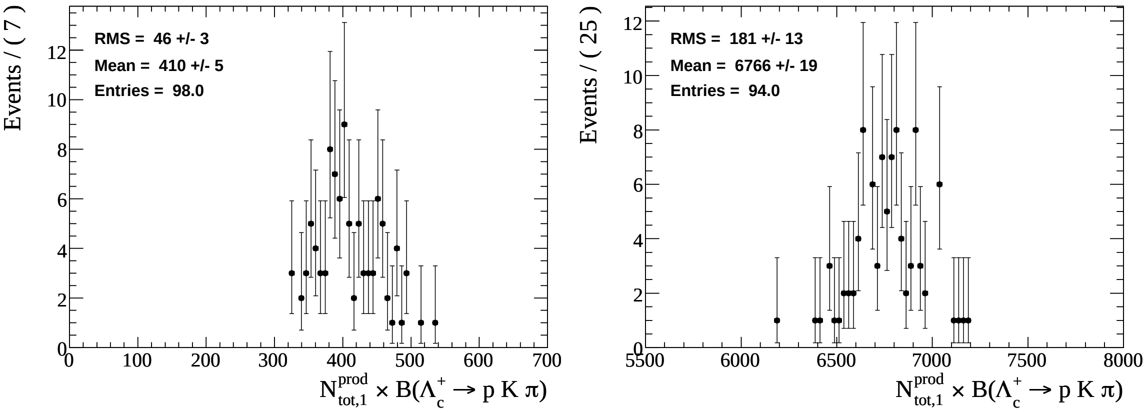

(a) $\overline{B}^0 \to \Lambda_c^+ \overline{p}$

(b) $B^- \to \Lambda_c^+ \overline{p} \pi^-$

Figure 8.4: Distributions of $N_{tot}^{prod} \times \mathcal{B}(\Lambda_c^+ \to pK^-\pi^+)$ from 100 simultaneous fits across Λ_c^+ decay modes for $\overline{B}^0 \to \Lambda_c^+ \overline{p}$ (a) and $B^- \to \Lambda_c^+ \overline{p} \pi^-$ (b). The means of the distributions are consistent with expectations.

Chapter 9

Results of the Fit to Data

The signal region in $(m_{\text{miss}} + m_B)/2$ and $(m_{\text{rec}} - m_B)$ is unblinded and a simultaneous fit to the data in the fit region is performed. For the mode $\overline{B}^0 \to \Lambda_c^+ \overline{p}$, the following four Λ_c^+ decay modes are fit (simultaneously, as described in Chapter 8.1):

- $\Lambda_c^+ \to pK^-\pi^+$
- $\Lambda_c^+ \to pK_S^0$
- $\Lambda_c^+ \to pK_S^0\pi^+\pi^-$
- $\Lambda_c^+ \to \Lambda\pi^+$.

Similarly, for $B^- \to \Lambda_c^+ \overline{p}\pi^-$, we include five Λ_c^+ decay modes in the simultaneous fit:

- $\Lambda_c^+ \to pK^-\pi^+$
- $\Lambda_c^+ \to pK_S^0$
- $\Lambda_c^+ \to pK_S^0\pi^+\pi^-$
- $\Lambda_c^+ \to \Lambda\pi^+$
- $\Lambda_c^+ \to \Lambda\pi^+\pi^-\pi^+$.

The fit results are described in this section. These results are used to calculate ${}_s\mathcal{P}lot$ weights for each data point (as described in Chapter 10). The sum of the ${}_s\mathcal{P}lot$ weights, including an efficiency correction and a peaking background correction for $B^- \to \Lambda_c^+ \overline{p}\pi^-$, will be used to determine the branching fractions $\mathcal{B}(\overline{B}^0 \to \Lambda_c^+ \overline{p})$ and $\mathcal{B}(B^- \to \Lambda_c^+ \overline{p}\pi^-)$.

9.1 $\overline{B}^0 \longrightarrow \Lambda_c^+ \overline{p}$ 2-D Simultaneous Fit Results

The result of the 2-D fit is shown in projections of $(m_{\rm miss} + m_B)/2$ and $(m_{\rm rec} - m_B)$ for each Λ_c^+ decay mode in Figure 9.1. In the projection of $(m_{\rm miss} + m_B)/2$, $|(m_{\rm rec} - m_B)| < 0.030\,{\rm GeV}/c^2$ and in the projection of $(m_{\rm rec} - m_B)$, $(m_{\rm miss} + m_B)/2 > 5.27\,{\rm GeV}/c^2$. The final parameter values, including the signal yields, are summarized in Table 9.1.

Table 9.1: Fit results for $\overline{B}^0 \to \Lambda_c^+ \overline{p}$.

Variable	Fit Parameter	Value
$(m_{\rm miss} + m_B)/2$	μ (GeV/c^2)	5.2791 ± 0.0003
	σ (GeV/c^2)	0.0026 ± 0.0003
	c_{ARG}	−23 ± 3
	m^0_{ARG} (GeV/c^2)	5.2890
$(m_{\rm rec} - m_B)$	μ (GeV/c^2)	−0.002 ± 0.002
	σ (GeV/c^2)	0.013 ± 0.001
	$a_{pK^-\pi^+}$ (1/ GeV/c^2)	−1.3 ± 0.5
	$a_{pK^0_S}$ (1/ GeV/c^2)	−2 ± 1
	$a_{pK^0_S\pi^+\pi^-}$ (1/ GeV/c^2)	−2 ± 1
	$a_{\Lambda\pi^+}$ (1/ GeV/c^2)	−3 ± 1
	N_{bkg} $(pK^-\pi^+)$	1130 ± 34
	N_{bkg} (pK^0_S)	276 ± 17
	N_{bkg} $(pK^0_S\pi^+\pi^-)$	304 ± 18
	N_{bkg} $(\Lambda\pi^+)$	230 ± 15
	N_{sig} $(pK^-\pi^+)$	90 ± 11
	N_{sig} (pK^0_S)	10 ± 4
	N_{sig} $(pK^0_S\pi^+\pi^-)$	14 ± 5
	N_{sig} $(\Lambda\pi^+)$	3 ± 3

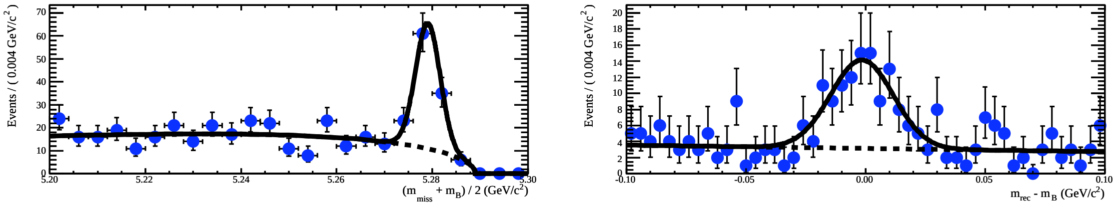

(a) $\Lambda_c^+ \to pK^-\pi^+$, $(m_{\rm miss} + m_B)/2$ (b) $\Lambda_c^+ \to pK^-\pi^+$, $(m_{\rm rec} - m_B)$

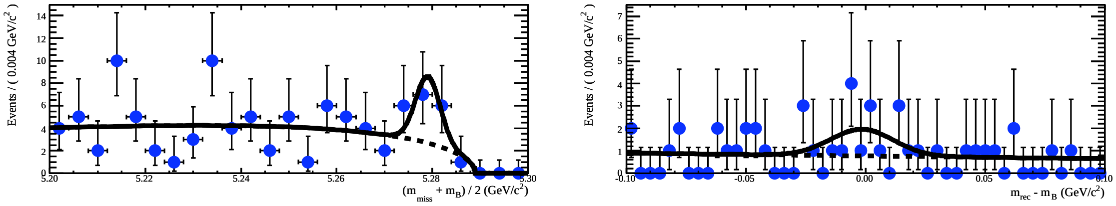

(c) $\Lambda_c^+ \to pK_S^0$, $(m_{\rm miss} + m_B)/2$ (d) $\Lambda_c^+ \to pK_S^0$, $(m_{\rm rec} - m_B)$

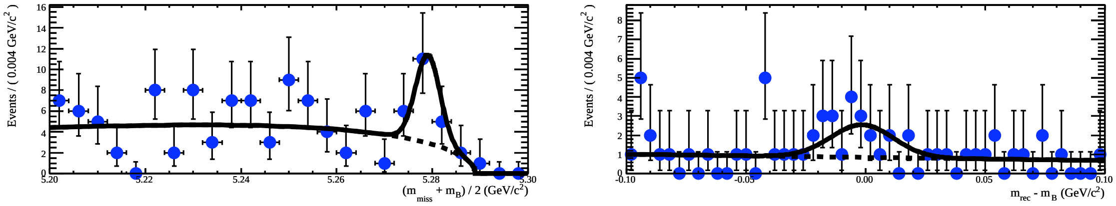

(e) $\Lambda_c^+ \to pK_S^0\pi^+\pi^-$, $(m_{\rm miss} + m_B)/2$ (f) $\Lambda_c^+ \to pK_S^0\pi^+\pi^-$, $(m_{\rm rec} - m_B)$

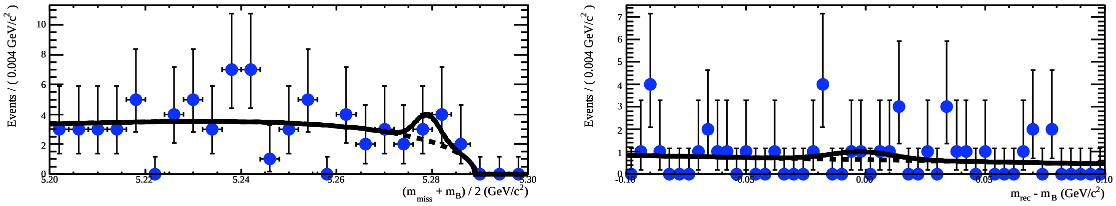

(g) $\Lambda_c^+ \to \Lambda\pi^+$, $(m_{\rm miss} + m_B)/2$ (h) $\Lambda_c^+ \to \Lambda\pi^+$, $(m_{\rm rec} - m_B)$

Figure 9.1: Projections of $(m_{\rm miss} + m_B)/2$ (left) and $(m_{\rm rec} - m_B)$ (right) in data for $\overline{B}^0$ candidates, separated by Λ_c^+ decay mode. The $(m_{\rm miss} + m_B)/2$ projection is for $|(m_{\rm rec} - m_B)| < 0.030\,{\rm GeV}/c^2$ and the $(m_{\rm rec} - m_B)$ projection is for $(m_{\rm miss} + m_B)/2 > 5.27\,{\rm GeV}/c^2$. Superimposed is the resulting PDF from the simultaneous 2-D fit.

9.2 $B^- \rightarrow \Lambda_c^+ \overline{p} \pi^-$ 2-D Simultaneous Fit Results

The result of the 2-D fit is shown in projections of $(m_{\text{miss}} + m_B)/2$ and $(m_{\text{rec}} - m_B)$ for each Λ_c^+ decay mode in Figure 9.2. In the projection of $(m_{\text{miss}} + m_B)/2$, $|(m_{\text{rec}} - m_B)| < 0.030\,\text{GeV}/c^2$ and in the projection of $(m_{\text{rec}} - m_B)$, $(m_{\text{miss}} + m_B)/2 > 5.27\,\text{GeV}/c^2$. The final parameter values, including the signal yields, are summarized in Table 9.2.

Table 9.2: Fit results for $B^- \rightarrow \Lambda_c^+ \overline{p} \pi^-$.

Variable	Fit Parameter	Value
$(m_{\text{miss}} + m_B)/2$	μ (GeV/c^2)	5.27873 ± 0.00009
	σ (GeV/c^2)	0.00251 ± 0.00009
	c_{ARG}	-25.1 ± 0.8
	m^0_{ARG} (GeV/c^2)	5.2890
$(m_{\text{rec}} - m_B)$	μ (GeV/c^2)	-0.0015 ± 0.0004
	σ_1 (GeV/c^2)	0.0101 ± 0.0005
	σ_2 (GeV/c^2)	0.030 ± 0.007
	f	0.82 ± 0.06
	$a_{pK^-\pi^+}$ (1/ GeV/c^2)	-1.2 ± 0.1
	$a_{pK^0_S}$ (1/ GeV/c^2)	-0.7 ± 0.4
	$a_{pK^0_S\pi^+\pi^-}$ (1/ GeV/c^2)	-2.2 ± 0.3
	$a_{\Lambda\pi^+}$ (1/ GeV/c^2)	-0.8 ± 0.4
	$a_{\Lambda\pi^+\pi^-\pi^+}$ (1/ GeV/c^2)	-2.6 ± 0.3
	N_{bkg} $(pK^-\pi^+)$	13689 ± 121
	N_{bkg} (pK^0_S)	1665 ± 42
	N_{bkg} $(pK^0_S\pi^+\pi^-)$	3584 ± 61
	N_{bkg} $(\Lambda\pi^+)$	1541 ± 40
	N_{bkg} $(\Lambda\pi^+\pi^-\pi^+)$	3005 ± 56
	N_{sig} $(pK^-\pi^+)$	991 ± 45
	N_{sig} (pK^0_S)	165 ± 15
	N_{sig} $(pK^0_S\pi^+\pi^-)$	86 ± 14
	N_{sig} $(\Lambda\pi^+)$	114 ± 13
	N_{sig} $(\Lambda\pi^+\pi^-\pi^+)$	88 ± 13

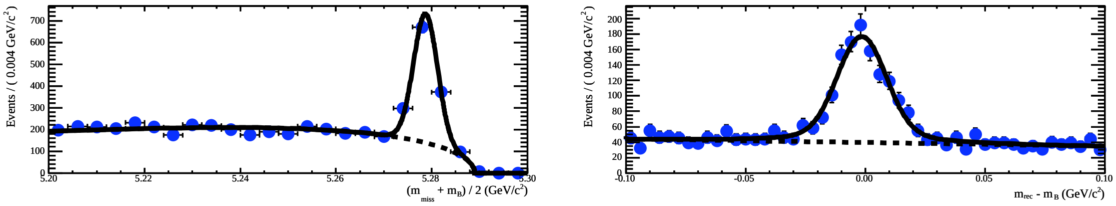

(a) $\Lambda_c^+ \to pK^-\pi^+$, $(m_{\rm miss} + m_B)/2$ (b) $\Lambda_c^+ \to pK^-\pi^+$, $(m_{\rm rec} - m_B)$

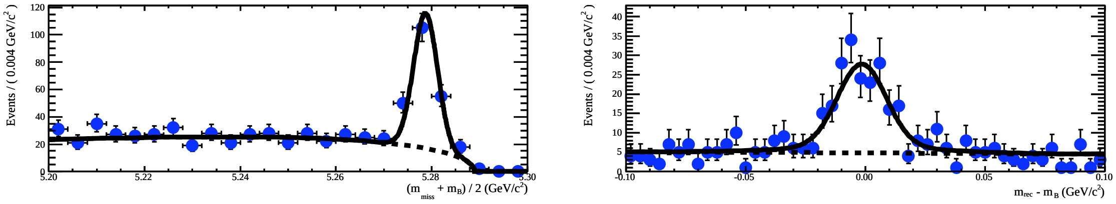

(c) $\Lambda_c^+ \to pK_S^0$, $(m_{\rm miss} + m_B)/2$ (d) $\Lambda_c^+ \to pK_S^0$, $(m_{\rm rec} - m_B)$

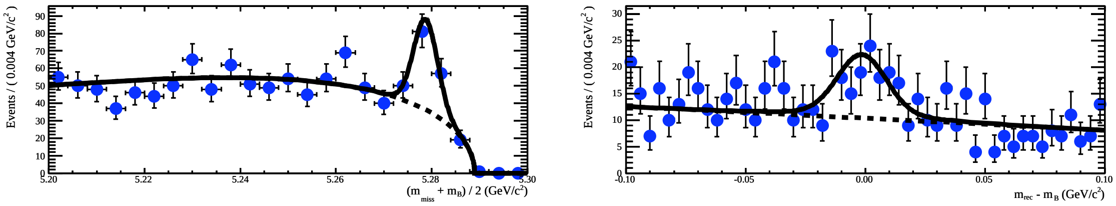

(e) $\Lambda_c^+ \to pK_S^0\pi^+\pi^-$, $(m_{\rm miss} + m_B)/2$ (f) $\Lambda_c^+ \to pK_S^0\pi^+\pi^-$, $(m_{\rm rec} - m_B)$

Figure 9.2: Projections of $(m_{\rm miss} + m_B)/2$ (left) and $(m_{\rm rec} - m_B)$ (right) in data for B^- candidates, separated by Λ_c^+ decay mode. The $(m_{\rm miss} + m_B)/2$ projection is for $|(m_{\rm rec} - m_B)| < 0.030\,{\rm GeV}/c^2$ and the $(m_{\rm rec} - m_B)$ projection is for $(m_{\rm miss} + m_B)/2 > 5.27\,{\rm GeV}/c^2$. Superimposed is the resulting PDF from the simultaneous 2-D fit.

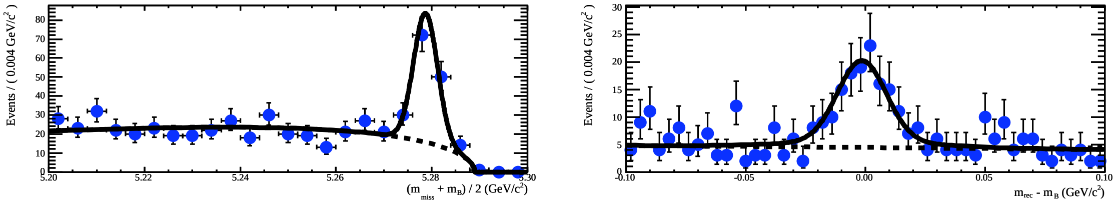

(g) $\Lambda_c^+ \rightarrow \Lambda\pi^+$, $(m_{\rm miss} + m_B)/2$ (h) $\Lambda_c^+ \rightarrow \Lambda\pi^+$, $(m_{\rm rec} - m_B)$

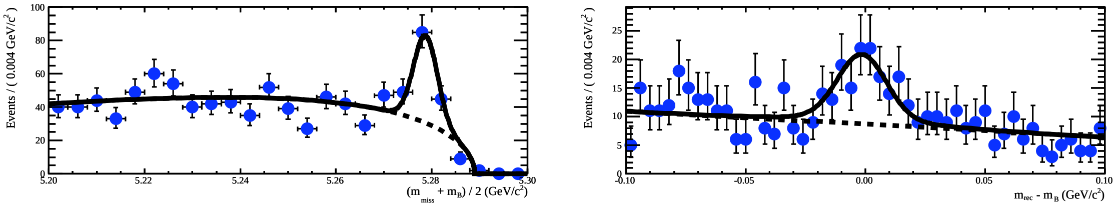

(i) $\Lambda_c^+ \rightarrow \Lambda\pi^+\pi^-\pi^+$, $(m_{\rm miss} + m_B)/2$ (j) $\Lambda_c^+ \rightarrow \Lambda\pi^+\pi^-\pi^+$, $(m_{\rm rec} - m_B)$

Figure 9.2: (cont.)

Chapter 10

$B^- \to \Lambda_c^+ \overline{p} \pi^-$ ${}_s\mathcal{P}lot$ and Efficiency Weights

Building on the the fit results of Chapter 9, we calculate an ${}_s\mathcal{P}lot$ weight and an efficiency weight for each data event. We then use these weights to project the signal and background distributions for the study of $B^- \to \Lambda_c^+ \overline{p} \pi^-$ resonant substructure.

10.1 ${}_s\mathcal{P}lot$ Weight Determination

The ${}_s\mathcal{P}lot$ method is described in detail in Ref. [51]. We have $N_s = 2$ species (signal and background) for each Λ_c^+ decay mode. We define f_j as the signal ($j = 1$) or background ($j = 2$) PDF. We calculate the ${}_s\mathcal{P}lot$ weights for event e based on the 2-D fit to the variable(s) y (in this case $(m_{\text{miss}} + m_B)/2$ and $(m_{\text{rec}} - m_B)$) according to the following equation:

$$
{}_s\mathcal{P}_n(y_e) = \frac{\sum_{j=1}^{N_s} \mathbf{V}_{nj} f_j(y_e)}{\sum_{k=1}^{N_s} N_k f_k(y_e)}, \tag{10.1}
$$

where ${}_s\mathcal{P}_n(y_e)$ is the ${}_s\mathcal{P}lot$ weight for species n, $\mathbf{V}$ is the covariance matrix for signal and background yields, and $f_j(y_e)$ is the value of PDF f_j for event e (y_e is the $(m_{\text{miss}} + m_B)/2$ and $(m_{\text{rec}} - m_B)$ value for event e). The elements of the inverse of the covariance matrix $\mathbf{V}$ are calculated directly as follows:

$$
\mathbf{V}_{nj}^{-1} = \frac{\partial^2(-\mathcal{L})}{\partial N_n \partial N_j} = \sum_{e=1}^{N} \frac{f_n(y_e) f_j(y_e)}{\left(\sum_{k=1}^{N_s} N_k f_k(y_e)\right)^2}. \tag{10.2}
$$

Note that in the calculation of the covariance matrix, the data is refit to the same simultaneous PDF described in Section 8.1, except that all fit parameters other than the yields are fixed to the values in Table 9.2. We check the likelihood normalization and that the covariance matrix is invertible and normalized properly, and that the sum of the $_s\mathcal{P}lot$ weights for each species is equal to the yield from the fit.

The result of this method is that each event is assigned a signal and a background $_s\mathcal{P}lot$ weight. The distributions are shown in Figure 10.1.

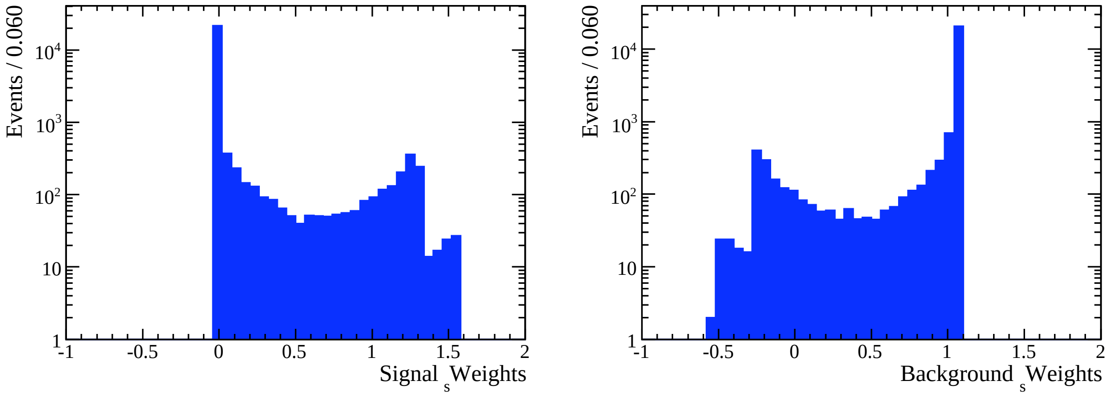

Figure 10.1: Distributions of signal (left) and background (right) $_s\mathcal{P}lot$ weights for all events in the fit region. Note the logarithmic scale on the ordinate axis.

We can use these $_s\mathcal{P}lot$ weights to plot any quantity that is not correlated with $(m_{\text{miss}} + m_B)/2$ or $(m_{\text{rec}} - m_B)$. In this analysis, the quantities of interest that satisfy this requirement are the invariant masses $m(d_i d_j)$, where d_i is any of the B daughters Λ_c^+, $\overline{p}$, π^-, and the helicity angle distributions. The invariant mass distributions $m(d_i d_j)$ are shown in Figure 10.2 for signal and background (combined Λ_c^+ decay modes). We show the $m_{\Lambda_c \pi}$ region of the $\Sigma_c(2455)^0$ and $\Sigma_c(2520)^0$ (Figure 10.4), and the $\Sigma_c(2800)^0$ (Figure 10.6). We also show the $_s\mathcal{P}lot$ weights for the Dalitz plot of $m^2_{p\pi}$ vs. $m^2_{\Lambda_c \pi}$ in Figure 10.8. Note that the negative bins are suppressed in the 2-D Dalitz plot.

A limitation of this method is that the uncertainties on bins with zero signal events are underestimated.

10.2 Efficiency Weights

Each candidate is assigned a weight of $1/\varepsilon$, where the efficiency ε is determined by its location in the $\cos\theta_h(\Lambda_c\pi)$ vs. $m_{\Lambda_c\pi}$ plane. The full binned efficiency determination is described in Section 6.4. This efficiency weight can be combined with the $_s\mathcal{P}lot$ weight for each event e: $_s\mathcal{P}_n(y_e)/\varepsilon_e$. We show the resulting effect on the $m(d_id_j)$ distributions in Figures 10.3, 10.5, and 10.7, as well as the Dalitz plot of $m^2_{p\pi}$ vs. $m^2_{\Lambda_c\pi}$ in Figure 10.9. Note that the negative bins are suppressed in the 2-D Dalitz plot.

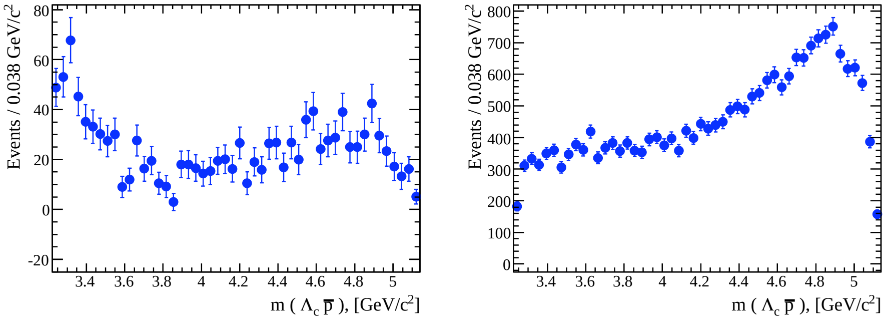

(a) $m_{\Lambda_c p}$ ($m_{\Lambda_c \pi} > 2.5\,\mathrm{GeV}/c^2$)

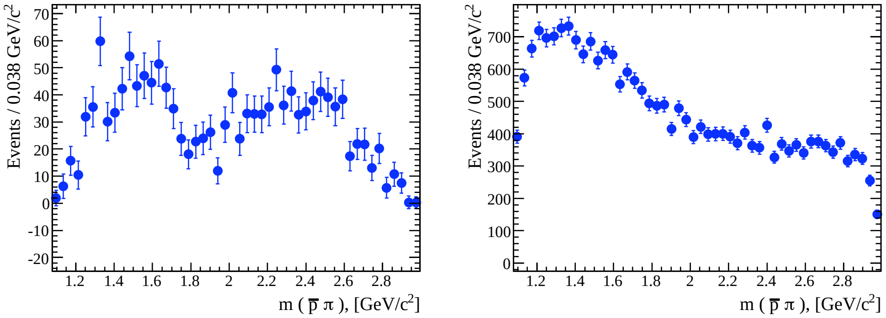

(b) $m_{p\pi}$

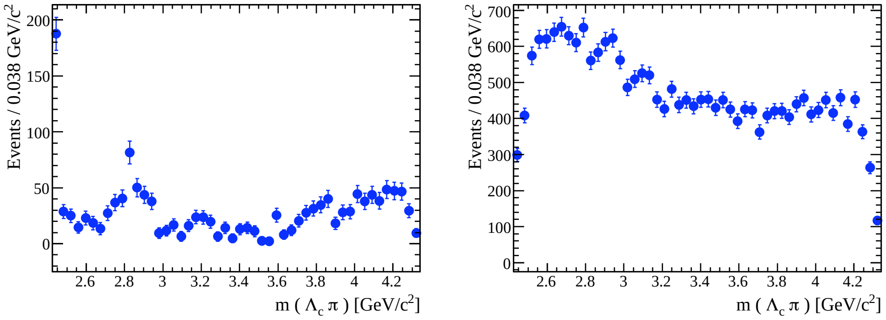

(c) $m_{\Lambda_c \pi}$

Figure 10.2: Projections of $m(d_i d_j)$, where d_i is Λ_c^+, $\overline{p}$, π^-. Each event is given a signal (left) or background (right) ${}_s\mathcal{P}lot$ weight. The $\Lambda_c^+ \overline{p}$ threshold enhancement is visible in (a), and the $\Sigma_c(2455)^0$ and $\Sigma_c(2800)^0$ are visible in (c). Note that the $\Sigma_c(2455)^0$ region is removed in (a).

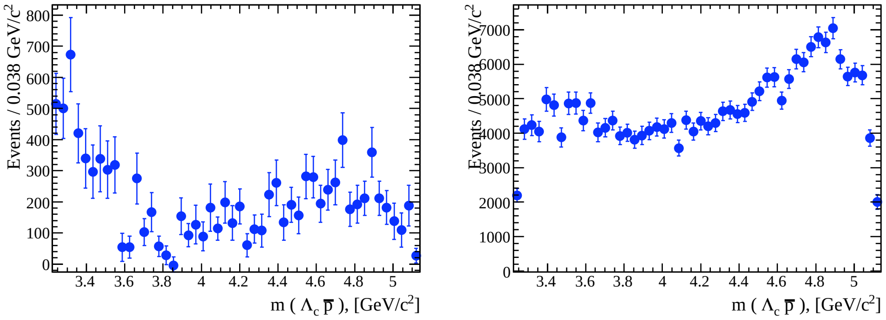

(a) $m_{\Lambda_c p}$ ($m_{\Lambda_c \pi} > 2.5\,\mathrm{GeV}/c^2$)

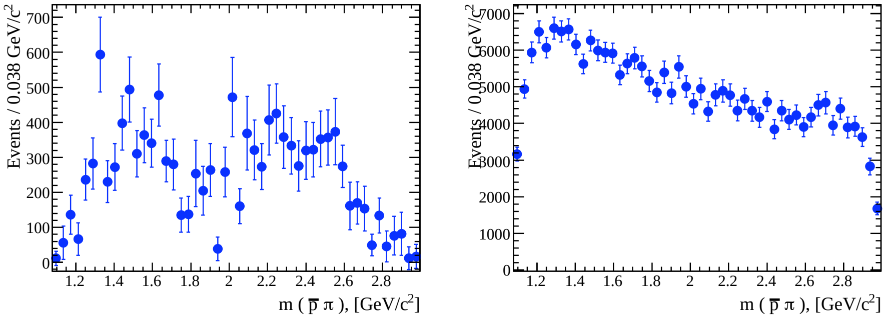

(b) $m_{p\pi}$

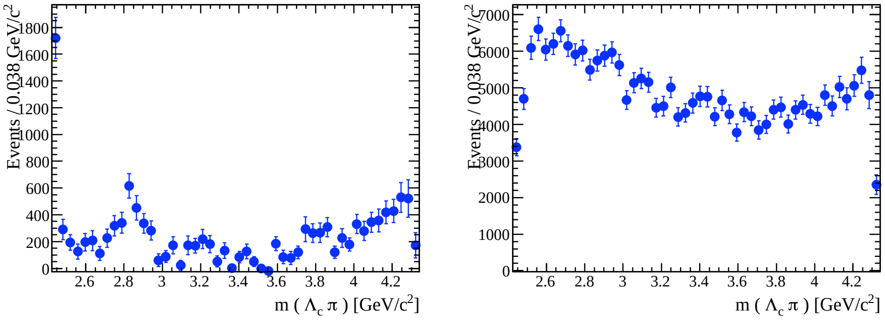

(c) $m_{\Lambda_c \pi}$

Figure 10.3: Projections of $m(d_i d_j)$, where d_i is Λ_c^+, $\overline{p}$, π^-. Each event is **efficiency-corrected** and given a signal (left) or background (right) ${}_s\mathcal{P}lot$ weight. The $\Lambda_c^+\overline{p}$ threshold enhancement is visible in (a), and the $\Sigma_c(2455)^0$ and $\Sigma_c(2800)^0$ are visible in (c). Note that the $\Sigma_c(2455)^0$ region is removed in (a).

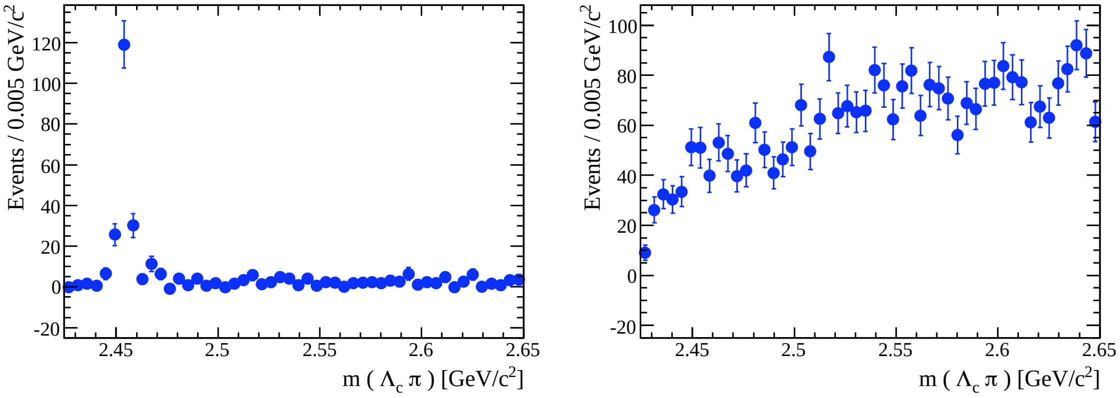

Figure 10.4: Projections of $m_{\Lambda_c\pi}$ in the region of the $\Sigma_c(2455)^0$ and $\Sigma_c(2520)^0$. There is no evidence for the $\Sigma_c(2520)^0$. Each event is given a signal (left) or background (right) $_s\mathcal{P}lot$ weight.

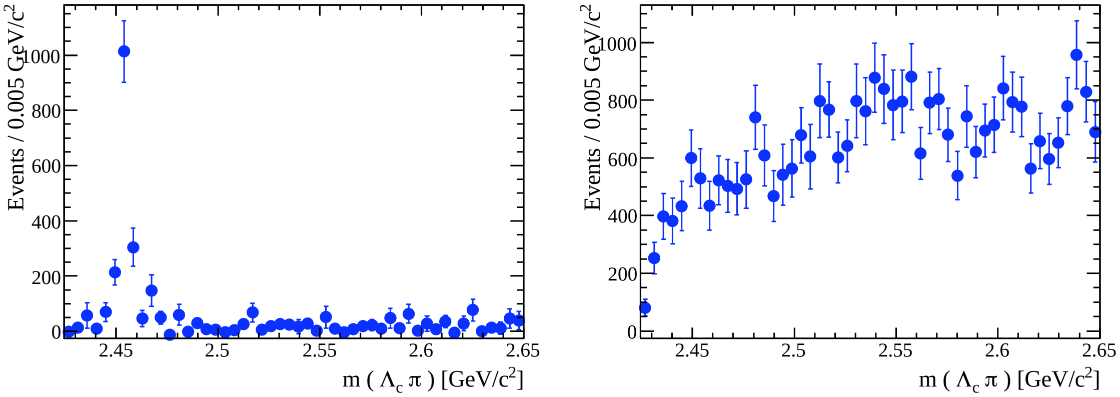

Figure 10.5: Projections of $m_{\Lambda_c\pi}$ in the region of the $\Sigma_c(2455)^0$ and $\Sigma_c(2520)^0$. There is no evidence for the $\Sigma_c(2520)^0$. Each event is **efficiency-corrected** and given a signal (left) or background (right) $_s\mathcal{P}lot$ weight.

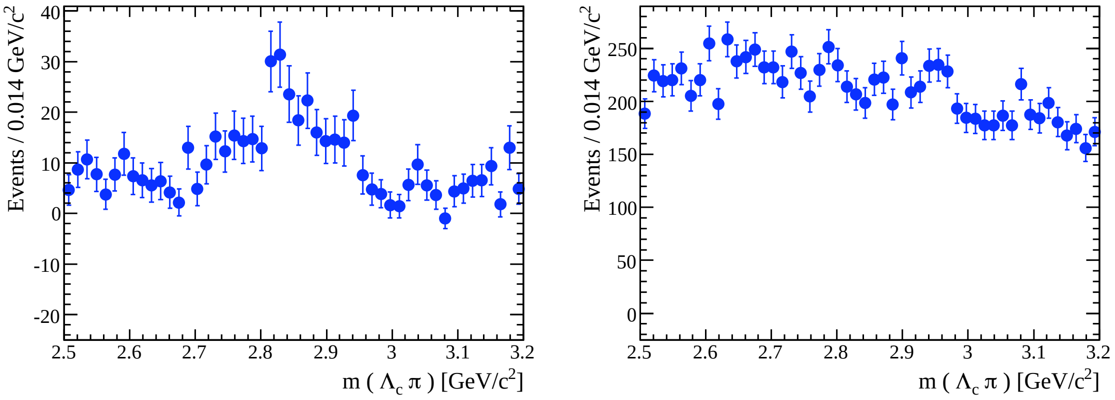

Figure 10.6: Projections of $m_{\Lambda_c\pi}$ in the region of the $\Sigma_c(2800)^0$. Each event is given a signal (left) or background (right) $_s\mathcal{P}lot$ weight.

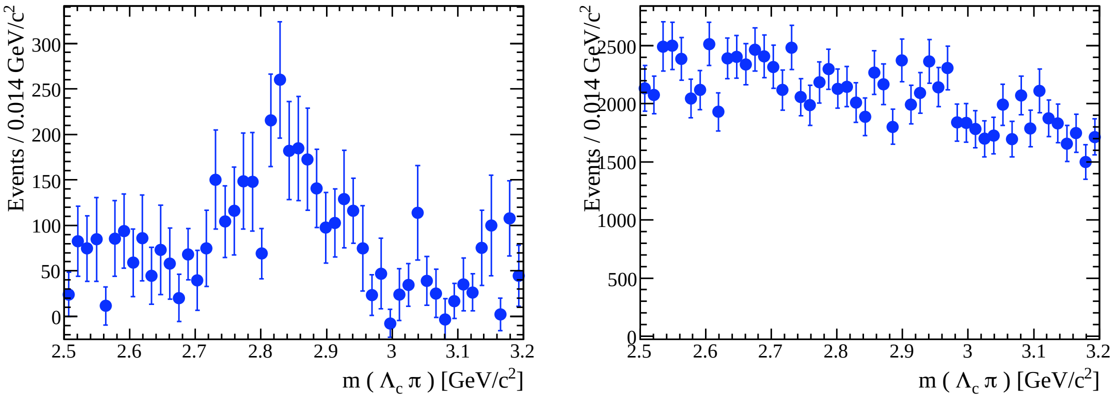

Figure 10.7: Projections of $m_{\Lambda_c\pi}$ in the region of the $\Sigma_c(2800)^0$. Each event is **efficiency-corrected** and given a signal (left) or background (right) $_s\mathcal{P}lot$ weight.

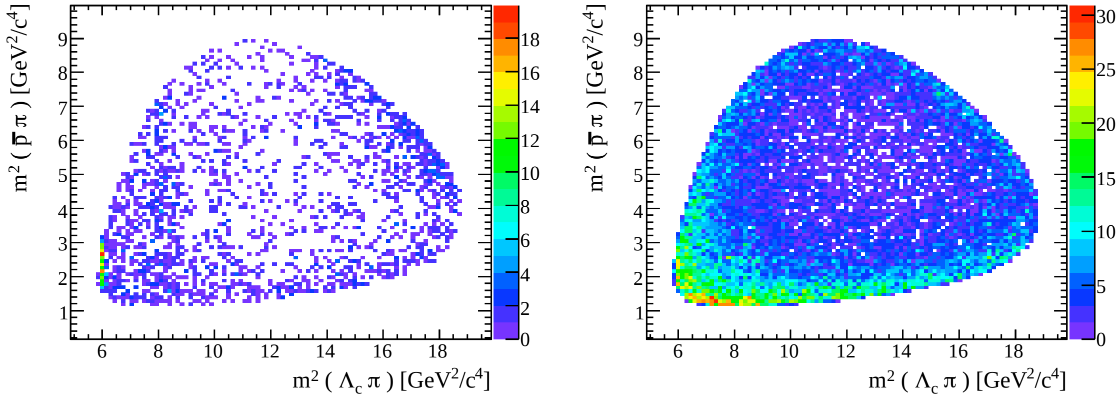

Figure 10.8: Dalitz plot of $m^2_{p\pi}$ vs. $m^2_{\Lambda_c\pi}$. Each event is given a signal (left) or background (right) ${}_s\mathcal{P}lot$ weight. Note that the vertical scales on the left- and right-hand plots are different, and negative bins are suppressed.

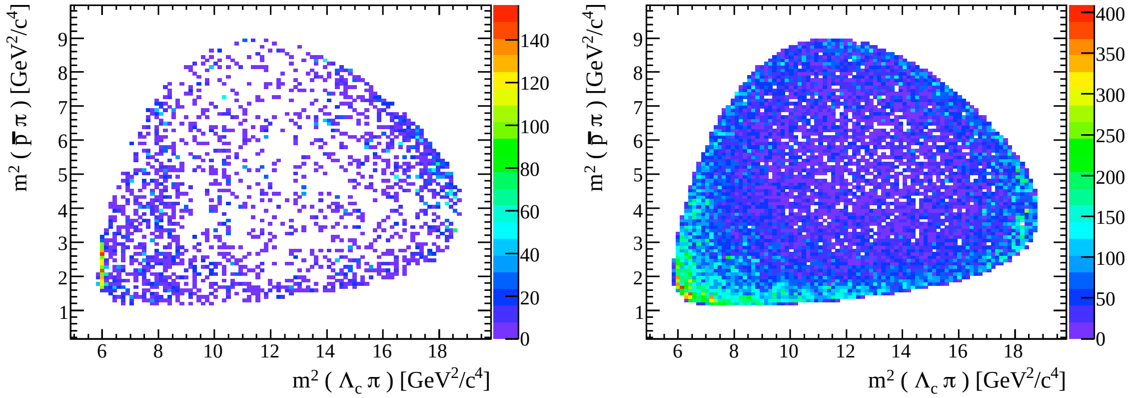

Figure 10.9: Dalitz plot of $m^2_{p\pi}$ vs. $m^2_{\Lambda_c\pi}$. Each event is **efficiency-corrected** and given a signal (left) or background (right) ${}_s\mathcal{P}lot$ weight. Note that the vertical scales on the left- and right-hand plots are different, and negative bins are suppressed.

Chapter 11

Branching Fraction Measurements

In this Chapter, we use the fit results presented in Chapter 9 and the ${}_s\mathcal{P}lot$ weighting technique described in Chapter 10 to calculate the branching fractions $\mathcal{B}(\overline{B}^0 \to \Lambda_c^+\overline{p})$ and $\mathcal{B}(B^- \to \Lambda_c^+\overline{p}\pi^-)$. We quote separate branching fractions for each Λ_c^+ decay mode, and then quote a combined result. We also report a measurement of the branching ratio $\mathcal{B}(\overline{B}^0 \to \Lambda_c^+\overline{p})/\mathcal{B}(B^- \to \Lambda_c^+\overline{p}\pi^-)$. The sources of the systematic uncertainties reported in this Chapter are described in detail in Chapter 12.

11.1 Measurement of $\mathcal{B}(\overline{B}^0 \to \Lambda_c^+\overline{p})$

The fit yields and efficiencies for $\overline{B}^0 \to \Lambda_c^+\overline{p}$ can be taken as-is to compute the branching fraction of this mode. We calculate $\mathcal{B}(\overline{B}^0 \to \Lambda_c^+\overline{p})$ separately for each Λ_c^+ decay mode. For $\Lambda_c^+ \to pK^-\pi^+$, we calculate

$$\begin{aligned}\mathcal{B}(\overline{B}^0 \to \Lambda_c^+\overline{p})_{pK^-\pi^+} &= \frac{N_{sig}(pK^-\pi^+)}{N_{B\overline{B}} \ \times \ \varepsilon(pK^-\pi^+) \ \times \ \mathcal{B}(\Lambda_c^+ \to pK^-\pi^+)} \\ &= \frac{90 \pm 11}{(382.9 \pm 0.1) \times 10^6 \ \times \ 0.229 \ \times \ (5.0 \pm 1.3)\%} \\ &= (2.05 \pm 0.25 \pm 0.05 \pm 0.53) \times 10^{-5},\end{aligned} \tag{11.1}$$

where the uncertainties are statistical, systematic, and from $\mathcal{B}(\Lambda_c^+ \to pK^-\pi^+)$, respectively. The evaluation of the systematic uncertainties are described in Chapter 12. For the other Λ_c^+ decay modes, we define $\mathcal{R}$ as the ratio of each Λ_c^+ branching fraction to $\mathcal{B}(\Lambda_c^+ \to pK^-\pi^+)$

and include the K^0_S or Λ tracking correction to the efficiency:

$$\begin{aligned}\mathcal{B}(\overline{B}^0 \to \Lambda_c^+ \overline{p})_{pK^0_S} &= \frac{N_{sig}(pK^0_S)}{N_{B\overline{B}} \times \varepsilon(pK^0_S) \times \mathcal{R}(pK^0_S) \times \mathcal{B}(\Lambda_c^+ \to pK^-\pi^+)} \\ &= \frac{10 \pm 4}{(382.9 \pm 0.1) \times 10^6 \times 0.216 \times 0.162 \times (5.0 \pm 1.3)\%} \\ &= (1.49 \pm 0.60 \pm 0.17 \pm 0.39) \times 10^{-5}\end{aligned} \tag{11.2}$$

$$\begin{aligned}\mathcal{B}(\overline{B}^0 \to \Lambda_c^+ \overline{p})_{pK^0_S\pi^+\pi^-} &= \frac{N_{sig}(pK^0_S\pi^+\pi^-)}{N_{B\overline{B}} \times \varepsilon(pK^0_S\pi^+\pi^-) \times \mathcal{R}(pK^0_S\pi^+\pi^-) \times \mathcal{B}(\Lambda_c^+ \to pK^-\pi^+)} \\ &= \frac{14 \pm 5}{(382.9 \pm 0.1) \times 10^6 \times 0.096 \times 0.176 \times (5.0 \pm 1.3)\%} \\ &= (4.3 \pm 1.5 \pm 0.6 \pm 1.1) \times 10^{-5}\end{aligned} \tag{11.3}$$

$$\begin{aligned}\mathcal{B}(\overline{B}^0 \to \Lambda_c^+ \overline{p})_{\Lambda\pi^+} &= \frac{N_{sig}(\Lambda\pi^+)}{N_{B\overline{B}} \times \varepsilon(\Lambda\pi^+) \times \mathcal{R}(\Lambda\pi^+) \times \mathcal{B}(\Lambda_c^+ \to pK^-\pi^+)} \\ &= \frac{3 \pm 3}{(382.9 \pm 0.1) \times 10^6 \times 0.172 \times 0.129 \times (5.0 \pm 1.3)\%} \\ &= (0.71 \pm 0.71 \pm 0.18 \pm 0.18) \times 10^{-5}\end{aligned} \tag{11.4}$$

These results are combined using the BLUE method [52] as described in Section 11.3.

11.2 Measurement of $\mathcal{B}(B^- \to \Lambda_c^+ \overline{p}\pi^-)$

The branching fraction for the three-body B decay $B^- \to \Lambda_c^+ \overline{p}\pi^-$ is calculated using ${}_s\mathcal{P}lot$ and efficiency correction weights. We simplify notation by using ${}_sW_i$ to denote the value of the signal ${}_s\mathcal{P}lot$ weight for event i. A correction for peaking background is also included.

11.2.1 Peaking Background Correction

We correct for the peaking background from $\overline{B}^0 \to \Sigma_c(2455)^+\overline{p}$, $\Sigma_c(2455)^0 \to \Lambda_c^+\pi^-$ events by applying a 1% correction ($0.01 \times \sum_i \frac{{}_sW_i}{\varepsilon_i}$). The amount of peaking background was determined from toy studies to be 1% of the expected $\Lambda_c^+ \to pK^-\pi^+$ yield; we assume that the amount of peaking background contamination is the same regardless of Λ_c^+ decay mode. See Chapter 7.3 for more details.

11.2.2 Branching Fraction Result

We calculate $\mathcal{B}(B^- \to \Lambda_c^+ \overline{p} \pi^-)$ for the $\Lambda_c^+ \to pK^-\pi^+$ decay mode as follows:

$$\begin{aligned}
\mathcal{B}(B^- \to \Lambda_c^+ \overline{p}\pi^-)_{pK^-\pi^+} &= \frac{(1-1\%) \times \sum_i \frac{{}_sW_i(pK^-\pi^+)}{\varepsilon_i(pK^-\pi^+)}}{N_{B\bar{B}} \ \times \ \mathcal{B}(\Lambda_c^+ \to pK^-\pi^+)} \\
&= \frac{(1-1\%) \times (6463 \pm 241)}{(382.9 \pm 0.1) \times 10^6 \ \times \ (5.0 \pm 1.3)\%} \\
&= (3.38 \pm 0.13 \pm 0.11 \pm 0.88) \times 10^{-4},
\end{aligned} \tag{11.5}$$

where ${}_sW_i$ is the ${}_s\mathcal{P}lot$ weight on event i and the uncertainties are statistical, systematic, and from $\mathcal{B}(\Lambda_c^+ \to pK^-\pi^+)$, respectively. For the other Λ_c^+ decay modes, we define $\mathcal{R}$ as the ratio of each Λ_c^+ branching fraction to $\mathcal{B}(\Lambda_c^+ \to pK^-\pi^+)$ and include the K_S^0 or Λ tracking correction in the efficiency weights:

$$\begin{aligned}
\mathcal{B}(B^- \to \Lambda_c^+ \overline{p}\pi^-)_{pK_S^0} &= \frac{(1-1\%) \times \sum_i \frac{{}_sW_i(pK_S^0)}{\varepsilon_i(pK_S^0)}}{N_{B\bar{B}} \ \times \ \mathcal{R}(pK_S^0) \ \times \ \mathcal{B}(\Lambda_c^+ \to pK^-\pi^+)} \\
&= \frac{(1-1\%) \times (1185 \pm 108)}{(382.9 \pm 0.1) \times 10^6 \ \times \ (0.162) \ \times \ (5.0 \pm 1.3)\%} \\
&= (3.82 \pm 0.35 \pm 0.38 \pm 0.99) \times 10^{-4}
\end{aligned} \tag{11.6}$$

$$\begin{aligned}
\mathcal{B}(B^- \to \Lambda_c^+ \overline{p}\pi^-)_{pK_S^0\pi^+\pi^-} &= \frac{(1-1\%) \times \sum_i \frac{{}_sW_i(pK_S^0\pi^+\pi^-)}{\varepsilon_i(pK_S^0\pi^+\pi^-)}}{N_{B\bar{B}} \ \times \ \mathcal{R}(pK_S^0\pi^+\pi^-) \ \times \ \mathcal{B}(\Lambda_c^+ \to pK^-\pi^+)} \\
&= \frac{(1-1\%) \times (1542 \pm 237)}{(382.9 \pm 0.1) \times 10^6 \ \times \ (0.176) \ \times \ (5.0 \pm 1.3)\%} \\
&= (4.58 \pm 0.70 \pm 0.66 \pm 1.19) \times 10^{-4}
\end{aligned} \tag{11.7}$$

$$\begin{aligned}\mathcal{B}(B^- \to \Lambda_c^+ \bar{p}\pi^-)_{\Lambda\pi^+} &= \frac{(1-1\%) \times \sum_i \frac{{}_sW_i(\Lambda\pi^+)}{\varepsilon_i(\Lambda\pi^+)}}{N_{B\bar{B}} \ \times \ \mathcal{R}(\Lambda\pi^+) \ \times \ \mathcal{B}(\Lambda_c^+ \to pK^-\pi^+)} \\ &= \frac{(1-1\%) \times (982 \pm 110)}{(382.9 \pm 0.1) \times 10^6 \ \times \ (0.129) \ \times \ (5.0 \pm 1.3)\%} \\ &= (3.98 \pm 0.45 \pm 0.39 \pm 1.03) \times 10^{-4}\end{aligned} \tag{11.8}$$

$$\begin{aligned}\mathcal{B}(B^- \to \Lambda_c^+ \bar{p}\pi^-)_{\Lambda\pi^+\pi^-\pi^+} &= \frac{(1-1\%) \times \sum_i \frac{{}_sW_i(\Lambda\pi^+\pi^-\pi^+)}{\varepsilon_i(\Lambda\pi^+\pi^-\pi^+)}}{N_{B\bar{B}} \ \times \ \mathcal{R}(\Lambda\pi^+\pi^-\pi^+) \ \times \ \mathcal{B}(\Lambda_c^+ \to pK^-\pi^+)} \\ &= \frac{(1-1\%) \times (2247 \pm 325)}{(382.9 \pm 0.1) \times 10^6 \ \times \ (0.336) \ \times \ (5.0 \pm 1.3)\%} \\ &= (3.49 \pm 0.51 \pm 0.38 \pm 0.91) \times 10^{-4}\end{aligned} \tag{11.9}$$

11.3 Combined Measurements

The BLUE (Best Linear Unbiased Estimate) technique is used as described in Ref. [52] to combine the *correlated* branching fraction measurements for different Λ_c^+ decay modes. The premise of the method is to obtain an estimate $\hat{y}$ that is is a linear combination of n individual measurements (y_i), is unbiased, and has the minimum possible variance $\hat{\sigma}^2$. The estimate, $\hat{y}$ is defined

$$\hat{y} = \sum_i \alpha_i y_i. \tag{11.10}$$

The condition $\sum_i \alpha_i = 1$ ensures that the method is unbiased. Each coefficient α_i is a constant weight for measurement y_i and is not necessarily positive. The set of coefficients, $\boldsymbol{\alpha}$ (a vector with n elements) is determined by

$$\boldsymbol{\alpha} = \frac{\mathbf{E}^{-1}\,\mathbf{U}}{\mathbf{U}_T\,\mathbf{E}^{-1}\,\mathbf{U}}, \tag{11.11}$$

where $\mathbf{U}$ is an n-component vector whose elements are all 1 and $\mathbf{E}$ is the $(n \times n)$ error matrix. The diagonal elements of $\mathbf{E}$ are the individual variances, σ_i^2. The off-diagonal elements are the covariances between measurements ($r\sigma_i\sigma_j$, where r is the correlation between measurements i and j).

We construct error matrices for the sets of $\overline{B}^0 \to \Lambda_c^+ \overline{p}$ and $B^- \to \Lambda_c^+ \overline{p}\pi^-$ branching fraction measurements described in Sections 11.1 and 11.2. The error matrices are linear, so we can define $\mathbf{E} = \mathbf{E}_{stat} + \mathbf{E}_{syst}$. $\mathbf{E}_{stat}$ includes the uncertainties on the fit yields and the correlations between yields from the simultaneous fit result[1]. $\mathbf{E}_{syst}$ includes the systematic uncertainties described in Section 12. The uncertainties on the Λ_c^+ branching fractions and due to MC statistics are completely uncorrelated. The systematic uncertainties due to tracking, displaced vertices, and particle identification (separated by particle type) are fully correlated among the measurements. The correlation matrix from the fit is used to determine the correlations between fitting systematic uncertainties.

The solutions for $\boldsymbol{\alpha}$ are

$$\begin{aligned} \overline{B}^0 \to \Lambda_c^+ \overline{p}: \ \boldsymbol{\alpha} &= \begin{pmatrix} 0.757 & 0.128 & 0.019 & 0.096 \end{pmatrix} \\ B^- \to \Lambda_c^+ \overline{p}\pi^-: \ \boldsymbol{\alpha} &= \begin{pmatrix} 0.913 & 0.043 & -0.003 & 0.029 & 0.018 \end{pmatrix}. \end{aligned} \tag{11.12}$$

We then calculate the best estimate $\hat{y}$ according to Eqn. 11.10 and the variance of $\hat{y}$

$$\hat{\sigma}^2 = \boldsymbol{\alpha}_T \, \mathbf{E} \, \boldsymbol{\alpha}. \tag{11.13}$$

Since the error matrices are linear, we can quote separate statistical and systematic uncertainties

$$\hat{\sigma}^2 = \hat{\sigma}^2_{stat} + \hat{\sigma}^2_{syst} = \boldsymbol{\alpha}_T \, \mathbf{E}_{stat} \, \boldsymbol{\alpha} + \boldsymbol{\alpha}_T \, \mathbf{E}_{syst} \, \boldsymbol{\alpha}. \tag{11.14}$$

Thus the combined branching fraction measurements are

$$\begin{aligned} \mathcal{B}(\overline{B}^0 \to \Lambda_c^+ \overline{p}) &= (1.89 \pm 0.21 \pm 0.06 \pm 0.49) \times 10^{-5} \\ \mathcal{B}(B^- \to \Lambda_c^+ \overline{p}\pi^-) &= (3.38 \pm 0.12 \pm 0.12 \pm 0.88) \times 10^{-4}. \end{aligned}$$

We can determine if the individual measurements are self-consistent by calculating a weighted sum of squares

$$S = \sum_i \sum_j (\hat{y} - y_i)(\hat{y} - y_j)(\mathbf{E}^{-1})_{ij}. \tag{11.15}$$

The quantity S should be distributed as χ^2 with $n-1$ degrees of freedom (DOF). For

---

[1] Overall multiplicative constants ($N_{B\overline{B}}$ and $\mathcal{B}(\Lambda_c^+ \to pK^-\pi^+)$) that are common to all of the measurements and their uncertainties are not included in the BLUE method.

$\overline{B}^0 \to \Lambda_c^+\overline{p}$, $S = 5.74$ with 3 DOF; the χ^2 probability of exceeding this value of S is 12.5%. For $B^- \to \Lambda_c^+\overline{p}\pi^-$, $S = 3.09$ with 4 DOF; the χ^2 probability of exceeding this value of S is 54.2%. Both values are satisfactory, so the measurements are self-consistent.

11.4 Branching Ratio Result

For each Λ_c^+ decay mode, we compute the branching ratio $\mathcal{B}(B^- \to \Lambda_c^+\overline{p}\pi^-)/\mathcal{B}(\overline{B}^0 \to \Lambda_c^+\overline{p})$. In these ratios, many of the quantities and systematic uncertainties cancel (e.g., $N_{B\overline{B}}$, $\mathcal{B}(\Lambda_c^+ \to pK^-\pi^+)$ and the Λ_c^+ branching ratios for the other modes, and most of the PID and tracking uncertainties).

The branching ratios for each Λ_c^+ decay mode are

$$\begin{aligned}
\Lambda_c^+ \to pK^-\pi^+ :\ & \frac{\mathcal{B}(B^- \to \Lambda_c^+\overline{p}\pi^-)}{\mathcal{B}(\overline{B}^0 \to \Lambda_c^+\overline{p})} = 16.3 \pm 2.1 \pm 0.3 \\
\Lambda_c^+ \to pK_S^0 :\ & \frac{\mathcal{B}(B^- \to \Lambda_c^+\overline{p}\pi^-)}{\mathcal{B}(\overline{B}^0 \to \Lambda_c^+\overline{p})} = 25.3 \pm 10.4 \pm 2.0 \\
\Lambda_c^+ \to pK_S^0\pi^+\pi^- :\ & \frac{\mathcal{B}(B^- \to \Lambda_c^+\overline{p}\pi^-)}{\mathcal{B}(\overline{B}^0 \to \Lambda_c^+\overline{p})} = 10.5 \pm 4.1 \pm 0.9 \\
\Lambda_c^+ \to \Lambda\pi^+ :\ & \frac{\mathcal{B}(B^- \to \Lambda_c^+\overline{p}\pi^-)}{\mathcal{B}(\overline{B}^0 \to \Lambda_c^+\overline{p})} = 55.7 \pm 56.1 \pm 13.6,
\end{aligned}$$

where the uncertainties are statistical and systematic, respectively.

Using the BLUE method described in Section 11.3 to combine the results, we obtain

$$\boldsymbol{\alpha} = \begin{pmatrix} 0.784 & 0.026 & 0.192 & -0.001 \end{pmatrix}. \tag{11.16}$$

The combined branching ratio is:

$$\frac{\mathcal{B}(B^- \to \Lambda_c^+\overline{p}\pi^-)}{\mathcal{B}(\overline{B}^0 \to \Lambda_c^+\overline{p})} = 15.4 \pm 1.8 \pm 0.3. \tag{11.17}$$

From Eqn. 11.15, we compute $S = 3.73$. Given 3 DOF; the associated χ^2 probability is 29.2%, so the measurements are self-consistent.

11.5 Summary of Branching Fraction Measurements

We summarize the branching fraction measurements for $\overline{B}^0 \to \Lambda_c^+ \overline{p}$ and $B^- \to \Lambda_c^+ \overline{p} \pi^-$ in Table 11.1. The systematic uncertainties are described in detail in Chapter 12.

We also report the ratio of the branching fractions $\mathcal{B}(B^- \to \Lambda_c^+ \overline{p} \pi^-)/\mathcal{B}(\overline{B}^0 \to \Lambda_c^+ \overline{p})$.

Table 11.1: Comparison of the branching fraction measurements for $\overline{B}^0 \rightarrow \Lambda_c^+\overline{p}$ and $B^- \rightarrow \Lambda_c^+\overline{p}\pi^-$. We present the individual measurements and the combined measurement from this analysis. Uncertainties are statistical, systematic, and due to $\mathcal{B}(\Lambda_c^+ \rightarrow pK^-\pi^+)$, respectively. The $\mathcal{B}(\Lambda_c^+ \rightarrow pK^-\pi^+)$ value and uncertainty cancels in the branching ratio $\mathcal{B}(B^- \rightarrow \Lambda_c^+\overline{p}\pi^-)/\mathcal{B}(\overline{B}^0 \rightarrow \Lambda_c^+\overline{p})$.

$\overline{B}^0 \rightarrow \Lambda_c^+\overline{p}$

Mode	$\mathcal{B}$
$\Lambda_c^+ \rightarrow pK^-\pi^+$	$(2.05 \pm 0.25 \pm 0.05 \pm 0.53) \times 10^{-5}$
$\Lambda_c^+ \rightarrow pK_S^0$	$(1.49 \pm 0.60 \pm 0.17 \pm 0.39) \times 10^{-5}$
$\Lambda_c^+ \rightarrow pK_S^0\pi^+\pi^-$	$(4.33 \pm 1.55 \pm 0.57 \pm 1.13) \times 10^{-5}$
$\Lambda_c^+ \rightarrow \Lambda\pi^+$	$(0.71 \pm 0.71 \pm 0.18 \pm 0.18) \times 10^{-5}$
combined	$(1.89 \pm 0.21 \pm 0.06 \pm 0.49) \times 10^{-5}$

$B^- \rightarrow \Lambda_c^+\overline{p}\pi^-$

Mode	$\mathcal{B}$
$\Lambda_c^+ \rightarrow pK^-\pi^+$	$(3.38 \pm 0.13 \pm 0.11 \pm 0.88) \times 10^{-4}$
$\Lambda_c^+ \rightarrow pK_S^0$	$(3.82 \pm 0.35 \pm 0.38 \pm 0.99) \times 10^{-4}$
$\Lambda_c^+ \rightarrow pK_S^0\pi^+\pi^-$	$(4.58 \pm 0.70 \pm 0.66 \pm 1.19) \times 10^{-4}$
$\Lambda_c^+ \rightarrow \Lambda\pi^+$	$(3.98 \pm 0.45 \pm 0.39 \pm 1.03) \times 10^{-4}$
$\Lambda_c^+ \rightarrow \Lambda\pi^+\pi^-\pi^+$	$(3.49 \pm 0.51 \pm 0.38 \pm 0.91) \times 10^{-4}$
combined	$(3.38 \pm 0.12 \pm 0.12 \pm 0.88) \times 10^{-4}$

$\mathcal{B}(B^- \rightarrow \Lambda_c^+\overline{p}\pi^-)/\mathcal{B}(\overline{B}^0 \rightarrow \Lambda_c^+\overline{p})$

Mode	$\mathcal{B}$
$\Lambda_c^+ \rightarrow pK^-\pi^+$	$16.3 \pm 2.1 \pm 0.3$
$\Lambda_c^+ \rightarrow pK_S^0$	$25.3 \pm 10.4 \pm 2.0$
$\Lambda_c^+ \rightarrow pK_S^0\pi^+\pi^-$	$10.5 \pm 4.1 \pm 0.9$
$\Lambda_c^+ \rightarrow \Lambda\pi^+$	$55.7 \pm 56.1 \pm 13.6$
combined	$15.4 \pm 1.8 \pm 0.3$

Chapter 12

Systematic Studies

Various sources of systematic uncertainties on the branching fractions of $\overline{B}^0 \rightarrow \Lambda_c^+ \overline{p}$ and $B^- \rightarrow \Lambda_c^+ \overline{p} \pi^-$ are investigated. The contributions are summarized in Tables 12.1 and 12.2, and are dominated by the uncertainties on the Λ_c^+ branching ratios compared to $\Lambda_c^+ \rightarrow pK^-\pi^+$. The tracking systematic uncertainties dominate the $\Lambda_c^+ \rightarrow pK^-\pi^+$ decay mode for both $\overline{B}^0 \rightarrow \Lambda_c^+ \overline{p}$ and $B^- \rightarrow \Lambda_c^+ \overline{p} \pi^-$. The statistical uncertainties from the simultaneous fit results are provided for comparison; all modes have comparable or lower systematic uncertainties. In this section, we present the details of the following quantitative studies:

- B-counting: standard 1.1% of $N_{B\overline{B}}$
- Λ_c^+ branching ratios: uncertainties on $\mathcal{B}/\mathcal{B}(\Lambda_c^+ \rightarrow pK^-\pi^+)$
- MC statistics: simple for $\overline{B}^0 \rightarrow \Lambda_c^+ \overline{p}$; an independent $\pm 1\sigma$ variation of each Dalitz bin for $B^- \rightarrow \Lambda_c^+ \overline{p} \pi^-$
- Charged particle tracking: average of 0.38% per track for ChargedTracks; average of 0.45% per track for GTL tracks
- Displaced vertex tracking (K_S^0, Λ): correction implemented; systematic applied according to Tracking Efficiency Task Force K_S^0 Recipe
- Particle identification: comparison of control MC samples to signal MC sample; systematic on PID weighting method
- Fitting: peaking background; variation of $(m_{\text{miss}} + m_B)/2$ endpoint; floating ARGUS parameter.

Table 12.1: Summary of the contributions to the relative systematic uncertainty on $\mathcal{B}(\overline{B}^0 \to \Lambda_c^+ \overline{p})$ for each Λ_c^+ decay mode. The total for each mode is determined by adding the uncertainty from each source in quadrature. The statistical uncertainty on the fit yield for each mode is provided for comparison.

Source	$\overline{B}^0 \to \Lambda_c^+ \overline{p}$ Systematic Uncertainty			
	$\Lambda_c^+ \to pK^-\pi^+$	$\Lambda_c^+ \to pK_S^0$	$\Lambda_c^+ \to pK_S^0\pi^+\pi^-$	$\Lambda_c^+ \to \Lambda\pi^+$
B-counting	1.1%	1.1%	1.1%	1.1%
Λ_c^+ $\mathcal{B}/\mathcal{B}_{pK^-\pi^+}$	–	8.5%	11.8%	8.9%
MC statistics	0.4%	0.6%	0.6%	0.4%
Tracking	1.7%	1.9%	2.8%	1.7%
Displ. Vertices	–	1.1%	1.1%	1.1%
PID	1.5%	2.1%	1.7%	1.6%
Fitting	0.9%	7.0%	4.9%	24.2%
Total	2.7%	11.5%	13.3%	25.9%
Statistical	12.2%	40.0%	35.7%	100%

Table 12.2: Summary of the contributions to the relative systematic uncertainty on $\mathcal{B}(B^- \rightarrow \Lambda_c^+ \overline{p} \pi^-)$ for each Λ_c^+ decay mode. The total for each mode is determined by adding the uncertainty from each source in quadrature. The statistical uncertainty on the fit yield for each mode is provided for comparison.

Source	$B^- \rightarrow \Lambda_c^+ \overline{p} \pi^-$ Systematic Uncertainty				
	$\Lambda_c^+ \rightarrow pK^-\pi^+$	$\Lambda_c^+ \rightarrow pK_S^0$	$\Lambda_c^+ \rightarrow pK_S^0\pi^+\pi^-$	$\Lambda_c^+ \rightarrow \Lambda\pi^+$	$\Lambda_c^+ \rightarrow \Lambda\pi^+\pi^-\pi^+$
B-counting	1.1%	1.1%	1.1%	1.1%	1.1%
Λ_c^+ $\mathcal{B}/\mathcal{B}_{pK^-\pi^+}$	–	8.5%	11.8%	8.9%	6.1%
MC statistics	0.6%	2.1%	3.1%	2.0%	3.0%
Tracking	2.6%	2.3%	3.2%	2.1%	2.9%
Displ. Vertices	–	1.1%	1.1%	1.1%	1.1%
PID	0.8%	1.8%	2.5%	1.8%	3.5%
Fitting	1.6%	3.2%	6.5%	2.5%	2.4%
Total	3.4%	9.9%	14.5%	10.0%	8.7%
Statistical	4.5%	9.1%	16.3%	11.4%	14.8%

Table 12.3: Uncertainties on Λ_c^+ branching fractions with respect to $\Lambda_c^+ \to pK^-\pi^+$ [9]. The uncertainties are added in quadrature with $\delta\left(\mathcal{B}(K_S^0 \to \pi^+\pi^-)\right)$ for $\Lambda_c^+ \to pK_S^0$ and $\Lambda_c^+ \to pK_S^0\pi^+\pi^-$ and $\delta\left(\mathcal{B}(\Lambda \to p\pi^-)\right)$ for $\Lambda_c^+ \to \Lambda\pi^+$ and $\Lambda_c^+ \to \Lambda\pi^+\pi^-\pi^+$. These additional uncertainties are negligible compared to $\delta\left(\mathcal{B}/\mathcal{B}(\Lambda_c^+ \to pK^-\pi^+)\right)$.

Mode	$\delta\left(\mathcal{B}/\mathcal{B}(\Lambda_c^+ \to pK^-\pi^+)\right)$
$\Lambda_c^+ \to pK^-\pi^+$	–
$\Lambda_c^+ \to pK_S^0$	$8.5\% \oplus 0.7\%$
$\Lambda_c^+ \to pK_S^0\pi^+\pi^-$	$11.8\% \oplus 0.7\%$
$\Lambda_c^+ \to \Lambda\pi^+$	$8.9\% \oplus 0.8\%$
$\Lambda_c^+ \to \Lambda\pi^+\pi^-\pi^+$	$6.1\% \oplus 0.8\%$

12.1 B-counting Systematic Uncertainty

The systematic errors on the number of $B\overline{B}$ pairs produced by BABAR are itemized by Run in Table 3.1. The systematic errors for each Run are fully correlated, and so the total systematic error on the number of $B\overline{B}$ pairs reported is 1.1%: $(382.92 \pm 0.10 \pm 4.21) \times 10^6$ $B\overline{B}$ pairs [41].

12.2 Λ_c^+ Branching Ratio Systematic Uncertainty

The uncertainties due to the Λ_c^+ branching ratios of $\mathcal{B}/\mathcal{B}(\Lambda_c^+ \to pK^-\pi^+)$ are summarized in Table 12.3. The relative branching fractions for the modes $\Lambda_c^+ \to pK_S^0$ and $\Lambda_c^+ \to pK_S^0\pi^+\pi^-$ are multiplied by $\mathcal{B}(K_S^0 \to \pi^+\pi^-)$ and those for the modes $\Lambda_c^+ \to \Lambda\pi^+$ and $\Lambda_c^+ \to \Lambda\pi^+\pi^-\pi^+$ are multiplied by $\mathcal{B}(\Lambda \to p\pi^-)$.

12.3 Efficiency Systematic Uncertainty

The binned efficiency correction procedure is presented in Chapter 6.4. There are several sources of systematic uncertainty related to this procedure: MC statistics, tracking, and PID.

12.3.1 MC Sample Statistics

We independently vary the number of reconstructed signal MC events in each efficiency bin according to a Poisson distribution and calculate the number number of efficiency-corrected, ${}_s\mathcal{P}lot$ weighted signal events. We ensure that the efficiency corrections of data events in the same bin are correlated. We perform 500 trials and construct the fractional difference in efficiency for each trial t compared to the central value $\left(\sum_i \frac{{}_sW_i}{\varepsilon_i}\right)_0$:

$$\frac{\left(\sum_i \frac{{}_sW_i}{\varepsilon_i}\right)_t - \left(\sum_i \frac{{}_sW_i}{\varepsilon_i}\right)_0}{\left(\sum_i \frac{{}_sW_i}{\varepsilon_i}\right)_0}. \tag{12.1}$$

This is repeated for each Λ_c^+ decay mode, and the width of the resulting distribution (see Figure 12.1) is taken as the fractional systematic uncertainty on the efficiency due to MC statistics.

12.3.2 Tracking

The tracking systematic uncertainties are determined from two separate studies. The first uses τ decays to determine the systematic uncertainties due to charged particle tracking in the detector. The second study compares charged particle trajectories found in the SVT alone to those found in the DCH. The uncertainties from each method are added in quadrature.

Tau Tracking Study

In the τ tracking study, four types of decays are analyzed:

- $\tau^- \to e^- \overline{\nu}_e \nu_\tau,\ \tau^- \to \rho\, \pi^- \nu_\tau$
- $\tau^- \to \mu^- \overline{\nu}_\mu \nu_\tau,\ \tau^- \to \rho\, \pi^- \nu_\tau$
- $\tau^- \to e^- \overline{\nu}_e \nu_\tau,\ \tau^- \to \pi^- \pi^+ \pi^- \nu_\tau$
- $\tau^- \to \mu^- \overline{\nu}_\mu \nu_\tau,\ \tau^- \to \pi^- \pi^+ \pi^- \nu_\tau$

Events are selected by requiring $3-5$ tracks per event, charge conservation, and that one of the tracks is a lepton. The event is "tagged" by the lepton from one τ decay, and then three tracks must be observed from the other (hadronic) τ decay. Given that two tracks are

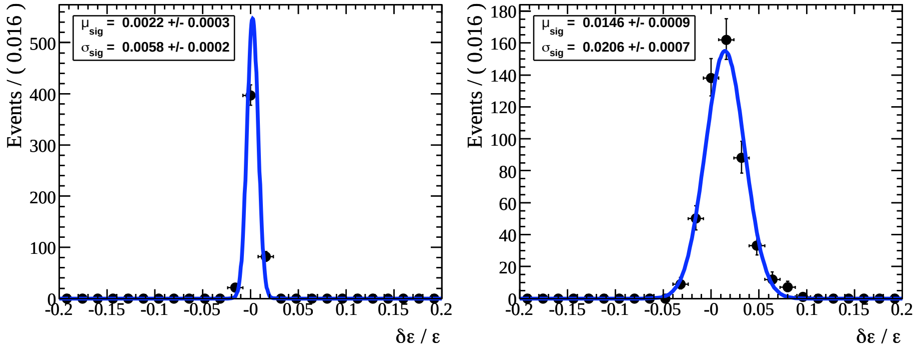

(a) $\Lambda_c^+ \to pK^-\pi^+$

(b) $\Lambda_c^+ \to pK_S^0$

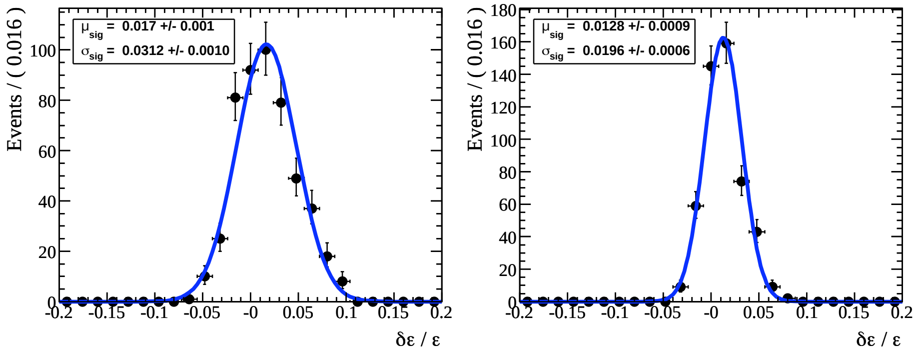

(c) $\Lambda_c^+ \to pK_S^0\pi^+\pi^-$

(d) $\Lambda_c^+ \to \Lambda\pi^+$

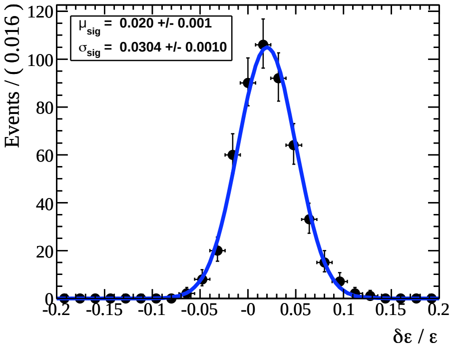

(e) $\Lambda_c^+ \to \Lambda\pi^+\pi^-\pi^+$

Figure 12.1: Distributions of the fractional efficiency for $B^- \to \Lambda_c^+\overline{p}\pi^-$ signal MC candidates across the Dalitz plane. Subfigures $(a)-(e)$ indicate the B candidate efficiency distribution for each Λ_c^+ decay mode.

reconstructed on the hadronic side, the tracking efficiency is determined by whether a third track is reconstructed. Data and MC samples are compared to determine the systematic uncertainty. From this study, there is a 0.45% systematic uncertainty for each *ChargedTrack* and a 0.38% systematic uncertainty for each *GoodTracksLoose* particle that is reconstructed. In this analysis, the tracking uncertainties are added linearly according to the number of total tracks in each category, in each decay mode. The uncertainties are summarized in Table 12.4.

SVT-based Tracking Study

This method is only used to correct for *GoodTracksLoose* (GTL) tracks (Λ_c^+ daughter protons, kaons and B daughter protons). Charged particle trajectories are found in the SVT alone, and then the efficiency for finding corresponding tracks in the DCH is measured. We define a pseudo-efficiency as

$$\varepsilon_{\text{pseudo}} = \frac{\#\text{GTL with 10 SVT hits}}{\#\text{GTVL with 10 SVT hits} - N_f}, \tag{12.2}$$

where 10 SVT hits are required to ensure that the particle traversed all five double layers of the SVT. N_f is the number of fake tracks in multihadron events. The fake track rate is measured in Bhabha events and is scaled to the multihadron event luminosity. The ratio of the pseudo-efficiency in data is compared to a MC sample in bins of p_T, θ, ϕ, and the number of *GoodTracksVeryLoose* (GTVL) tracks in the event[1]. In each bin, the data-to-MC $\varepsilon_{\text{pseudo}}$ ratio is computed and applied as a correction to the signal MC samples used in this analysis. The deviation of the weighted average from 1 is taken to determine the overall systematic uncertainty in each sample. These uncertainties are summarized in Table 12.4.

12.3.3 Displaced Vertex Tracking

Efficiency corrections have been applied to account for tracks originating from displaced vertices (such as K_S^0 and Λ daughters). These corrections originate from a study comparing large semi-inclusive data and MC samples of K_S^0 candidates. The systematic uncertainty on these corrections arises from two sources. The first is the statistical uncertainty on the samples used in the study. The second is the result of an additional comparison between

---

[1] Recall that *GoodTracksVeryLoose* has the same requirements as *GoodTracksLoose*, except that no DCH interactions are required.

Table 12.4: Summary of the systematic uncertainties due to tracking for $\overline{B}^0 \to \Lambda_c^+ \overline{p}$ and $B^- \to \Lambda_c^+ \overline{p} \pi^-$. The uncertainties for *ChargedTracks* (CT) are 0.38% per CT according to the τ method. The uncertainties for *GoodTracksLoose* (GTL) are determined from the τ method (0.45% per track) and the SVT-based method (the uncertainties from the two methods are added in quadrature). The resulting CT and GTL uncertainties are added linearly.

$\overline{B}^0 \to \Lambda_c^+ \overline{p}$ Systematic Uncertainty

	$\Lambda_c^+ \to pK^-\pi^+$	$\Lambda_c^+ \to pK_S^0$	$\Lambda_c^+ \to pK_S^0\pi^+\pi^-$	$\Lambda_c^+ \to \Lambda\pi^+$
CT	0.38%	0.76%	1.52%	1.14%
GTL (τ)	1.35%	0.90%	0.90%	0.45%
GTL (SVT)	0.21%	0.75%	0.87%	0.33%
Total	1.7%	1.9%	2.8%	1.7%

$B^- \to \Lambda_c^+ \overline{p} \pi^-$ Systematic Uncertainty

	$\Lambda_c^+ \to pK^-\pi^+$	$\Lambda_c^+ \to pK_S^0$	$\Lambda_c^+ \to pK_S^0\pi^+\pi^-$	$\Lambda_c^+ \to \Lambda\pi^+$	$\Lambda_c^+ \to \Lambda\pi^+\pi^-\pi^+$
CT	0.76%	1.14%	1.90%	1.52%	2.28%
GTL (τ)	1.35%	0.90%	0.90%	0.45%	0.45%
GTL (SVT)	1.18%	0.77%	0.89%	0.38%	0.42%
Total	2.6%	2.3%	3.2%	2.1%	2.9%

$B^0 \to D^-\pi^+, D^- \to K_S^0\pi^-$ data and MC control samples. The weighted average (over Run) of the systematic uncertainty for modes containing a K_S^0 or Λ candidate is 1.1%.

12.3.4 Particle Identification

The PID weighting technique is based on a comparison between MC and data samples in a control mode. A summary of the control modes used can be found in Table 12.5. The validity of using the PID weights for this analysis is dependent on how well our signal MC samples compare to the control MC samples. For example, the control samples have lower multiplicities than B decays and may have other subtle differences from the various signal MC sample momentum and angular distributions. To determine the systematic uncertainty on the PID weighting technique, we attempt to account for any differences between our

Table 12.5: Control modes used in determining PID systematic uncertainties.

Particle Type	PID Selector	Control Mode
p	*pLHVeryLoose*	$\Lambda \to p\pi^-$
K	*KLHVeryLoose*	$D^{*+} \to D^0\pi^+$, $D^0 \to K^-\pi^+$
π	*piLHLoose*	$D^{*+} \to D^0\pi^+$, $D^0 \to K^-\pi^+$
π	*piLHVeryLoose*	$D^{*+} \to D^0\pi^+$, $D^0 \to K^-\pi^+$

signal MC samples and the control MC samples from which the PID weights are derived.

The detailed procedure for determining the systematic uncertainties is as follows. All of the MC samples are divided up by Run. We determine the efficiency for each PID selector in bins of momentum and angle for each signal MC sample, $\epsilon_{\text{signal MC}}$. We then compare the signal MC efficiency in each momentum and angle bin to the efficiency in the control sample in that bin, $\epsilon_{\text{control, MC}}$. The uncertainty on the signal MC efficiency in each momentum and angle bin is binomial. We define r as the ratio of these two quantities in each momentum/angle bin i:

$$r_i = \left(\frac{\epsilon_{\text{control, MC}}}{\epsilon_{\text{signal MC}}}\right)_i . \tag{12.3}$$

The weighted average over the momentum and angle bins of the ratio is calculated, along with its error:

$$\bar{r} \pm \delta\bar{r} = \frac{\sum_i r_i/(\delta r_i)^2}{\sum_i 1/(\delta r_i)^2} \pm \left(\sum_i 1/(\delta r_i)^2\right)^{-1/2} . \tag{12.4}$$

We take the systematic error as the sum in quadrature of these two quantities: $|\bar{r}-1| \oplus \delta\bar{r}$. The resulting $|\bar{r}-1|$ and $\delta\bar{r}$ quantities are divided by particle type, charge, and Run, and the systematic uncertainty is then averaged over particle charge.

The results are combined by adding the "systematic" portion of the uncertainty linearly for same-type particles in each mode. For example, in $B^- \to \Lambda_c^+\bar{p}\pi^-$, $\Lambda_c^+ \to pK_S^0$, we add the computed $|\bar{r}-1|$ portion linearly for both protons in a given Run, since both numbers are derived from a comparison with the same tracks in the same control sample. We then add the resulting quantity in quadrature with the two "statistical" portions of the uncertainties ($\delta\bar{r}$). This is repeated for each Run, and then we take an average over all of the Runs, weighted by the number of $B^- \to \Lambda_c^+\bar{p}\pi^-$, $\Lambda_c^+ \to pK_S^0$ signal MC events in each Run to determine the overall systematic uncertainty for protons in this mode.

Table 12.6: Summary of the PID systematic uncertainties for $\overline{B}^0 \to \Lambda_c^+\overline{p}$ and $B^- \to \Lambda_c^+\overline{p}\pi^-$, Λ_c^+ decay mode and particle type. The total PID uncertainty for each mode is determined by adding the uncertainty from each particle type in quadrature.

Particle Type	$\overline{B}^0 \to \Lambda_c^+\overline{p}$ Systematic Uncertainty			
	$\Lambda_c^+ \to pK^-\pi^+$	$\Lambda_c^+ \to pK^0_S$	$\Lambda_c^+ \to pK^0_S\pi^+\pi^-$	$\Lambda_c^+ \to \Lambda\pi^+$
p	1.0%	2.1%	1.7%	1.5%
K	1.1%	–	–	–
π	0.1%	0.1%	0.3%	0.4%
Total	1.5%	2.1%	1.7%	1.6%

Particle Type	$B^- \to \Lambda_c^+\overline{p}\pi^-$ Systematic Uncertainty				
	$\Lambda_c^+ \to pK^-\pi^+$	$\Lambda_c^+ \to pK^0_S$	$\Lambda_c^+ \to pK^0_S\pi^+\pi^-$	$\Lambda_c^+ \to \Lambda\pi^+$	$\Lambda_c^+ \to \Lambda\pi^+\pi^-\pi^+$
p	0.4%	1.4%	2.4%	1.7%	3.2%
K	0.7%	–	–	–	–
π	0.2%	1.1%	0.9%	0.6%	1.3%
Total	0.8%	1.8%	2.5%	1.8%	3.5%

This procedure is repeated for each type of charged particle (p, K, or π) in each decay mode. We conservatively add the uncertainty from the *piLHLoose* selector linearly with the *piLHVeryLoose* selector, since the former is a subset of the latter.

A summary of the results of this study are presented in Table 12.6. The systematic uncertainties for each particle type in a given decay mode are added in quadrature to determine the overall PID systematic uncertainty in that mode.

12.4 Fitting Systematic Uncertainties

The sources of fit-related systematic uncertainties are peaking background and the choice of signal and background PDF.

Nearly all of the PDF parameters are allowed to float in the simultaneous fits to data. The signal PDF parameters are shared among the Λ_c^+ decay modes to allow a robust fit. The endpoint of the ARGUS function is fixed in the nominal fit, and so we vary this as a source of systematic uncertainty. The $(m_{\text{miss}} + m_B)/2$ background shape is allowed to float, although the ARGUS parameter (c) is constrained to be the same for all of the Λ_c^+ decay modes. This is investigated below. The $(m_{\text{rec}} - m_B)$ background slope is allowed to float independently for each Λ_c^+ decay mode, and so no systematic uncertainty is necessary.

12.4.1 Peaking Background (for $B^- \to \Lambda_c^+ \overline{p} \pi^-$)

As discussed previously, a 1.0% correction is made to account for peaking background due to $\overline{B}^0 \to \Sigma_c(2455)^+ \overline{p}$ events misreconstructed in the $B^- \to \Lambda_c^+ \overline{p} \pi^-$ mode. The details of the peaking background study can be found in Section 7.3. The correction assumes a branching fraction of $\mathcal{B}(\overline{B}^0 \to \Sigma_c(2455)^+ \overline{p}) = 3.7 \times 10^{-5}$ given a measurement of the decay $\mathcal{B}(B^- \to \Sigma_c(2455)^0 \overline{p}) = (3.7 \pm 0.7 \pm 0.4 \pm 1.0) \times 10^{-5}$ [30], where the errors are statistical, systematic, and due to $\mathcal{B}(\Lambda_c^+ \to pK^-\pi^+)$, respectively. If we take into account the statistical and systematic uncertainties on this measurement, for $\Lambda_c^+ \to pK^-\pi^+$ we obtain a range of $9 - 14$ out of 1053 expected events in the signal region due to peaking background. We therefore assign a 0.5% systematic uncertainty due to account for the uncertainty in $\mathcal{B}(\overline{B}^0 \to \Sigma_c(2455)^+ \overline{p})$.

12.4.2 $(m_{\text{miss}} + m_B)/2$ Endpoint

The $(m_{\text{miss}} + m_B)/2$ endpoint, m^0_{ARG} is varied by $\pm 0.5\,\text{MeV}/c^2$ from its nominal value of $5,289.0\,\text{MeV}/c^2$. The systematic uncertainty is taken as the larger deviation from the yield in each mode. The uncertainties range from $(0.2 - 1.5)$% for $\overline{B}^0 \to \Lambda_c^+ \overline{p}$, and $(0.5 - 0.8)$% for $B^- \to \Lambda_c^+ \overline{p} \pi^-$. The values are listed in Table 12.7.

We also perform fits using event-by-event $(m_{\text{miss}} + m_B)/2$ endpoints. This has negligible impact on the fit yields; the largest deviation is 0.1%. Therefore we take the more conservative $(m_{\text{miss}} + m_B)/2$ endpoint variation as the systematic uncertainty.

12.4.3 Variation of ARGUS Parameter

During the fit validation, it was determined to share the ARGUS parameter (c) among the Λ_c^+ decay modes to improve the robustness of the simultaneous fit. This is how the nominal fit to data was performed. As a systematic uncertainty, we allowed the ARGUS parameter to float among the Λ_c^+ decay modes. Both simultaneous fits did converge in data, and the difference is taken as a systematic uncertainty. These results are included in Table 12.7.

Table 12.7: Summary of the fit systematic uncertainties for $\overline{B}^0 \rightarrow \Lambda_c^+ \overline{p}$ and $B^- \rightarrow \Lambda_c^+ \overline{p} \pi^-$, including a variation of the $(m_{\text{miss}} + m_B)/2$ endpoint (m_0) by $\pm 0.5\,\text{MeV}/c^2$, the ARGUS parameter (c), and a contribution from peaking background for $B^- \rightarrow \Lambda_c^+ \overline{p} \pi^-$.

Source	$\overline{B}^0 \rightarrow \Lambda_c^+ \overline{p}$ Systematic Uncertainty			
	$\Lambda_c^+ \rightarrow pK^-\pi^+$	$\Lambda_c^+ \rightarrow pK_S^0$	$\Lambda_c^+ \rightarrow pK_S^0\pi^+\pi^-$	$\Lambda_c^+ \rightarrow \Lambda\pi^+$
m_{ARG}^0	0.2%	0.5%	0.5%	1.5%
c	0.9%	7.0%	4.9%	24.2%
Total	0.9%	7.0%	4.9%	24.2%

Source	$B^- \rightarrow \Lambda_c^+ \overline{p} \pi^-$ Systematic Uncertainty				
	$\Lambda_c^+ \rightarrow pK^-\pi^+$	$\Lambda_c^+ \rightarrow pK_S^0$	$\Lambda_c^+ \rightarrow pK_S^0\pi^+\pi^-$	$\Lambda_c^+ \rightarrow \Lambda\pi^+$	$\Lambda_c^+ \rightarrow \Lambda\pi^+\pi^-\pi^+$
Peaking bkg	0.5%	0.5%	0.5%	0.5%	0.5%
m_{ARG}^0	0.5%	0.6%	0.8%	0.7%	0.6%
c	1.4%	3.1%	6.4%	2.3%	2.3%
Total	1.6%	3.2%	6.5%	2.5%	2.4%

Chapter 13

Resonant Substructure

Building on the foundation established in Chapter 10, we can perform a binned χ^2 fit to the ${}_s\mathcal{P}lot$-weighted $m_{\Lambda_c\pi}$ invariant mass spectrum to discriminate between resonant ($B^- \rightarrow \Sigma_c^0\ \overline{p}$) signal and nonresonant ($B^- \rightarrow \Lambda_c^+\overline{p}\pi^-$) signal events. We find signals for the decays $B^- \rightarrow \Sigma_c(2455)^0\overline{p}$ and $B^- \rightarrow \Sigma_c(2800)^0\overline{p}$, but not for the decay $B^- \rightarrow \Sigma_c(2520)^0\overline{p}$. In each binned χ^2 fit, the PDF is numerically integrated over each (variable-sized) bin and the following quantity is minimized:

$$\chi^2 = \sum_{i}^{n_{\text{bins}}} \left(\frac{\int \left(N_{\text{sig}}\mathcal{P}_{\text{sig}} + N_{\text{nr}}\mathcal{P}_{\text{nr}}\right)\, dm_i \ - \ N_i}{\sigma_i} \right)^2 , \tag{13.1}$$

where $\mathcal{P}_{\text{sig}}$ is the resonant signal PDF, $\mathcal{P}_{\text{nr}}$ is the nonresonant signal PDF, N_{sig} is the expected number of resonant signal events, and N_{nr} is the expected number of nonresonant signal events. The range of the integral over the quantity dm_i takes into account the (variable) bin width, N_i is the number of weighted data events and σ_i is the uncertainty on the number of weighted data events for bin i.

There is an issue to take into consideration in examining these fit results: the projections correspond to ${}_s\mathcal{P}lot$ signal weights, and therefore suffer from underestimated errors in bins with few signal events. An attempt is made to eliminate this effect by employing variable binning; bins near the Σ_c resonances are narrower than bins that contain mostly nonresonant signal events.

13.1 $\Sigma_c(2455)^0$ Mass Region

We project the signal ${}_s\mathcal{P}lot$ weights (from the fit to $(m_{\rm miss}+m_B)/2$ vs. $(m_{\rm rec}-m_B)$) onto the $m_{\Lambda_c\pi}$ axis in the vicinity of the $\Sigma_c(2455)^0$. A 1-D binned χ^2 fit is performed to discriminate between resonant signal ($B^- \to \Sigma_c(2455)^0\overline{p}$) and non-resonant signal ($B^- \to \Lambda_c^+\overline{p}\pi^-$) events.

Resonant Signal PDF

The resonant signal PDF is parameterized as a non-relativistic Breit-Wigner distribution $\mathcal{P}_{BW}$ convolved with the sum of two Gaussian distributions $\mathcal{P}_{2G}$ (to form a "Voigtian" distribution), and multiplied by a phase-space function $\mathcal{P}_{PS}$.

$$(\mathcal{P}_{BW} \otimes \mathcal{P}_{2G}) \times \mathcal{P}_{PS}. \tag{13.2}$$

The non-relativistic Breit-Wigner PDF is

$$\mathcal{P}_{BW}(m_{\Lambda_c\pi}; m_r, \Gamma_r) \propto \frac{1}{(m_{\Lambda_c\pi} - m_r)^2 + \frac{1}{4}\Gamma_r^2}, \tag{13.3}$$

where m_r is the mass of the resonance and Γ_r is the width (both are allowed to float in the fit). The world average values for the $\Sigma_c(2455)^0$ are $m_r = 2453.8 \pm 0.2\,\mathrm{MeV}/c^2$ and $\Gamma_r = 2.2 \pm 0.4\,\mathrm{MeV}$ [9]. The resolution of the $\Sigma_c(2455)^0$ is measured from a $B^- \to \Sigma_c(2455)^0\overline{p}$, $\Sigma_c(2455)^0 \to \Lambda_c^+\pi^-$, $\Lambda_c^+ \to pK^-\pi^+$ signal MC sample by comparing the measured $\Sigma_c(2455)^0$ mass to the true $\Sigma_c(2455)^0$ mass for each candidate. The distribution of $m_{\Lambda_c\pi}(\text{meas.}) - m_{\Lambda_c\pi}(\text{true})$ is shown in Figure 13.1.

The resolution function is parameterized as the sum of two Gaussian distributions:

$$\mathcal{P}_{2G}(m_{\Lambda_c\pi}; m_r, \sigma_1, \sigma_2, f) \propto \left(\frac{f}{\sigma_1\sqrt{2\pi}}\, e^{(m_{\Lambda_c\pi}-m_r)^2/2\sigma_1^2} + \frac{1-f}{\sigma_2\sqrt{2\pi}}\, e^{(m_{\Lambda_c\pi}-m_r)^2/2\sigma_2^2} \right), \tag{13.4}$$

where the mean (m_r) is the same parameter as in $\mathcal{P}_{BW}$. The values of σ_1, σ_2, and the fraction f are fixed to the values obtained from the fit to the signal MC sample ($\sigma_1 = 0.297 \pm 0.009\,\mathrm{MeV}/c^2$, $\sigma_2 = 0.66 \pm 0.03\,\mathrm{MeV}/c^2$, and $f = 0.50 \pm 0.03$).

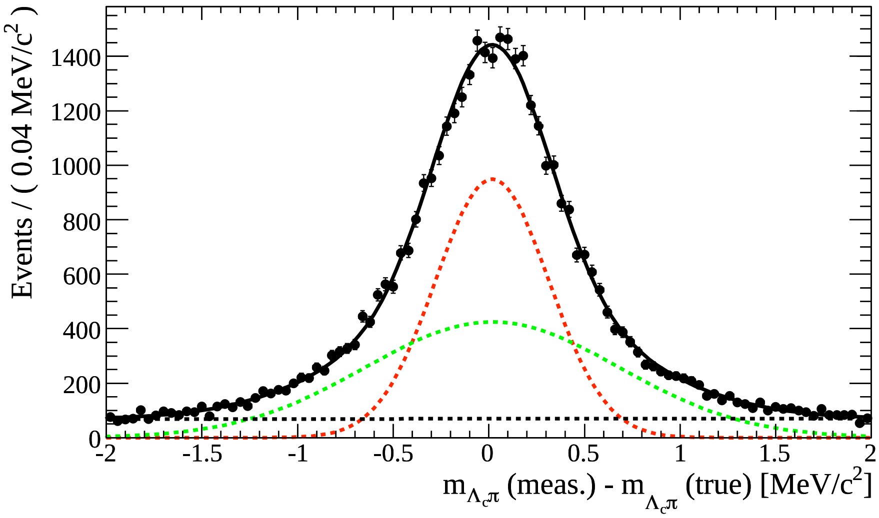

Figure 13.1: Distribution of $m_{\Lambda_c\pi}(\text{meas.}) - m_{\Lambda_c\pi}(\text{true})$ in a signal MC sample of $B^- \to \Sigma_c(2455)^0\overline{p}$, $\Sigma_c(2455)^0 \to \Lambda_c^+\pi^-$, $\Lambda_c^+ \to pK^-\pi^+$ candidates. The distribution is fit to two Gaussian distributions (red and green dashed lines) plus a linear background (black dashed line); the RMS of the two Gaussian distributions is $\sigma_{RMS} = 0.51 \pm 0.01\,\text{MeV}/c^2$.

The two-body phase-space function is

$$\mathcal{P}_{PS}(m_{\Lambda_c\pi}) \propto \frac{\sqrt{\left(m_{\Lambda_c\pi}^2 - (m_{\Lambda_c} + m_\pi)^2\right)\left(m_{\Lambda_c\pi}^2 - (m_{\Lambda_c} - m_\pi)^2\right)}}{2\,m_{\Lambda_c\pi}}, \tag{13.5}$$

where $m_{\Lambda_c\pi}$ is the invariant mass of the $\Lambda_c^+\pi$ system and m_{Λ_c} and m_π are constants. This function goes to zero at the kinematic threshold, $m^0_{\Lambda_c\pi} = 2426.03\,\text{MeV}/c^2$.

Non-resonant Signal PDF

The form of the non-resonant signal PDF is an ARGUS function where the threshold is set to the same kinematic threshold, $m^0_{\Lambda_c\pi}$, as in the phase-space function in Eqn. 13.5:

$$\mathcal{P}_{nr}(m_{\Lambda_c\pi}; c_{ARG}) \propto m_{\Lambda_c\pi}\left[\left(\frac{m_{\Lambda_c\pi}}{m^0_{\Lambda_c\pi}}\right)^2 - 1\right]^{\frac{1}{2}} \exp\left[-c_{ARG}\left(\left(\frac{m_{\Lambda_c\pi}}{m^0_{\Lambda_c\pi}}\right)^2 - 1\right)\right], \tag{13.6}$$

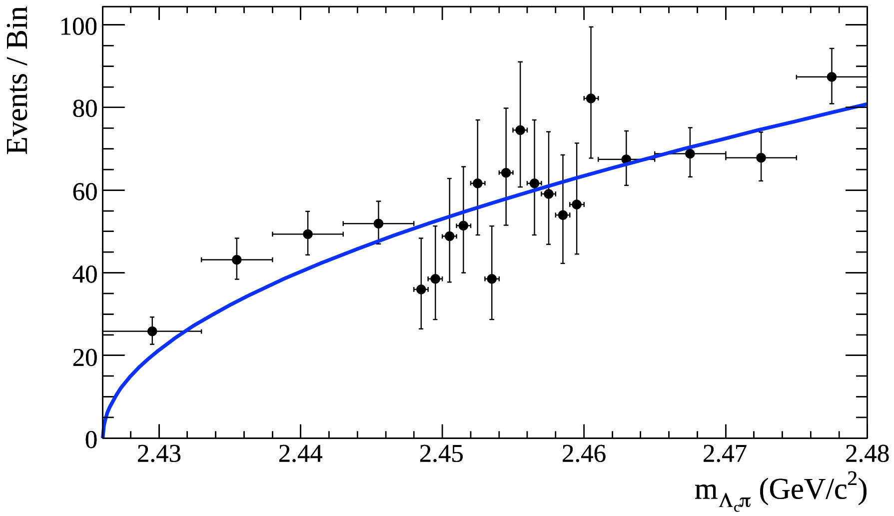

Figure 13.2: Distribution of $m_{\Lambda_c\pi}$ in a nonresonant signal MC sample of $B^- \to \Lambda_c^+\overline{p}\pi^-$, $\Lambda_c^+ \to pK^-\pi^+$ candidates. The distribution is fit to an ARGUS function with a threshold at $2426\,\mathrm{MeV}/c^2$. The result of the fit is $c = -0.0011 \pm 0.0008$. The binning is purposefully narrower in the region of the $\Sigma_c(2455)^0$ to match the binning in Figure 13.3.

where c_{ARG} is the ARGUS function shape parameter. The shape of the non-resonant signal PDF is verified by fitting the $B^- \to \Lambda_c^+\overline{p}\pi^-, \Lambda_c^+ \to pK^-\pi^+$ signal MC sample in the same region (see Figure 13.2). We fix the ARGUS parameter to $c = -0.0011$ from the fit to the non-resonant signal MC sample and vary it to determine the systematic uncertainties.

Fit Results

The nominal fit results are summarized in Table 13.1. Note that the event yields are **efficiency-corrected**; we obtain 1522 ± 149 resonant signal events. The χ^2 from the fit is 15.3 with 17 degrees of freedom (DOF), so the χ^2/DOF is 0.90 and the χ^2 probability is 57%.

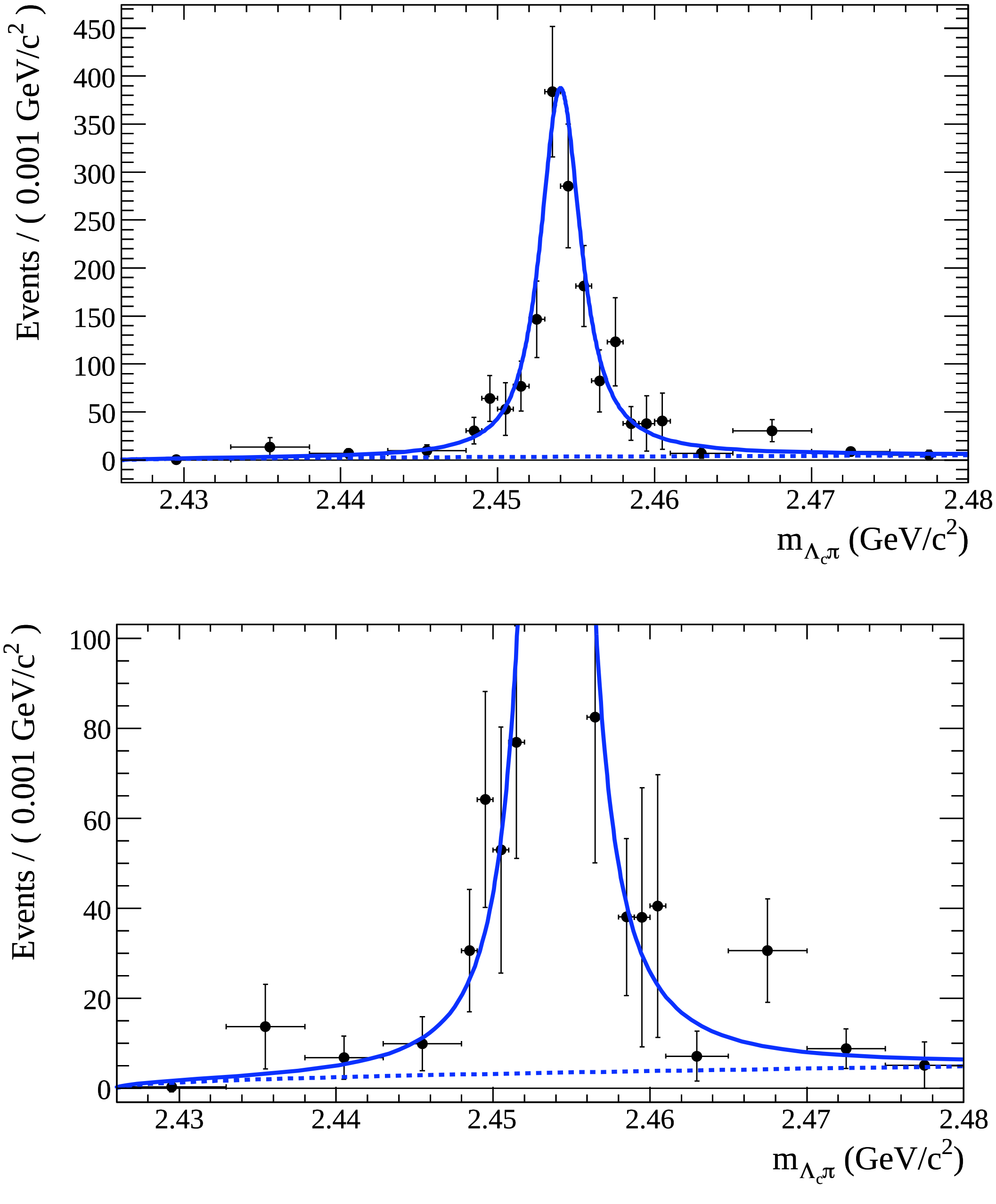

Figure 13.3: (top) Projection of $m_{\Lambda_c\pi}$ in the region of the $\Sigma_c(2455)^0$ resonance. Events are **efficiency-corrected** and weighted using the ${}_s\mathcal{P}lot$ technique, and the result of a binned χ^2 fit to a Voigtian signal plus a linear background is overlaid. The variable bin sizes range from $1-7\,\mathrm{MeV}/c^2$. (bottom) The same fit result and data is shown on a smaller vertical scale to show the behavior of the PDF at threshold.

Table 13.1: Fit results for $B^- \rightarrow \Sigma_c(2455)^0\overline{p}$. N_{nr} is the non-resonant signal yield and N_{sig} is the resonant signal yield in the fit range. The resolution parameters (σ_1, σ_2, f) are fixed to the values obtained in the MC sample. The world average values of the mass and width of the $\Sigma_c(2455)^0$ are included [9].

Fit Parameter	Value	PDG Value [9]
N_{sig}	1522 ± 149	
m_r (GeV/c^2)	2.4540 ± 0.0002	2.4538 ± 0.0002
Γ_r (MeV/c^2)	2.6 ± 0.5	2.2 ± 0.4
σ_1 (MeV/c^2)	0.297	
σ_2 (MeV/c^2)	0.66	
f	0.50	
N_{nr}	162 ± 102	
c	−0.0011	

13.2 $\Sigma_c(2800)^0$ Mass Region

The existence of the $\Sigma_c(2800)^0$ resonance was reported by the Belle Collaboration in 2006 [14] along with its isospin partners $\Sigma_c(2800)^+$ and $\Sigma_c(2800)^{++}$. The $\Sigma_c(2800)^0$ resonance was fit with a D-wave Breit-Wigner distribution. Belle measured $\Delta m = m_{\Sigma_c(2800)^0} - m_{\Lambda_c^+} = 515 \pm 3 {}^{+\,2}_{-\,6}\,\mathrm{MeV}/c^2$, which corresponds to an absolute mass of $2802 {}^{+\,4}_{-\,7}\,\mathrm{MeV}/c^2$ [9]. The natural width of the resonance is $61^{+\,28}_{-\,18}\,\mathrm{MeV}$ [14]. The Δm distributions for each of the three $\Sigma_c(2800)$ states are shown in Figure 13.4.

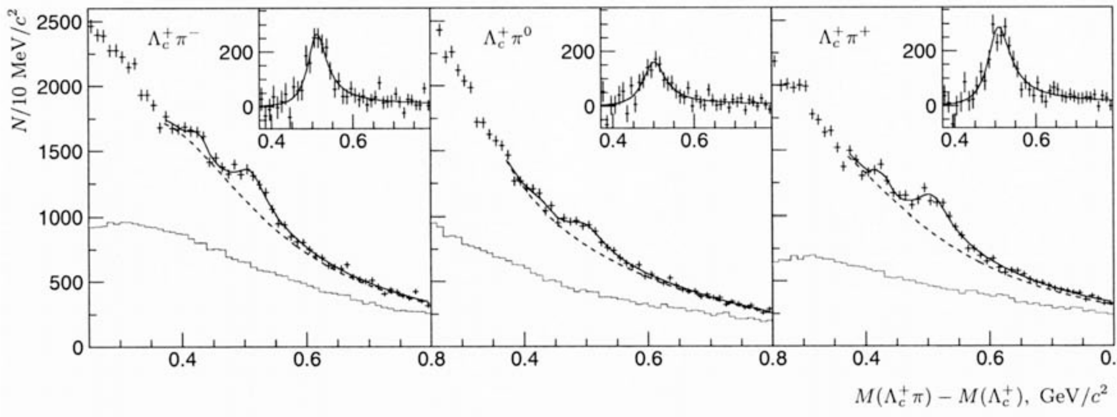

Figure 13.4: Distributions of $\Delta m = m_{\Sigma_c(2800)} - m_{\Lambda_c^+}$ in continuum $\Lambda_c\pi$ data from the Belle Collaboration showing enhancements near $\Delta m = 0.51\,\mathrm{GeV}/c^2$ [14]. The $\Sigma_c(2800)^0$ resonance is shown in the left subfigure. The additional enhancement near $\Delta m = 0.43\,\mathrm{GeV}/c^2$ is attributed to feed-down from $\Lambda_c(2880)^+ \to \Lambda_c^+\pi^+\pi^-$ and $\Lambda_c(2880)^+ \to \Lambda_c^+\pi^0\pi^0$ decays. The insets show background-subtracted events.

There are some limitations to the descriptions of these new states. The background shape shown in Figure 13.4 is an inverse third order polynomial, but does not describe the background distribution in the region below $\Delta m \sim 0.35\,\mathrm{GeV}/c^2$. Also, the shape of the $\Lambda_c^+\pi^-$ background PDF near $\Delta m = 0.43\,\mathrm{GeV}/c^2$ is concave down, which seems inappropriate compared to the overall background distribution. The fit region and background parameterization are the dominant contributions to the systematic uncertainties in the Belle measurement. However, the observation of all three charge states is quite compelling evidence for the existence of the $\Sigma_c(2800)$.

The evidence for the $\Sigma_c(2800)^0$ in continuum $\Lambda_c\pi$ events prompted the search for the

$\Sigma_c(2800)^0$ in B decays. In our data sample, figure 13.5 illustrates the signal ${}_s\mathcal{P}lot$ weights projected onto the $m_{\Lambda_c\pi}$ axis in the vicinity of the $\Sigma_c(2800)^0$. A signal is evident for an excited Σ_c^0 state, which we will call the $\Sigma_c(2800)^0$ with the caveat that there is some evidence (to be discussed later) that the state we observe is not the same excited Σ_c state that the Belle Collaboration has observed.

We describe the 1-D binned χ^2 fit to discriminate between resonant signal ($B^- \to \Sigma_c(2800)^0\overline{p}$) and non-resonant signal ($B^- \to \Lambda_c^+\overline{p}\pi^-$) events.

Resonant Signal PDF

The form of the resonant signal PDF is a relativistic Breit-Wigner distribution:

$$\mathcal{P}_{relBW}(m_{\Lambda_c\pi}; m_r, \Gamma(q)) \propto \frac{\Gamma(q)}{(m_r - m_{\Lambda_c\pi})^2 + m_r^2\Gamma^2(q)}, \tag{13.7}$$

where m_r is the mass of the resonance. Note that the width Γ, is mass-dependent ($\Gamma(q) = \Gamma_r$ at $m = m_r$ and $\Gamma(q) = 0$ at threshold):

$$\Gamma(q) = \Gamma_r \left(\frac{q}{q_r}\right)^{2L+1} \left(\frac{m_r}{m_{\Lambda_c\pi}}\right) B'_L(q, q_r)^2. \tag{13.8}$$

The quantity L is the angular momentum ($L = 0, 1, 2$ is S-wave, P-wave, D-wave, respectively) and q is the momentum of the Λ_c^+ (= the momentum of the π^-) in the $\Sigma_c(2800)^0$ rest frame:

$$q = |\vec{p}_{\Lambda_c^+}| = |\vec{p}_{\pi^-}| = \frac{\sqrt{\left(m_{\Lambda_c\pi}^2 - (m_{\Lambda_c} + m_\pi)^2\right)\left(m_{\Lambda_c\pi}^2 - (m_{\Lambda_c} - m_\pi)^2\right)}}{2\, m_{\Lambda_c\pi}}. \tag{13.9}$$

Note that q is identical to the phase-space function introduced in Eqn. 13.5. The quantity q_r is defined as $q(m_{\Lambda_c\pi} = m_r)$. In Eqn. 13.8, $B'_L(q, q_r)$ is the Blatt-Weisskopf barrier factor [9]:

$$\begin{aligned} B'_0(q, q_r) &= 1 \\ B'_1(q, q_r) &= \sqrt{\frac{1 + q_r^2\, d^2}{1 + q^2\, d^2}} \\ B'_2(q, q_r) &= \sqrt{\frac{(q_r^2\, d^2 - 3)^2 + 9q_r^2\, d^2}{(q^2\, d^2 - 3)^2 + 9q^2\, d^2}}, \end{aligned} \tag{13.10}$$

where we define a constant impact parameter $d = 1\,\text{fm} = 5.0677\,\text{GeV}^{-1}$ (the approximate radius of a baryon). Blatt-Weisskopf barrier factors are weights to account for the fact that the maximum angular momentum (L) in a strong decay is limited by the linear momentum (q). Slow Λ_c^+ and π^- daughters in a $\Sigma_c(2800)^0$ decay have difficulty generating enough angular momentum to conserve the $\Sigma_c(2800)^0$ spin.

In the fit to the $\Sigma_c(2800)^0$, we use the relativistic D-wave ($L = 2$) Breit-Wigner and Blatt-Weisskopf factors. Since the resonance is quite wide, we do not need to include a resolution function in the resonant signal PDF. The two fit parameters (m_r and Γ_r) of the $\Sigma_c(2800)^0$ are free in the fit.

Non-resonant Signal PDF

The form of the non-resonant signal PDF is a first-order polynomial, with one free shape parameter, a (the slope, in GeV^{-1}):

$$\mathcal{P}_{nr}(m_{\Lambda_c\pi}; a) \propto \left(1 + a\,(m_{\Lambda_c\pi} - 2.800)\right). \tag{13.11}$$

Fit Results

The nominal fit results are summarized in Table 13.2. The event yields are again **efficiency-corrected**. We obtain 1449 ± 284 resonant signal events. The χ^2 from the fit is 37 with 31 degrees of freedom (DOF), so the χ^2/DOF is 1.19 and the χ^2 probability is 22%. If the signal yield is fixed[1] to zero, the resulting χ^2 is 78 with 34 DOF (χ^2/DOF = 2.29, χ^2 probability = 2.8×10^{-5}). The significance can be calculated by comparing the χ^2 value with and without a signal: $\Delta\chi^2 = 40.9$, which is equivalent to 5.8σ for the joint estimation of three parameters.

Note that our measured width ($86\,^{+\,33}_{-\,22}\,\text{MeV}/c^2$) is consistent with the width measured by Belle. However, our measured mass for the $\Sigma_c(2800)^0$ is $2846 \pm 0.008\,\text{MeV}/c^2$, $40\,\text{MeV}/c^2$ and 3.9σ higher than Belle's measured mass for this state.

---

[1] The mean and width are fixed to the central values from the nominal fit.

Table 13.2: Fit results for $B^- \rightarrow \Sigma_c(2800)^0\overline{p}$. N_{nr} is the non-resonant signal yield and N_{sig} is the resonant signal yield in the fit range. The world average values of the mass and width of the $\Sigma_c(2800)^0$ are included [9].

Fit Parameter	Value	PDG Value [9]
N_{sig}	1449 ± 284	
m_r (GeV/c^2)	2.846 ± 0.008	$2.802\,^{+\,0.004}_{-\,0.007}$
Γ_r (MeV/c^2)	$86\,^{+\,33}_{-\,22}$	$61\,^{+\,28}_{-\,18}$
N_{nr}	2619 ± 367	
a (GeV $^{-1}$)	-1.1 ± 0.3	

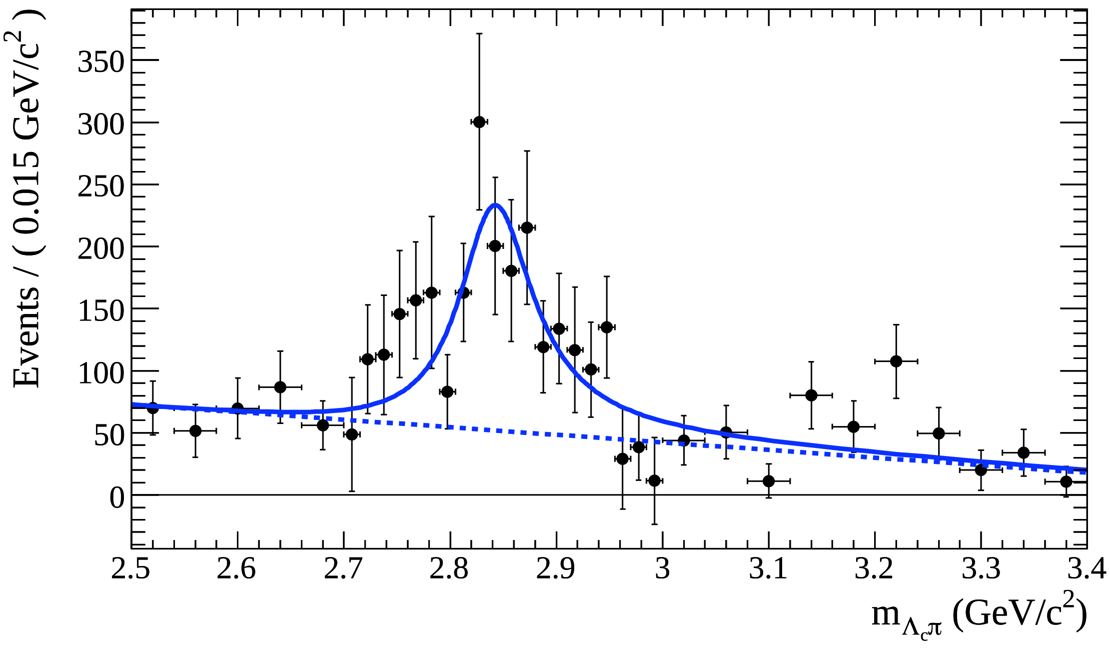

Figure 13.5: Projection of $m_{\Lambda_c\pi}$ in the region of the $\Sigma_c(2800)^0$ resonance. Events are **efficiency-corrected** and weighted using the ${}_s\mathcal{P}lot$ technique. The result of a binned χ^2 fit to a relativistic D-wave Breit-Wigner signal with a mass-dependent width plus a linear background is overlaid. The variable bin sizes range from $15 - 40\,\mathrm{MeV}/c^2$.

13.3 Systematic Uncertainties

Fit systematic uncertainties for the two $\varSigma_c$ resonances can be evaluated by modifying the binning, and the signal and background PDF shapes.

$\boldsymbol{\varSigma_c(2455)^0}$ Systematic Uncertainties

The following sources were considered in evaluating the $\varSigma_c(2455)^0$ fit systematic uncertainty:

- **Resonant Signal PDF:** A relativistic Breit-Wigner PDF was used (without a resolution function) instead of the nominal non-relativistic Breit-Wigner PDF. No significant change in N_{sig}, m_r, or Γ_r was observed for the S-wave, P-wave, or D-wave Breit-Wigner.

- **Non-resonant Signal PDF:** The (fixed) ARGUS parameter (c_{ARG}) was varied $\pm 1\sigma$ (where σ is the statistical uncertainty from the MC fit). No significant change in N_{sig}, m_r, or Γ_r was observed.

- **Binning:** The bin width in the peak region was decreased from the nominal $1\,\mathrm{MeV}/c^2$ to $0.5\,\mathrm{MeV}/c^2$. This is the dominant systematic uncertainty on N_{sig}, 6.9%. In this fit there is a 15% change in the $\varSigma_c(2455)^0$ width (Γ_r) but no significant change in m_r.

The fit results are summarized in Table 13.3 and compared to the nominal fit result. The χ^2 probability is reported for each fit as well.

$\boldsymbol{\varSigma_c(2800)^0}$ Systematic Uncertainties and Cross-checks

The following sources were considered in evaluating the $\varSigma_c(2800)^0$ fit systematic uncertainty:

- **Resonant Signal PDF:** An S-wave and P-wave relativistic Breit-Wigner PDF was used instead of the nominal D-wave relativistic Breit-Wigner PDF. The largest deviation is taken as the systematic uncertainty: 5.9% on N_{sig} and 8.1% on Γ_r. No significant change in m_r is observed.

- **Non-resonant Signal PDF:** A second-order polynomial is used for the background shape (introducing an additional parameter b); the resulting systematic uncertainty is 1.2% on N_{sig} and 2.3% on Γ_r. No significant change in m_r is observed.

- **Binning:** The bin width in the peak region was varied from $10-20\,\mathrm{MeV}/c^2$ (compared to the nominal $15\,\mathrm{MeV}/c^2$). This is the dominant systematic uncertainty. The largest deviation is taken as the systematic uncertainty: 20% on N_{sig}, 0.4% on m_r, and 26% on Γ_r.

The fit results are summarized in Table 13.4 and compared to the nominal fit result. The χ^2 probability and significance is reported for each fit result as well.

A cross-check is performed to make sure the $\mathit{\Sigma}_c(2800)^0$ signal is not the result of interference with a $\Delta(1232)^{++}$, for example (although no significant $\Delta(1232)^{++}$ signal is seen in the $m_{p\pi}$ distribution). The nominal fit is performed in the $\mathit{\Sigma}_c(2800)^0$ mass region with $m_{p\pi} > 1.5\,\mathrm{GeV}/c^2$. We obtain 1329 ± 230 resonant signal events (compared to 1449 ± 284 events for the nominal fit) and a consistent mass and width.

An additional cross-check is performed to make sure that there are appropriate fractions of resonant $\mathit{\Sigma}_c(2800)^0$ events in different $\mathit{\Lambda}_c^+$ decay modes. This is accomplished by dividing the ${}_s\mathcal{P}lot$-weighted, efficiency-corrected data into two samples according to the $\mathit{\Lambda}_c^+$ decay mode. Note that this neglects statistical correlations from the combined $(m_{\mathrm{rec}} - m_B)$ vs. $(m_{\mathrm{miss}} + m_B)/2$ fit (maximally 15%) among the $\mathit{\Lambda}_c^+$ decay modes. A binned χ^2 fit to only $\mathit{\Lambda}_c^+ \to pK^-\pi^+$ candidates gives $N_{sig} = 776 \pm 160$, compared to 6463 ± 241 total non-resonant $B^- \to \mathit{\Lambda}_c^+\overline{p}\pi^-$, $\mathit{\Lambda}_c^+ \to pK^-\pi^+$ events ($(12 \pm 3)\%$). A binned χ^2 fit to a combined sample[2] of $\mathit{\Lambda}_c^+ \to pK_S^0$, $\mathit{\Lambda}_c^+ \to pK_S^0\pi^+\pi^-$, $\mathit{\Lambda}_c^+ \to \mathit{\Lambda}\pi^+$, and $\mathit{\Lambda}_c^+ \to \mathit{\Lambda}\pi^+\pi^-\pi^+$ candidates gives $N_{sig} = 530 \pm 177$ compared to 5956 ± 431 non-resonant events ($(9 \pm 3)\%$). The fractions are consistent in the two samples and the total (1306 ± 239 events) is consistent with the nominal fit result within uncertainties.

---

[2] In order for this fit to converge, m_r and Γ_r were fixed to their nominal values.

Table 13.3: Fit results for different binning and resonant signal, non-resonant signal, and background PDF shapes for the $\Sigma_c(2455)^0$. Varying the bin size in the signal region from 1.0 MeV/c^2 to 0.5 MeV/c^2 causes the largest variation in the number of resonant signal events (N_{sig}) and in the width (Γ_r).

Fit Parameter	Nominal	$S/P/D$-wave Rel BW	ARGUS		Binning
N_{sig}	1522 ± 149	1522 ± 149	1522 ± 149	1522 ± 149	1417 ± 141
m_r (GeV/c^2)	2.4540 ± 0.0002	2.4540 ± 0.0002	2.4540 ± 0.0002	2.4540 ± 0.0002	2.4540 ± 0.0002
Γ_r (MeV/c^2)	2.6 ± 0.5	2.6 ± 0.5	2.6 ± 0.5	2.6 ± 0.5	2.2 ± 0.4
σ_1 (MeV/c^2)	0.297	–	0.297	0.297	0.297
σ_2 (MeV/c^2)	0.66	–	0.66	0.66	0.66
f	0.50	–	0.50	0.50	0.50
N_{nr}	162 ± 102	162 ± 102	131 ± 82	161 ± 101	192 ± 98
c	−0.0011	−0.0011	−0.0003	−0.0019	−0.0011
χ^2	15.3	15.3	15.3	15.3	21.4
DOF	17	17	17	17	22
$P(\chi^2)$	57%	57%	57%	57%	50%

Table 13.4: Fit results for different binning and resonant signal, non-resonant signal, and background PDF shapes for the $\Sigma_c(2800)^0$.

Fit Parameter	Nominal	S-wave Rel BW	P-wave Rel BW	NR Polynomial	10 MeV/c^2 Bins	20 MeV/c^2 Bins
N_{sig}	1449 ± 284	1534 ± 312	1505 ± 301	1467 ± 369	1159 ± 246	1335 ± 295
m_r (GeV/c^2)	2.846 ± 0.008	2.846 ± 0.007	2.846 ± 0.008	2.846 ± 0.008	2.837 ± 0.007	2.836 ± 0.007
Γ_r (MeV/c^2)	86 ± 25	93 ± 28	91 ± 27	88 ± 29	64 ± 20	76 ± 29
N_{nr}	2619 ± 367	2541 ± 388	2569 ± 380	2599 ± 447	2506 ± 340	2570 ± 377
a	-1.1 ± 0.3	-1.0 ± 0.3	-1.1 ± 0.3	-1.2 ± 0.8	-1.1 ± 0.3	-1.1 ± 0.3
b	–	–	–	0.1 ± 1.7	–	–
χ^2	36.8	36.0	36.2	36.8	62.1	42.7
DOF	31	31	31	30	41	26
$P(\chi^2)$	21.7%	24.5%	23.9%	18.2%	1.8%	2.1%
$\Delta(\chi^2)$	40.9	41.7	41.5	33.6	36.6	38.9
Significance	5.8σ	5.9σ	5.8σ	5.2σ	5.4σ	5.6σ

13.4 $\Sigma_c(2520)^0$ Mass Region

We also perform a fit in the region of the $\Sigma_c(2520)^0$, though no significant signal is evident. We fix the mass and width of the state to the world average values [9]: $m_r = 2518.0 \pm 0.5\,\text{MeV}/c^2$ and $\Gamma_r = 16.1 \pm 2.1\,\text{MeV}/c^2$, and use the same PDF as for the $\Sigma_c(2800)^0$ described in Section 13.2. Figure 13.6 illustrates the signal ${}_s\mathcal{P}lot$ weights projected onto the $m_{\Lambda_c\pi}$ axis in the vicinity of the $\Sigma_c(2520)^0$. The result of the binned χ^2 fit is summarized in Table 13.5.

The χ^2 from the fit is 34 with 33 degrees of freedom (DOF), so the χ^2/DOF is 1.03 and the χ^2 probability is 43%. If the signal yield is fixed to zero, the resulting χ^2 is 34 with 34 DOF (χ^2/DOF = 1.00, χ^2 probability = 47%). The significance can be calculated by comparing the χ^2 value with and without a signal: $\Delta\chi^2 = 0.14$, which is equivalent to 0.4σ for the joint estimation of one parameter.

Table 13.5: Fit results for $B^- \to \Sigma_c(2520)^0\overline{p}$. N_{nr} is the non-resonant signal yield and N_{sig} is the resonant signal yield. The measured values of the mass and width of the $\Sigma_c(2800)^0$ are included [9].

Fit Parameter	Value	PDG Value [9]
N_{sig}	27 ± 69	
m_r (GeV/c^2)	2.518	2.5180 ± 0.0005
Γ_r (MeV/c^2)	16.1	16.1 ± 2.1
N_{nr}	289 ± 113	
a (GeV $^{-1}$)	2 ± 8	

$\Sigma_c(2520)^0$ Systematic Uncertainties and Upper Limit

We determine a systematic uncertainty on the fit yield by varying the mean m_r and width Γ_r by ±1σ from the PDG values. The maximum deviation due to the uncertainty on m_r is −2 events, and the maximum deviation due to the uncertainty on Γ_r is −3 events.

To determine the 90% confidence level (C.L.) upper limit on the number of $B^- \to \Sigma_c(2520)^0\overline{p}$ events, we compute $N_{sig} + 1.28\sigma$. This method assumes that the distribution of the measured number of signal events is Gaussian. We verify this assumption by mapping the $\Delta(\chi^2)$ distribution between a fixed number of signal events and the nominal fit (Figure 13.7). The distribution is a parabola, so the uncertainties are sufficiently Gaussian.

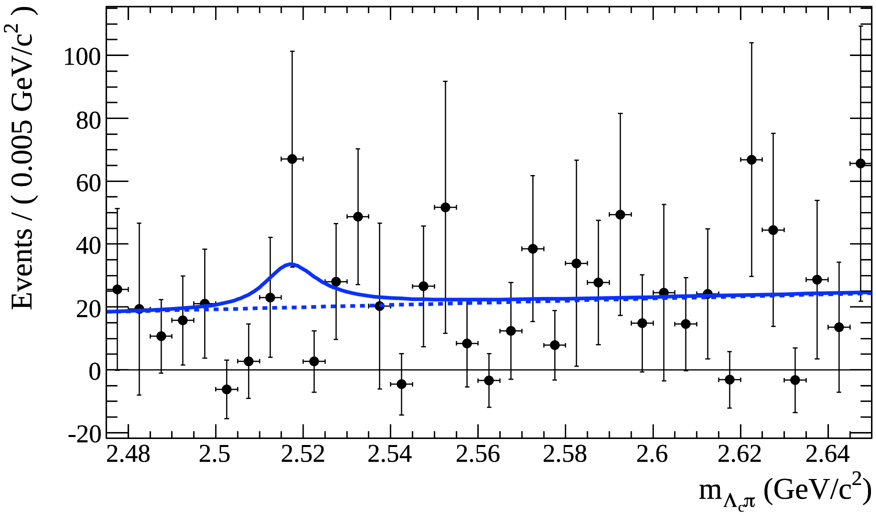

Figure 13.6: Projection of $m_{\Lambda_c\pi}$ in the region of the $\Sigma_c(2520)^0$ resonance. Events are **efficiency-corrected** and weighted using the $_s\mathcal{P}lot$ technique, and the result of a binned χ^2 fit to a relativistic D-wave Breit-Wigner signal with a mass-dependent width plus a linear background is overlaid. The bin size is 5 MeV/c^2. No significant signal is seen.

If we include the systematic uncertainties, the 90% C.L. upper limit is

$$N_{sig} + 1.28\sqrt{\sigma^2_{\text{stat}} + \sigma^2_{\text{syst}}} = 109 \text{ events.}$$

13.5 Summary of Measurements

We measure the fraction of $B^- \to \Lambda_c^+ \overline{p}\pi^-$ decays that proceed through $B^- \to \Sigma_c(2455)^0\overline{p}$ and $B^- \to \Sigma_c(2800)^0\overline{p}$:

$$\begin{aligned} \frac{\mathcal{B}(B^- \to \Sigma_c(2455)^0\overline{p})}{\mathcal{B}(B^- \to \Lambda_c^+\overline{p}\pi^-)} &= (12.3 \pm 1.2 \pm 0.8)\% \\ \frac{\mathcal{B}(B^- \to \Sigma_c(2800)^0\overline{p})}{\mathcal{B}(B^- \to \Lambda_c^+\overline{p}\pi^-)} &= (11.7 \pm 2.3 \pm 2.4)\%. \end{aligned} \tag{13.12}$$

In the branching ratios, the dominant uncertainties are from the $\Sigma_c(2455)^0$ and $\Sigma_c(2800)^0$ yields and fitting systematics. We assume that there is an equivalent contribution from each Λ_c^+ decay mode for events in the Σ_c regions compared to the measured contribution

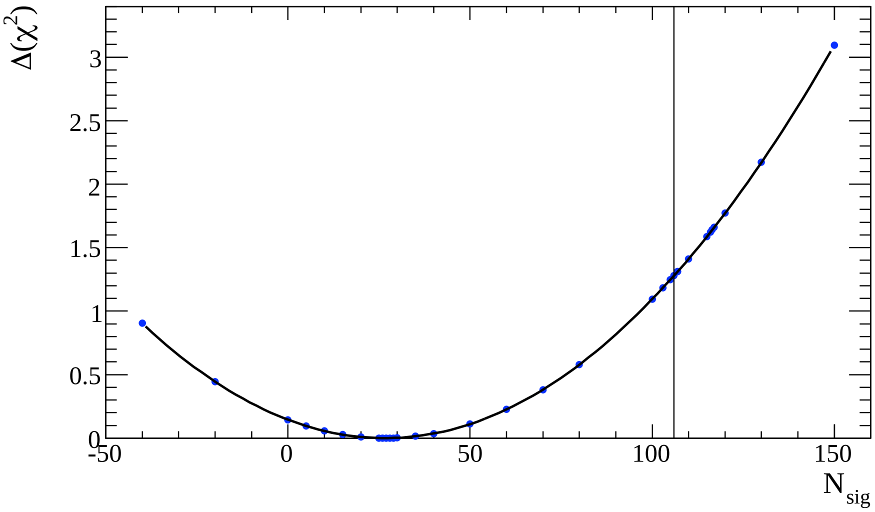

Figure 13.7: Distribution of $\Delta(\chi^2)$ compared to the nominal fit. Each point represents a fit where N_{sig} is fixed to the given value. A second-order polynomial is overlaid. The one-sided 90% C.L. upper limit is at $\Delta(\chi^2) = 1.28$ (indicated by the vertical line).

from each Λ_c^+ decay mode in all (resonant and non-resonant) $B^- \to \Lambda_c^+ \overline{p} \pi^-$ events.

We also set an 90% C.L. upper limit on $\mathcal{B}(B^- \to \Sigma_c(2520)^0 \overline{p})$:

$$\frac{\mathcal{B}(B^- \to \Sigma_c(2520)^0 \overline{p})}{\mathcal{B}(B^- \to \Lambda_c^+ \overline{p} \pi^-)} < 0.9\%. \tag{13.13}$$

13.6 Baryon-antibaryon Threshold Enhancement

The baryon-antibaryon threshold enhancement can be seen in $B^- \to \Lambda_c^+ \overline{p} \pi^-$ decays as an enhancement in $m_{\Lambda_c p}$ near the kinematic limit, $m^0_{\Lambda_c \overline{p}} = 3224.8\,\mathrm{MeV}/c^2$. Figure 13.8 illustrates the signal ${}_s\mathcal{P}lot$ weights projected onto the $m_{\Lambda_c p}$ axis. Superimposed is the expectation from three-body phase space.

We can also correct each ${}_s\mathcal{P}lot$-weighted bin by a phase-space factor. This is shown in Figure 13.9. Enhancements in both Figure 13.8 and 13.9 are clearly visible.

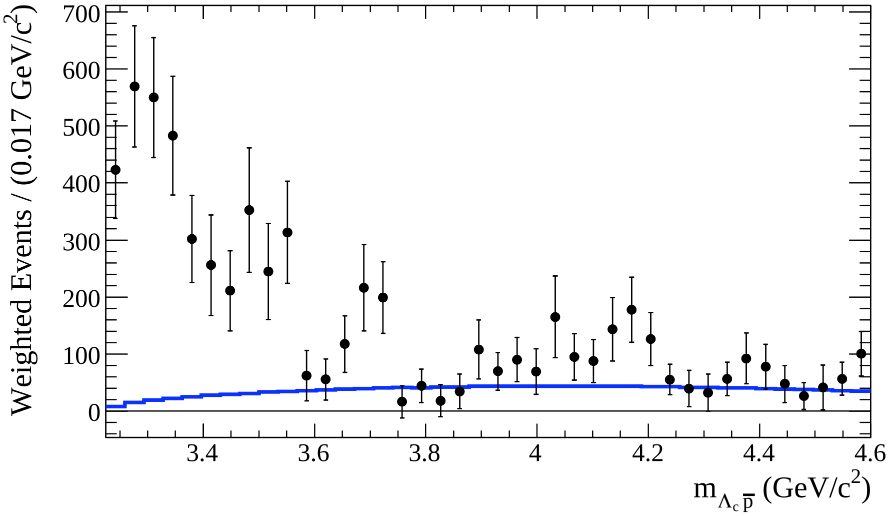

Figure 13.8: Projection of $m_{\Lambda_c p}$ near threshold. Events are **efficiency-corrected** and weighted using the ${}_s\mathcal{P}lot$ technique, and the expected distribution from three-body phase space is overlaid. An enhancement in $m_{\Lambda_c p}$ is clearly visible near threshold.

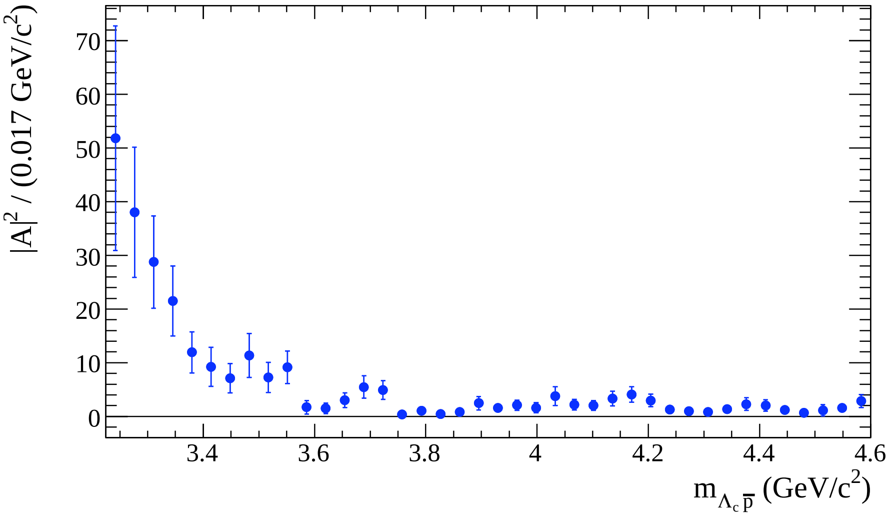

Figure 13.9: Projection of $m_{\Lambda_c p}$ near threshold. Events are **efficiency-corrected**, weighted using the ${}_s\mathcal{P}lot$ technique, and corrected according to three-body phase space. An enhancement is clearly visible near threshold; this is the baryon-antibaryon *threshold enhancement* seen in all baryonic B meson decays.

Chapter 14

Measurement of the $\Sigma_c(2455)^0$ Spin

In this chapter, we provide a quantitative evaluation of the spin-1/2 and spin-3/2 hypotheses for the $\Sigma_c(2455)^0$ baryon. The $\Sigma_c(2455)^0$ is the lowest mass Σ_c state. In the quark model, it is expected to have $J^P = \frac{1}{2}^+$, where J is the spin and P is the parity.

We determine the spin of the $\Sigma_c(2455)^0$ through an angular analysis of the decay $B^- \to \Sigma_c(2455)^0\overline{p}$, $\Sigma_c(2455)^0 \to \Lambda_c^+\pi^-$. We define a helicity angle θ_h as the angle between the momentum vector of the Λ_c^+ and the momentum vector of the recoiling B-daughter $\overline{p}$ in the rest frame of the $\Sigma_c(2455)^0$. If we assume $J(\Lambda_c^+) = 1/2$, the angular distributions for the spin-1/2, spin-3/2, and spin-5/2 hypotheses for the $\Sigma_c(2455)^0$ are[1]

$$\begin{aligned}
J(\Sigma_c^0) = \frac{1}{2}: &\quad \frac{dN}{d\cos\theta_h} \propto 1 \\
J(\Sigma_c^0) = \frac{3}{2}: &\quad \frac{dN}{d\cos\theta_h} \propto 1 + 3\cos^2\theta_h \\
J(\Sigma_c^0) = \frac{5}{2}: &\quad \frac{dN}{d\cos\theta_h} \propto 1 - 2\cos^2\theta_h + 5\cos^4\theta_h.
\end{aligned} \tag{14.1}$$

With only $\sim$ 100 events, discriminating between spin-3/2 and spin-5/2 would be nearly impossible; nevertheless, we include the spin-5/2 distribution for completeness.

These angular distributions are the ideal distributions; the measured angular distributions will be somewhat degraded due to nonuniform detector efficiencies, finite experimental

---

[1] Derivations of these angular distributions can be found in Appendix B.

resolution for measuring θ_h, and background contamination. We estimate the effects of inefficiencies and background contamination by performing toy MC studies to quantify the decrease in sensitivity to discriminate between possible spin values. The finite experimental resolution is measured from a $B^- \to \Lambda_c^+ \overline{p} \pi^-, \Lambda_c^+ \to p K^- \pi^+$ signal MC sample by comparing the measured value of $\cos\theta_h$ to the true value.

The $m_{\Lambda_c\pi}$ distribution in the vicinity of the $\Sigma_c(2455)^0$ is shown in Figure 14.1 (no ${}_s\mathcal{P}lot$ weights or efficiency correction is applied). These candidates are selected from a $\pm 2\sigma$ signal region in $(m_{\text{miss}} + m_B)/2$ and $(m_{\text{rec}} - m_B)$. There are 127 events in the $\Sigma_c(2455)^0$ signal region and 27 events in the $\Sigma_c(2455)^0$ background regions. We can scale the number of events in the background region by the ratio of the total width of the background regions compared to the width of the signal region. We therefore expect 7.2 ± 1.3 background events in the signal region. Note that the background regions include true background events (non-$B^- \to \Lambda_c^+ \overline{p} \pi^-$ events) and non-resonant $B^- \to \Lambda_c^+ \overline{p} \pi^-$ signal events.

14.1 Helicity Angle Resolution

We measure the experimental resolution of $\cos\theta_h$ by comparing the measured $\cos\theta_h$ to the true $\cos\theta_h$ in $B^- \to \Lambda_c^+ \overline{p} \pi^-, \Lambda_c^+ \to p K^- \pi^+$ events in a signal MC sample. Figure 14.2 illustrates the profile of $\cos\theta_h(\text{meas.}) - \cos\theta_h(\text{true})$ as a function of the true $m_{\Lambda_c\pi}$ and as a function of $\cos\theta_h(\text{true})$. The points represent the mean of the $\cos\theta_h(\text{meas.}) - \cos\theta_h(\text{true})$ distribution in each bin, and the error bars represent the RMS of the $\cos\theta_h(\text{meas.}) - \cos\theta_h(\text{true})$ distribution in each bin.

From the maximum RMS of $\cos\theta_h(\text{meas.}) - \cos\theta_h(\text{true})$ in the $\Sigma_c(2455)^0$ signal region, we determine the helicity angle resolution $\sigma(\cos\theta_h) < 0.03$. Therefore the finite experimental resolution is small compared to any features in the spin-1/2 or spin-3/2 angular distributions.

14.2 Toy MC Studies

We investigate the discrimination power between spin hypotheses using toy MC studies. For illustration, we generate toy MC samples of 127 events according to both the spin-1/2 and spin-3/2 hypotheses. Figure 14.3 demonstrates one toy distribution generated according to each hypothesis, with each hypothesis overlaid for comparison.

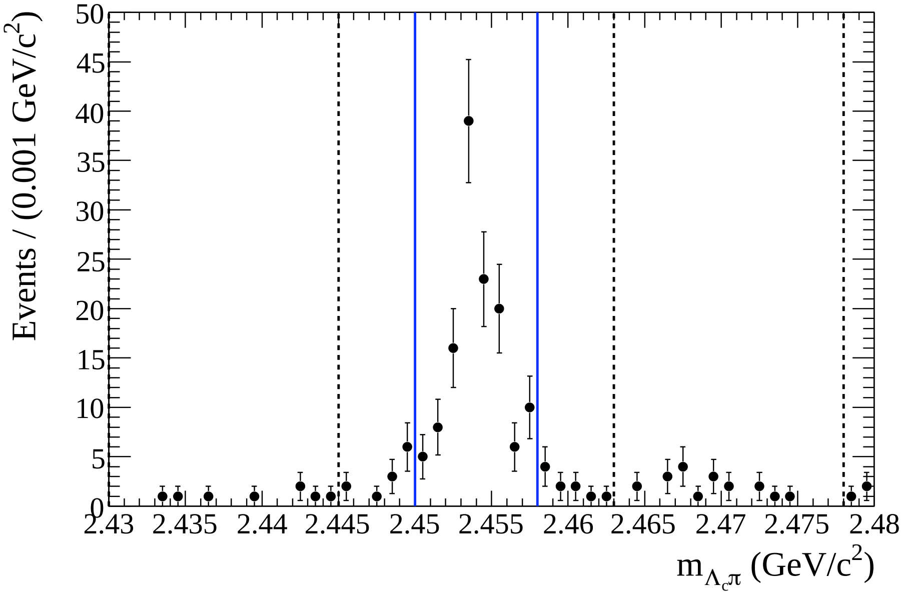

Figure 14.1: The distribution of $m_{\Lambda_c\pi}$ in data in the vicinity of the $\Sigma_c(2455)^0$. No ${}_s\mathcal{P}lot$ weights or efficiency corrections are applied. The $\Sigma_c(2455)^0$ signal region is indicated by the two solid blue lines. There are two symmetric background regions ($2.430 < m_{\Lambda_c\pi} < 2.445\,\mathrm{GeV}/c^2$ and $2.463 < m_{\Lambda_c\pi} < 2.478\,\mathrm{GeV}/c^2$) indicated by the dashed vertical lines and the lower boundary of the plot. There are 127 events in the signal region and 27 events in the background regions.

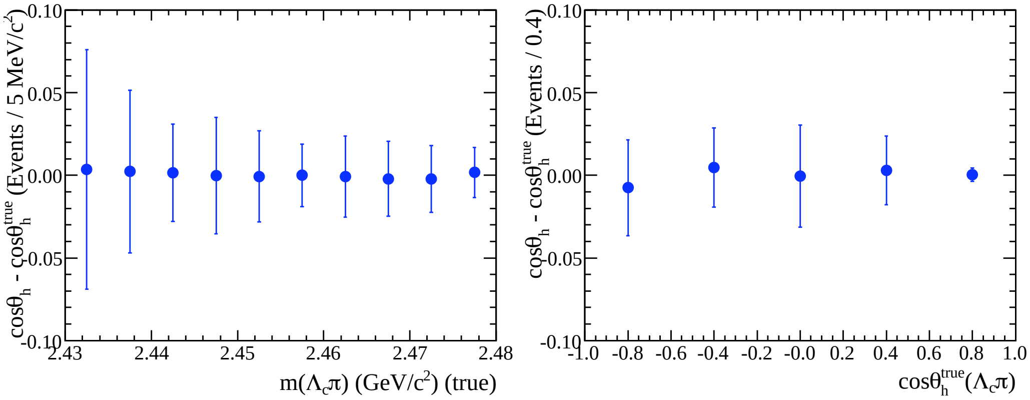

(a) (b)

Figure 14.2: Profile distributions of $\cos\theta_h(\text{meas.}) - \cos\theta_h(\text{true})$ vs. (a) the true $m_{\Lambda_c\pi}$ and (b) $\cos\theta_h(\text{true})$ in a $B^- \to \Lambda_c^+ \overline{p} \pi^-$ signal MC sample. The points represent the mean of the $\cos\theta_h(\text{meas.}) - \cos\theta_h(\text{true})$ distribution in each bin, and the error bars represent the RMS of the $\cos\theta_h(\text{meas.}) - \cos\theta_h(\text{true})$ distribution in each bin. In (b), the distribution is plotted for the mass range $2.450 < m_{\Lambda_c\pi} < 2.458\,\text{GeV}/c^2$ (the $\Sigma_c(2455)^0$ signal region).

In general, the log likelihood is computed $\ln\mathcal{L} = \sum_i w_i \ln(y_i)$, where y_i is the probability density for observing event i. The weight w_i for the toy MC studies is $w_i = \varepsilon_i$, where ε_i is the efficiency for event i. We can compute a log likelihood for each hypothesis:

$$\ln\mathcal{L}(1/2) = \sum_i w_i \ln\tfrac{1}{2} \tag{14.2}$$

$$\ln\mathcal{L}(3/2) = \sum_i w_i \ln\left[\tfrac{1}{4}\left(1 + 3\cos^2\theta_{h,i}\right)\right] \tag{14.3}$$

Note that $\ln\mathcal{L}(1/2)$ does not depend on the measured values of $\theta_{h,i}$.

We then generate 500 samples (127 events each) and compute the likelihood $\mathcal{L}$ that each generated toy distribution is uniform in $\cos\theta_h$ (spin-1/2) or distributed as $1 + 3\cos^2\theta_h$ (spin-3/2). We define the quantity $\Delta\ln\mathcal{L} = \ln\mathcal{L}(1/2) - \ln\mathcal{L}(3/2)$. Figure 14.4 (a) shows the distribution $\Delta\ln\mathcal{L}$ for events generated with each hypothesis. The red distribution (negative values of $\Delta\ln\mathcal{L}$) corresponds to samples generated according to the spin-1/2 hypothesis, and the blue distribution (positive values of $\Delta\ln\mathcal{L}$) corresponds to samples generated according to the spin-3/2 hypothesis. For each distribution, the separation from zero illustrates how well we can discriminate between hypotheses given 127 signal events.

We repeat the toy study several times, in increasing order of complexity. The stages are

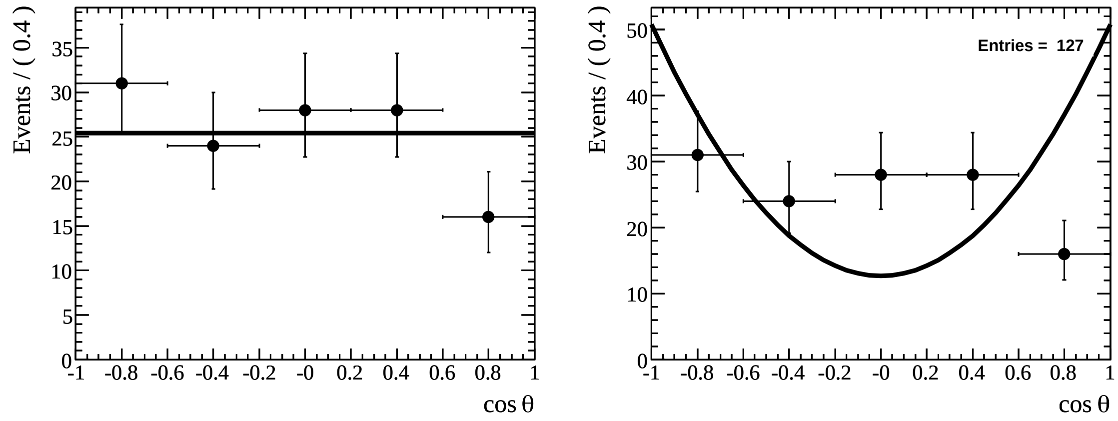

(a) generated as spin-1/2

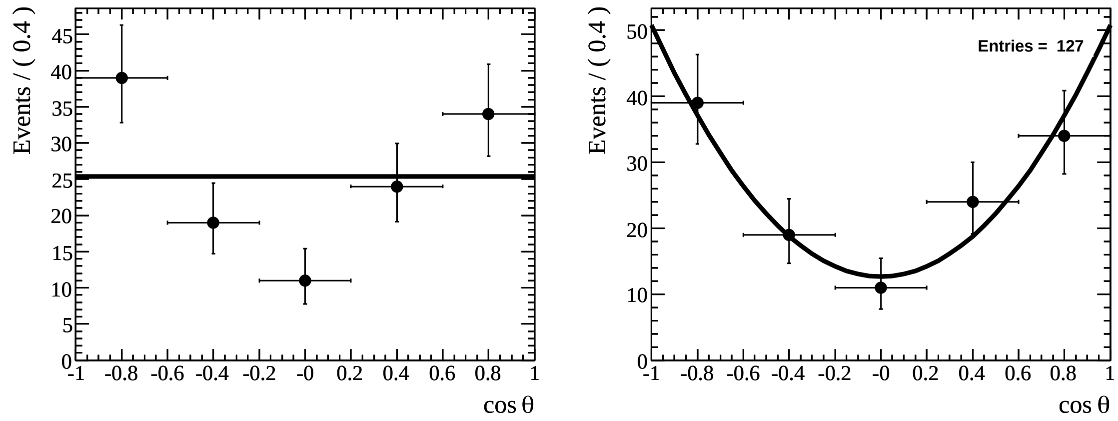

(b) generated as spin-3/2

Figure 14.3: A toy sample generated with (a) a flat distribution and (b) a $1 + 3\cos^2\theta_h$ distribution. The (left) spin-1/2 and (right) spin-3/2 hypotheses are overlaid.

(a) signal events only,

(b) signal and background events,

(c) signal events with a non-uniform binned inefficiency,

(d) signal and background events with a non-uniform binned inefficiency,

(e) signal and background events with a non-uniform binned inefficiency, varying the efficiencies within their uncertainties.

The results of each study are shown in the corresponding subfigure of Figure 14.4. Additional details about the background parameterization and the effects of the inefficiencies follow.

Background Events

The shape of the $\cos\theta_h$ distribution for background events comes from the shape of the helicity distribution for events in the background regions in Figure 14.1. The helicity distribution for these events is illustrated in Figure 14.5 as a non-parametric PDF (a histogram). This PDF is used to generate the number of background events in the signal region with a Poisson uncertainty (7.2 ± 2.7). The total number of events in the sample is fixed to 127, so the background effectively dilutes the signal distribution.

Effect of Binned Inefficiency

The efficiency depends on $\cos\theta_h$, so we multiply each toy MC event by ε_i, where ε_i is the same efficiency described in Chapter 6. In the $\Delta \ln \mathcal{L}$ calculation, the weights are scaled such that $\langle w_i \rangle = 1$. The efficiency in each Λ_c^+ decay mode varies significantly. Therefore, in calculating the efficiency for the combination of all five Λ_c^+ decay modes, the ratios of Λ_c^+ decay modes are fixed according to the yields obtained in the branching fraction measurement. The correction is reduced to 10 bins across $\cos\theta_h$; all signal and background events fall in a single $m_{\Lambda_c\pi}$ bin (see Figure 6.4).

Variation on the Binned Inefficiency

The binned efficiencies described in Chapter 6 have uncertainties due to MC sample statistics. We vary these uncertainties in each bin according to a Gaussian distribution with a

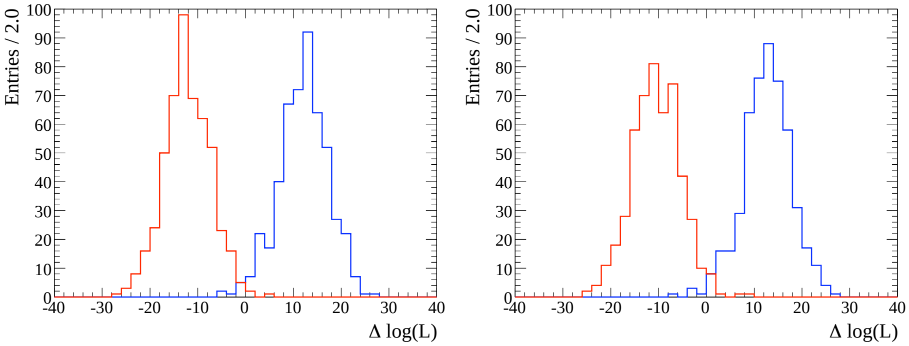

(a) signal

(b) signal and background

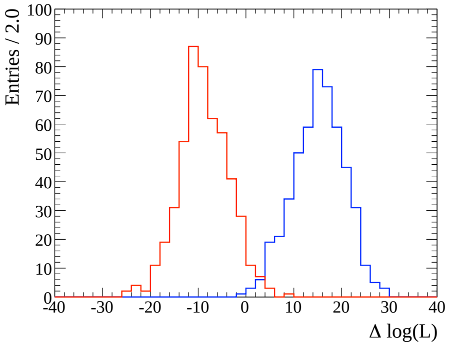

(c) signal, binned efficiency

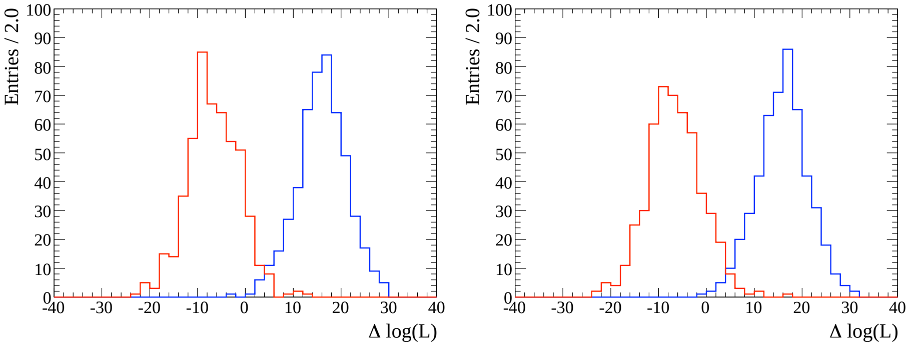

(d) signal and background, binned efficiency

(e) signal and background, varied efficiency

Figure 14.4: Distribution of $\Delta \ln \mathcal{L} = \ln \mathcal{L}(1/2) - \ln \mathcal{L}(3/2)$ for toy MC samples generated with a uniform distribution in $\cos\theta_h$ (blue, positive values) and a $1 + 3\cos^2\theta_h$ distribution (red, negative values). For $\Delta \ln \mathcal{L} > 0$, $J(\Sigma_c^0) = \frac{1}{2}$ is favored.

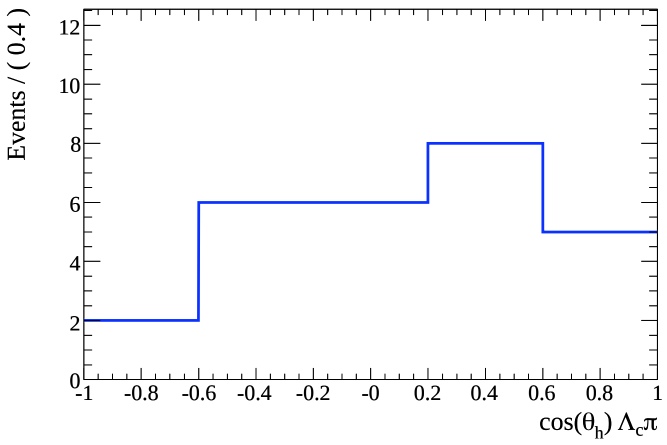

Figure 14.5: Helicity angle distribution for the combined sample of background and non-resonant signal events, a non-parameteric PDF.

mean of ε and a width of $\delta(\varepsilon)$.

Conclusion

The conclusion from these toy MC studies is that the inefficiencies and background contamination do not significantly degrade the power to distinguish between spin-1/2 and spin-3/2 hypotheses. The addition of inefficiencies and background contamination tend to make the spin-1/2 hypothesis appear to be more likely. We correct for the inefficiencies in data, but we do not attempt to correct for the background contamination. Instead, we compare the observed $\Delta \ln \mathcal{L}$ to Figure 14.4(b).

14.3 Spin Measurement of the $\Sigma_c(2455)^0$ in Data

The helicity angle distribution for events in the signal region around the $\Sigma_c(2455)^0$ is shown in Figure 14.6. The points are efficiency-corrected. Functions corresponding to the spin-1/2 (left) and spin-3/2 (right) hypotheses are overlaid. We compute the change in log likelihood between the hypotheses: $\Delta \ln \mathcal{L} = +19.2$. We show Figure 14.4(b) again, enlarged, in Figure 14.7, indicating the value of $\Delta \ln \mathcal{L}$ in data with a vertical line. The observed value of $\Delta \ln \mathcal{L}$ strongly favors the spin-1/2 hypothesis over the spin-3/2 hypothesis for the $\Sigma_c(2455)^0$.

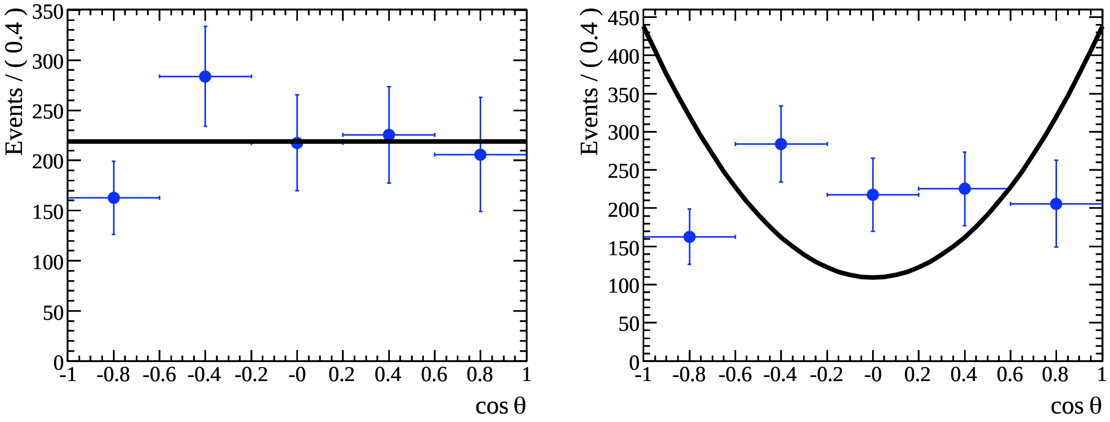

Figure 14.6: The helicity angle distribution in data for the $\Sigma_c(2455)^0$. The points are efficiency-corrected $B^- \to \Sigma_c(2455)^0\overline{p}$ candidates. The (left) spin-1/2 and (right) spin-3/2 hypotheses are overlaid.

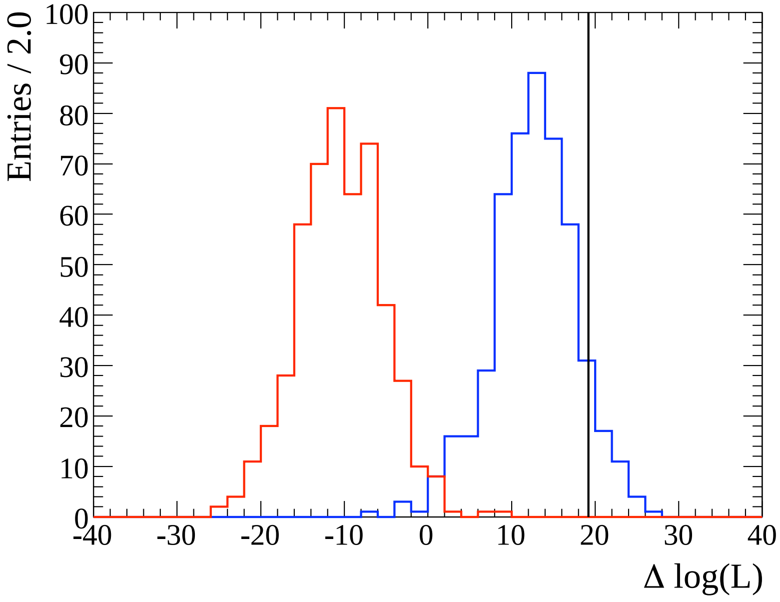

Figure 14.7: Distribution of $\Delta \ln \mathcal{L}$ for signal events generated with a uniform distribution in $\cos\theta_h$ (blue, positive values) and a $1 + 3\cos^2\theta_h$ distribution (red, negative values). Background events are included, and all events are efficiency-corrected. We measure $\Delta \ln \mathcal{L} = +19.2$ in data (indicated by the vertical line), so we accept the spin-1/2 hypothesis.

Chapter 15

Conclusions

15.1 Summary of Branching Fraction Measurements

This dissertation has presented branching fraction measurements of the decays $\overline{B}^0 \rightarrow \Lambda_c^+ \overline{p}$ and $B^- \rightarrow \Lambda_c^+ \overline{p} \pi^-$:

$$\mathcal{B}(\overline{B}^0 \rightarrow \Lambda_c^+ \overline{p}) = (1.89 \pm 0.21 \pm 0.06 \pm 0.49) \times 10^{-5},$$
$$\mathcal{B}(B^- \rightarrow \Lambda_c^+ \overline{p} \pi^-) = (3.38 \pm 0.12 \pm 0.12 \pm 0.88) \times 10^{-4},$$

where the uncertainties are statistical, systematic, and due to the uncertainty on $\mathcal{B}(\Lambda_c^+ \rightarrow pK^-\pi^+)$, respectively. These measurements are based on 383 million $B\overline{B}$ events produced by the SLAC B Factory and recorded by the BABAR detector.

If we combine the statistical and systematic uncertainties only, we obtain $\mathcal{B}(\overline{B}^0 \rightarrow \Lambda_c^+ \overline{p}) = (1.9 \pm 0.2) \times 10^{-5}$, which is consistent with a previous measurement by the Belle Collaboration of $\mathcal{B}(\overline{B}^0 \rightarrow \Lambda_c^+ \overline{p}) = (2.2 \pm 0.6) \times 10^{-5}$ [31]. Both measurements use the same value of $\mathcal{B}(\Lambda_c^+ \rightarrow pK^-\pi^+)$. However, our measurement of the three-body mode, $\mathcal{B}(B^- \rightarrow \Lambda_c^+ \overline{p} \pi^-) = (3.4 \pm 0.2) \times 10^{-4}$, does not agree as with the prior measurement of $\mathcal{B}(B^- \rightarrow \Lambda_c^+ \overline{p} \pi^-) = (2.1 \pm 0.3) \times 10^{-4}$ [30]; our measurement is nearly 4σ larger. The Belle Collaboration measurement uses six coarse regions across the $B^- \rightarrow \Lambda_c^+ \overline{p} \pi^-$ Dalitz plane to correct for variations in efficiency; we use much finer regions and see significant variation near the edges of the Dalitz plane. We believe that this difference in efficiency treatment dominates the discrepancy between the two results.

15.2 Implications for Baryonic B Decays

One of the main motivations for studying baryonic B-meson decays is to gain knowledge about baryon-antibaryon production in meson decays. This dissertation contributes to the growing information about baryon production by comparing two-body and three-body decay rates. We have measured the ratio of the two branching fractions,

$$\frac{\mathcal{B}(B^- \to \Lambda_c^+ \overline{p} \pi^-)}{\mathcal{B}(\overline{B}^0 \to \Lambda_c^+ \overline{p})} = 15.4 \pm 1.8 \pm 0.3. \tag{15.1}$$

This quantity is particularly useful because the 26% uncertainty on $\mathcal{B}(\Lambda_c^+ \to pK^-\pi^+)$ cancels in the branching ratio.

We have also measured the fractions of $B^- \to \Lambda_c^+ \overline{p} \pi^-$ decays that proceed through a Σ_c resonance:

$$\begin{aligned} \frac{\mathcal{B}(B^- \to \Sigma_c(2455)^0 \overline{p})}{\mathcal{B}(B^- \to \Lambda_c^+ \overline{p} \pi^-)} &= (12.3 \pm 1.2 \pm 0.8)\% \\ \frac{\mathcal{B}(B^- \to \Sigma_c(2800)^0 \overline{p})}{\mathcal{B}(B^- \to \Lambda_c^+ \overline{p} \pi^-)} &= (11.7 \pm 2.3 \pm 2.4)\%. \end{aligned} \tag{15.2}$$

About 1/4 of $B^- \to \Lambda_c^+ \overline{p} \pi^-$ decays proceed through a Σ_c resonance. The branching fractions of these resonant two-body decays are the same order of magnitude as $\overline{B}^0 \to \Lambda_c^+ \overline{p}$.

The order of magnitude difference between the decay rates of $B^- \to \Lambda_c^+ \overline{p} \pi^-$ and two-body decays such as $\overline{B}^0 \to \Lambda_c^+ \overline{p}$, $B^- \to \Sigma_c(2455)^0 \overline{p}$, and $B^- \to \Sigma_c(2800)^0 \overline{p}$ is consistent with the theoretical description that baryonic B decays are favored when the baryon and antibaryon are close together in phase space. This interpretation is also supported by the observation of the enhancement in rate when $m_{\Lambda_c p}$ is near threshold. Although the $\Lambda_c^+ \overline{p}$ threshold enhancement alone could indicate a resonance below threshold, enhancements have been observed in other baryon-antibaryon systems and in decays such as $e^+e^- \to p\overline{p}\gamma$. Therefore the body of measurements indicates that we are observing a phenomenon that is common to baryon production from meson decays, and possibly common to baryon production in general.

15.3 Contributions to Charm Baryon Spectroscopy

We have used the angular distribution of the decay $B^- \to \Sigma_c(2455)^0\overline{p}$ to study the spin of the Σ_c^0 baryon. The helicity angle distribution is measured to be uniform, which indicates that the Σ_c^0 has $J = 1/2$ assuming that the ground state Λ_c^+ also has $J = 1/2$. This is consistent with quark model expectations for the lowest Σ_c baryon state.

In addition to measuring baryon spin from resonant B-meson decays, we have also searched for excited Σ_c states. This dissertation presented an observation of B-meson decays through an excited Σ_c^0 resonance. We measure the mass of this resonance to be $2846 \pm 8\,\mathrm{MeV}/c^2$ and the width to be $86\,^{+\,33}_{-\,22}\,\mathrm{MeV}/c^2$. It is possible that this observation is a confirmation of a triplet of Σ_c states called the $\Sigma_c(2800)$ and seen in $\Lambda_c^+\pi^-$ continuum production [14]. However, the neutral $\Sigma_c(2800)^0$ has a measured mass of $2802\,^{+\,4}_{-\,7}\,\mathrm{MeV}/c^2$ and width of $61\,^{+\,28}_{-\,18}\,\mathrm{MeV}/c^2$. The widths of the $\Sigma_c(2800)$ and the state observed in B decays are consistent, but the masses are 4σ apart! If these are indeed the same state, then the large discrepancy in mass measurements must be explained.

Another possible interpretation is that the excited Σ_c^0 resonance seen in this analysis is not the $\Sigma_c(2800)^0$ that was previously observed. A clear signal is evident for $B^- \to \Sigma_c(2455)^0\overline{p}$ decays, but we do not see any evidence for the expected process $B^- \to \Sigma_c(2520)^0\overline{p}$. The absence of the decay $B^- \to \Sigma_c(2520)^0\overline{p}$ is in contrast to a claimed 2.9σ signal from an analysis by the Belle Collaboration based on 152 million $B\overline{B}$ events [30]. Also, an examination of the $B^- \to \Lambda_c^+\overline{p}\pi^-$ Dalitz plot shows no evidence for the decay $B^- \to \Lambda_c^+\bar{\Delta}(1232)^{--}$. The $\Sigma_c(2520)^0$ is a well-established state, and so is the $\Delta(1232)^{++}$. Both are expected to have $J = 3/2$, and there is some evidence that the $\Sigma_c(2800)^0$ is $J = 3/2$ or $5/2$. It is therefore possible that B decays to higher-spin baryons are suppressed, perhaps due to the same baryon production mechanisms that suppress two-body baryonic decays, and that the excited Σ_c^0 state that we have observed is a newly-observed spin-1/2 state.

In conclusion, B Factories have opened up a new laboratory for studying baryon production in meson decays. This dissertation has used B-meson decays to study baryon production and the spectroscopy and spin of charm baryons. We have also revealed new questions to investigate. Why are some baryons produced in B decays and others appear to be suppressed? Have we confirmed the existence of the $\Sigma_c(2800)^0$, or have we observed a different excited Σ_c state? We hope that the answers to these questions can be answered in the large data samples still being recorded at the B Factories.

Appendix A

Λ_c^+ Resolution

The invariant $pK^-\pi^+$ mass for each signal MC sample (with all other optimized selection applied) is plotted in Figures A.1 and A.2. Each sample is fit to a double Gaussian distribution, and the RMS of the standard deviation of the Gaussians determines the Λ_c^+ resolution in each decay mode. These resolutions are also summarized in Table A.1.

Table A.1: Λ_c^+ resolution for $\overline{B}^0$ and B^- candidates determined from fits to $pK^-\pi^+$ invariant mass distributions in signal MC samples.

	Λ_c^+ Resolution (MeV/c^2)	
Mode	$\overline{B}^0$ candidates	B^- candidates
$\Lambda_c^+ \to pK^-\pi^+$	6.81 ± 0.06	6.07 ± 0.03
$\Lambda_c^+ \to pK_S^0$	7.36 ± 0.08	6.87 ± 0.05
$\Lambda_c^+ \to pK_S^0\pi^+\pi^-$	7.23 ± 0.07	7.31 ± 0.10
$\Lambda_c^+ \to \Lambda\pi^+$	7.58 ± 0.07	7.30 ± 0.08
$\Lambda_c^+ \to \Lambda\pi^+\pi^-\pi^+$	7.73 ± 0.10	8.1 ± 0.1

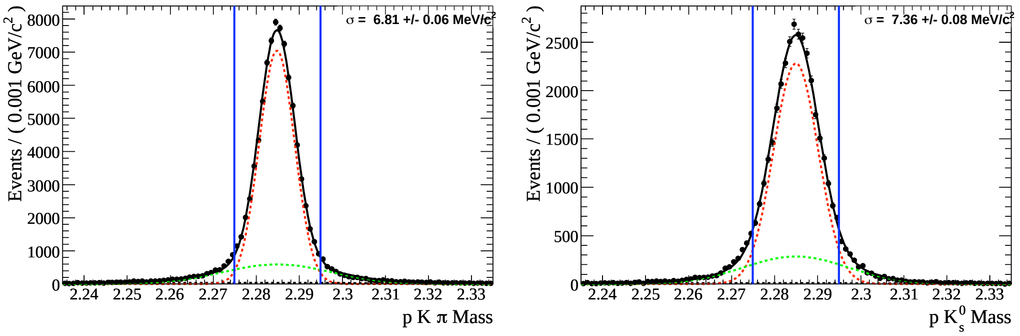

(a) $\Lambda_c^+ \to pK^-\pi^+$

(b) $\Lambda_c^+ \to pK_S^0$

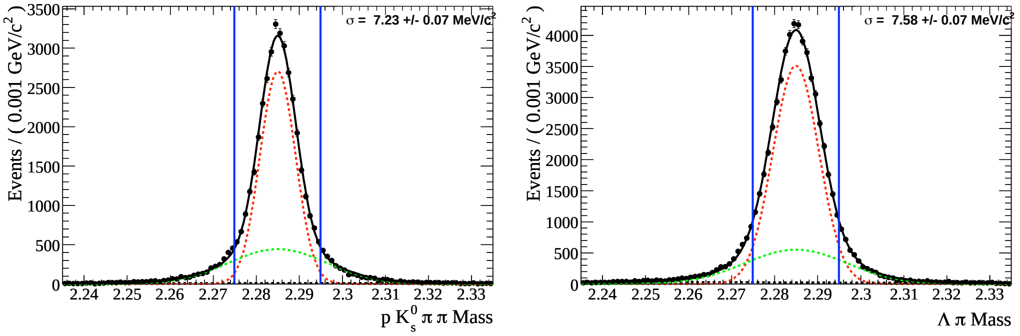

(c) $\Lambda_c^+ \to pK_S^0\pi^+\pi^-$

(d) $\Lambda_c^+ \to \Lambda\pi^+$

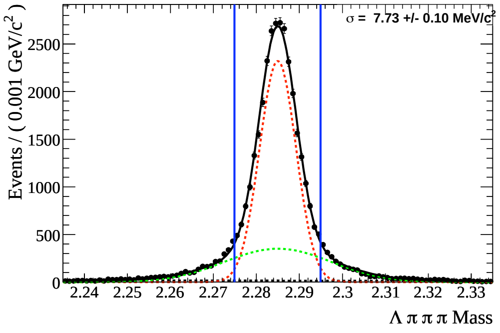

(e) $\Lambda_c^+ \to \Lambda\pi^+\pi^-\pi^+$

Figure A.1: $pK^-\pi^+$ invariant mass distributions for $\overline{B}^0 \to \Lambda_c^+\overline{p}$ candidates in signal MC samples. The resolution is the RMS of the standard deviations from the two Gaussians. All other optimized selection criteria are applied.

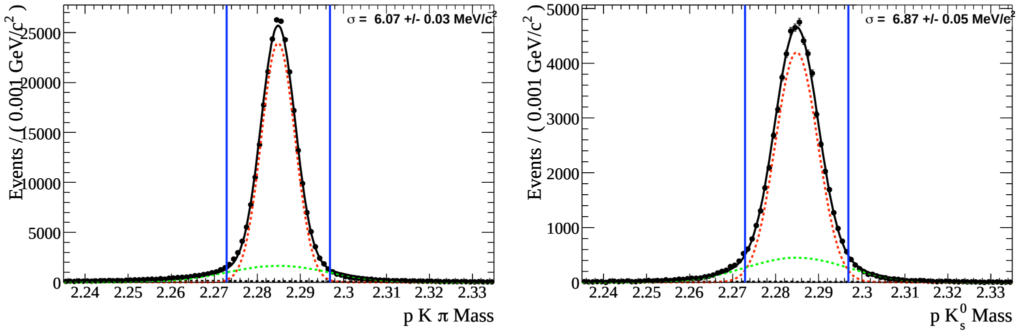

(a) $\Lambda_c^+ \to pK^-\pi^+$ (b) $\Lambda_c^+ \to pK_S^0$

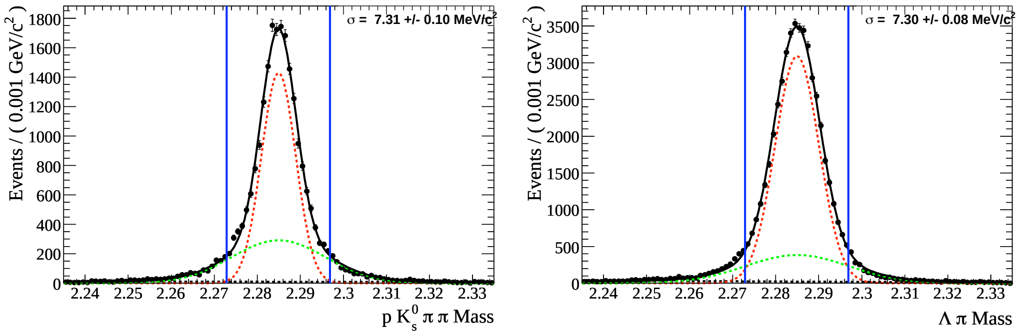

(c) $\Lambda_c^+ \to pK_S^0\pi^+\pi^-$ (d) $\Lambda_c^+ \to \Lambda\pi^+$

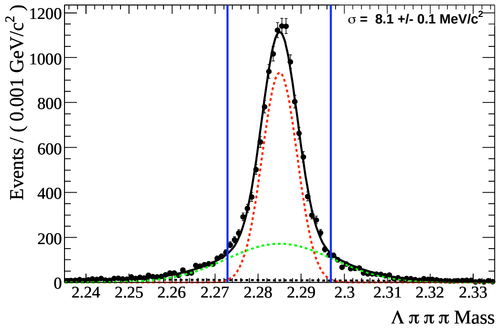

(e) $\Lambda_c^+ \to \Lambda\pi^+\pi^-\pi^+$

Figure A.2: $pK^-\pi^+$ invariant mass distributions for $B^- \to \Lambda_c^+\overline{p}\pi^-$ candidates in signal MC samples. The resolution is the RMS of the standard deviations from the two Gaussians. All other optimized selection criteria are applied.

Appendix B

Angular Analysis Formalism

In this appendix, we derive the angular distribution of the decay $B^- \rightarrow \Sigma_c(2455)^0\overline{p}$, $\Sigma_c(2455)^0 \rightarrow \Lambda_c^+\pi^-$, using the formalism originally developed by Jacob and Wick [53], following the pedagogical explanation and notation established in Ref. [54]. We also use a notebook developed for `Mathematica` to check the calculations [55].

The angular distribution of a decay depends on the spins of the parent and daughter paricles in the decay process. If we can measure the angular distribution of a decay, we can determine the spin of an intermediate particle. A description of the first baryonic application of this technique that was used to measure the spin of the Ω^- can be found in Ref. [34]. By deriving the angular distribution of the decay $B^- \rightarrow \Sigma_c(2455)^0\overline{p}$, $\Sigma_c(2455)^0 \rightarrow \Lambda_c^+\pi^-$, we can determine the spin of the $\Sigma_c(2455)^0$, assuming the spin of the Λ_c^+ is 1/2.

For a generic decay process $a \rightarrow b+c$, we arbitrarily define a z-axis, where particle a has spin J and spin-projection M along that axis. Particles b and c have equal and opposite momenta in the a rest frame. We can thus characterize the decay by the linear momenta and the helicities λ_a, λ_b. The magnitude of the momentum of each daughter is fixed, but the direction can be described by θ, ϕ. In particular, these angles define the direction of particle b w.r.t. the z-axis. Through rotational invariance of the helicities and conservation of angular momentum, we can determine the decay amplitude:

$$\mathcal{A} \propto D^{J*}_{M\,(\lambda_b-\lambda_c)}\,(\phi, \theta, -\phi)\,A_{\lambda_b\,\lambda_c}.$$

The quantity $A_{\lambda\,\lambda'}$ is a constant that describes the coupling between the final state helicities.

D represents a Wigner D-function defined in the following manner:

$$D^{j*}_{m'\,m}(\phi,\theta,-\phi) = d^{j}_{m'\,m}(\theta)e^{i\phi(m'-m)},$$

and the d-function is related to the spherical harmonics (using the notation defined in [9]). The d-functions of interest are:

$$\begin{aligned}
d^{0}_{0\,0} &= constant \\
d^{\frac{1}{2}}_{\frac{1}{2}\,\frac{1}{2}} &= \cos\frac{\theta}{2} \\
d^{\frac{1}{2}}_{\frac{1}{2}\,-\frac{1}{2}} &= -\sin\frac{\theta}{2} \\
d^{\frac{3}{2}}_{\frac{1}{2}\,\frac{1}{2}} &= \frac{3\cos\theta-1}{2}\cos\frac{\theta}{2} \\
d^{\frac{3}{2}}_{\frac{1}{2}\,-\frac{1}{2}} &= -\frac{3\cos\theta+1}{2}\sin\frac{\theta}{2}.
\end{aligned}$$

The d-functions also have special properties under the transformation of indices $\{m', m\} \rightarrow \{m, m'\}$, $\{m', m\} \rightarrow \{-m, -m'\}$, and $\{m', m\} \rightarrow \{-m', -m\}$. For example:

$$\begin{aligned}
d^{j}_{-\frac{1}{2}\,\frac{1}{2}} = -d^{j}_{\frac{1}{2}\,-\frac{1}{2}} &\implies \left(d^{j}_{-\frac{1}{2}\,\frac{1}{2}}\right)^2 = \left(d^{j}_{\frac{1}{2}\,-\frac{1}{2}}\right)^2 \\
d^{j}_{-\frac{1}{2}\,-\frac{1}{2}} = d^{j}_{\frac{1}{2}\,\frac{1}{2}} &\implies \left(d^{j}_{-\frac{1}{2}\,-\frac{1}{2}}\right)^2 = \left(d^{j}_{\frac{1}{2}\,\frac{1}{2}}\right)^2. \\
d^{j}_{-\frac{1}{2}\,-\frac{1}{2}} = d^{j}_{\frac{1}{2}\,\frac{1}{2}} &\implies \left(d^{j}_{-\frac{1}{2}\,-\frac{1}{2}}\right)^2 = \left(d^{j}_{\frac{1}{2}\,\frac{1}{2}}\right)^2.
\end{aligned}$$

For a sequence of decays, the amplitudes for each decay are multiplied. We apply this general formalism to the $B^- \rightarrow \Sigma_c(2455)^0\overline{p}$, $\Sigma_c(2455)^0 \rightarrow \Lambda_c^+\pi^-$ decay.

Helicity formalism for $B^- \to \Sigma_c(2455)^0\overline{p}$, $\Sigma_c(2455)^0 \to \Lambda_c^+\pi^-$

This section describes the helicity formalism for $B^- \to \Sigma_c(2455)^0\overline{p}$, $\Sigma_c(2455)^0 \to \Lambda_c^+\pi^-$. The spins of the relevant particles are listed:

$$\begin{aligned} J(B^-) &= 0 \\ J(\Sigma_c(2455)^0) &= \frac{1}{2}, \frac{3}{2}, \frac{5}{2} \\ J(\overline{p}) &= \frac{1}{2} \\ J(\Lambda_c^+) &= \frac{1}{2} \\ J(\pi^-) &= 0. \end{aligned}$$

The spin of the Λ_c^+ has not been measured [9], but we will assume $J(\Lambda_c^+) = \frac{1}{2}$.

The total decay amplitude for the sequence of two-body decays $B^- \to \Sigma_c(2455)^0\overline{p}$, $\Sigma_c(2455)^0 \to \Lambda_c^+\pi^-$ is thus[1]:

$$\begin{aligned} \mathcal{A}\left(M, \lambda_{\overline{p}}, \lambda_{\Lambda_c^+}\right) = {} & D^{J(B^-)*}_{M\,(\lambda_{\overline{p}} - \lambda_{\Sigma_c^0})}\left(\phi, \theta, -\phi\right) A_{\lambda_{\overline{p}}\,\lambda_{\Sigma_c^0}} \\ & \times D^{J(\Sigma_c^0)*}_{-\lambda_{\Sigma_c^0}\,(\lambda_{\Lambda_c^+} - \lambda_{\pi^-})}\left(\phi', \theta', -\phi'\right) B_{\lambda_{\Lambda_c^+}\,\lambda_{\pi^-}} \end{aligned} \tag{B.1}$$

We define the z-axis along the momentum direction of the $\overline{p}$ in the B^- rest frame and the z'-axis along the momentum direction of the Λ_c^+ in the Σ_c^0 rest frame. There is only one initial state of the B^- (only $M = 0$). Since the helicities of the $\overline{p}$ and Λ_c^+ are not measured, we sum over final states after squaring the amplitude to get the angular distribution:

$$\frac{d^2\sigma}{d\Omega} = \sum_{\lambda_{\overline{p}}, \lambda_{\Lambda_c^+}} |\mathcal{A}\left(0, \lambda_{\overline{p}}, \lambda_{\Lambda_c^+}\right)|^2 \tag{B.2}$$

Because the B^- is a scalar, the spin and helicity (λ) of the $\overline{p}$ defines the helicity of the

---

[1] See p.30, equation 6.16 in [54], where $\psi = B^-, \gamma_1 = \overline{p}, \eta' = \Sigma_c^0, \gamma_2 = \Lambda_c^+, \rho^0 = \pi^-$.

Σ_c^0, $\lambda_{\Sigma_c^0} = \lambda_{\overline{p}} = \pm\frac{1}{2}$. The allowed helicities of the relevant particles are listed:

$$\begin{aligned}
\lambda_{\Sigma_c^0} = \lambda_{\overline{p}} &= \pm\frac{1}{2} \\
\lambda_{\Lambda_c^+} &= \pm\frac{1}{2} \\
\lambda_{\pi^-} &= 0.
\end{aligned}$$

There are four distinct decay amplitudes:

$$\begin{aligned}
\mathcal{A}\left(0, \frac{1}{2}, \frac{1}{2}\right) &= \left[D^{0*}_{0\,0}\left(\phi, \theta, -\phi\right) A_{\frac{1}{2}\,\frac{1}{2}}\right] \left[D^{J(\Sigma_c^0)*}_{-\frac{1}{2}\,\frac{1}{2}}\left(\phi', \theta', -\phi'\right) B_{\frac{1}{2}\,0}\right] \\
\mathcal{A}\left(0, \frac{1}{2}, -\frac{1}{2}\right) &= \left[D^{0*}_{0\,0}\left(\phi, \theta, -\phi\right) A_{\frac{1}{2}\,\frac{1}{2}}\right] \left[D^{J(\Sigma_c^0)*}_{-\frac{1}{2}\,-\frac{1}{2}}\left(\phi', \theta', -\phi'\right) B_{-\frac{1}{2}\,0}\right] \\
\mathcal{A}\left(0, -\frac{1}{2}, \frac{1}{2}\right) &= \left[D^{0*}_{0\,0}\left(\phi, \theta, -\phi\right) A_{-\frac{1}{2}\,-\frac{1}{2}}\right] \left[D^{J(\Sigma_c^0)*}_{\frac{1}{2}\,\frac{1}{2}}\left(\phi', \theta', -\phi'\right) B_{\frac{1}{2}\,0}\right] \\
\mathcal{A}\left(0, -\frac{1}{2}, -\frac{1}{2}\right) &= \left[D^{0*}_{0\,0}\left(\phi, \theta, -\phi\right) A_{-\frac{1}{2}\,-\frac{1}{2}}\right] \left[D^{J(\Sigma_c^0)*}_{\frac{1}{2}\,-\frac{1}{2}}\left(\phi', \theta', -\phi'\right) B_{-\frac{1}{2}\,0}\right].
\end{aligned}$$

We take the magnitude squared of each term, collecting constants (neglecting overall constants), and inserting d-functions. Note that the only angular dependence is on θ':

$$\begin{aligned}
\left|\mathcal{A}\left(0, \frac{1}{2}, \frac{1}{2}\right)\right|^2 &\propto \left|A_{\frac{1}{2}\,\frac{1}{2}}\right|^2 \left|B_{\frac{1}{2}\,0}\right|^2 \left(d^{J(\Sigma_c^0)}_{-\frac{1}{2}\,\frac{1}{2}}\left(\theta'\right)\right)^2 \\
\left|\mathcal{A}\left(0, \frac{1}{2}, -\frac{1}{2}\right)\right|^2 &\propto \left|A_{\frac{1}{2}\,\frac{1}{2}}\right|^2 \left|B_{-\frac{1}{2}\,0}\right|^2 \left(d^{J(\Sigma_c^0)}_{-\frac{1}{2}\,-\frac{1}{2}}\left(\theta'\right)\right)^2 \\
\left|\mathcal{A}\left(0, -\frac{1}{2}, \frac{1}{2}\right)\right|^2 &\propto \left|A_{-\frac{1}{2}\,-\frac{1}{2}}\right|^2 \left|B_{\frac{1}{2}\,0}\right|^2 \left(d^{J(\Sigma_c^0)}_{\frac{1}{2}\,\frac{1}{2}}\left(\theta'\right)\right)^2 \\
\left|\mathcal{A}\left(0, -\frac{1}{2}, -\frac{1}{2}\right)\right|^2 &\propto \left|A_{-\frac{1}{2}\,-\frac{1}{2}}\right|^2 \left|B_{-\frac{1}{2}\,0}\right|^2 \left(d^{J(\Sigma_c^0)}_{\frac{1}{2}\,-\frac{1}{2}}\left(\theta'\right)\right)^2.
\end{aligned} \tag{B.3}$$

We can now compute the angular distribution for $B^- \to \Sigma_c(2455)^0\overline{p}$, $\Sigma_c(2455)^0 \to \Lambda_c^+\pi^-$ by summing the magnitudes of the decay amplitudes, again neglecting any overall constants:

$$\begin{aligned}\frac{dN}{d\cos\theta'} &\propto \left|A_{\frac{1}{2}\,\frac{1}{2}}\right|^2\left[\left|B_{\frac{1}{2}\,0}\right|^2\left(d^{J(\Sigma_c^0)}_{-\frac{1}{2}\,\frac{1}{2}}(\theta')\right)^2+\left|B_{-\frac{1}{2}\,0}\right|^2\left(d^{J(\Sigma_c^0)}_{\frac{1}{2}\,\frac{1}{2}}(\theta')\right)^2\right]\\ &+\left|A_{-\frac{1}{2}\,-\frac{1}{2}}\right|^2\left[\left|B_{\frac{1}{2}\,0}\right|^2\left(d^{J(\Sigma_c^0)}_{\frac{1}{2}\,\frac{1}{2}}(\theta')\right)^2+\left|B_{-\frac{1}{2}\,0}\right|^2\left(d^{J(\Sigma_c^0)}_{-\frac{1}{2}\,\frac{1}{2}}(\theta')\right)^2\right]\\ &\propto \left(d^{J(\Sigma_c^0)}_{\frac{1}{2}\,\frac{1}{2}}(\theta')\right)^2+\alpha\left(d^{J(\Sigma_c^0)}_{\frac{1}{2}\,-\frac{1}{2}}(\theta')\right)^2,\end{aligned} \tag{B.4}$$

collecting constants and defining an intermediate parameter α as:

$$\alpha\equiv\frac{\left|A_{\frac{1}{2}\,\frac{1}{2}}\right|^2\left|B_{-\frac{1}{2}\,0}\right|^2+\left|A_{-\frac{1}{2}\,-\frac{1}{2}}\right|^2\left|B_{\frac{1}{2}\,0}\right|^2}{\left|A_{\frac{1}{2}\,\frac{1}{2}}\right|^2\left|B_{\frac{1}{2}\,0}\right|^2+\left|A_{-\frac{1}{2}\,-\frac{1}{2}}\right|^2\left|B_{-\frac{1}{2}\,0}\right|^2}. \tag{B.5}$$

If $J(\Sigma_c^0)=\frac{1}{2}$,

$$\begin{aligned}\frac{dN}{d\cos\theta'} &\propto \left(\cos\frac{\theta'}{2}\right)^2+\alpha\left(-\sin\frac{\theta'}{2}\right)^2\\ &\propto 1+\frac{1-\alpha}{1+\alpha}\cos\theta'.\end{aligned} \tag{B.6}$$

If $J(\Sigma_c^0)=\frac{3}{2}$,

$$\begin{aligned}\frac{dN}{d\cos\theta'} &\propto \left(\frac{1}{2}\left(3\cos\theta'-1\right)\cos\frac{\theta'}{2}\right)^2+\alpha\left(-\frac{1}{2}\left(3\cos\theta'+1\right)\sin\frac{\theta'}{2}\right)^2\\ &\propto \left(3\cos\theta'-1\right)^2\cos^2\frac{\theta'}{2}+\alpha\left(3\cos\theta'+1\right)^2\sin^2\frac{\theta'}{2}\\ &\propto 1+3\cos^2\theta'+\frac{1-\alpha}{1+\alpha}\left(9\cos^3\theta'-5\cos\theta'\right).\end{aligned} \tag{B.7}$$

And if $J(\Sigma_c^0)=\frac{5}{2}$,

$$\frac{dN}{d\cos\theta'}\propto\left(2\cos\frac{\theta'}{2}+\cos\frac{3\theta'}{2}+5\cos\frac{5\theta'}{2}\right)^2+\alpha\left(-2\sin\frac{\theta'}{2}+\sin\frac{3\theta'}{2}-5\sin\frac{5\theta'}{2}\right)^2. \tag{B.8}$$

Note that if $\alpha = 1$ the angular distributions become symmetric. To simplify these relations a bit more, we can now define an asymmetry parameter β:

$$\beta \equiv \frac{1-\alpha}{1+\alpha} = \left(\frac{\left|A_{\frac{1}{2}\frac{1}{2}}\right|^2 - \left|A_{-\frac{1}{2}-\frac{1}{2}}\right|^2}{\left|A_{\frac{1}{2}\frac{1}{2}}\right|^2 + \left|A_{-\frac{1}{2}-\frac{1}{2}}\right|^2} \right) \left(\frac{\left|B_{\frac{1}{2}0}\right|^2 - \left|B_{-\frac{1}{2}0}\right|^2}{\left|B_{\frac{1}{2}0}\right|^2 + \left|B_{-\frac{1}{2}0}\right|^2} \right). \tag{B.9}$$

The asymmetry β may be non-zero if we were considering a weak decay. Although we do not need to introduce β, we do so for easy comparison with the literature (e.g., Ref. [34]).

The $B_{\lambda\lambda'}$ coefficients describe the helicity couplings for $\mathit{\Sigma}_c(2455)^0 \to \mathit{\Lambda}_c^+\pi^-$, and are related through

$$B_{\frac{1}{2}0} = \eta_{\overline{p}}\eta_{\mathit{\Lambda}_c^+}\eta_{\mathit{\Sigma}_c^0}\,(-1)^{\left(J(\overline{p})+J(\mathit{\Lambda}_c^+)+J(\mathit{\Sigma}_c^0)\right)}\,B_{-\frac{1}{2}0}, \tag{B.10}$$

where η_i is the parity of particle i. We can only write down the relation in Eqn. B.10 because $\mathit{\Sigma}_c(2455)^0 \to \mathit{\Lambda}_c^+\pi^-$ is a strong decay, which means that *parity is conserved.* The parities of the p and $\mathit{\Lambda}_c^+$ are defined to be positive [9], but we do not know the parity of the $\mathit{\Sigma}_c^0$. Also recall that $\eta(\text{fermion}) = -\eta(\text{antifermion})$. From Eqn. B.10, we see that an overall minus sign is irrelevant in the squared amplitudes, and $\left|B_{\frac{1}{2}0}\right|^2 = \left|B_{-\frac{1}{2}0}\right|^2$. Therefore, $\beta = 0$ (Eqn. B.9).

Following from Eqn. B.6, the angular distribution for $J(\mathit{\Sigma}_c^0) = \frac{1}{2}$ is

$$\frac{dN}{d\cos\theta_h} \propto 1. \tag{B.11}$$

Following from Eqn. B.7, the angular distribution for $J(\mathit{\Sigma}_c^0) = \frac{3}{2}$ is

$$\frac{dN}{d\cos\theta_h} \propto 1 + 3\cos^2\theta'. \tag{B.12}$$

And following from Eqn. B.8, the angular distribution for $J(\mathit{\Sigma}_c^0) = \frac{5}{2}$ is

$$\frac{dN}{d\cos\theta_h} \propto 1 - 2\cos^2\theta' + 5\cos^4\theta'. \tag{B.13}$$

To match the notation in the rest of this document, we substitute $\theta' \to \theta_h$. In summary, the possible angular distributions for $B^- \to \mathit{\Sigma}_c(2455)^0\overline{p}$, $\mathit{\Sigma}_c(2455)^0 \to \mathit{\Lambda}_c^+\pi^-$ are

$$\begin{aligned}
J(\mathit{\Sigma}_c^0) = \frac{1}{2} \quad &: \quad \frac{dN}{d\cos\theta_h} \propto 1 \\
J(\mathit{\Sigma}_c^0) = \frac{3}{2} \quad &: \quad \frac{dN}{d\cos\theta_h} \propto 1 + 3\cos^2\theta_h \\
J(\mathit{\Sigma}_c^0) = \frac{5}{2} \quad &: \quad \frac{dN}{d\cos\theta_h} \propto 1 - 2\cos^2\theta_h + 5\cos^4\theta_h.
\end{aligned}$$

Bibliography

[1] *BABAR* Collaboration, B. Aubert *et al.*, "Measurement of the $B^+ \to p\overline{p}K^+$ branching fraction and study of the decay dynamcs," Phys. Rev. D **72**, 051101 (2005).

[2] *BABAR* Collaboration, B. Aubert *et al.*, "Measurements of the decays $B^0 \to \overline{D}^0 p\overline{p}$, $B^0 \to \overline{D}^{*0} p\overline{p}$, $B^0 \to D^- p\overline{p}\pi^+$, and $B^0 \to D^{*-} p\overline{p}\pi^+$," Phys. Rev. D **74**, 051101 (2006).

[3] Heavy Flavor Averaging Group, E. Barberio *et al.*, "Averages of b-hadron properties at the end of 2005," hep-ex/0603003 (2006);

BABAR Collaboration, B. Aubert *et al.*, "Measurement of the branching fraction and photon energy moments of $B \to X_s\gamma$ and $A_{CP}(B \to X_{s+d}\gamma)$," Phys. Rev. Lett. **97**, 171803 (2006);

BABAR Collaboration, B. Aubert *et al.*, "Measurement of the $B \to X_s\gamma$ branching fraction and photon spectrum from a sum of exclusive final states," Phys. Rev. D **72**, 052004 (2005);

Belle Collaboration, P. Koppenburg *et al.*, "Inclusive measurement of the photon energy spectrum in $b \to s\gamma$ decays," Phys. Rev. Lett. **93**, 061803 (2004);

Belle Collaboration, K. Abe *et al.*, "A measurement of the branching fraction for the inclusive $B \to X_s\gamma$ decays with the Belle detector," Phys. Lett. B **511**, 151 (2001);

CLEO Collaboration, S. Chen *et al.*, "Branching fraction and photon energy spectrum for $b \to s\gamma$," Phys. Rev. Lett. **87**, 251807 (2001).

[4] Belle Collaboration, "Study of $B^+ \to p\overline{\Lambda}\gamma, p\overline{\Lambda}\pi^0$, and $B^0 \to p\overline{\Lambda}\pi^-$," hep-ex/0704.2672 (2007).

[5] M. Misiak *et al.*, “Estimate of $\mathcal{B}(\overline{B} \to X_s\gamma)$ at $\mathcal{O}(\alpha_s^2)$,” Phys. Rev. Lett. **98**, 022002 (2007);

T. Becher and M. Neubert, “Analysis of $\mathcal{B}(\overline{B} \to X_s\gamma)$ at NNLO with a cut on photon energy,” Phys. Rev. Lett. **98**, 022003 (2007).

[6] C. Q. Geng and Y. K. Hsiao, “Radiative baryonic B decays,” Phys. Lett. B **610**, 67 (2005);

H.-Y. Cheng and K.-C. Yang, “Penguin induced radiative baryonic B decays,” Phys. Lett. B **533**, 271 (2002).

[7] Unless specifically stated, conjugate decay modes are assumed throughout this dissertation.

[8] A. V. Manohar and C. T. Sachrajda, “Quark Masses,” in [9], pp. 505 – 525.

[9] Particle Data Group, W.-M. Yao *et al.*, “The Review of Particle Physics,” J. Phys. **G33**, 1 (2006) and 2007 partial update for the 2008 edition.

[10] C. Amsler, T. DeGrand, and B. Krusche, “Quark Model,” in [9], pp. 165 – 184.

[11] SELEX Collaboration, M. Mattson *et al.*, “First observation of the doubly charmed baryon $\Xi_c^+ c$,” Phys. Rev. Lett. **89**, 112001 (2002);

SELEX Collaboration, M. A. Moinester *et al.*, “First observation of doubly charmed baryons,” Czech. J. Phys. **53**, B201 (2003);

SELEX Collaboration, A. Ocherashvili *et al.*, “Confirmation of the double charm baryon $\Xi_{cc}(3520)^+$ via its decay to pD^+K^-,” Phys. Lett. B **628**, 18 (2005).

[12] FOCUS Collaboration, C. Riccardi *et al.*, “Charmed baryons and heavy quark spectroscopy results from FOCUS,” Prepared for 31st International Conference on High Energy Physics (ICHEP 2002), Amsterdam, The Netherlands, 24 – 31 Jul 2002.

[13] *BABAR* Collaboration, B. Aubert *et al.*, “Search for doubly charmed baryons Ξ_{cc}^+ and Ξ_{cc}^{++} in *BABAR*,” Phys. Rev. D **74**, 011103 (2006).

[14] Belle Collaboration, R. Mizuk *et al.*, “Observation of an isotriplet of excited charmed baryons decaying to $\Lambda_c^+\pi$,” Phys. Rev. Lett. **94**, 122002 (2005).

[15] C. G. Wohl, "Charmed Baryons," in [9], pp. 1078 – 1082.

[16] Diagram courtesy of M. Thompson, Ph. D., University of Cambridge.

[17] ARGUS Collaboration, H. Albrecht *et al.*, "Measurement of inclusive baryon production in B meson decays," Z. Phys. C **56**, 1 (1992).

[18] ARGUS Collaboration, H. Albrecht *et al.*, "Observation of the charmless B meson decays," Phys. Lett. B **209**, 119 (1988).

[19] CLEO Collaboration, C. Bebek *et al.*, "A search for $b \to u$ transitions in exclusive hadronic B meson decays," Phys. Rev. Lett. **62**, 2436 (1989).

[20] M. Jarfi *et al.*, "Pole model of B-meson decays into baryon-antibaryon pairs," Phys. Rev. D **43**, 1599 (1991).

[21] N. G. Deshpande *et al.*, "Remarks on B decays into baryonic modes and possible implications for V_{ub}," Mod. Phys. Lett. **A3**, 749 (1988).

[22] H.-Y. Cheng and K.-C. Yang, "Hadronic B decays to charmed baryons," Phys. Rev. D **67**, 034008 (2003).

[23] H.-Y. Cheng and K.-C. Yang, "Charmful baryonic B decays $\overline{B}^0 \to \mathit{\Lambda}_c^+ \overline{p}$ and $B^0 \to \mathit{\Lambda}_c^+ \overline{p} \pi(\rho)$," Phys. Rev. D **65**, 054028 (2002).

[24] P. Ball and H. G. Dosch, "Branching ratios of exclusive decays of bottom mesons into baryon-antibaryon pairs," Z. Phys. C **51**, 445 (1991).

[25] L. J. Reinders *et al.*, "Hadron properties from QCD sum rules," Phys. Rep. **127**, 1 (1985).

[26] V. Chernyak and I. Zhitnitsky, "B-meson exclusive decays into baryons ," Nucl. Phys. B **345**, 137 (1990).

[27] T. D. Cohen *et al.*, "QCD sum rules and applications to nuclear physics," Prog. Part. Nucl. Phys. **35**, 221 (1995).

[28] W.-S. Hou and A. Soni, "Pathways to rare baryonic B decays," Phys. Rev. Lett. **86**, 4247 (2001).

[29] CLEO Collaboration, S. A. Dytman *et al.*, "Measurement of exclusive B decays to final states containing a charmed baryon," Phys. Rev. D **66**, 091101 (2002).

[30] Belle Collaboration, N. Gabyshev *et al.*, "Study of decay mechanisms in $B^- \to \Lambda_c^+ \overline{p} \pi^-$ decays and observation of low-mass structure in the $\Lambda_c^+ \overline{p}$ system," Phys. Rev. Lett. **97**, 242001 (2006).

[31] Belle Collaboration, N. Gabyshev *et al.*, "Observation of the decay $\overline{B}^0 \to \Lambda_c^+ \overline{p}$," Phys. Rev. Lett. **90**, 121802 (2003).

[32] Belle Collaboration, N. Gabyshev *et al.*, "Study of exclusive B decays to charmed baryons," Phys. Rev. D **66**, 091102 (2002).

[33] *BABAR* Collaboration, B. Aubert *et al.*, "Meausrement of the branching fractions of the decays $\overline{B}^0 \to \Lambda_c^+ \overline{p}$ and $B^- \to \Lambda_c^+ \overline{p} \pi^-$," hep-ex/0607055, presented at ICHEP 2006.

[34] *BABAR* Collaboration, B. Aubert *et al.*, "Measurement of the spin of the Ω^- hyperon," Phys. Rev. Lett. **97**, 112001 (2006).

[35] *BABAR* Collaboration, B. Aubert *et al.*, "The *BABAR* Detector," Nucl. Instr. Methods Phys. Res., Sect. A **479**, 1 (2002).

[36] J. Seeman *et al.*, "A luminosity of 10^{34} cm^{-2}s^{-1} in the PEP-II B Factory," Proceedings of the European Particle Accelerator Conference, Edinburgh, 643 (2006).

[37] V. Re *et al.*, "Radiation hardness and monitoring of the *BABAR* vertex tracker," Nucl. Instr. Methods Phys. Res., Sect. A **518**, 290 (2004).

[38] G. Benelli *et al.*, "The *BABAR* LST Detector High Voltage System: Design and Implementation," Nuclear Science Symposium Conference Record, 2005 (IEEE, New York, 2005), Vol. 2, p. 1145.

[39] W. Menges *et al.*, "The *BABAR* Muon System Upgrade," Nuclear Science Symposium Conference Record, 2005 (IEEE, New York, 2005), Vol. 3, p. 1470.

[40] M. R. Convery *et al.*, "A novel technique for the production of large area z-coordinate readout planes for the *BABAR* muon system," Nucl. Instr. Methods Phys. Res., Sect. A **556**, 134 (2006).

[41] C. Hearty, "Hadronic Event Selection and B-Counting for Inclusive Charmonium Measurements," *BABAR* Analysis Document 30 (2000).

[42] D. J. Lange, Nucl. Instrum. Methods Phys. Res., Sect. A **462**, 152 (2001).

[43] T. Sjostrand *et al.*, JHEP 0605, 026 (2006).

[44] S. Agostinelli *et al.* (GEANT4 Collaboration), Nucl. Instrum. Methods Phys. Res., Sect. A **506**, 250 (2003).

[45] R. E. Kalman, "A new approach to linear filtering and prediction problems," Trans. ASME—J. Basic Eng., **82** Series D, 35 (1960).

[46] W. D. Hulsbergen, "Decay chain fitting with a Kalman filter," Nucl. Instr. Methods Phys. Res., Sect. A **552**, 566 (2005).

[47] W. Hulsburgen, *et al.*, "Measurement of the branching ratio and the time-dependent CP asymmetries for $B^0 \to K^0_S \pi^0$ decays on run $1-4$ data," *BABAR* Analysis Document 904 (2005).

[48] ARGUS Collaboration, H. Albrecht *et al.*, "Exclusive hadronic decays of B mesons," Z. Phys. C **48**, 543 (1990).

[49] R. H. Dalitz, "On the analysis of τ-meson data and the nature of the τ-meson," Phil. Mag. **44**, 1068 (1953).

[50] W. Dunwoodie, "Suggestion for the parameterization of Dalitz plot efficiency," unpublished (2004); this document can be found in an appendix of *BABAR* Analysis Document 1670; the original version is located at `http://www.slac.stanford.edu/~wmd/bbkinematics/dalitz_efficiency.note`.

[51] M. Pivk and F. R. Le Diberder, Nucl. Instr. Methods Phys. Res., Sect. A **555**, 356 (2005).

[52] L. Lyons *et al.*, Nucl. Instr. Methods Phys. Res., Sect. A **270**, 110 (1988).

[53] M. Jacob and G. C. Wick, "On the general theory of collisions for particles with spin," Annals Phys. **7** 404 (1959).

[54] J. Richman, "An experimenter's guide to the helicity formalism," CALT-68-1148 (1984).

[55] D. Kirkby, "Helicity Formalism," a `Mathematica` notebook (2005); `http://www.slac.stanford.edu/~bondioli/Baryonic%20B%20decays/Tools/helicityformalism.nb`.